UNIVERSITÀ DEGLI STUDI DI PALERMO

PhD Course in Chemical, Environmental, Biomedical, Hydraulic and Materials Engineering
Dipartimento di Ingegneria
Settore Scientifico Disciplinare (ING-IND/24)

Photocatalysis Applications: Photoreforming of Biomass Derivatives and Organic Drugs Removal. Preparation and Characterization of Nanocomposites Materials

PhD Candidate:
Muhammad Umair

PhD Course Coordinator:
Prof. Giorgio Domenico Maria Micale

Supervisors:
Prof. Vittorio Loddo

Co-Supervisors:
Prof. Marianna Bellardita

XXXVII CYCLE
GRADUATION YEAR 2025

UNIVERSITÀ DEGLI STUDI DI PALERMO

PhD Course in Chemical, Environmental, Biomedical, Hydraulic and Materials Engineering
Dipartimento di Ingegneria
Settore Scientifico Disciplinare (ING-IND/24)

Photocatalysis Applications: Photoreforming of Biomass Derivatives and Organic Drugs Removal. Preparation and Characterization of Nanocomposites Materials

PhD Candidate:
Muhammad Umair

PhD Course Coordinator:
Prof. Giorgio Domenico Maria Micale

Supervisors:
Prof. Vittorio Loddo

Co-Supervisors:
Prof. Marianna Bellardita

XXXVII CYCLE
GRADUATION YEAR 2025

Dedicated to

my loving parents

and

late sister (Sheeza Khizar)

ACKNOWLEDGEMENT

Writing an acknowledgement means that I am going to complete my Ph.D. journey; most important, it is very close to completing one important chapter of my life. At this moment, I would like to express my gratitude to all those people who in any way have accompanied me on my journey, not only with a concrete contribution to my research, but also by accompanying me with a cup of coffee in my daily life.

All praise is due to **Allah**, the Creator and Sustainer of the universe. I am deeply thankful for His countless blessings, which have guided me through the challenges of this Ph.D. research and granted me the ability to achieve my targets.

I would like to express my sincerest gratitude to my dearest supervisors, **Prof. Vittorio Loddo** and **Prof. Marianna Bellardita,** for their support, encouragement and inspiration towards the completion of my Ph.D. journey. With their continuing guidance throughout these three years of my Ph.D., I gained professional skills in the field of photocatalysis that will surely benefit me for my future career. Their suggestions, insights and discussions helped me in shaping this thesis. They are more than supervisors; I will remember everything that they did for me to boost my career and improve my human experience.

I would like to acknowledge **Prof. Leonardo Palmisano** for his valuable suggestions, guidance and constant support throughout my Ph.D. journey.

I would like to thank **Prof. Monica Santamaria** and **Prof. Francesco di Franco** for their valuable suggestions and collaboration.

I would like to thank **Prof. Giovanni Palmisano and Prof. Albin Pintar** for helping me with characterizations and collaboration.

I would like to express special gratitude to **Prof. Sixto Malato Rodríguez** for allowing me to gain practical experience in the field of photocatalysis at Plataforma Solar de Almería (PSA) during my mobility period.

I would like to thank the departmental coordinator **Prof. Giorgio Domenico Maria Micale** for helping me with the administration work. He is more than a coordinator and always motivated me during this journey.

I would like to express my heartful gratitude to my lab mates **Tayyaba Kanwal** and **Claudio Maria Pecoraro** not only for the help and support but also for the happy moments in the lab.

I would like to thank colleagues from Applied Electrochemistry Lab; **Dr. Andrea Zaffora**, **Dr. Giada Tranchida**, **Davide Pupillo**, **Valentina Maria Volanti**, **Vincenzo Verro**, **Nicola Ingargiola**, **Maria Lucia Lazzara**, and **Elena Giordano** for help in doing experiments and happy moments in the lab.

I would like to express my heartful gratitude to **Ahmed Malek Djaballah** for collaboration, support and happy moments in the lab.

I would like to thank **Government of Italy** for providing me a fully funded scholarship to complete my higher education at Università degli Studi di Palermo.

My sincere gratitude to my friends **Syed Ibrar Hussain**, **Muhammad Adnan**, **Fazal Subhan, Malik Ali Judge, Muhammad Uzair,** and **Hanif Ullah** for their friendship, affection, and love. Thank you for being my source of joy and happiness through this journey. Our hikes and gatherings gave me strength whenever I needed it most. Your companionship provided an opportunity to see the beauty of life beyond the thesis and to keep the balance between academic and social life.

I would like to express deepest gratitude to my teacher and friend **Muhammad Kashif Sabree** for his endless efforts, help and guidance throughout my study.

I would like to say thank to my best friends since childhood **Muhammad Zeeshan**, **Sajid Ali Dogar,** and **Amir Sohail** for your friendship, love, and happy moment that we spent together.

I would like to express special gratitude to my beloved father **Khizar Hayat** and mother **Farzana Khizar** whose support, love, and belief in my abilities have been the foundation of all that I have accomplished. Your guidance and endless sacrifices have not only shaped my career but also the person that I have become. You have been always a source of inspiration for me throughout my life. This Ph.D. journey would not have been possible without your belief in me and for everything, I am thankful to you.

I would like to thank my family members **Zahoor Hussain**, **Manzoor Hussain**, **Khalid Nawaz**, **Muhammad Waqar**, **Rizwan Jaffar**, **Adeel Saleem** for continuing support and motivation throughout my academic carrier.

I would like to special thank my sisters and younger brother **Muhammad Ali Hamza** who have always been there for me and silently supporting me in my life. Your humor and guidance always kept me motivated through the challenges and I am lucky to have you all by my side. In this Ph.D. journey, I tragically lost my sister **Sheeza Khizar**, your memories will always stay with me. Though you are not with me but your endless love and the bond we have had together guided me through every step. This achievement is dedicated to you, I will always remember you in my prayers.

Thank you everyone for everything during this journey.

Muhammad Umair

JOURNAL PUBLICATIONS

1. **Muhammad Umair**, Alba Ruiz-Aguirre, Ilaria Berruti, Sixto Malato Rodríguez, Leonardo Palmisano, Vittorio Loddo, Marianna Bellardita. Biomass derivatives photoreforming in pilot plant scale to obtain H_2 under green conditions by using ball milling Cu_2O-TiO_2 P25 photocatalysts. *Chemical Engineering Journal* **2025,** 504, 158585. https://doi.org/10.1016/j.cej.2024.158585
2. **Muhammad Umair,** Claudio Maria Pecoraro, Francesco Di Franco, Monica Santamaria, Leonardo Palmisano, Vittorio Loddo, Marianna Bellardita. Enhanced aqueous photocatalytic selective oxidation of HMF using simulated sunlight: Comparison of the performance of different photocatalysts. *Sustainable Materials and Technologies* **2025**, 43, e01188. https://doi.org/10.1016/j.susmat.2024.e01188
3. **Muhammad Umair,** Vittorio Loddo, Leonardo Palmisano, Marianna Bellardita, in Advances in Photocatalysis, Electrocatalysis and Photoelectrocatalysis for Hydrogen Production, ed. R. G. Balakrishna, R. Shwetharani, and T. Jayaraman, Royal Society of Chemistry, **2024**, 47, ch. 1, pp. 1-29. https://doi.org/10.1039/9781837674664-00001
4. **Muhammad Umair**, Claudio Maria Pecoraro, Francesco Di Franco, Monica Santamaria, Leonardo Palmisano, Vittorio Loddo, Marianna Bellardita. Efficient Photocatalytic Partial Oxidation of Aromatic Alcohols by Using $ZnIn_2S_4$ under Green Conditions. *ChemSusChem* **2024**, 17, e202400404. https://doi.org/10.1002/cssc.202400404
5. **Muhammad Umair,** Ahmed Malek Djaballah, Marianna Bellardita, Radia Bagtache, Leonardo Palmisano, Mohamed Trari. Visible-Light Photoreforming of Biomass Derivatives through MBi_2O_4-P25 Heterostructures: Study of the Influence of Metals (M= Cu, Ni, Zn, Co). *Advanced Sustainable Systems* **2024**, 8, 2400298. https://doi.org/10.1002/adsu.202400298
6. **Muhammad Umair**, Giovanni Palmisano, Reem Al Sakkaf, Samar Al Jitan, Albin Pintar, Gregor Žerjav, Leonardo Palmisano, Vittorio Loddo, Marianna Bellardita. Pt-Nb_2O_5-TiO_2 based semiconductors for photo-reforming of glucose and fructose aqueous solutions. *Applied Surface Science* **2024**, 648, 159030. DOI: https://doi.org/10.1016/j.apsusc.2023.159030
7. **Muhammad Umair**, Vittorio Loddo, Leonardo Palmisano, Albin Pintar, Gregor Žerjav, Giovanni Palmisano, Samar Al Jitan, Marianna Bellardita. Investigating the activity of modified TiO_2 photocatalysts used for the photoreforming of biomass derivatives. *Journal of Photochemistry and Photobiology A: Chemistry* **2024**, 453, 115654. https://doi.org/10.1016/j.jphotochem.2024.115654
8. **Muhammad Umair**, Tayyaba Kanwal, Vittorio Loddo, Leonardo Palmisano, Marianna Bellardita. Review on Recent Advances in the Removal of Organic Drugs by Advanced Oxidation Processes. *Catalysts* **2023**, 13(11), 1440. https://doi.org/10.3390/catal13111440
9. Ahmed Malek Djaballah, Marianna Bellardita, Leonardo Palmisano, Vittorio Loddo, **Muhammad Umair**, Claudio Maria Pecoraro, Radia Bagtache, Mohamed Trari. Facile preparation of $CuBi_2O_4$/TiO_2 hetero-systems employed for simulated solar-light selective

oxidation of 4-methoxybenzyl alcohol model compound. *Molecular Catalysis* **2023**, 546, 113251. https://doi.org/10.1016/j.mcat.2023.113251

10. **Muhammad Umair**, Leonardo Palmisano, Marianna Bellardita. Comparison between the efficiency of bare and Pt-loaded TiO_2 and $ZnIn_2S_4$ for H_2 production in the presence of triethanolamine, methanol, furfuryl alcohol used as sacrificial agents. *Inorganic Chemistry Communications*. Under review.
11. **Muhammad Umair**, Alba Ruiz Aguirre, Ilaria Berruti, Leonardo Palmisano, Sixto Malato Rodríguez, Vittorio Loddo, Marianna Bellardita. Investigating the photoactivity of Cu_2O-TiO_2 (Home Prepared) composites for H_2 production by photoreforming under natural solar light in a pilot plant photoreactor. *Internation Journal of Hydrogen Energy* . Under review.
12. **Muhammad Umair**, Vittorio Loddo, Tayyaba Kanwal, Leonardo Palmisano, Marianna Bellardita. Efficient photocatalytic removal of drugs in aqueous dispersions by using different TiO_2 based semiconductors. In preparation.
13. Joyce Gloria Villachica Llamosas*, **Muhammad Umair***, Alba Ruiz Aguirre, Ilaria Berruti, Sixto Malato Rodríguez. Effect of the ball milling parameters in the photocatalyst CuO-TiO_2 for hydrogen production. In preparation (* Equal authors).

CONFERENCES PARTICIPATION

1. **Muhammad Umair,** Reem Al Sakkaf, Marianna Bellardita, Vittorio Loddo, Giovanni Palmisano, Leonardo Palmisano, Albin Pintar. Biomass derivatives photoreforming in the presence of TiO_2 based samples. Presented as a poster at 8th International Conference on Semiconductor Photochemistry (SP8), September 11-15, 2023, Strasbourg, France.
2. **Muhammad Umair,** Vittorio Loddo, Leonardo Palmisano, Marianna Bellardita. Glucose and fructose photo-reforming by using modified TiO_2 photocatalysts. Presented as a poster at Congresso Congiunto delle Sezioni Sicilia e Calabria, December 11-12, 2023, Palermo, Italy.
3. Marianna Bellardita, **Muhammad Umair,** Leonardo Palmisano, Vittorio Loddo. Effect of the addition of different metal species on TiO_2 photocatalysts used for glucose and fructose reforming. November 7-8, 2022. Presented as a poster at XXII Congresso Nazionale della Divisione di Chimica Industriale, 2022, Catania, Italy.

LIST OF ABBREVIATIONS

ALD	Aldehyde
AOPs	Advanced oxidation processes
BA	Benzyl alcohol
BET	Brunauer–Emmett–Teller
CA	Cinnamyl alcohol
CB	Conduction band
CDs	Carbon quantum dots
CPC	Compound parabolic collector
DRIFTS	Diffuse reflectance infrared Fourier transform spectroscopy
DRS	Diffuse reflectance spectroscopy
EGD	European green deal
EPR	Electron paramagnetic resonance
FA	Furfuryl alcohol
FTIR	Fourier-transform infrared spectroscopy
HMF	5-hydroxymethyl furfural
HP	Home prepared TiO_2
2-HBA	2-hydroxybenzyl alcohol
4-HBA	4-hydroxybenzyl alcohol
IC	Ionic chromotography
ICP-MS	Inductively coupled plasma mass spectrometry
LCM	Lincomycin
MOF	Metal-organic frameworks
4-MBA	4-methoxy benzyl alcohol
4-MBA	4-methoxybenzyl alcohol
NHE	Normal hydrogen electrode
4-NBA	4-nitrobenzyl alcohol
OP	Oxidation photocatalyst
OTC	Oxytetracycline
PA	Piperonyl alcohol
PL	Photoluminescence spectroscopy
RP	Reduction photocatalyst
SC	Semiconductor
SDGs	Sustainable development goals
SEM	Scanning electron microscopy
STH	Solar to hydrogen conversion

TC	Tetracycline
TEM	Transmission electron microscopy
TEOA	Triethanolamine
TNA	TiO_2 nanotube arrays
TNWs	TiO_2 nanowires
TOC	Total organic carbon
TPD	Temperature programmed desorption
UN	United nations
UV	Ultraviolet
VA	Vanillyl alcohol
VB	Valance band
XPS	X-ray photoelectron spectroscopy
XRD	X-ray diffraction
ZIS	$ZnIn_2S_4$

ABSTRACT

To meet the energy needs of the world, most of the energy is still being obtained from fossil fuels including coal, oil and natural gas. Fossil fuels are not considered environmentally friendly because their combustion releases greenhouse gas emissions that cause global warming. There are several potential advantages to using more renewable energy, such as lowering emissions that contribute to global warming, diversifying energy sources, and reducing reliance on the fossil fuel energy market. Biomass includes all organic material that is derived from plants. The total carbon footprint associated with energy generation can be decreased by combining the use of solar light and fuels obtained from biomass. Hydrogen gas (H_2) is considered as a very efficient, clean and promising energy source. It can be generated from water and renewable energy resources. The importance of using H_2 as a fuel derives from the fact that it has an energy efficiency of 122 $kJ \cdot mol^{-1}$, which is higher than that of gasoline or of any other fossil fuel.

It is a big challenge to develop sustainable options for green H_2 production. In this context, photocatalysis is considered an environmentally friendly process used in photoreforming of organic compounds and pollutant removal to produce contemporary H_2 and high added value compounds. The use of photocatalysis has several advantages for the environment, including mild operating conditions (i.e. room temperature and ambient pressure), the absence of harmful chemical solvents, utilization of solar light as irradiation source, the easy integration with other physical and chemical technologies, e.g. membrane separation.

The main focus of this Ph.D. thesis is to synthesize different TiO_2 based and alternative photocatalysts and investigate their applications towards production of high value chemicals, H_2 production and organic drugs removal. The prepared photocatalysts were characterized by XRD, SEM, TEM, Raman, BET, EPR, PL, DRS, DRIFTS, TPD, FTIR, XPS and EDS. Biomass derivatives including glucose, fructose, glycerol, furfuryl alcohol, ethanol, methanol, formic acid and triethanolamine have been used to produce H_2 and high valuable chemicals, for instance, arabinose, erythrose, gluconic acid, formic acid, furfural, glyceraldehyde, dihydroxyacetone and glycolic acid, are of particular interest for further applications. The results obtained in laboratory scale were extended to pilot plant scale in the Plataforma Solar de Almería (Spain). Notably, the prepared photocatalysts were used for H_2 production in a 25L photoreactor through photoreforming of glycerol (waste generated in biodiesel industries) and other organic compounds under direct sunlight in environmentally green conditions.

$ZnIn_2S_4$, synthesized by a simple hydrothermal method in which the carcinogen thioacetamide, universally used as a precursor, for the first time, replaced successfully the harmless thiourea, was synthetized as alternative TiO_2 photocatalyst and was activated by solar light irradiation. Its photocatalytic efficiency was investigated for the selective oxidation of aromatic alcohols to their corresponding aldehyde, of the lignocellulose derivative 5-hydroxymethyl-2-furfural (HMF) in water solution, and photoreforming of furfuryl alcohol under green conditions. The high value HMF derivatives were 2,5-diformylfuran (FDC), 5-formyl-2-furancarboxylic acid (FCA) and 5-hydroxymethyl-2-furan carboxylic acid (HMFCA), that are of particular interest for the polymer industry; H_2 was produced from triethanolamine, methanol and furfuryl alcohol.

With the growth of population and industrialization, almost all water sources are contaminated mainly by agricultural and industrial waste. Molecules of pharmacological importance present in drugs are widespread in the environment. Their concentrations have been found to range between ng and μg per liter in seawater, lakes, rivers, surface waters, urban wastewater and drinking water. A part of this thesis has been also focused on the photocatalytic degradation of most used organic drugs such as tetracycline, oxytetracycline and lincomycin in the presence of different photocatalysts.

TABLE OF CONTENTS

LIST OF FIGURES

LIST OF TABLES

CHAPTER 1

Introduction

CHAPTER 1

1. Introduction

1.1 Energy

Energy is the backbone of any economy and plays a major role in world progress. A sustainable, safe, and clean energy supply is one of the technological problems addressed with greater intensity in recent decades by scientists as energy consumption in all sectors has grown significantly throughout the world [1, 2]. For this purpose, the production of energy and its sources are very important.

Energy sources can be divided into two main groups, renewable and non-renewable. Solar, biomass, wind, water, and geothermal are renewable energy sources and they can naturally regenerate themselves and have an endless supply. The sources of non-renewable energy are coal, gas, oil, and nuclear power. These sources cannot be recycled or replenished, and their supply is limited. Moreover, non-renewable sources cannot be replicated or recreated to the same extent after they are depleted, their use cannot continue forever. According to predictions, the world's energy consumption will increase to five times its current level by the year 2100 [3].

1.2 Fossil fuels and environmental remediation

Nowadays most of the energy is obtained from fossil fuels including coal, oil and natural gas. Fossil fuels are not considered environmentally friendly because their combustion release 70-75% of greenhouse gas emissions (CO_2) that cause global warming [4]. The temperature of the earth has increased up to 0.6 ^oC since 1900, and if CO_2 emission is not controlled, greenhouse gas emissions could reach the double of its preindustrial level ca. 560 ppm as early as 2035, resulting in a temperature rise that could surpass 5°C [5].

Heat stress, illness, tropical storm intensity, ocean acidity, sea levels, and the melting of glaciers, snowpack, and sea ice are all being increased by global warming [6]. In addition, it damages ecosystems and animal habitats, moves the position of productive crops, and modifies the timing and volume of water supplies. The reason is the worldwide difference among cooling contributors i.e., non-soot aerosol particles and heating contributors such as greenhouse gases, fossil fuels plus biofuels, the soot particles, and the urban heat island effect [7].

In this context, several nations including Italy are closely monitoring the effects of climate change and thinking about how to adapt to negative effects by creating plans with the goals of coordinated solutions to such issue. Promoting investment in low-carbon and renewable energy technology will be crucial to minimizing pollution.

There are several potential advantages to using more renewable energy, such as lowering emissions that contribute to global warming, diversifying energy sources, and reducing reliance on the fossil fuel energy market. Furthermore, carbon-intensive energy sources can be substituted by renewable energy initiatives. Due to the higher labor intensity of the renewable energy sector, expanding the supply of renewable energy may lead to an increase in jobs by creating opportunities in new "green" technologies [8].

1.3 Biomass

Biomass is a term that is associated with all organic materials that are derived from plants. Green plants convert sunlight into plant material through photosynthesis. Chemical energy is released by substances during digestion, combustion, or decomposition when the bonds between adjacent molecules of carbon, hydrogen, and oxygen are broken [9]. Biomass is an excellent alternative energy source for fossil fuels for a more sustainable and clean application because of its organic nature [10, 11].

The environment is not only suffering from the overconsumption of fossil fuels but also for the generation of waste. The use of waste biomass as a substrate is a more appealing option than improper and unscientific methods of disposal because it is readily available, abundant, and non-competitive with food. The conversion of waste biomass into fuels and high value-added products is similar to fossil fuels that were formed a million years ago from biomass [12]. Biomass includes agricultural waste, crops, animal feed waste, wood and wood waste, and wastewater [13]. The total carbon footprint associated with energy generation can be decreased by combining the use of solar light and fuels obtained from biomass [14].

1.4 Solar light

Sunlight can be considered the biggest energy source because its average daily energy (10^{22}J) and its utilization can meet not only the world's annual energy needs but also overcome the pollution problems arising from the use of traditional methods of energy production based on fossil fuels [15].

The conversion of sunlight into a usable form of energy (chemical, electrical or fuel production) has attracted much attention and is recognized as a form of green technology. In the past, for example, fuel cells have been developed to convert solar energy into electricity and many improvements have been made to increase their efficiency, but large-scale energy production is still limited. Furthermore, regarding the transformation of sunlight into chemical fuels, there are two possible ways, one is the reduction of carbon dioxide (CO_2) into hydrocarbons [16-19] and the other is the production of hydrogen (H_2) [20-22].

1.5 Hydrogen (H_2) as an energy source

The UN 2030 Agenda outlines 17 Sustainable Development Goals (SDGs), of which SDG 7 is on cheap and clean energy goals to provide access to sustainable energy technology and services, thereby contributing to the challenge of climate change on a global scale [23].

In an effort to advance the SDGs, the European Union has announced a number of initiatives that have improved Europe's energy consumption and green energy supply. The European Green Deal (EGD)’s aim is to reduce net greenhouse gas emissions by 2030 up to 55% and to achieve carbon neutrality by 2050 [24]. These guidelines encourage scientific society to find ways for the transition of society into carbon neutrality, renewable energy production, end use efficiency, carbon capture and storage, and production of green fuels [25]. Later are the replacement of fossil fuels (natural gas, gasoline, and coal).

In this context, H_2 can be considered as a very efficient, clean and promising energy source playing an important role in the decarbonization process [26, 27]. It can be generated from water and renewable energy resources [28-32] and during its combustion, for example in a fuel cell, only water (H_2O) is produced when H_2 reacts with oxygen (O_2) (Equation 1.1).

$$2H_2 + O_2 \rightarrow \ 2H_2O \tag{1.1}$$

The importance of using H_2 as a fuel derives from the fact that it has an energy efficiency of 122 kJ·mol, which is higher than that of gasoline or of any other fossil fuel [33]. Table 1.1 shows the energy content of different fuels.

Current and future applications of H_2 have been divided into three groups (Figure 1.1): (i) power and heat generation, (ii) industrial feedstock, and (iii) transportation [34].

Table 1.1 Energy content of different fuels [30]

Fuel	Energy content (MJ/kg)
Hydrogen	120
Liquefied natural gas	54.4
Propane	49.6
Aviation gasoline	46.8
Automotive gasoline	46.4
Automotive diesel	45.6
Ethanol	29.6
Methanol	19.7
Coke	27
Wood (dry)	16.2
Bagasse	9.6

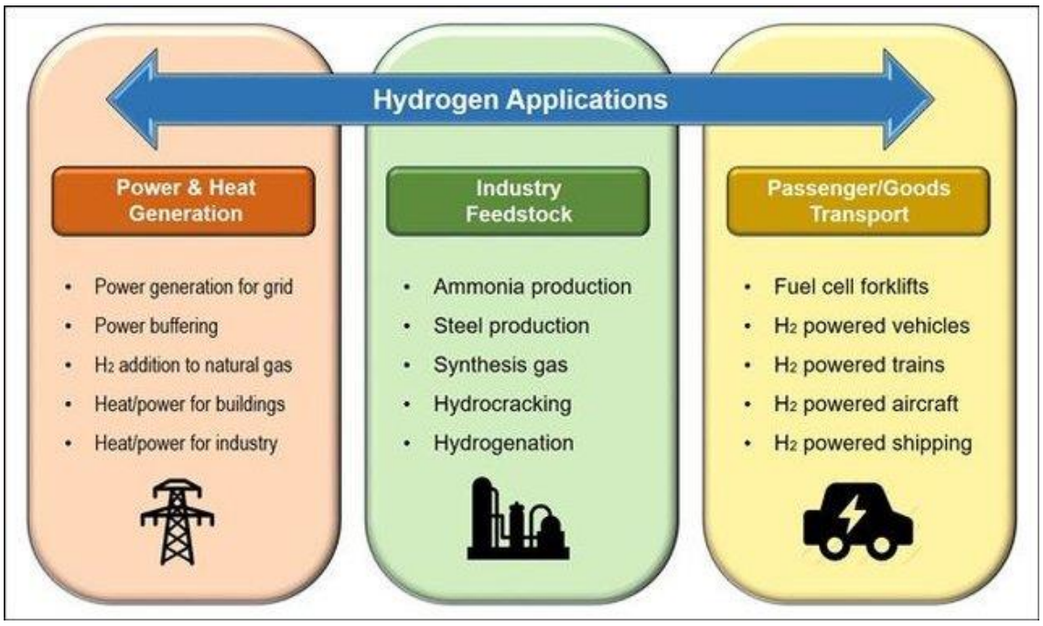

Figure 1.1 Current and future applications of H_2 [34]

1.6 H_2 production methods

The actual industrial H_2 production is still based on the use of fossil resources such as oxidation of hydrocarbons, steam reforming of the gas and gasification of coal [35-37]. Though a significant amount of H_2 can be generated through these processes at a reasonable cost, the usage of fossil fuels causes the release of greenhouse gases [38, 39]. Therefore, it is essential to establish a green, sustainable, and effective approach for H_2 production.

Compared to conventional methods based on non-renewable resources, recent research has revealed that the synthesis of H_2 using technologies (i.e., photocatalysis) involving sunlight is potentially competitive [40]. Water and biomass represent renewable resources for green hydrogen production. In particular, photocatalytic water splitting, and biomass reforming (discussed later) use renewable energy such as sunlight to produce H_2 that can power everything from laptops to submarines [41]. Hydrogen production methods based on renewable and non-renewable energy sources are shown in Figure 1.2 [42].

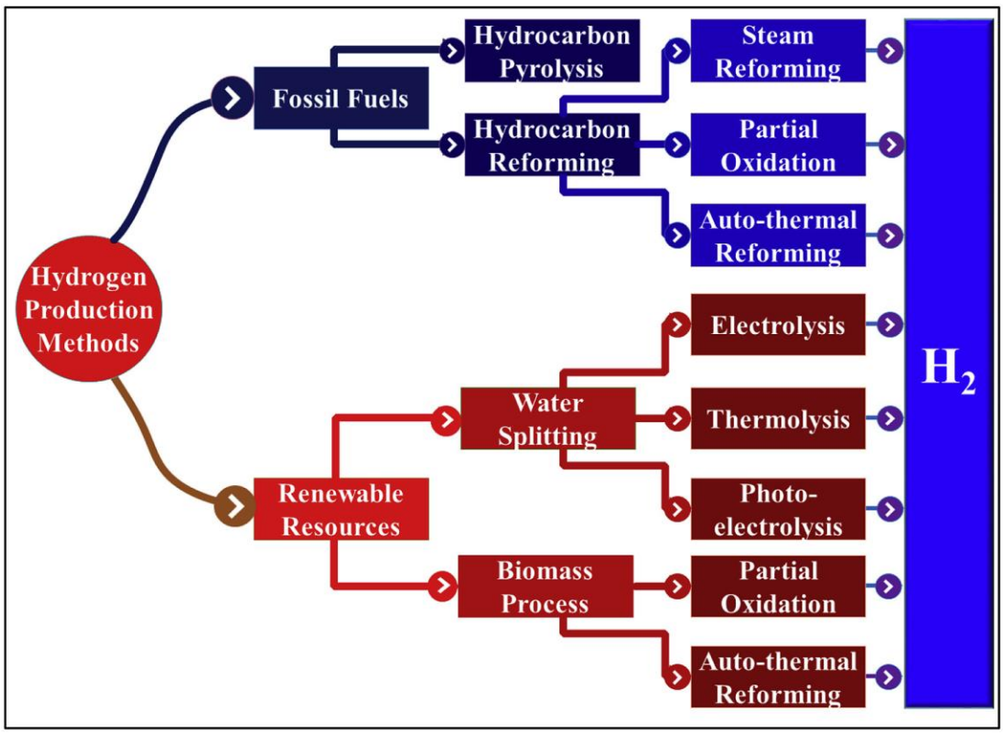

Figure 1.2 H_2 production methods based on renewable and non-renewable energy sources [42]

1.7 Photocatalysis and photocatalytic H_2 production principles

Photocatalysis is a branch of chemistry in which the reaction rate is increased in the presence of light and a photocatalyst. There are three types of photocatalysis: heterogeneous, homogeneous, and plasmonic antenna-reactor catalysis. Here we discuss heterogeneous photocatalysis.

Heterogeneous photocatalysis has emerged as a viable approach to transform solar light into H_2 production since Fujishima and Honda [43] in 1972 realized the photoelectrochemical water splitting on titanium dioxide (TiO_2) (rutile) anode, although the reaction proposed by the Authors cannot be considered, strictly speaking, a photocatalytic reaction. Since then, a very large number of papers have been published, ranging from environmental clean-up [44-48] to the synthesis of high value-added products [31, 49-51] to hydrogen production [52-56].

A photocatalytic process carried out by using solar light could be an economical way to produce H_2 on an industrial scale since often the synthesis of the photocatalyst and the design of the photoreactor present no particular difficulties [57-59].

Photocatalytic technology has numerous applications such as H_2 generation, production of high value chemicals, CO_2 reduction and wastewater treatment. Figure 1.3 shows the number of publications related to photocatalysis applications since 1970.

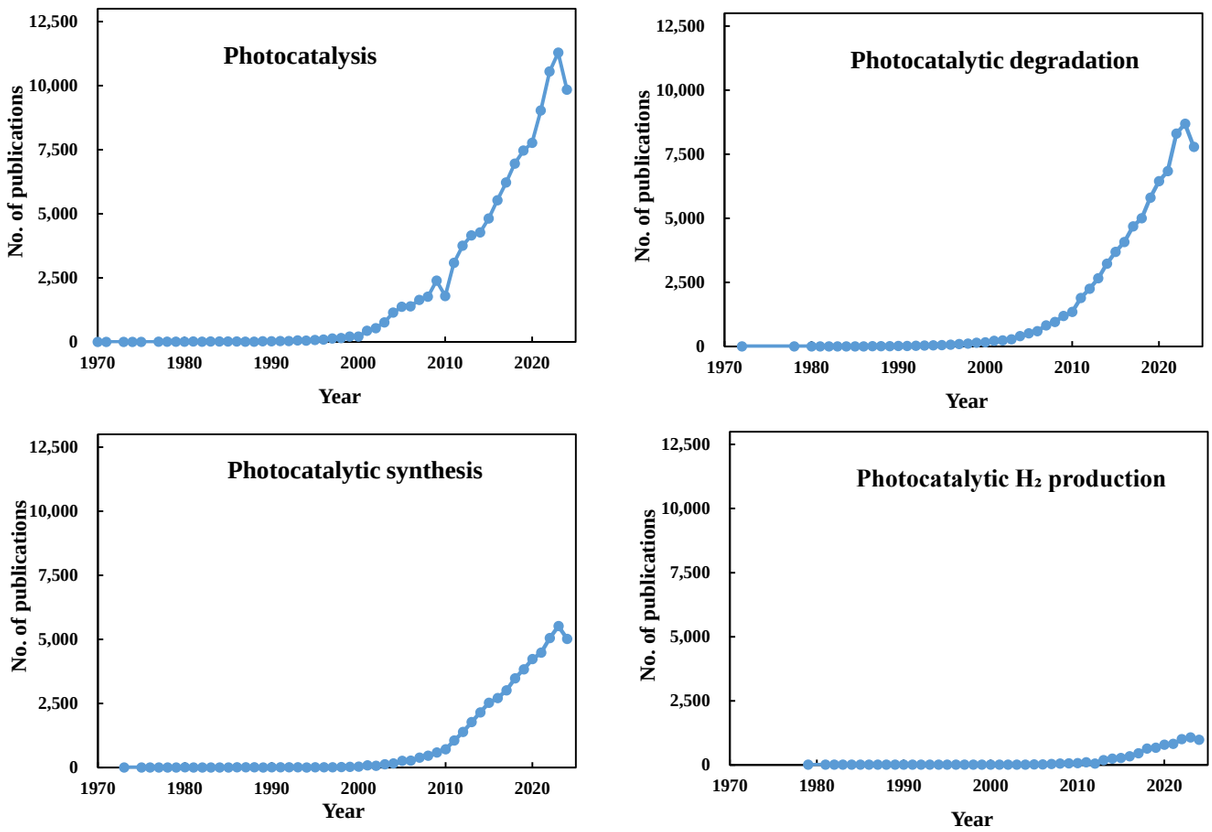

Figure 1.3 Number of publications related to photocatalysis applications since 1970. (Scopus; September, 2024)

"Band gap" is the term that describes the energy difference between the lower edge of the conduction band (CB) and the upper edge of the valence band (VB) of a semiconductor (SC). Upon irradiation with light of energy higher than that of the band gap (Figure 1.4), electrons (e^-) in the VB move to the CB and positive holes (h^+) remain in the VB. Both ultraviolet (UV) and visible (Vis) light can be used depending on the band gap value of a photocatalyst. The photoproduced electron-hole can recombine and dissipate the input energy or move to the surface to give rise to oxidation and reduction reactions with adsorbed species. In the presence of a SC, H_2O, O_2 and organics the following reactions can take place (Equation 1.2-1.9):

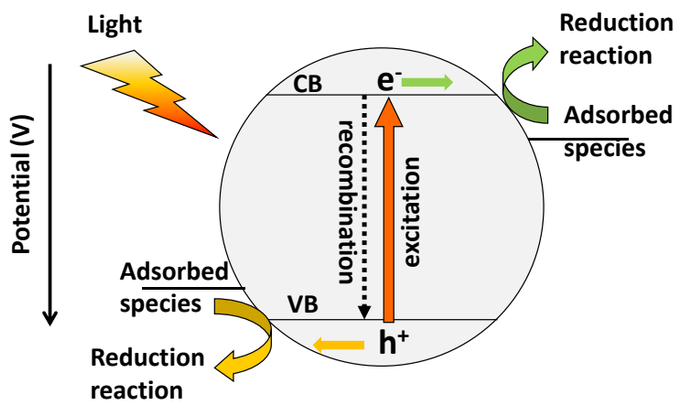

Figure 1.4 Schematic diagram of photocatalytic mechanism

$$SC + h\nu \rightarrow SC\ (e^-_{(CB)} + h^+_{(VB)}) \quad (1.2)$$

$$H_2O + h^+_{(VB)} \rightarrow {}^{\cdot}OH + H^+ \quad (1.3)$$

$$OH^- + h^+_{(VB)} \rightarrow {}^{\cdot}OH \quad (1.4)$$

$$O_2 + e^-_{(CB)} \rightarrow {}^{\cdot}O_2{}^- \quad (1.5)$$

$${}^{\cdot}O_2{}^- + H^+ \rightarrow {}^{\cdot}HO_2 \quad (1.6)$$

$$2\,{}^{\cdot}HO_2 \rightarrow O_2 + H_2O_2 \quad (1.7)$$

$$H_2O_2 + {}^{\cdot}O_2{}^- \rightarrow OH^{\cdot} + {}^{\cdot}OH + O_2 \quad (1.8)$$

$${}^{\cdot}OH + organic\ compounds \rightarrow CO_2 + H_2O\ \ or\ partial\ oxidation\ derivatives \quad (1.9)$$

Very briefly, the three key steps that are typically involved in the photocatalytic production of H_2 (Figure 1.5) are: (1) the activation of the photocatalyst which consists in the formation of electron-hole pairs (e^-/h^+); (2) the transfer of these charges to the surface of the photocatalyst particles; (3) the occurrence of oxidation and reduction reactions due to the presence of photo-produced charges. It should be noted that not all couples give rise to reactive acts, but some recombine, and the number that in the unit of time induce redox processes depends on the type and features of photocatalyst used. The recombination rate is an important parameter affecting the efficiency in all heterogeneous photocatalytic processes [60] and the conduction band and the valence band edge energies must be compatible with the redox potential of the desired reactions [61, 62].

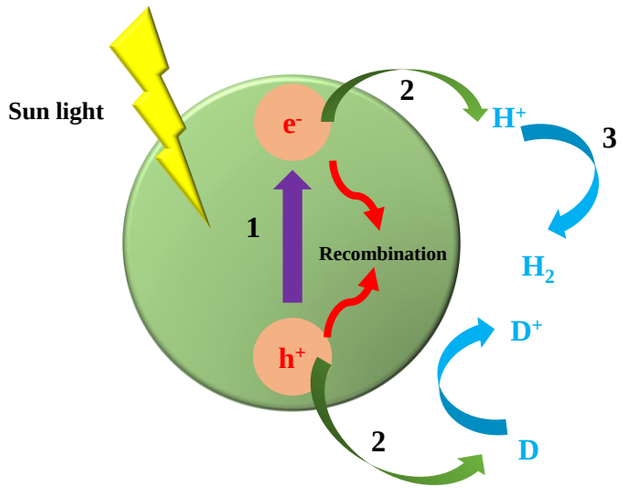

Figure 1.5 Schematic photocatalytic H_2 production on the surface of a semiconductor

The realization of a specific reaction is strictly related to the actual energy levels of the two bands of a photocatalyst as the CB and VB edge potentials define the reduction and oxidation ability of e^- and h^+, respectively.

The photoexcited e^- and h^+ in the presence of pure water can give rise to H_2 and O_2, respectively, by the so-called water splitting mechanism, discussed later in detail. For H_2 production the bottom of the CB must be more negative than the H^+/H_2 redox couple (0 V vs. NHE, pH 0) and the top of the VB should be more positive than the oxidation potential of O_2/H_2O (1.23 V vs. NHE, pH 0) (Figure 1.6) [63]. Thus, for the photocatalytic reaction, the band gap energy (E_g) of the semiconductor must be >1.23 eV. This is the theoretical minimal value as, owing to kinetic overpotentials and energy losses during the process, the real value must rise to 2.0–2.4 eV; moreover, for activation by visible light, the band gap energy must be less than 3.0 eV (related to wavelengths >400 nm) [64, 65]. In Figure 1.6 are reported the band gap values and the actual

band structure of the most common photocatalysts and the redox potentials related to the H_2 and O_2 evolution [54].

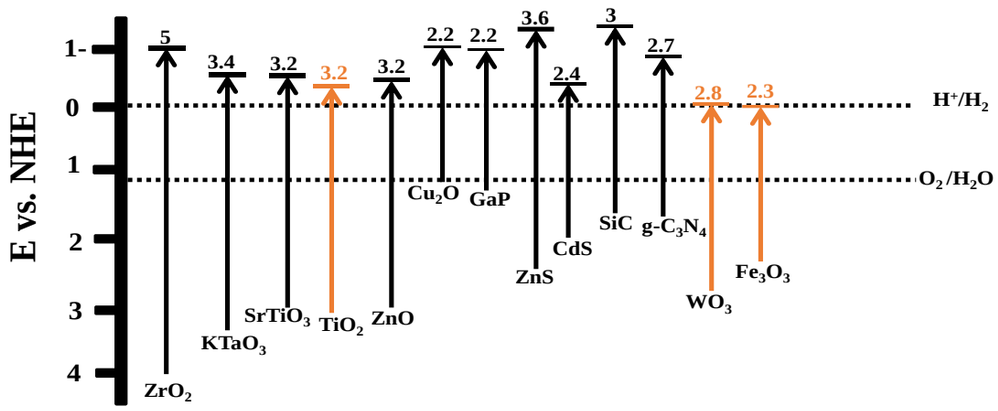

Figure 1.6 Different semiconductors showing different band gap energies and band positions relative to the NHE at pH 0.

TiO_2 is the most studied photocatalyst and considered highly desirable for different applications. The three main polymorphic forms of TiO_2 are anatase, brookite and rutile. Numerous synthetic techniques are known in the literature for the production of TiO_2 which can also be obtained in the form of various types of polymorphs as a mechanical mixture or mixed material (when there is an interface between particles of one polymorph and another) [66]. Anatase, which has a tetragonal crystal configuration with each octahedron sharing corners to generate planes (0 0 1), is the most widely employed polymorph in heterogeneous photocatalysis. Rutile, which on the other hand is mainly used as a white pigment, even if its use in photocatalysis and photoelectrocatalysis is quite frequent, has a tetragonal crystalline configuration made up of octahedra sharing the edges that form the planes (0 0 1). Angular and edge-sharing octahedra form the orthorhombic crystal structure of brookite. Anatase is the polymorph that generally gives the best performance for the photocatalytic production of H_2 because it has better stability, the photoproduced pairs are better separated and its band gap is slightly smaller [67-69].

TiO_2 has characteristics such as low cost, non-toxicity, low environmental impact, significant oxidizing power, outstanding photocatalytic activity, and long-term (photo)stability [70-72]. However, TiO_2 presents some disadvantages. Because of large band energy, it can only be activated by UV light and the fast recombination rate of the photoexcited e^-/h^+ makes its use not very effective. To address this issue, different strategies can be pursued as doping with metal and non-metal species, coupling with other semiconductors, morphological or crystal lattice control, surface modification, sensitizing or the use of alternatives photocatalysts [70-72]. The coupling of TiO_2 with other suitable semiconductor materials can improve the solar light absorption, enhance the photocatalytic activity and change the surface acidity [73]. Moreover, the doping with metals (i.e., Nb, Cu, Co, Ni, Au) has been reported to be effective in the reduction of the recombination rate of photoexcited e^-/h^+ and modification of some surface and electronic features [74a-81].

1.8 Heterojunctions

It is difficult for a single-phase photocatalyst to exhibit both good redox capability and a broad light absorption spectrum at the same time. Furthermore, in single component photocatalysts, there is the possibility of recombination of the photogenerated charges with a consequent reduction in the efficiency of the process [82]. Based on the band structures of photocatalyst heterostructures, there are mainly four types of heterojunctions (type-I, type-II, Z-scheme, and S-scheme). Here we discuss Z-scheme and S-scheme.

1.8.1 Z-scheme

A Z-scheme heterojunction system is shown in Figure 1.7. After irradiation, the electrons of the CB of semiconductor 2 recombine with the holes of the VB of semiconductor 1. Thus, electrons with high reduction capacity are available in the CB of semiconductor 1 and holes with high oxidation power in the VB of the semiconductor 2 [83]. The artificial Z-scheme heterojunction structure has received much attention, and several Z-scheme structures of various types have been created to make some photocatalytic reactions more efficient. The disadvantage of type I and type II heterojunctions is that at each active site, the light-induced electrons and holes lose some of their redox capacity after migration [84]. The Z-scheme heterojunction system has the advantage not only of ensuring an efficient spatial separation of the electron and hole pairs, but also the production of electrons and holes with remarkably reducing and oxidizing power, respectively.

Nevertheless, also the Z-scheme heterojunction system has some problems to face: one is that the photoreduction and photooxidation reactions can influence the behaviour of the photocatalysts for which the more or less marked accumulation of e^- and h^+ takes place. The other problem is the occurrence of light-induced recombination of e^- and h^+, which although efficiently separated by light, cause them to be consumed in significant quantities. However, the Z-pattern heterojunction system is attractive due to the particular type of e^- transfer [85, 86]. The direct Z-scheme system is useful towards H_2 production when the potential of CB edge of semiconductor 1 is more negative than H^+/H_2 redox potential [87-89].

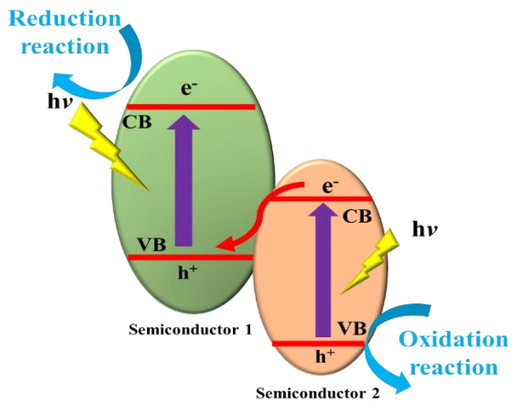

Figure 1.7 Z-scheme heterojunction scheme

1.8.2 S-scheme

The S-scheme heterojunction system (Step-scheme) is illustrated in Figure 1.8. Considering the level of the energy bands, the two coupled photocatalysts involved can be classified one as an oxidation photocatalyst (OP) and one as a reduction photocatalyst (RP) [90-92]. The first photocatalyst presents lower CB and VB positions, and consequently a lower Fermi level than the second one. The work function of OP results larger than that of RP.

When the OP and RP are in close contact, the transfer of the photoproduced charges occurs according to the following steps:

(1) After simple contact between the two materials, the e^- will move spontaneously from RP with a lower work function to OP until their Fermi energy levels (E_f) reach equilibrium (Figure 1.8b). This results in different charges on the two sides of the contact surface, with negative and positive charges on the OP and RP sides, respectively. Thus, an internal electric field (IEF) is formed.

(2) Under irradiation (Figure 1.8c), the formed IEF accelerates the e^- transfer from OP to RP. Furthermore, its formation enhances the bending of the energy bands, downwards in OP and

upwards in RP. At the interface, the photogenerated e^- in the CB of OP and h^+ in the VB of RP recombine under the coulombic attraction. Thus, e^- and h^+ in OP and RP, respectively, are consumed, but e^- with strong reducing ability in RP and holes with strong oxidizing ability in OP remain. Consequently, the S-scheme heterojunction photocatalyst with such mechanism has strong oxidation and reduction ability [93] and thus can be used for effective H_2 production.

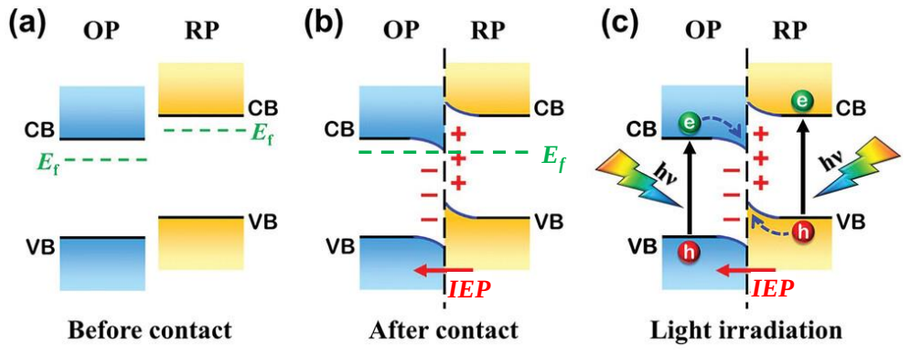

Figure 1.8 Charge-transfer processes in an S-Scheme heterojunction: a) before contact; b) after contact before irradiation; and c) photogenerated charge carrier transfer under light irradiation [90].

1.9 Cocatalyst

Many catalysts are inactive to produce H_2 in the absence of a cocatalyst. Noble metal nanoparticles have been considered excellent cocatalysts for H_2 photoproduction. A widely used way to improve photocatalytic efficiency is to load the cocatalyst on the surface of a photocatalyst, promoting charge separation and providing more reaction sites. In fact, due to the difference in Fermi levels between the semiconductor and the noble metal nanoparticles, a Schottky barrier is formed and the e^- move from the semiconductor CB towards the noble metals [94].

The use of an optimal amount of cocatalyst is important for the photocatalytic production of H_2 and depends on the cocatalyst used, as well as the surface area available on the photocatalyst particle. By increasing the amount of cocatalyst present on the photocatalyst surface, the photocatalytic efficiency increases but for some amounts it starts to decrease. This is due to the increase in the particles size, the unsatisfactory dispersion on the surface (accumulation phenomena can occur with an increase in the dimensions of the cocatalyst nanoparticles), the shielding effect of the active sites of the photocatalyst [54].

The noble metals Pd, Ru and Pt are considered the best candidates for their broad work function [21]. Cu_3P cocatalyst on the surface of g-C_3N_4, [95, 96], metal borides, and carbides due to their semi-metallic characteristics [97, 98], were also used to produce H_2. Notably, the cocatalysts NiS and CuS played a crucial role for the production of H_2 on g-C_3N_4 [20, 99, 100]. To improve the efficiency in the production of H_2, the co-loading of the reduction and oxidation cocatalysts has also been extensively studied, which has improved effects in the separation and in the movements of the charges [101].

1.10 Synthetic and reactive conditions influencing the photocatalytic activity

1.10.1 Irradiation sources

One renewable and essentially unlimited source of energy is sunlight. Consequently, the use, transformation and/or storage of solar energy is a popular goal in place of competing renewable or non-renewable sources. In this regard, scientists around the world consider photocatalysis to be a fascinating scientific method for producing fuels by absorbing solar energy.

It has been demonstrated that the photoreforming of oxygenated compounds derived from biomass in the presence of some photocatalysts can occur easily and with good efficiency [102-105].

1.10.2 Temperature

The Arrhenius equation describes how the rate of photoreforming changes with temperature according to the activation energy of the limiting kinetic step. The movement of charge from the active sites on the surface of the irradiated material and the adsorbed species in the elementary steps of a photocatalytic reaction is a process driven by the absorption of light [106, 107]. The dual use of solar radiation through both the effective use of light by the semiconductor and its local heating (photo-thermal process) [108, 109] is a process that offers evident advantages on the production of H_2, especially taking into account the improvement of the efficiency of the photoreforming by increasing the temperature. It should also be noted that the performance of the photocatalytic processes under examination is considerably improved using reactors that are suitably designed and with particular configurations and symmetries with respect to the position of the irradiating source [110].

1.10.3 pH

Photocatalytic activity can be influenced in various ways by the acidity or basicity of the solution used. In fact, the processes are affected by the pH value of the medium which can also significantly influence the energy position of the semiconductor bands, the redox potentials of the molecules, the speciation of the substrate and the extent of its protonation (for acidic or basic species), the surface charge of the semiconductor used, the electrokinetic potential (zeta potenzial, ζ), the surface adsorption of the species involved in the reaction, the stabilization of reaction products or intermediates, and the aggregation of photocatalyst particles. While the surface reaction and charge transfer depend on the type of interface and therefore also strongly on the pH, the bulk structure of a photocatalyst is unlikely to change significantly as a function of pH [111].

1.10.4 Substrate concentration

Substrate concentration has a large impact on H_2 production. As substrate concentration increases, the rate of H_2 production increases to a certain point, but then begins to decrease as excessive amounts of substrate can compete with H_2O adsorption [112].

Water is typically required for the stoichiometric synthesis of H_2 in the photoreforming of oxygenated compounds. Consequently, the water/substrate ratio is crucial for the selectivity of the process, although it is possible to carry out some reforming processes in the absence of water such as for example the dehydrogenation of formic acid or the decomposition of formic acid. It should also be noticed that the water adsorbed on the photocatalyst surface can act as an oxidant forming intermediate hydroxyl radicals or function as a proton carrier, influencing the rate at which the reaction occurs [113, 114].

1.10.5 Catalyst quantity

The amount of the photocatalyst, as in any heterogeneous photocatalytic reaction, is important and influences many parameters relating to photoactivity such as, for example, the reaction kinetics, and the yield and selectivity towards the products. It is necessary to establish experimentally the optimal amount of photocatalyst for the photoreactor used, taking into account not only the volume of liquid used but also the geometry of the photoreactor. Light scattering, transmission, and reflection should be minimized while ensuring that all or most of the incident photons are absorbed by the reacting system. In cylindrical photoreactors, for example, a commonly used methodology is to gradually add the powdered photocatalyst to the aqueous reacting system and measure the transmitted light with a radiometer until it reaches very low values close to zero. It can be assumed in this way that most of the photons remain in the reacting system and give rise to the formation of e^-/h^+ pairs which induce the reaction, or which recombine

generating heat. Obviously, determining the optimal amount of photocatalyst is not very easy for other photoreactor geometries [115-118].

1.10.6 Crystal structure

The crystal structure was considered as an important factor influencing the photoactivity. In the case of TiO_2, anatase is generally more active than brookite and rutile. In anatase TiO_2, the oxygen vacancies can trap the photo-excited electrons, and it is easier for them to reach the Pt particles present on the surface which act as a trap and which are used in the case of H_2 production. The low activity of rutile TiO_2 can be attributed to the fact that the photoproduced electrons are trapped in intrinsic structural defect [119-121]. Surprisingly, brookite turned out to be very active in the production of H_2 [22, 122]. Mixed phases of TiO_2 were more active than pure ones [123-125]. The transfer of electrons at the phase junction is important to produce H_2, while lattice defects act as recombination centers for photoexcited e^-/h^+ with decreased photocatalytic performance. A good crystallinity significantly improves e^- transport [126].

1.10.7 Morphology modification

In general, particle size is a fundamental aspect in electron-hole recombination and charge transfer which is mainly controlled by the quantum confinement [66]. Nanomaterials have been widely used in heterogeneous photocatalysis. The decrease of particle size is beneficial for the photocatalytic performance as electron-hole recombination is reduced relative to bulk materials [127-129]. Reducing particle size increases surface area and provides more surface sites. High photocatalytic performance has been observed in the photocatalytic reaction with smaller particle size and higher surface area for $NaTaO_3$ [130]. The reason for this is the increased surface interaction capacity of electrons and holes instead of mass recombination [131].

1.11 Photocatalytic water splitting

Photocatalytic water splitting involves the breakdown of H_2O into H_2 and O_2 and is an up-hill reaction that is followed mainly by a positive shift in the Gibbs free energy (ΔG° = 237 kJ/mol) under standard temperature and pressure conditions. This reaction is similar to the photosynthesis by green plants, also known as artificial photosynthesis [132]. A scheme of photocatalytic generation of H_2 in water systems is shown in Figure 1.9. This method is environmentally friendly and is gaining more and more importance in our globalized world [133]. In fact, it can be considered an independent procedure that allows the conversion of solar energy into chemical energy.

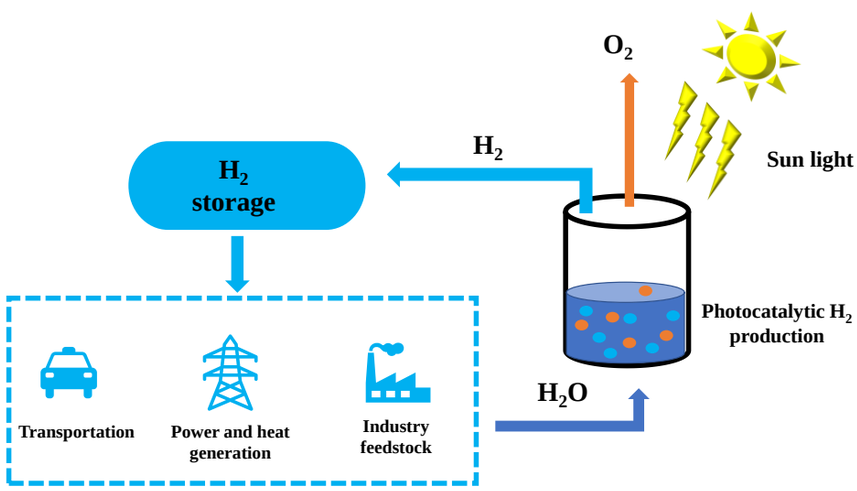

Figure 1.9 H_2 production in water system

The photocatalytic production of H_2 is proportional to the amount of photogenerated electrons. To improve the efficiency of H_2 production, the phenomena that consume photoexcited electrons must be avoided or reduced. Any process that tends to increase the formation of electrons must be given in great consideration; at the same time a photocatalyst must have a small band gap and reflection or scattering of incident light on its surface must be minimized to absorb more light.

1.12 Photoreforming

Photoreforming, on the other hand, along with water splitting involves the presence of organic compounds as sacrificial agents and increases the yield of H_2 compared to the use of pure water and can contemporarily give rise to the formation of valuable chemicals. When the sacrificial compounds are bioavailable oxygenated organic species and the sunlight is the source of irradiation, the process has virtually zero net greenhouse gas emissions. The source of the organic substrate has a large impact on the overall sustainability [134].

1.13 Sacrificial agents

Photocatalytic H_2 production from water in the presence of different organic compounds i.e., sugars [31], aromatic compounds [135, 136], biomass [137], methanol [138], ethanol [139], ethylene [140], amino acids [141], fossil fuels [142], and lactic acids [143] has been carried out in the presence of different semiconductors. It was noticed that a significant amount of H_2 was obtained through photoreforming reactions compared to what was found with simple water splitting.

Most of the studies done using various organic compounds have been carried out by testing more or less sophisticated materials as photocatalysts to improve their performance but have also concerned mechanistic issues and the influence on the activity of the various organic compounds often used as sacrificial agents. Methanol is the most frequently used molecule as its simple structure allows an easier understanding of the reaction mechanisms. Particularly interesting for the photoreforming process are some bioavailable substrates such as glycerol, ethanol and sugars that come from biological substrates [111]. Notably, these molecules, in addition to functioning as sacrificial agents, can form high added value compounds by partial oxidation that occurs simultaneously and in tandem with the production of H_2, discussed later. The type of sacrificial agent and the possibly used co-catalyst are two particularly important factors for the photocatalytic performance. In the following section, some sacrificial agents are discussed in more detail.

1.13.1 Methanol

Methanol is considered an ideal molecule for the production of H_2, and in early research it was hypothesized that it was the best and ideal feedstock for photoreforming. The photoreforming of methanol, in fact, produces formaldehyde and formic acid and, after further oxidation, only H_2 and CO_2. It is the most used sacrificial agent because it produces the greatest amount of H_2 with the same initial concentration, but no valuable compounds are obtained from its partial oxidation [144, 145].

1.13.2 Glucose

Since the Gibbs free energy of the reaction has a negative value, the production of H_2 from saccharides such as glucose reforming is thermodynamically advantageous. Hydrolysis of cellulose can provide glucose. Wastewater from food processing also has a high concentration of sugars. Consequently, a variety of catalysts for the photoproduction of H_2 using glucose as biomass have been investigated and the presence of Pt has been shown to be essential for a good efficiency [112, 146, 147].

1.13.3 Fructose

Fructose, derived from cellulose, can be used to produce high-value compounds in a sustainable mode. In particular, they can be used to produce ethanol, mannitol and sorbitol through hydrogenation, 5-hydroxymethyl furfural through dehydration, gluconic acid, arabinose and erythrose and H_2 by partial oxidation [50, 148-154].

1.13.4 Glycerol

It is very interesting to use glycerol as a sacrificial agent to produce H_2 through the photoreforming reaction. Glycerol is produced and accumulated in large quantities as it constitutes approximately 10% of by-products from the biodiesel manufacturing industry. Consequently, it is considered a waste and its valorization by producing H_2 and compounds with high added value by using the photocatalytic method in a green condition is desirable. Several photocatalysts have been tested with glycerol, but TiO_2 was the most popular one [155-158].

1.13.5 Ethanol

Ethanol, which can be produced on an industrial scale from renewable biomass (cellulose or lignocellulose), is widely studied as a sacrificial agent for H_2 production. The products formed from the photoreforming of ethanol are acetaldehyde and acetic acid which, however, can undergo further oxidation depending on the reaction times and the experimental conditions used. Some other products i.e., carbon dioxide (CO_2), ethane (C_2H_4), methane (CH_4), carbon monoxide (CO), and ethylene (C_2H_6) were also found [134, 159, 160].

1.13.6 Furfuryl alcohol

Furfuryl alcohol is used as an intermediate in the production of furoic acid and furfural which is widely employed in agrochemical, pharmaceutical and plastic industries and considered a large source of biofuel [56, 161-163].

1.13.7 Triethanolamine

Triethanolamine (TEOA) is widely used in paints, cosmetics, polymers and other fields, however, being an organic pollutant and a carcinogenic molecule it is harmful for human beings and animals when present in ecosystem [164]. Due to its complex structure, it can be interesting to combine its degradation process with photocatalytic H_2 production [165, 166].

1.14 High value-added products

Hexose sugars, which derive from cellulose (an abundant biomass constituent), can be further dehydrated to platform molecules as 5-hydroxymethyl furfural (HMF) [167-170]. Particularly, glucose and fructose, the most abundant carbohydrates, can be used to produce high-value compounds such as arabinose, erythrose, gluconic acids, and formic acid in a sustainable mode.

Gluconic acid and its derivative compounds are widely used as flavoring and chelating agents to eliminate calcareous and corrosion pledges from metals in food, medicine, and cleansing agent industries. Worldwide, gluconic acid have 0.1 million tons production annually, mostly produced by the biotechnological techniques [31]. Formic acid is a common chemical intermediate utilized in the biochemical, agrarian, pharmaceutical, fabric, and rubber manufacturing industries. It's usually made from fossil fuels or as a derivative of the production of other compounds [171]. D-arabinose is required for the production of DNA, vitamin B2, and erythritol, which is used as a food sweetener [172]. D-Erythrose is a cancer preventive compound because it slows the formation of tumors in mice [173].

1.15 Alcohols and aldehydes

For the selective oxidation of aromatic alcohols to the corresponding aldehydes, industrial methods usually use organic solvents at severe conditions in the presence of chromate and permanganate ions as stoichiometric oxygen donors. This leads to high energy cost and dangerous waste which can be eliminated through efficient, green and cheap semiconductor materials. Aldehydes and their by-products have several applications in food, beverages, dyes, resins, fragrances and pharmaceuticals [174-177].

1.16 Organic drugs removal

1.16.1 Advanced oxidation processes

Water is the fundamental need of human beings, and its main sources are rivers, lakes, aquifers and the desalination of sea water which, however, is exploited in a more limited way. With the growth of population and industrialization, almost all water sources are contaminated mainly by agricultural and industrial waste. As a result, one of the biggest problems facing humanity in the 21st century may be the sustainable use of water. Scientific society is attracted to the development of sustainable and green technologies [178].

Due to the rapidly growing demand for various products to treat humans and animals, pharmaceutical companies are expanding significantly. Molecules of pharmacological importance present in drugs are widespread in the environment [179, 180]. In seawater, lakes, rivers, surface waters, urban wastewater and drinking water, their concentrations have been found to range between ng and μg per liter [181-183]. Furthermore, it must be kept in mind that, due to their presence, synergistic interactions can occur in these water systems which generally significantly increase ecotoxicity [184].

Drugs are difficult to be removed from water systems through traditional wastewater treatment methods due to their particularly stable structure which hinders their complete degradation and their high hydrophilic properties [185, 186]. Traditional methods such as biological treatment [187], adsorption [188], nanofiltration [189], and membrane bioreactors [190] have been used for their removal, but these methods are often not very efficient and/or they give rise to a transfer of the pollutant rather than its total abatement [185]. In this context, drug metabolites are not completely removed thus increasing the concentration of drugs in wastewater from treatment plants [191]. Therefore, alternative technologies have been developed [179].

Among the different methods for drug removal, advanced oxidation processes (AOPs) can be considered economical, flexible and highly efficient technologies to destroy persistent organic molecules [192, 193]. AOPs are generally known for in situ production of strongly and unselective oxidizing species such as hydroxyl radicals ($^{\bullet}OH$), O_3, H_2O_2, and superoxide anion radicals ($O_2^{\bullet-}$). These species almost always cause complete mineralization to CO_2, H_2O and inorganic compounds of the attacked molecule and, under certain operating conditions, could be preferred from an environmental point of view [194]. For example, they are highly effective in providing clean drinking water free of organic, inorganic substances and microorganisms [195]. The main advantage of AOPs compared to other available methods, however, is that they are completely ecological not only because they do not involve the removal of pollutants from one place to another (think for example of the precipitation of pollutants by chemical substances or their adsorption) but also do not produce large quantities of harmful waste [196, 197].

AOPs can be used alone or in combination with biological and physico-chemical processes, depending on the properties of the wastewater to be treated and the purposes of the treatment. In principle, process coupling is advantageous because it generally increases the efficiency of the treatment. For example, AOPs could be used as a pre-treatment step to transform originally biorecalcitrant molecules into other more easily biodegradable species, which would then be subjected to biological post-treatment. However, for drugs containing biodegradable substances,

biological pre-treatment following chemical post-treatment might also be desirable since, even if biodegradable substances can be easily eliminated initially, the effectiveness of biodegradation is not comparable to that of a chemical oxidizing treatment [198].

All AOPs involve the in-situ production of the main oxidant species and the consequent combination of these species with contaminants. Reactor design and drug composition have an impact on the formation of the reactive species, which are mainly radicals. In addition to radicals scavenging, other factors including hydrodynamics and mass transfer of radicals are crucial to effectively destroy drugs [178]. Different types of AOPs are illustrated in Figure 1.10. Here we discuss heterogeneous photocatalysis.

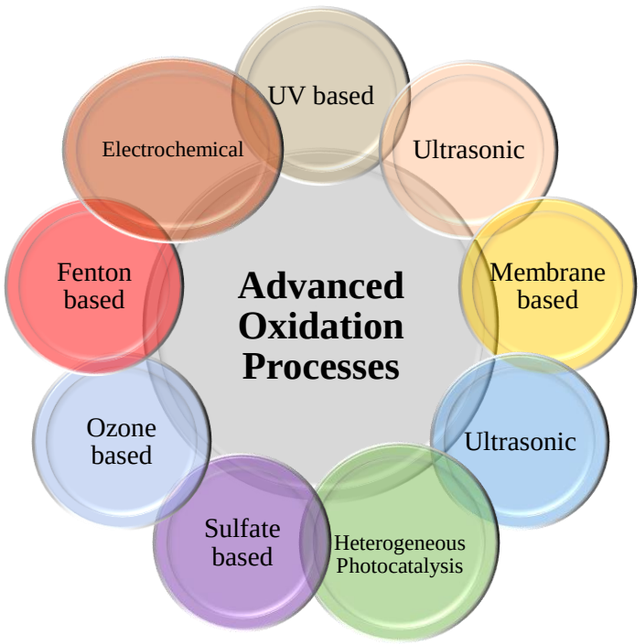

Figure 1.10 Different advanced oxidation processes

Heterogeneous photocatalysis is an example of AOP and it has been extensively studied over the past two decades and applied to drug degradation. This method appears to be more effective than other AOPs since some semiconductors are generally economic and non-selective, i.e. they can easily mineralize a large variety of toxic organic molecules [199, 200]. The molecules can be degraded in subsequent steps and are transformed into non-toxic products until complete mineralization into H_2O and CO_2 and any inorganic ions containing heteroatoms present in the treated organic molecules [201]. The photocatalytic mechanism of drug degradation is reported in Figure 1.11:

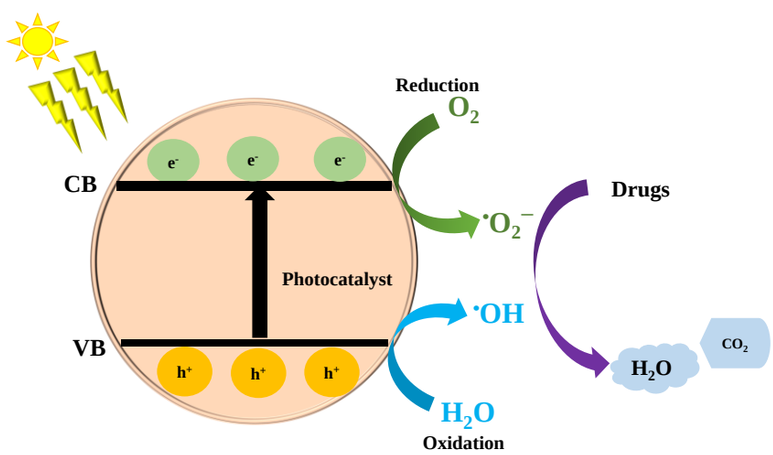

Figure 1.11 Photocatalytic mechanism of drugs degradation

In this study, attention was placed on commonly used organic drugs such as tetracycline, oxytetracycline and lincomycin.

1.16.2 Tetracycline

Tetracycline (TC), a traditional antibiotic, is widely employed in medicine for the prevention and cure of infectious diseases in humans and animals [202]. TC contains different functional groups, such as acylamino, phenolic hydroxyl, dimethylamino, and ketone enol conjugated double bond structure. TC, together with sewage, is directly released into ecological systems because it cannot be completely absorbed by organisms [203]. Additionally, when excessive doses of TC enter the human body, problems like nausea, vomiting, and kidney failure can occur [204]. So, it is important to develop a technology that can degrade TC at an affordable cost.

1.16.3 Oxytetracycline

Oxytetracycline (OTC) that belongs to the family of tetracycline is a widely used antibiotic for human and animal beings [205]. OTC is used to treat a variety of diseases, including pneumonia, chronic bronchitis, and urethritis, as well as for boosting animal growth. Due to its worldwide application, OTC has been found within the range of mg L^{-1} to μg L^{-1} in soil, fresh water and wastewater treatments plants [48, 206]. Due to bioaccumulation, OTC is harmful to aquatic organisms and ecosystems when it is released into water supplies. It can harm the natural cycle of the ecosystem and environment [206]. Therefore, it is necessary to create an effective technique to remove OTC from water supplies.

1.16.4 Lincomycin

Lincomycin (LCM), one of the commonly used antibiotics, has been found in natural water and wastewater treatment plants [207, 208]. LCM is resistant to degradation owing to its stable structure and physicochemical characteristics [209]. In aquatic ecosystems, the use of LCM may lead to bacterial resistance and the dissemination of resistance genes [210, 211]. It is unfortunate that some research has indicated that these resistant genes can be transferred from animals to humans through food chains [212]. Furthermore, it has a number of hazardous effects on organisms, including genotoxicity and growth inhibition [213].

1.17 Photocatalytic Reactors

In general, the photoreactors used should have some characteristics necessary to correctly obtain the concentration data of both the substrate in the liquid phase and the H_2 in the gaseous phase. First of all, the reactor volume should be sealed appropriately during the reaction to avoid the inlet of air which could decrease the efficiency of the reduction reaction. Furthermore, the exchange of gaseous species between the reactor and the external environment could compromise the correct determination of the H_2 developed. For this reason, all the ports of the reactor should be equipped with valves inert materials made. Moreover, a common feature of all photocatalytic devices is a suitable positioning of the radiation source with respect to the reagent volume. Indeed, it is very important to have a uniform distribution of the radiant field within the reactant volume. For irradiation systems placed outside the reactor, there are no particular problems, while in the case of lamps immersed directly in the reactant volume, it is necessary to seal the casing containing the reactor and the lamp.

Another important characteristic of the reacting system is the presence of a headspace which allows the accumulation of the gaseous species produced during the reaction. At least three ports are required at the top of the reactor: the first one to allow an inert gas to bubble into the liquid dispersion in order to purge the O_2 present in the headspace and avoid its dissolution in the reacting volume. The second and third ones from which gas and liquid can be withdrawn, respectively. As far as the continuous reactors are concerned, what has been said previously

regarding tightness remains valid. However, continuous systems often do not allow accurate chromatographic analysis of H_2 due to its low productivity. Therefore, it is necessary to provide an accumulation volume of H_2 at the outlet which allows it to be separated from the liquid phase. The reactor configuration, in general, is shown in Figure 1.12.

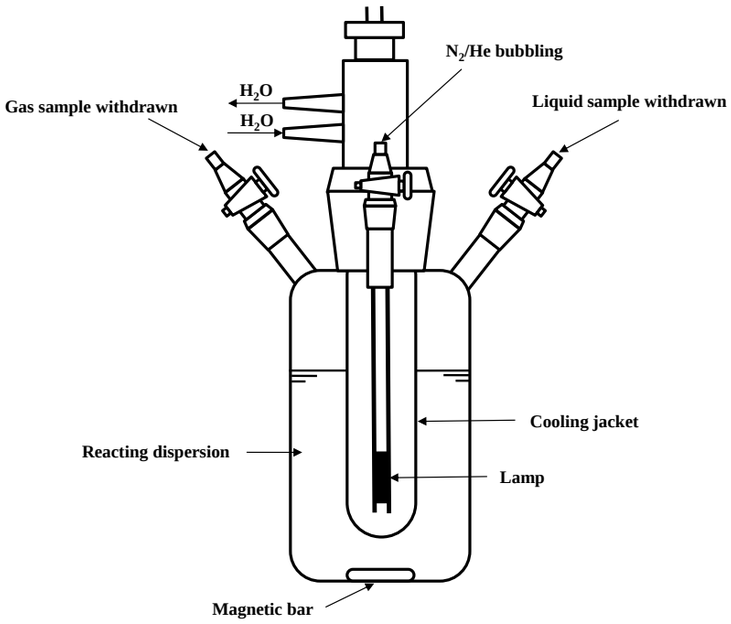

Figure 1.12 Reactor configuration for photocatalytic H_2 production

CHAPTER 2

State of the art

CHAPTER 2

2. State of the art

2.1 Photoreforming of biomass derivatives

Several studies are in progress to minimize the energy crises and find alternative fuels such as hydrogen gas through the photoreforming of biomass derivatives by means of different TiO_2 based and alternative TiO_2 photocatalysts.

Jiang et al. [144] investigated methanol photoreforming in the presence of commercial TiO_2 (P25) loaded with Pt obtaining a H_2 productivity of 3800 ± 130 $mmolg^{-1}$ h^{-1}. Yang et al. [214] used the synthesized TiC@C-TiO_2 for the photoreforming of methanol (initial concentration: 16.66%) and the produced H_2 was 558.46 μmol g^{-1}. Yuan et al. [215] investigated MoS_2/TiO_2 photocatalyst (1 g/l) for the photoreforming of methanol (initial concentration: 10%), H_2 production was 2145 μmol g^{-1} h^{-1}, 36.4 times higher than TiO_2 nanosheets.

The selective glucose oxidation to gluconic, formic, levulinic and lactic acids and to arabinose and erythrose is particularly attractive because they are platform chemicals industrially employed. In particular, gluconic acid and its derivatives are largely applied in pharmaceutical, detergents and food industries [216, 217]. Fructose is the monomer of cellulose which can be converted into 5-hydroxymethylfurfural in a catalytical reaction carried out in hot compressed water by microwave heating or can be converted selectively in lactic acid by using BiOBr/Zn@SnO_2 material. Bellardita et al. [31] studied the photoreforming of glucose using different Pt-TiO_2-based photocatalysts obtaining H_2 and high added-value products at the same time. Cai et al. [218] synthesized a novel biochar supported CdS/TiO_2 catalyst tested for the photoreforming of glucose. The H_2 production was of ca. 12.77 mmol $g^{-1}\cdot h^{-1}$ and the selectivity towards acetic acid was 63.94% in 25 mM of NaOH solution, while a formic acid selectivity of 60.29% and a H_2 production of 10.29 mmol $g^{-1}\cdot h^{-1}$ ca. was observed in 3 mM Na_2CO_3 solution.

Eisapour et al. [219] obtained H_2 and liquid products such as 1,3-dihydroxyacetone and glyceraldehyde in liquid phase from glycerol photoreforming by using NiO-TiO_2 photocatalysts.

In this work TiO_2 is selected due to its characteristics such as non-toxicity, cheap, low environmental impact, significant oxidizing power, outstanding photocatalytic activity, and long-term photostability [220-222], as previously discussed; photocatalysts alternative to TiO_2 were explored in order to overcome some of the limitations of TiO_2 such as UV light activation and low selectivity towards selected chemicals in photocatalytic syntheses. In particular, commercial and home prepared TiO_2 and TiO_2-based photocatalysts were synthesized by different methods and used in the presence of different biomass derivatives used as sacrificial agents. The three crystalline phases of TiO_2 were investigated in different reactors and light intensity first in the lab and later on a pilot plant scale photoreactor. TiO_2 was modified with some other catalysts such as Cu_2O, CuO, Nb_2O_5, and platinum by means of ball milling or photodeposition, respectively to improve the photocatalytic efficiency for H_2 production.

Table 2.1 summarized some literature results related to the use of TiO_2 based catalysts for the photocatalytic hydrogen production in the presence of different sacrificial agents.

Table 2.1 TiO_2-based catalysts used for H_2 production

Photocatalyst	Light source	Catalyst loading g/L	Sacrificial agent	H_2 production rate [mmol $h^{-1}g^{-1}$]	Irradiation time [h]	References
NiO-TiO_2	UV 300 W High pressure Hg lamp, λ > 400 nm	0.2	Methanol	813	>5	[223]
Cu_2O/TiO_2	300 W xenon lamp, λ > 420 nm	1	Methanol	24.83	10	[224]
Cu_2O/TiO_2	visible light, λ > 400 nm	0.21	Ethylene glycol	130	-	[225]
NiO_x-TiO_2	500 W high-pressure Hg lamp	0.02	Glycerol	0.320	4	[226]
Pt-P25	Natural sun light	1	Glucose	2218 μmol.g^{-1}	3.5	[227]
Pt-TiO_2 -W0.25	Natural sun light	1	Glucose	3734 μmol.g^{-1}	3.5	[50]
Cu-TiO_2	500W halogen lamp, λ > 400 nm	0.4	Methanol	0.283	5	[228]
Fe_2O_3-TiO_2	300W Xe lamp, λ ≥ 420 nm	0.34	Na_2S/Na_2SO_3	7.253	7	[229]
Au-Graphene-TiO_2	3W LED lamp, λ=420 nm	0.625	Methanol	0.296		[230]
Pt-Cu_2O-P25	125W Hg lamp	0.3	Glycerol	0.17	5	[55]
Fe-$CaIn_2O_4$-TiO_2Ni/NiO/$NaTaO_3$	450W Hg lamp	0.6	Methanol	0.013	4	[231]
Pt-$AgGaS_2$-TiO_2	450W Hg lamp, λ > 420 nm	1	Na_2S/Na_2SO_3	4.2	3.5	[232]
Pt-Fe-$CaIn_2O_4$-TiO_2	300 W Xe, λ ≥ 420 nm	0.2	KI	0.28	5	[233]
Pt-Ta_2O_5- In_2O_3	300 W Xe, λ ≥ 420 nm	1.5	Methanol	0.01	8	[234]

2.2 Partial oxidation of HMF and alcohols

2.2.1 HMF

HMF is a promising and useful biomass derivative because its further oxidation produces value-added compounds such as 2,5-diformylfuran (FDC), 5-formyl-2-furancarboxylic acid

(FCA) and 5-hydroxymethyl-2-furan carboxylic acid (HMFCA) [235-237]. FDC is used in the pharmaceutical industry, as antifungal agent, for the synthesis of organic substances and cross-relating agents of poly vinyl alcohol to be used in batteries; HMFCA is an interleukin inhibitor used in medical field [238]. For the oxidation of HMF into FDC, noble metal-based catalysts are used which, although they are very effective, are also very expensive and unstable catalysts. As a result, it can be challenging to design high performance heterogeneous catalysts based on non-precious metals for the oxidation of HMF to FDC.

Ilkaeva et al. [239] investigated the oxidation of 5-hydroxymethylfurfural (HMF) to 2,5-furandicarboxaldehyde (FDC) through polymeric carbon nitride-hydrogen peroxide adduct (PCN-H_2O_2) under natural solar light with a HMF conversion and a FDC selectivity of 21 and 88 % respectively. Siyo et al. [240] obtained a selectivity towards 2,5-furandicarboxylic acid (FDCA) higher than 90% through the oxidation of HMF by using Pd/ZrO_2/La_2O_3 as the photocatalyst. The intermediate products formed were 5-hydroxymethyl-furan-2-carboxylic acid (HMFCA) and 5-formyl-furan-2-carboxylic acid (FFCA).

2.2.2 Alcohols

One of the main objectives of recent studies on organic synthesis is to replace environmentally harmful conditions of the industrial process with green and sustainable ones. Among these, the selective oxidation of hydroxyl groups to carbonyl ones has a major impact [241, 242].

Bellardita et al. [243] explored the selective oxidation of different alcohols: benzyl alcohol (BA), 4-methoxy benzyl alcohol (4-MBA) and piperonyl alcohol (PA) towards the corresponding aldehydes by using P-doped graphitic carbon nitride (g-C_3N_4) in pure water and simulated solar light irradiation. Qamar et al. [244] investigated the selective oxidation of 4-MBA (conversion >95 %, selectivity >99%) and 4-nitrobenzyl alcohol (4-NBA) (conversion >85 %, selectivity >99%) into their corresponding aldehydes in the presence of Pt-Bi_2WO_6. Qing et al. [245] synthesized Ni-Au modified g-C_3N_4 photocatalyst by a step-by-step photodeposition method and tested it for the production of H_2 (471.35 μmol·gcat^{-1}h^{-1}) and furfural formation (206.19 μmol·gcat^{-1}h^{-1}) from furfural-alcohol aqueous solution. Table 2.2 shows the oxidation of different alcohols to their corresponding aldehydes with different catalysts.

Table 2.2 Partial oxidation of different alcohols to their corresponding aldehydes over different catalysts in the presence of water or different solvents

Catalyst	Alcohol	Products	Catalyst dosage (g/l)	Solvent	Initial concentration (mmol)	References
TiO_2 (HP)	BA 2-MBA 3-MBA 4-MBA 2,4 DMBA 4-HBA 4-H-3-MBA (x=50%)	BAld (S=22%) 2-MBAld (S=56.5%) 3-MBAld (S=35%) 4-MBAld (S=70%) 2,4 DMBAld (S=60%) 4-HBAld (S=13%) 4-H-3-MBAld (S=1.8%)	0.2	Water	1	[246]
Ti_3C_2-TiO_2 (MT5)	FA (X≥ 99%) CA (X≥ 99%) VA (X= 43%)	FAld (S≥99%) CA (S≥99%) VA (S≥ 99%)	0.015	ACN	0.5	[247]
PdOx-WO_3	2-propanol (X= 96%)	Acetone (S≥ 80%)	1	Water	130 µmol	[248]
$ZnIn_2S_4$	BA (X=69.8%)	BAld (S=86.1%)	0.08	-	0.5	[249]
Au/CuO	BA (X=58.5%)	BAld (S=98.2%)	0.1 g in 10 mmol BA	No solvent	10	[250]
Au/MnO_2	BA (X=12.2%)	BAld (S=87.7%)	0.1 g in 10 mmol BA	No solvent	10	[250]
Au/NiO	BA (X=40.7%)	BAld (S=68.7%)	0.1 g in 10 mmol BA	No solvent	10	[250]
Au/CoOx	BA (X=28.7%)	BAld (S=71.6%)	0.1 g in 10 mmol BA	No solvent	10	[250]
Au/Fe_2O_3	BA (X=35%)	BAld (S=72.1%)	0.1 g in 10 mmol BA	No solvent	10	[250]
Au/Cr_2O_3	BA (X=3.3%)	BAld (S=94.8%)	0.1 g in 10 mmol BA	No solvent	10	[250]
Au/Al_2O_3	BA (X=30%)	BAld (S=98.2%)	0.1 g in 10 mmol BA	No solvent	10	[250]
Au/SiO_2	BA (X=30.1%)	BAld (S=98.2%)	0.1 g in 10 mmol BA	No solvent	10	[250]
3 wt. % Au/Ni_3Al HT	Phenylethanol (X=89.1%)	Acetophenone (S= > 99%)	0.05g in 0.5mmol of Phenylethanol	Benzotrifluoride	0.5	[251]
Au/CeO_2	PA (X= 46%)	PAld (S=100%)		No solvent		[252]
Au/CeO_2	PA (X= 68%)	PAld (S=100%)		No solvent		[252]

2.3 Organic drugs removal

The first photochemical oxidation of TC was reported by Davies et al. [253] in 1979 who studied the behavior of TC under UV light irradiation. The Authors demonstrated that the process proceeds by several steps through photo-deamination of TC followed by the interaction of the formed tetracycline radical with molecular oxygen forming a peroxyl radical, which abstracts H_2 giving rise to a hydroperoxide. Finally, hydroperoxide decomposes losing water. Addamo et al. [254] carried out the photocatalytic degradation of three different drugs, i.e. tetracycline, lincomycin, and ranitidine in the presence of TiO_2 powders (Degussa P25 and Merck) under UV irradiation. TC was almost completely mineralized in the presence of TiO_2 Degussa P25, whereas the initial TOC of ranitidine and lincomycin was reduced by 60% ca. Table 2.3 shows the results of TC degradation with different catalysts.

The photocatalytic method in the presence of persulfate (PS) and Fe_3O_4/MIL-101(Fe) allowed the occurrence of 87.1% degradation of 70 mg L^{-1} of OTC in 60 minutes [277]. MWCNTs-$CuNiFe_2O_4$ nanomaterials were utilized to effectively remove OTC from aqueous solution containing persulfate [278]. Excellent adsorption characteristics toward OTC were shown by the MWCNTs-$CuNiFe_2O_4$ combination, which also successfully activated potassium persulfate (KPS) for drug removal. By using 10 mg L^{-1} catalyst with an initial concentration of OTC equal to 300 mg L^{-1}, 88.6% degradation was achieved. $SO_4^{\cdot-}$ and $^{\bullet}OH$ radicals capturing agents such ethanol and isopropyl alcohol were used to investigate the reaction mechanism. The outcomes showed that the presence of these quenching agents reduced the removal effectiveness of MWCNTs-$CuNiFe_2O_4$ confirming the active role of these radicals in the degradation process.

Di Paola et al. [279], investigated the degradation and mineralization of lincomycin (LCM) with three different concentrations (10, 20, and 50 ppm) under UV irradiation in a Pyrex batch reactor with commercial TiO_2 Degussa P25. Sulfate, ammonium, and nitrate ions were formed as a result of the LCM mineralization.

Gao et al. [280], synthesized $ZnIn_2S_4$ photocatalyst and tested it for the degradation of LCM, within 90 minutes under visible light the complete degradation was observed with pseudo-first-order constant of 0.0285 min^{-1}.

TiO_2-based nanomaterials, including TNAs (TiO_2 nanotube arrays), TNWs/TNAs (TiO_2 nanowires on nanotube arrays), Au-TNAs, and Au-TNWs/TNAs, were developed for enhanced photocatalytic degradation of antibiotics in aquaculture wastewater [281]. TNWs/TNAs showed higher activity than TNAs due to larger surface area. Au-TNWs/TNAs showed the highest activity under UV-VIS or VIS irradiation exhibiting 100% efficiency in 20 minutes (LCM concentration 500 ng mL^{-1}) with reaction rates of 0.26 min^{-1} and 0.096 min^{-1}, respectively. The high activity of Au-TNWs/TNAs can be ascribed to the synergistic effects between high surface area and surface plasmonic effect in Au nanoparticles. Augugliaro et al. [282] reported that LCM is broken down by photocatalytic oxidation in aqueous suspensions of Degussa P25 polycrystalline TiO_2, using a hybrid system consisting of a solar photoreactor and a membrane module. The initial LCM concentration was 20 μM. The reported kinetics are pseudo-first order with high membrane rejection for LCM and its oxidation products.

Table 2.3 Results related to TC degradation with different photocatalytic systems

Photocatalyst	Irradiation	TC Concentration (mg L^{-1})	Catalyst quantity (g L^{-1})	TC degradation	Refrences
TiO_2	Ultraviolet	32.44	0.5	100% 50 % mineralization	[257]
C–N–S tri doped TiO_2	Visible light	5.0	0.5	99% 180 min 26 % mineralization	[258]
α-Fe_2O_3/TiO_2	500 W Halogen	30	0.614	97.5%	[259]
Cu_2O–TiO_2 Cu_2O coupled with TiO_2 nanotubes	Visible light	100	1.5	100%, 60 min	[260]
MWCNT/TiO_2 nano-composite	UVC irradiation	10	0.2	100% 100 min 37.3% mineralization	[261]
TiO_2@g-C_3N_4	Xenon Lamp	20	0.1	100%	[262]
Graphitic carbon nitride	Visible Light	10	1	77% 120 min	[263]
5-PANI/$CuFe_2O_4$	UV-Vis	50	0.1	86% 120 min 95 % mineralization	[264]
$Bi_2Ti_2O_7$ (BTO)	Visible light	25	0.1	88.2% 150 min	[265]
CuO/Fe_2O_3	UV	20	0.05	88% 50 min	[266]
ZnO/γ-Fe_2O_3	UV-visible light	30	0.01	88.52% 150 min	[267]
Black graphitic carbon nitride (CN-B)	UV-Vis	30	0.05	92% 120 min	[268]
AgI/$BiVO_4$	300 W Xenon lamp	20	0.03	94.91% 60 min 90.5 % mineralization	[269]
UiO-66-NDC/P–C_3N_4	UV Visible light	30	1	95% 120 min 49 % mineralization	[270]
3% SnO_2/g-C_3N_4	Visible Light	30	0.5	95.90% 120 min	[271]
[(L1(Ag_4I_7)]CH_3CN	Visible light	20	0.01	97.91% 180 min	[272]
ZnO/$NiFe_2O_4$/Co_3O_4	Natural solar Light	30	0.02	98% 20 min 90 % mineralization	[273]
$Bi_2Sn_2O_7$/Bi_2MoO_6	300 W-Xenon lamp	20	0.035	98.7% 100 min 56.4 % mineralization	[274]
MIL-88A	Visible light	200	0.25	99.8%	[275]
UiO-66-NH_2@WO_3/CC	Visible Light	20	0.02	100% 60 min	[276]

As a highly effective metal-free photo-catalyst, graphitic carbon nitride (g/C_3N_4) shows promising behaviour for the degradation of drugs. By adjusting the energy band, improving charge extraction, and adding a co-catalyst, the photocatalytic activity of g/C_3N_4 was enhanced and both the degradation rate and conversion degree of LCM under visible light irradiation increased [283]. Carbon quantum dots (CDs) were added as cocatalysts to improve the formation of $\cdot O_2^-$; graphene oxide (rGO) was employed to improve the charge mobility. The most active improved

photocatalyst resulted CD-rGO-O-g/C_3N_4 exhibiting a tenfold increase in degradation rate when compared to the original g/C_3N_4. After 180 minutes, 99% degradation was achieved starting from an initial drug concentration of 100 mg L^{-1}. The active species, such as $O_2^{\bullet-}$, $^{\bullet}OH$, and h^+, contribute differently to the degradation for each photocatalyst.

Metal-organic frameworks (MOF)-based photocatalytic treatment of LCM using Basolite F300 as catalyst in the presence of two oxidants (H_2O_2, $S_2O_8^{2-}$) was reported by Kontogiannis et al. [284] . Results showed that the drug elimination was completed within 2 hours, and the oxidant concentration (0–300 mg/L) affected the process rate. The best concentration to attain maximum degradation was 100 mg/L for both oxidants. After 120 minutes, just 8% of MOFs was degraded according to photolysis studies. The photo catalyst Basolite® F300 was activated using H_2O_2 as an oxidant in order to study the photo catalytic process. MIL-100 surface iron sites showed Fenton-type activity, which synergistically increased degradation. When H_2O_2 was added, the rate of degradation increased to 95% in 90 minutes, indicating catalyst activation and a conceivable heterogeneous photo-Fenton reaction involving Fe-sites and H_2O_2.

2.4 Aim and structure of the work

The aim of this work consists of three parts:

1. The production of high value chemicals and H_2 through photoreforming of different sacrificial agents in the presence of TiO_2 modified and alternative photocatalysts.
2. Partial oxidation of aromatic alcohols and HMF.
3. Removal of organic drugs

In particular, the first part will be covered in **Chapter 4** to **Chapter 7**. In **Chapter 4-I**, the photoreforming of aqueous glucose and fructose solutions in the presence of 0.5 wt% Pt-loaded homemade bare and Nb_2O_5-TiO_2 catalysts was investigated to maximize the activity of titania for both hydrogen and valuable chemical production. **Chapter 4-II** focused on comparison of noble metal loaded (Pt-TiO_2) and noble metal free catalysts (Cu-TiO_2) for photoreforming glucose and fructose at ambient conditions with the aim of linking the photoactivity to some structural and surface characteristics. In **Chapter 5**, MBi_2O_4-TiO_2 P25 (M = Cu, Ni, Co, Zn) were successfully synthesized by a simple ball milling method by varying some parameters. The noble metal-free TiO_2-based photocatalysts were used to carry out the partial oxidation of glucose and glycerol with simultaneous H_2 production under simulated solar light irradiation. In **Chapter 6**, the photoactivity of TiO_2 and non-TiO_2 ($ZnIn_2S_4$) catalysts was compared for the H_2 production in the presence of different sacrificial agents (furfuryl alcohol, methanol and triethanolamine). Furfuryl alcohol also produced the formation of furfural in parallel with that of H_2. In **Chapter 7-I**, the commercial samples (Cu_2O-P25) prepared through ball milling were tested for production of hydrogen through photoreforming of biomass derivatives (glycerol, glucose, ethanol and biodiesel wastewater) on a pilot plant scale photoreactor under direct sunlight in green conditions. In this study, the effect of Cu_2O percentages and ball milling parameters such as rotation speed and time was studied. **Chapter 7-II** covered the investigation of home prepared catalyst (HP) modified with Cu_2O via ball milling for photocatalytic hydrogen production through photoreforming of glycerol, formic acid, ethanol, and glucose at a pilot plant scale photoreactor.

The second part will be mainly described in **Chapter 8 and 9.** In **Chapter 8**, the ternary chalcogenide $ZnIn_2S_4$ was prepared by a simple hydrothermal method in which the carcinogen thioacetamide, universally used as a precursor, has been, for the first time, replaced successfully with the harmless thiourea. $ZnIn_2S_4$ was tested for the partial oxidation of different aromatic alcohols to their corresponding aldehyde in water solution under simulated solar light irradiation. The photocatalytic performance of $ZnIn_2S_4$ was compared with that of TiO_2 P25. In **Chapter 9**, the partial oxidation of HMF to high value compounds under green conditions was investigated by using various photocatalysts and irradiation sources. In particular, TiO_2 based and alternative photocatalysts (Bi_2O_3, Cu_2O, C_3N_4, $ZnIn_2S_4$) were chosen with the aim of not only increasing the activity but also the selectivity in the partial oxidation of HMF under environmentally friendly conditions.

The last part of work will cover **Chapter 10** in which the degradation of organic drugs such as tetracycline, oxytetracycline and lincomycin was described in the presence of different photocatalysts. In this study, mineralization of drugs was also investigated.

CHAPTER 3

Materials and methods

CHAPTER 3

3. Materials and methods

3.1 Chemicals

Titanium tetrachloride, hydrochloric acid, ethanol, titanium(IV) isopropoxide named as TIP, niobium(V) chloride, Pluronic P127, copper(I) chloride, niobium(V) chloride, platinum chloride, zinc chloride, thiourea, benzyl alcohol, benzaldehyde, benzoic acid, 4-nitrobenzyl alcohol, 4-nitrobenzaldehyde, 4-nitrobenzoic acid, 4-methoxybenzaldehyde, 4-methoxybenzoic acid, 2-hydroxybenzyl alcohol, 2-hydroxybenzyl aldehyde, 2-hydroxybenzoic acid, 4-hydroxybenzyl alcohol, 4-hydroxybenzyl aldehyde, 4-hydroxybenzoic acid, furfuryl alcohol, furfural, 2-furoic acid, piperonyl alcohol, piperonal, piperonylic acid, cinnamyl alcohol, cinnamic aldehyde, cinnamic acid, vanillyl alcohol, vanillin, vanillic acid, melamine, zinc acetate dehydrate, niobium(V) oxide, glucose, fructose, arabinose, erythrose, gluconic acid, formic acid, glycerol, cobaltous nitrate hexahydrate, nickel(II) nitrate hexahydrate, zinc nitrate hexahydrate, citric acid were purchased from Sigma-Aldrich.

Indium chloride from Labfor, 4-methoxybenzyl alcohol from Fluka, Copper(II) nitrate trihydrate $Cu(NO_3)_2{\cdot}3H_2O$ and bismuth(III) nitrate pentahydrate $Bi(NO_3)_3{\cdot}5H_2O$ from Merck and were used without further purification.

The commercial samples used were titanium dioxide from BDH, Aeroxide P25 and copper(I) oxide (Cu_2O) from Riedel-de Haën. Ultrapure deionized water was used throughout the study.

3.2 Analytical determinations

3.2.1 HPLC-1

HPLC-1 was employed for the identification of high value chemicals in the case of glucose, fructose, glycerol, furfuryl alcohol and HMF used as sacrificial agents.

A Thermo Scientific Dionex ultimate 3000 HPLC, equipped with a Diode Array and refractive index detectors, was used for the quantitative determination of glucose and fructose and for identifying their reaction products. The eluent was a 2.5 mM H_2SO_4 aqueous solution, the flow rate was 0.6 mL/min and the column was a Phenomenex REZEK ROA H^+ Organic acid H^+.

3.2.2 HPLC-II

HPLC-1I was used to examine the degradation of aromatic alcohols into their corresponding aldehydes and also for removal of organic drugs.

A Beckman coulter HPLC apparatus supplied with a Diode Array detector was used to identify and to calculate the concentrations of the substrates and of the produced intermediates. A Phenomenex KINETEK 5 μm C18 column was used, and the eluent (flow 0.8 mL min^{-1}) consisted of a mixture of acetonitrile and 13 mM trifluoroacetic acid (20:80 v:v). Standards of alcohols and their intermediates allowed to identify the products and to obtain the calibration curves.

3.2.3 GC

On lab scale, a HP 6890 Series GC System equipped with a Supelco packed column GC 60/80 Carboxen^{TM}-1000 and a thermal conductivity detector (TCD) was used to measure the content of H_2 and CO_2 during the reactions carried out in the lab.

During the pilot plant scale study, an Agilent Technologies MicroGC 490 micro gas chromatograph with a thermal conductivity detector (TCD) and a CP MolSieve 5A column channel (10 m, with retention time stability and backflush) was used for the quantification of the generated

H_2, which was evaluated online with an average determination error of less than 2.5%. Measurements were done every 10 minutes. The transformation of the area peak into % of H_2 was done thanks to a calibration curve carried out with mixtures of H_2 and N_2 of known concentration.

3.2.4 Photons absorbance

A radiometer was used to check the optimum amount of the photocatalysts able to absorb ca. 90% of the photons emitted by the lamp by performing transmittance measurements.

3.2.5 Intensity of solar radiation

The solar irradiation was measured ($W \cdot m^{-2}$) every minute using a radiometer (Kipp & Zonen CUV3, 280-400 nm) installed on a platform at the same angle as the compound parabolic collector (CPC) (37º, local latitude).

3.2.6 Temperature

Using a Pt100 (HD2107.2-Data Logger Centesimal Thermometer Pt100) dipped in the reaction mixture inside the tank, the temperature was recorded.

3.2.7 pH

The pH was measured by using a multimeter (CRISON GLP22)

3.2.8 Total organic carbon (TOC) analyzer

Total organic carbon (TOC) was measured using a TOC Shimadzu 5000A analyzer, which was equipped with an autonomous auto sample injector ASI 5000 A, to monitor the mineralization of the drugs.

For pilot plant scale study, a TOC analyzer (Model TOC-L CSN, Shimadzu, Japan) was used to measure the dissolved organic carbon (DOC).

3.2.9 UV–vis spectrophotometry

A UV-visible Shimadzu 2401 PC spectrophotometer was used to record the absorption spectra of the samples that were taken during the runs.

For pilot plant scale study, glycerol concentration was analyzed by using a colorimetric analysis, in which a dark pink color was produced (Quinoneimine Dye intermediate) that can be determined by UV–vis spectrophotometry at a wavelength of 500 nm.

3.2.10 Ionic chromatography

Carboxylic acids formed during the photocatalytic reaction, before the complete mineralization of sacrificial agents, were determined by using ionic chromatography (940 Professional IC Vario adapted with the 942 extension module, Metrohm AG, Switzerland). The system was established in a METROSEP A Supp 7–250 (250 mm × 4.0 mm ID) column with a gradient of Na_2CO_3 0.53 $g \cdot L^{-1}$/H_2O as the mobile phase and a flow rate of 0.7 $mL \cdot min^{-1}$.

3.2.11 ICP-MS

ICP-MS (iCAP TQICP-MS, Thermo Scientific) was used for measuring the dissolved Cu with a standard deviation of less than 2% and a limit of detection of 2.2 $ng \cdot L^{-1}$.

3.3 Materials characterizations

3.3.1 X-ray diffraction (XRD)

X-ray diffraction (XRD) patterns of the investigated powders were obtained by a Philips diffractometer (operative at a current of 30 mA and a voltage of 40 kV) using the CuKα radiation. The morphology was examined by scanning electron microscopy (SEM) using a Nova NanoSEM instrument. A small amount of powder samples was placed on carbon tape attached to a stainless-steel stub.

3.3.2 Diffuse reflectance spectroscopy (DRS)

The UV-Vis diffuse reflectance spectra (DRS) were acquired in the 200-800 nm wavelength range at room temperature using a Shimadzu UV-2401 PC spectrophotometer with barium sulphate ($BaSO_4$) as the reference material. Band gap values were calculated by plotting the modified Kubelka-Munk function, $[F(R'_\infty)\cdot h\nu]^{½}$, against the energy of the stimulating light.

3.3.3 Brunauer–Emmett–Teller (BET)

The specific surface areas (SSA) were determined in a Flow Sorb 2300 apparatus (Micromeritics) by using the single-point BET method.

3.3.4 Raman spectroscopy

Raman spectra of the samples were recorded using a BWTek-i-micro Raman Plus system equipped with a 785 nm diode laser.

3.3.5 X-ray photoelectron spectroscopy (XPS)

X-ray photoelectron spectroscopy (XPS) was performed using a Thermo Fisher Scientific (TFS) Escalab Xi+ XPS with an AlKα X-ray source. Prior to the XPS measurements, the samples were etched *in situ* with an Ar beam to remove contaminants from the top layer.

3.3.6 Scanning electron microscopy (SEM)

A Nova NanoSEM scanning electron microscope (SEM) was used to study the morphology of the solid samples. It was operated at 20 kV on samples on which a thin layer of gold had been vapour deposited.

3.3.7 Transmission electron microscopy (TEM)

Transmission electron microscopy (TEM) was performed using a Titan transmission electron microscope operating at 300 kV. The samples were prepared by suspending the powder in 2-propanol, treating with ultrasound, and finally depositing 3 μL of the suspension two consecutive times on a 400-mesh Au grid provided by Tedpella. The solvent was then evaporated at room temperature. ImageJ was used to evaluate the lattice d-spacing and the size of the nanoparticles.

3.3.8 Photoluminescence spectroscopy (PL)

The solid-state photoluminescence spectra (PL) of the investigated photocatalysts were recorded with a Perkin Elmer UV-Vis fluorescence spectrometer LS 55 in the range of 300-600 nm at an excitation wavelength of 300 nm.

3.3.9 Temperature programmed desorption (TPD) spectroscopy

Surface acidic sites were revealed by using pyridine as a probe molecule and a Perkin Elmer Pyris 1 TGA instrument. Samples were first heated from 323 to 473 K and held at this temperature for 15 minutes to remove contaminants from the catalyst surface. The samples were then cooled to 393 K and pyridine was adsorbed with a saturated N_2 stream until the weight of the catalyst was constant (after about 20 minutes). The powders were then purged with N_2 and held at 393 K for 2 hours to remove excess pyridine. TPD (temperature-programmed desorption) profiles were recorded in the temperature range from 393 to 773 K.

3.3.10 CO_2 TPD

To determine basic properties of the surface of the investigated photocatalysts, CO_2 TPD profiles were obtained by heating samples in an O_2 (5%)/He stream (25 mL/min) from room temperature to 398 K (10 K/min) in the Micromeritics AutoChem II 2920 apparatus. After 10 minutes, the samples were cooled to 323 K and then the gas flow was changed to Ar (25 mL/min). CO_2 was introduced by dosing CO_2 (80 vol%)/Ar into the Ar stream (25 mL/min) flowing through the samples at 323 K. Desorption of CO_2 from the sample into the Ar stream (25 mL/min) was

monitored over the temperature range of 323-633 K (heating ramp 10 K/min) using the Pfeiffer Vacuum ThermoStar mass spectrometer.

3.3.11 Diffuse reflectance infrared Fourier transform spectroscopy (DRIFTS)

The Diffuse Reflectance Infrared Fourier Transform Spectroscopy (DRIFTS) spectra of the studied catalysts after adsorption of pyridine were recorded using a Perkin Elmer Frontier FT-IR spectrometer equipped with a mercury cadmium telluride (MCT) detector. A catalyst sample placed in a DRIFTS cell was first heated in an N_2 stream from room temperature to 473 K and then held at this temperature for 15 minutes to remove impurities from the catalyst surface. The sample was then cooled to 393 K in an N_2 stream, and a background spectrum was recorded. After saturating the catalyst surface with a pyridine containing N_2 stream for 20 minutes at 393 K, the catalyst sample was purged with pure N_2 and held at 393 K for additional 2 hours to remove the excess pyridine. The FT-IR spectra (an average of 64 scans, resolution of 4 cm^{-1}) were recorded at 393 K.

3.3.12 Zeta potential

Zeta potential measurements were performed using a Malvern Panalytical Zetasizer Ultra Red instrument equipped with a Malvern Multipurpose Titrator MPT-3. 25 mg of a photocatalyst was dispersed in 100 mL of ultrapure water and stirred for 30 minutes (400 rpm). 0.25 M and 0.025 M hydrochloric acid and 0.25 M sodium hydroxide were used to adjust the pH in the measurement range.

3.3.13 Electron paramagnetic resonance (EPR) spectroscopy

For the identification of the free radical species of the catalyst, electron paramagnetic resonance (EPR) was performed on an EMX-nano spectrometer (Bruker Biospin Corp., Karlsruhe, Germany). For the detection of transition metals and oxygen vacancies, the powder was placed in a tube and was fitted into the sample holder in the EPR test chamber for analysis. For the detection of superoxide anion radicals ($O_2^{\bullet-}$), the sample was dissolved in methanol to form a 1 mg/mL suspension which was then dispersed by using an ultrasound bath. Subsequently, 100 mM of trapping agent 5,5 Dimethyl-1-pyrroline N-oxide (DMPO) was added into the suspension. After stirring, the mixture was placed in a tube and was fitted into the sample holder in the EPR test chamber for analysis. For the detection of hydroxyl radical ($OH^{\bullet}$), the sample was dissolved in water to form a 1 mg/mL suspension which was then dispersed by using ultrasonication. Subsequently, 100 mM of trapping agent 5,5 Dimethyl-1-pyrroline N-oxide (DMPO) and 100 µL of 1 mM H_2O_2 were added into the suspension. After stirring, the mixture was placed in a tube and was fitted into the sample holder in the EPR test chamber for analysis. The sample was irradiated for 30 minutes using a UV (LOT-Quantum Design GmbH) lamp and data were recorded.

3.3.14 Fourier-transform infrared spectroscopy (FTIR)

The ATR-FTIR spectra were acquired by a Perkin Elmer FTIR spectrophotometer with a band width of 2 cm^{-1}.

3.4 Photocatalytic activity

3.4.1 Photocatalytic activity on lab scale

The photocatalytic activity was studied in anaerobic conditions by using different substrates, i.e. glucose and fructose, glycerol, methanol, TEOA, and furfuryl alcohol at room temperature and atmospheric pressure, monitoring the evolution of H_2 and CO_2 in the gas phase and the formation of the intermediates in the liquid phase. In cases of partial oxidation of alcohols, HMF, and drugs removal experiments were conducted in the reactor opened to atmospheric air.

Different Pyrex cylindrical reactors of different volumes 150, 500 and 800 mL were used for the various reactions. As far as the anaerobic conditions are concerned, He was bubbled into

the solution for 30 minutes to achieve the adsorption-desorption equilibrium of the substrate on the surface of the catalyst. After that, the reactor was sealed, and the near-UV lamp (125 W medium pressure Hg) or halogen lamp of 150 W (or 50W) was switched on. The initial concentrations of different substrates such as glucose, fructose, glycerol, furfuryl alcohol, TEOA and methanol were 1 mM, 1 mM, 2 mM, 0.5 mM, 10% by volume, and 10% by volume, respectively, and the reactions were carried out at "natural" pH of the aqueous suspension measured after adding the catalyst. For the different catalysts specific amounts were determined. To measure the substrates adsorption on the catalyst surface in the absence of light, their concentration values were measured after 30 minutes of stirring of the suspension containing the catalyst under dark conditions. The photocatalytic reactions lasted 5 h and samples were withdrawn periodically during the irradiation time, and filtered by 2 μm membranes (HA, Millipore). For selective oxidation of alcohols, HMF and removal of drugs, similar procedure was adopted but in aerobic conditions. An experimental setup is shown in Figure 3.1.

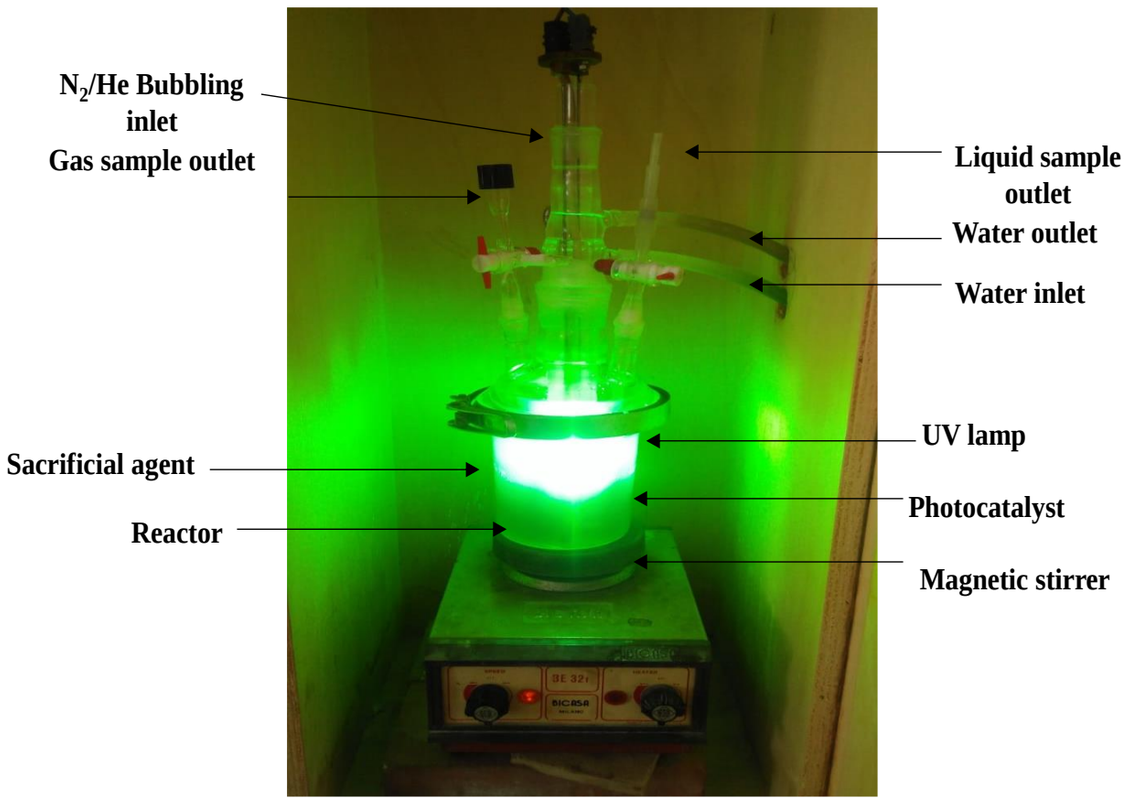

Figure 3.1. Experimental setup used for lab scale photocatalytic activities

3.4.2 Photocatalytic activity on pilot plant scale

The investigation was carried out at the Plataforma Solar de Almeria (latitude: 37.0909º N, longitude: 2.357º W) in a pilot plant designed with the possibility of creating a reductive atmosphere. It consisted of a 10L stainless-steel tank connected to a 14.25L Compound Parabolic Collector (CPC) photo-reactor, tilted at 37º, with a 2.10 m^2 sun-exposed surface. The N_2 gas flow controller (BRONKHORST HI-TEC; operating range: 20-500 NmL·min^{-1}) was utilized to both eliminate oxygen from the system, extract H_2 produced in the system and transport it to the MicroGC analyzer. Before irradiation, the nitrogen flow rate was adjusted to 500 NmL·min^{-1} (2 bars) to get anoxic conditions. Then, throughout the experiment, a flow of 60 NmL·min^{-1} (2 bar) was fixed. The solution was continuously recirculated from the tank to the CPC photo-reactor tubes, at 20 L·min^{-1} with a centrifugal pump (PanWorld NH-100PX). A WIKA pressure gauge (2.5% accuracy class) and a portable thermometer with a PT-100 Delta OHM HD2107.1 sensor were used to measure the pressure and the temperature, respectively, inside the CPC.

The plant was filled with 25 L of demineralized water in each experiment, causing that the tank headspace was 7.04 L. The airtight tank was closed after adding the photocatalyst and the sacrificial agent and for 75 minutes, a continuous flow rate of 500 $mL \cdot min^{-1}$ of N_2 was bubbled into the tank. After 75 minutes, the experiment started by adjusting the N_2 flow rate to 60 $NmL \cdot min^{-1}$, redirecting the exit of the gas stream from the atmosphere to the gas chromatograph, initializing the sample H_2 measurements and withdrawn the first sample of the reaction mixture as time zero. In the same moment, CPC was uncovered starting the experiment. The reaction was carried out for at least 4 hours under solar radiation. According to a previous study, the optimal amount of the catalyst and initial glycerol concentration were 100 $mg \cdot L^{-1}$ and 0.075M (6.9 $g \cdot L^{-1}$), respectively. The experimental setup used for pilot plant scale activities is shown in Figure 3.2.

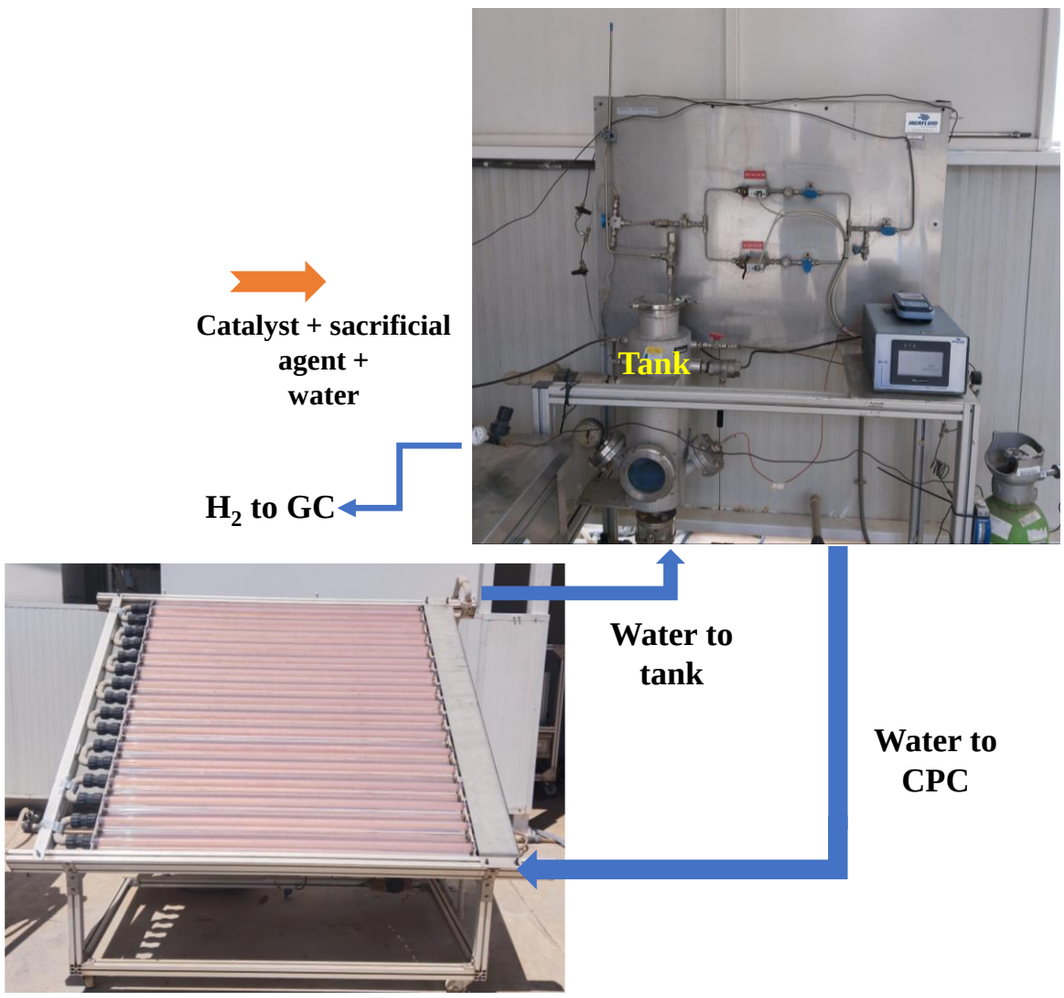

Figure 3.2. Pilot plant scale photoreactor

CHAPTER 4-I

Pt-Nb_2O_5-TiO_2 based semiconductors for photo-reforming of glucose and fructose aqueous solutions

In this chapter, text is adapted from the following publication.

Muhammad Umair, Giovanni Palmisano, Reem Al Sakkaf, Samar Al Jitan, Albin Pintar, Gregor Žerjav, Leonardo Palmisano, Vittorio Loddo, Marianna Bellardita. Pt-Nb_2O_5-TiO_2 based semiconductors for photo-reforming of glucose and fructose aqueous solutions. *Applied Surface Science* 2024, 648, 159030. DOI: https://doi.org/10.1016/j.apsusc.2023.159030

CHAPTER 4-I

Pt-Nb_2O_5-TiO_2 based semiconductors for photo-reforming of glucose and fructose aqueous solutions

4-I.1 Abstract

The conversion of biomass derivatives into fuels and valuable compounds under green conditions is increasingly attracting the attention of the scientific community. In this study, the photo-reforming of aqueous glucose and fructose solutions in the presence of 0.5 wt% Pt-loaded homemade bare and Nb_2O_5-TiO_2 catalysts was investigated to maximize the activity of titania for both hydrogen production and valuable chemical production. The samples were characterized by different surface and bulk techniques to discover a correlation between photoactivity and some catalyst properties. The most efficient sample was the home-prepared Pt-4%Nb_2O_5-HP, for both glucose and fructose conversion, with the highest H_2 productivity and the highest selectivity towards partially oxidized compounds. Photo-deposition of Pt was essential for H_2 production and, surprisingly, also increased the basicity of the TiO_2 surface; an increase in surface acidity was measured when only niobium oxide was added, whereas stronger basic sites were observed in the simultaneous presence of Pt and niobium oxide.

4-I.2 Photocatalysts preparation

4-I.2.1 Home prepared (HP)

The sample named as HP was prepared by adding titanium(IV) isopropoxide (TIP) to an aqueous solution containing HCl, Pluronic P127, and C_2H_5OH. The following molar ratios were used: TIP (1): H_2O (15): C_2H_5OH (40): HCl (0.5): P127 (0.005). The resulting solution was mixed at room temperature for about 4 h and then heated at 383 K overnight. The solid obtained was calcined at 773 K for 24 h.

4-I.2.2 x%Nb_2O_5-HP

The samples containing niobium were prepared by adding different amounts of $NbCl_5$ to the ethanolic solution before adding TIP. X% Nb-HP was the code used for these samples, where X% indicates the nominal weight percentage of Nb relative to TiO_2.

4-I.2.3 Pt-x% Nb_2O_5-HP

Some TiO_2 catalysts were loaded with 0.5 wt% Pt by a photo-deposition method. Distilled water (200 mL), ethanol (50 mL), $PtCl_4$ (5 mL), and the TiO_2 sample (1 g) were added to the photoreactor. The resulting mixture was stirred in the dark for 0.5 h with bubbling of He and then illuminated with a UV lamp (125 W) for 7 h. The resulting mixture was filtered, washed with distilled water, and then dried in an oven for 6 h.

4-I.3 Results and discussions

Solid acid catalysts with appropriate amount and strength of both Brønsted and Lewis acidic centers, such as Nb_2O_5, have been shown in literature to be effective in converting glucose and fructose to HMF mainly through catalytic processes [74b-f]. In addition, Nb_2O_5 is considered a water-tolerant solid acid and is therefore suitable for the dehydration of sugars in the aqueous phase via a catalytic route. Bare Nb_2O_5 has generally low photoactivity, then Nb_2O_5-TiO_2 coupled sample were prepared to exploit the features of both components [74g].

4-I.3.1 Specific surface area (SSA)

The S.S.A. of the home-prepared photocatalysts is higher than that of P25 and generally increases with increasing Nb_2O_5 content, with the highest value observed for the Pt-6% Nb_2O_5-HP sample.

Table 4-I.1 lists some physico-chemical properties of the photocatalysts used, such as the TiO_2 phases, band gap, specific surface areas, and isoelectric point (IEP) values of all the samples used.

Table 4-I.1 Some physico-chemical properties of the investigated photocatalysts

Sample	Phase	S.S.A. (m^2 g^{-1})	Band gap (eV)	pH_{PZC}
Pt-P25	Anatase + Rutile	50	3.09	5.00
Pt-HP	Anatase + Rutile	78	3.05	4.45
Pt-2%Nb_2O_5-HP	Anatase + Rutile	75	3.08	4.16
Pt-4%Nb_2O_5-HP	Anatase + Rutile	92	3.07	4.13
Pt-6%Nb_2O_5-HP	Anatase + Rutile	100	3.08	4.03
4%Nb_2O_5-HP	Anatase + Rutile	90	2.99	3.67

4-I.3.2 X-ray diffraction (XRD)

Figure 4-I.1A shows the XRD diffractograms of the prepared samples. The commercially widely available TiO_2 P25 was chosen as the standard. The prepared samples, as well as the P25 one, consist of a mixture of anatase and rutile, as shown by the XRD results. Also in the composite sample, anatase and rutile peaks are distinguishable, indicating that the presence of Nb does not alter the crystalline structure of TiO_2. No peaks associated with the other constituents (Pt, Nb) can be noticed, probably due to their small amount relative to TiO_2 and the high degree of dispersion. A close examination of the (101) peak of anatase (see Figure 4-I.1A) shows a slight shift to lower angles in the presence of an increasing amount of Nb, which is due to the substitution of the Ti^{4+} ions of the TiO_2 lattice by Nb ions [285, 286].

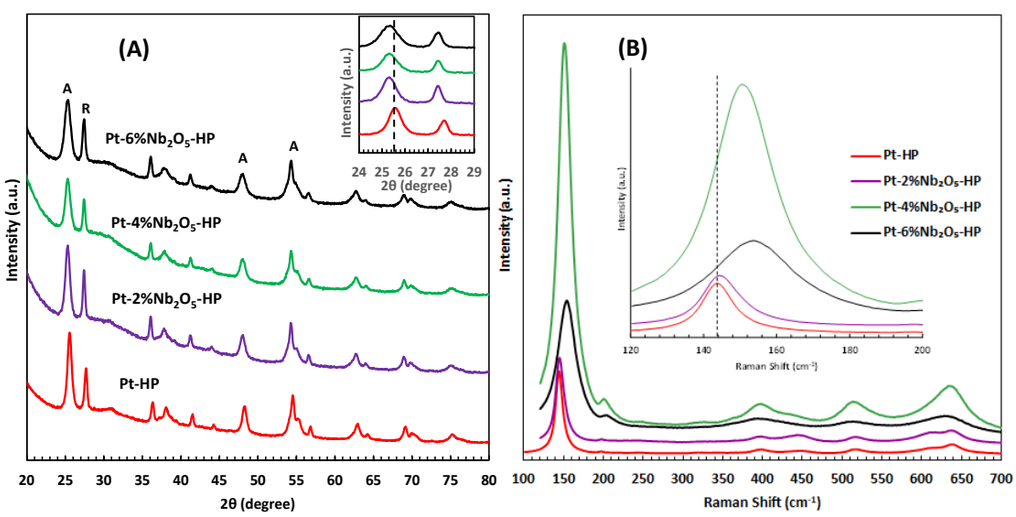

Figure 4-I.1 XRD patterns (A) and Raman spectra (B) of Pt-HP, Pt-2%Nb_2O_5-HP, Pt-4%Nb_2O_5-HP and Pt-6%Nb_2O_5-HP samples

4-I.3.3 Raman spectroscopy

The Raman spectra of all samples (Figure 4-I.1B) show the characteristic bands of anatase at 144 cm^{-1} (E_g), 197 cm^{-1} (E_g), 396 cm^{-1} (B_{1g}), 514 cm^{-1} (A_{1g}), and 637 cm^{-1} (B_{1g}) with high intensity, while the bands associated with rutile at 446 cm^{-1} and 613 cm^{-1} are not very clear because this polymorph is present in lower amounts than anatase. It can be noticed, in the XRD diffractograms, that there are no identifiable peaks associated with Pt and Nb_2O_5 species. By magnifying the main anatase peak at 144 cm^{-1} (see Figure 4-I.1B), a progressive shift to higher frequencies with increasing Nb_2O_5 content is visible compared to the Pt- HP sample. This can be attributed to the interaction of the TiO_2 lattice with Nb, which causes the formation of oxygen vacancies instead of Ti^{4+} ions in agreement with the XRD results [285,287]. Moreover, the Raman spectra recorded in different areas of the samples are superimposable, indicating a homogeneous composition of samples.

4-I.3.4 Scanning electron microscopy (SEM)

Figure 4-I.2 shows selected SEM micrographs of the synthesized semiconductors. All powders show irregular roundish particles with size in the range of 30-130 nm. Pt and Nb_2O_5 particles are indistinguishable, probably due to their small amount and uniform integration into the titanium dioxide matrix. After addition of the different amounts of niobium oxide, no differences in the morphology of the samples are observed.

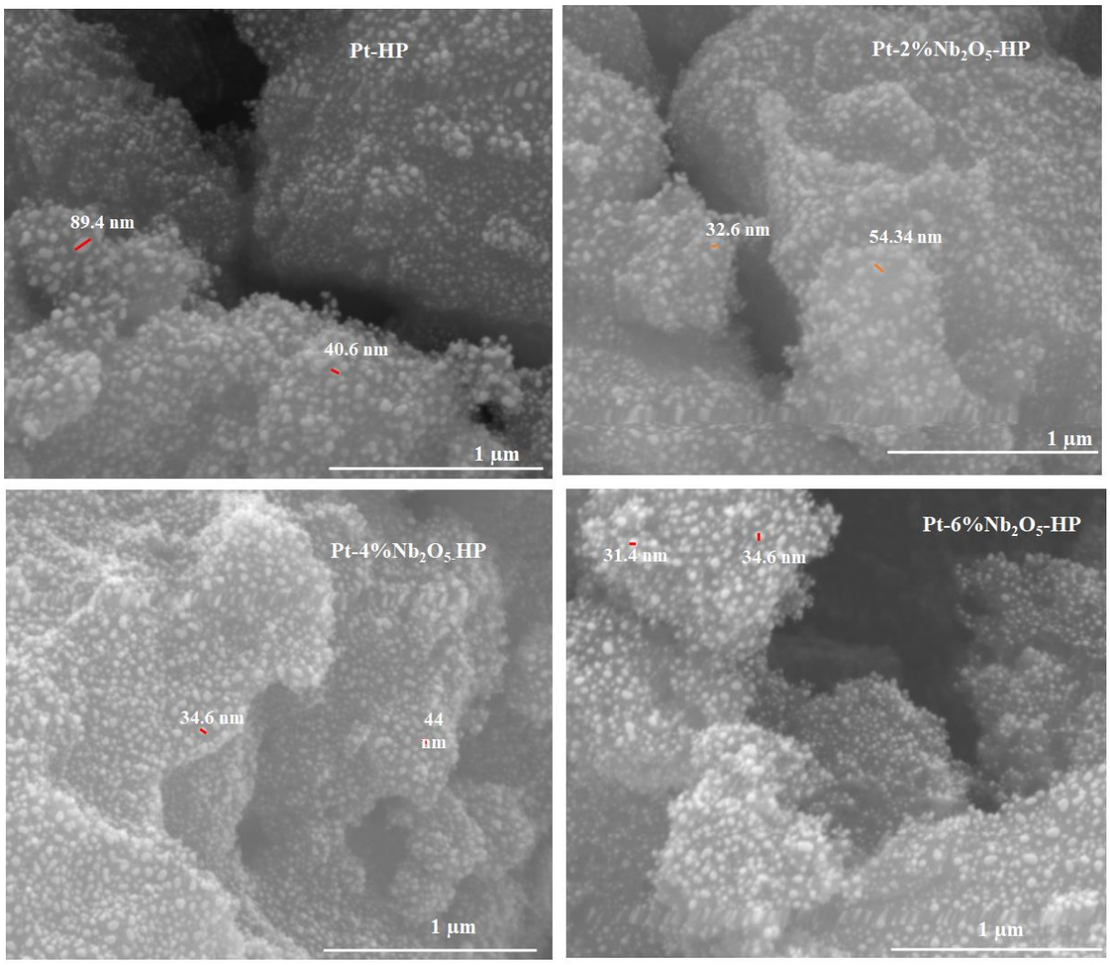

Figure 4-I.2 Selected SEM micrographs of the examined photocatalysts

4-I.3.5 UV-Vis diffuse reflectance spectroscopy (DRS)

Figure 4-I.3 shows the UV-Vis diffuse reflectance spectra (DRS) of the different photocatalysts. All the samples are active when irradiated with UV light and show a transition edge between 360 and 390 nm, which is typical for TiO_2-based semiconductors. Reflectance values of

less than 50% in the visible range are due to the presence of photo-deposited Pt, which gives the powders a greyish colour [31]. The sample 4%Nb_2O_5-HP, which does not contain Pt, has a reflectance of over 90% in the same region. The x%Nb_2O_5-TiO_2 based samples show similar band gap values between 2.99 and 3.09 eV.

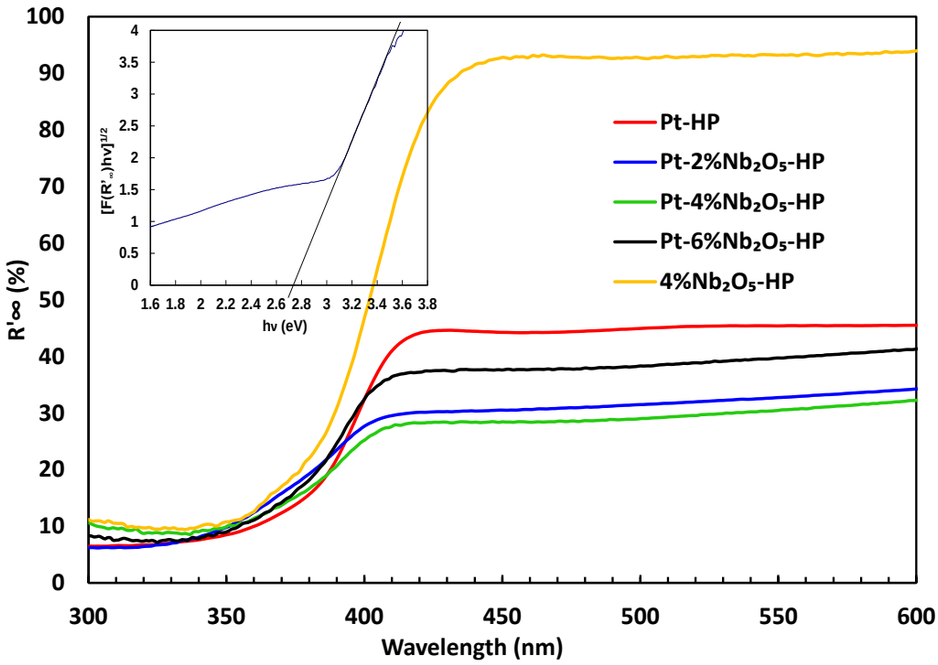

Figure 4-I.3 UV-Vis DRS spectra of the prepared photocatalysts

4-I.3.6 zeta potential measurements

Figure 4-I.4 shows the results of the zeta potential measurements as a function of pH of the TiO_2-based composites. The isoelectric point (IEP), given in Table 4-I.1, is the pH at which the net charge on the catalyst surface is zero. The values vary from 3.67 to 5.00, with the highest value for the Pt-P25 solid and the lowest for the 4%Nb_2O_5-HP sample. The progressive decrease in IEP with the addition of Nb_2O_5 indicates an increase in the acidity of the surface of the composite samples. The low value of the 4%Nb_2O_5-HP sample, which does not contain Pt, indicates that Pt induces the formation of basic sites, the presence of which decreases the acidity of the surface. The differences measured in the other samples with different Nb_2O_5 content (recall that the amount of Pt is 0.5 wt%, which is the same for all samples) are clearly due to the different amounts of oxide. Since the pH_{PZC} values of the photocatalysts are below 5 (approximately the value of the reacting solution), this means that the catalytic surface of all samples is negatively charged. However, since there are differences, even if they are not very large, coulombic interactions of different magnitudes can occur, affecting the photoactivity between the species in the reaction mixture and the surface of the different photocatalysts [288].

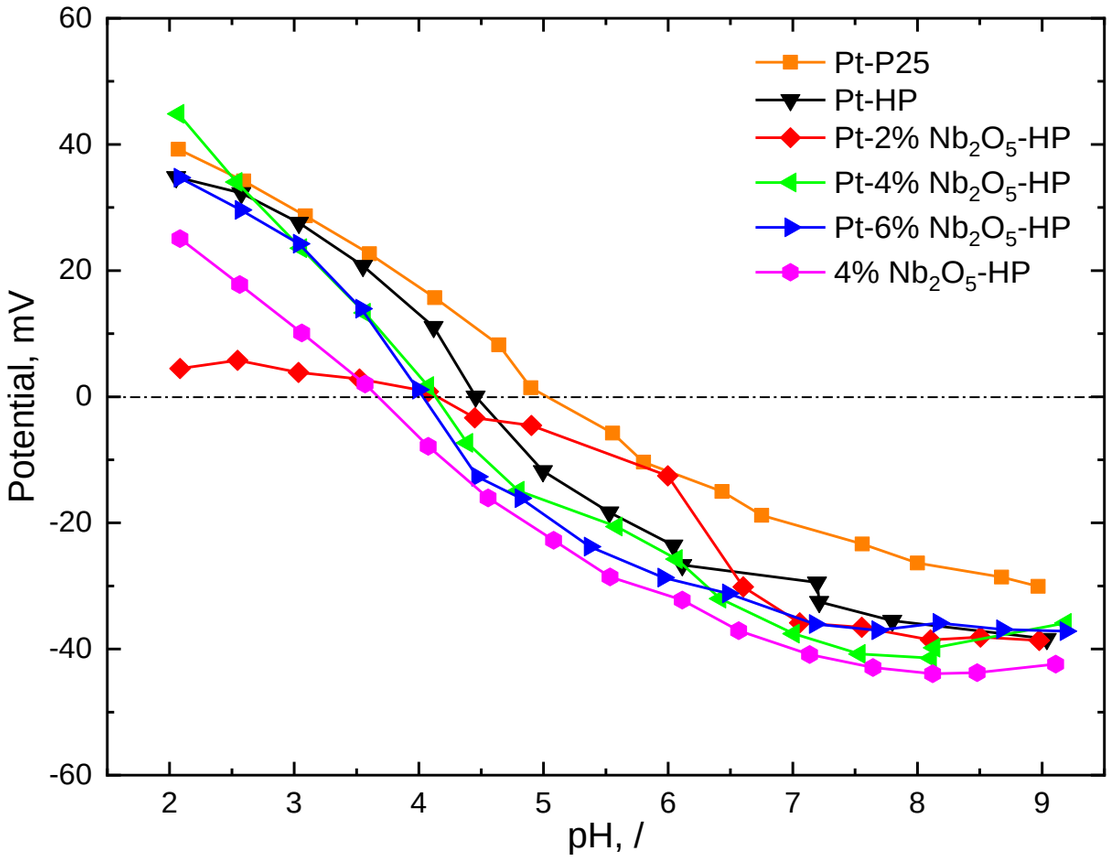

Figure 4-I.4 Results of the pH related zeta potential measurements

4-I.3.7 Photoluminescence spectroscopy (PL)

Figure 4-I.5 shows the solid-state photoluminescence spectra of the Nb_2O_5 based photocatalysts. The intensity of the spectra results from both the recombination of electron-hole pairs (the lower the intensity, the lower the recombination) and the presence of lattice defects or oxygen vacancies (higher the intensity, greater their number) [289, 290]. The shape of the spectra is the same for all samples, indicating that the addition of foreign species to TiO_2 does not induce new emission phenomena. When only Nb_2O_5 is present, a slight increase in PL intensity is observed, which is due to the presence of oxygen vacancies. When both Pt and niobia are present, a progressive decrease in photoluminescence is observed as the percentage of Nb_2O_5 is increased. This may be due to both a decrease in the recombination rate and the formation of oxygen vacancies. For all samples, the main emission band is around 423 nm and can be attributed to the indirect band-to-band transition of electrons in TiO_2 in agreement with the band gap values. Signals at higher wavelengths can be attributed to the non-radiative recombination of excited electrons in lattice defects [291].

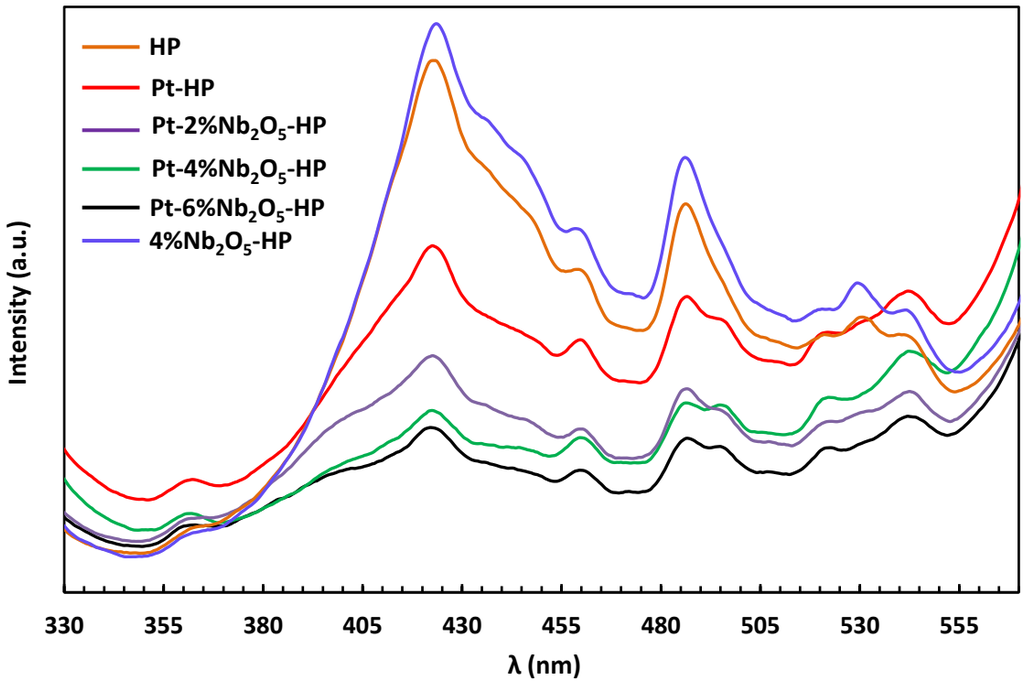

Figure 4-I.5 Solid-state photoluminescence spectra of the different samples

4-I.3.8 Temperature programmed desorption (TPD) spectroscopy

The investigation of the basic surface properties of the different catalysts was carried out after CO_2 adsorption on the TiO_2 surface using the TPD technique. Figure 4-I.6 shows the CO_2-TPD profiles of the photocatalysts used and Table 4-I.2 reports the amounts of basic sites.

Table 4-I.2. Amount and density of basic sites in the tested materials calculated by CO_2 TPD analyses

Sample	Mass of used catalyst (g)	Area (A s)	Amount of basic sites (µmol/g)	Density of basic sites (µmol/m^2)
HP	0.0499	7.38×10^{-12}	12.8	0.164
Pt-HP	0.0520	5.74×10^{-11}	53.6	0.687
4%Nb_2O_5-HP	0.0461	2.15×10^{-11}	21.0	0.269
Pt-2%Nb_2O_5-HP	0.0565	8.37×10^{-11}	46.7	0.622
Pt-4%Nb_2O_5-HP	0.0508	1.0×10^{-10}	83.7	0.909
Pt-6%Nb_2O_5-HP	0.0479	1.85×10^{-10}	121	1.210

The peak between 50-150°C could be attributed to the desorption of molecular CO_2, while the peak at temperatures around 300-350 °C is due to HCO_3^- or carboxylate originating from the interaction of CO_2 with the hydroxyl groups of the TiO_2 surface. The presence of peaks at temperatures above 400 °C indicates a stronger adsorption of CO_2 onto the solid; the samples containing contemporary Pt and Nb_2O_5 have stronger basic sites. The results presented in Table 4-I.2 show that the bare TiO_2 has the lowest number of basic sites, and that the presence of the noble metal or the niobium oxide significantly increases this number. A more pronounced effect is observed when both foreign species (Pt and Nb_2O_5) are present, and the higher the percentage of Nb_2O_5, the greater the number of basic sites, while the amount of Pt remains constant. This synergistic result is surprising, since it is commonly reported in the literature that the presence of

Pt on TiO_2 only enhances the separation of photogenerated charges, while the coupling of Nb_2O_5 with TiO_2 causes an increase in the acidity of the host.

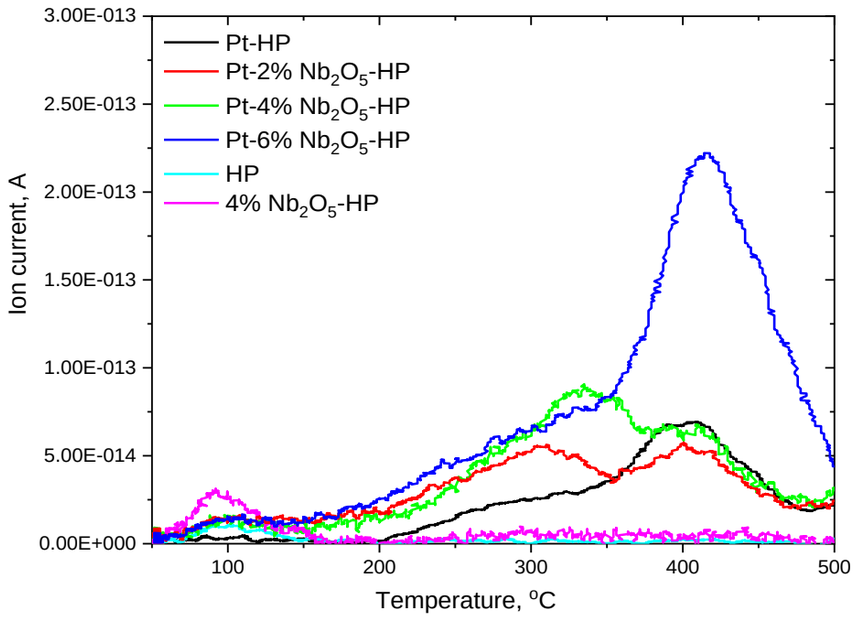

Figure 4-I.6 CO_2 TPD curves of tested materials

4-I.3.9 Diffuse reflectance infrared Fourier transform spectroscopy (DRIFTS)

In situ diffuse reflectance infrared Fourier transform spectroscopy (DRIFTS) in the presence of adsorbed pyridine was used to determine the nature and the density of acid sites on the surface as a function of the amount of Nb_2O_5. Figure 4-I.7 shows the spectra of the different TiO_2 HP samples. The bands at 1445 cm^{-1}, 1486 cm^{-1}, 1574 cm^{-1} and 1604 cm^{-1} are characteristic of the pyridine ring coordinated to the Lewis acid sites on the surface, while the bands at 1545 cm^{-1} and 1635 cm^{-1} correspond to the pyridinium ions adsorbed on the Brønsted acid sites. All the samples show a clear predominance of Lewis acid sites, and although these spectra provide essentially qualitative information, it can be said with good approximation that the intensity is related to the concentration of the acid sites. Bare TiO_2 HP shows intense and sharp peaks, the reduction of which can be detected after Pt photo-deposition (see Pt-HP sample), in agreement with the CO_2 TPD results. This confirms that the presence of Pt not only affects the separation of electrons and holes, but also the acidity of the surface. The sole presence of Nb_2O_5 increases the acidity of the TiO_2 surface, with the sample 4%Nb_2O_5-HP showing the most intense peaks, but no new peaks are present. In the simultaneous presence of Pt and niobium oxide, the intensity of the peaks is slightly higher at higher Nb_2O_5 contents than at pure TiO_2, while a slight change (appearance of a broad band) is observed in the spectrum around 1525 cm^{-1}. This effect is more pronounced for samples with a higher Nb_2O_5 content.

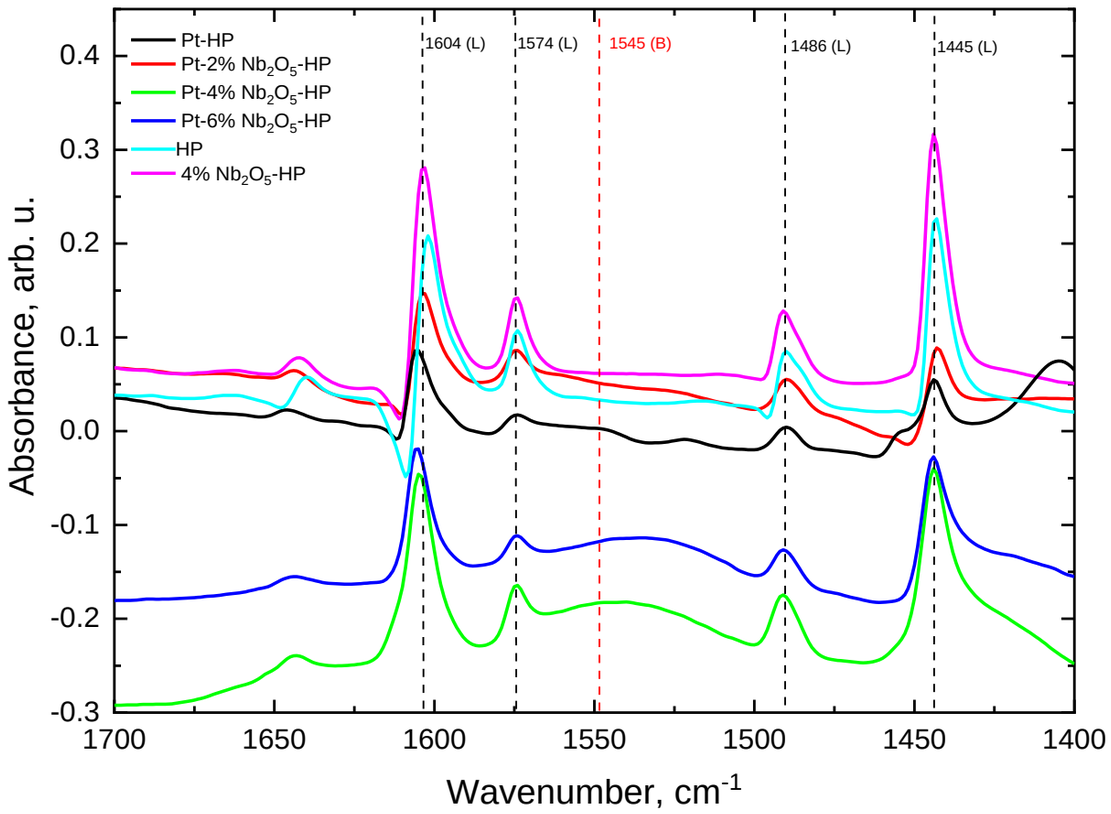

Figure 4-I.7 DRIFTS spectra of pyridine adsorbed on the surface of investigated materials

The amount and density of acidic sites were determined by pyridine TPD measurements. Figure 4-I.8 shows the TPD pyridine curves of the tested materials, and Table 4-I.3 gives the amount and density of acid sites on the catalytic surface along with the temperature of pyridine desorption.

Table 4-I.3 Amount and density of acid sites and the corresponding temperature of pyridine desorption from the surface of different samples

Sample	Amount of acid sites (mmol/g)	Density of acid sites (mmol/m^2)	Pyridine desorption temperature (°C)
HP	0.1605	0.0021	310
Pt-HP	0.1137	0.0015	375
4%Nb_2O_5-HP	0.2274	0.0029	331
Pt-2%Nb_2O_5-HP	0.1545	0.0021	341
Pt-4%Nb_2O_5-HP	0.1863	0.0020	341
Pt-6%Nb_2O_5-HP	0.2219	0.0022	331, 406

The addition of Pt decreases the density of acid sites, while Nb_2O_5 generally has an opposite effect. In the simultaneous presence of the two components, no significant changes in the total amount of acid sites are observed compared to bare TiO_2 due to their opposite behaviour. In any case, the addition of foreign species leads to an increase in the pyridine desorption temperature, indicating an increase in the strength of the acid sites.

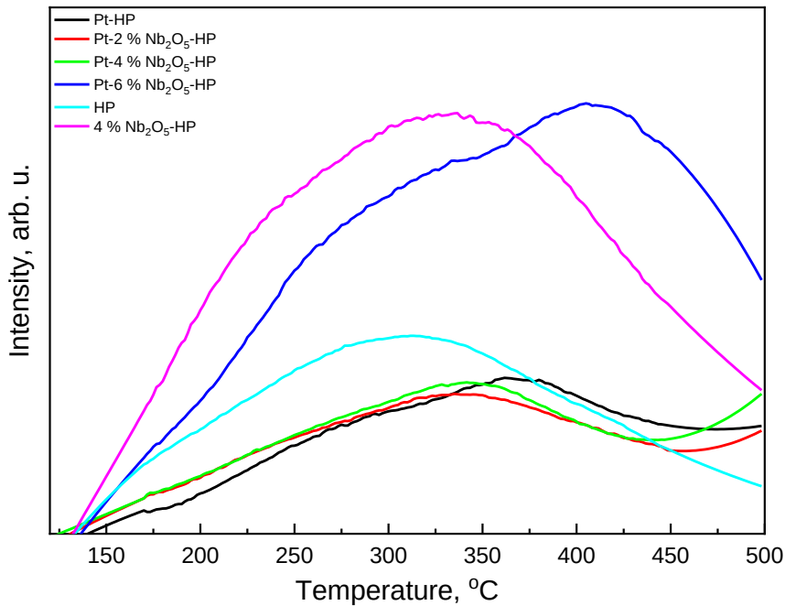

Figure 4-I.8 Pyridine TPD curves for the investigated photocatalysts

4-I.3.10 Transmission electron microscopy (TEM)

Figure 4-I.9 shows TEM images of samples Pt-HP and Pt-6%Nb_2O_5-HP. Pt nanoparticles (represented by small dark spheres) are concentrated in some areas of the TiO_2 surface. The size of Pt nanoparticles ranges from 5 to 25 nm; when the image is enlarged, two lattice fringes of about 0.35 nm and 0.32 nm can be seen, which are characteristic of the (1 0 1) anatase and (1 1 0) rutile planes, respectively [221].

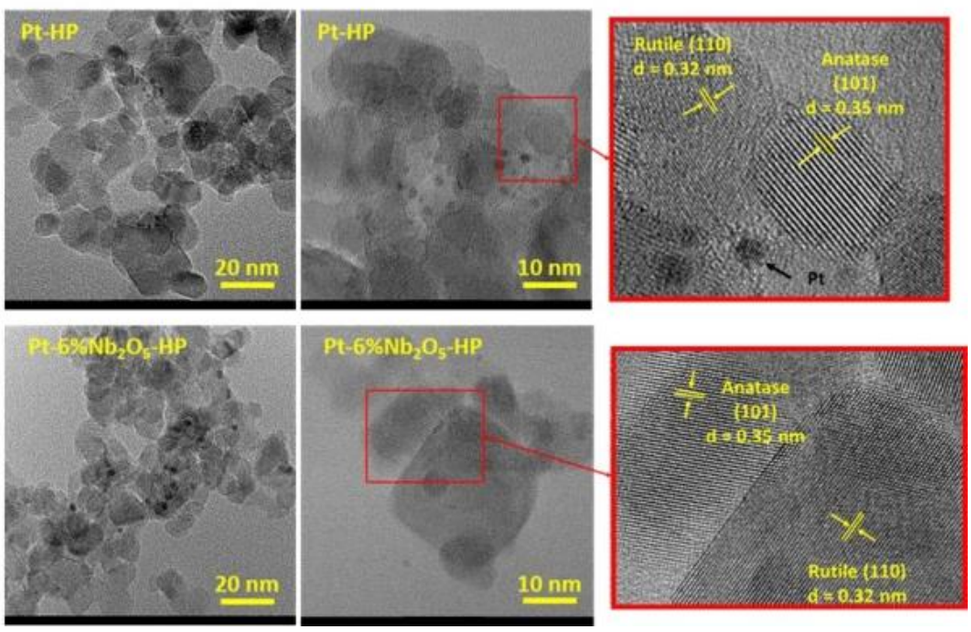

Figure 4-I.9 TEM images of samples Pt-HP and Pt-6%Nb_2O_5-HP

4-I.3.11 X-ray photoelectron spectroscopy (XPS)

In the XPS survey spectrum (not given for brevity), peaks for Ti, O, and Cl (as residues of HCl, $PtCl_4$, and $NbCl_5$ precursors) were detected in all samples. Peaks for Pt and Nb were rarely detected because of their low atomic concentration. When both are present, Cl and Nb are not clearly distinguishable because their peaks almost overlap.

Figure 4-I.10A shows the high-resolution XPS spectra of the Ti 2p peaks in Pt-HP and Pt-6%Nb_2O_5-HP samples. The two peaks of Ti $2p_{3/2}$ at 459.5 eV and Ti $2p_{1/2}$ at 465.3 eV with a binding energy gap of 5.8 eV are characteristic of Ti^{4+} in TiO_2 [292] The high-resolution O 1s spectra are shown in Figure 4-I.10B. For both samples, the main peak is the one at about 530.7 eV, which is assigned to the O^{2-} ions of the TiO_2 crystal lattice. In the presence of Nb_2O_5, the peaks are at ca. 532 eV and at ca. 533.0 eV, which are related (in agreement with Raman spectra) to oxygen vacancies in TiO_2 [292] and -OH groups [293], respectively. In Figure 4-I.10C, the main Pt peak at about 76 eV corresponds to Pt^0, and the less intense peaks at lower binding energy visible in the sample Pt-6%Nb_2O_5-HP are characteristic of partially oxidized Pt species [294]. Moreover, the peaks for Pt in the Pt-6%Nb_2O_5-HP sample are much more intense, indicating a higher atomic concentration of Pt in this sample. As can be seen in Figure 4-I.10D, no peaks were detected for Nb (the two peaks characteristic of Nb_2O_5 are at 209.9 eV and 207.1 eV [74, 294], which is probably due to the low atomic concentration. The small broad peak at lower binding energy is that of Cl 2p, the chlorine present in the precursor of Nb_2O_5.

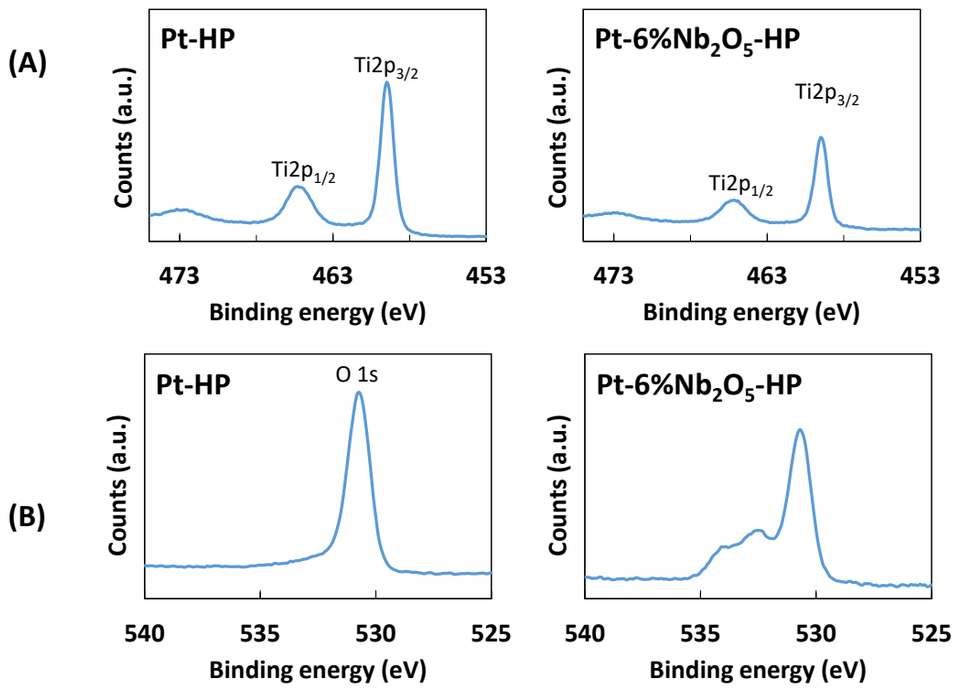

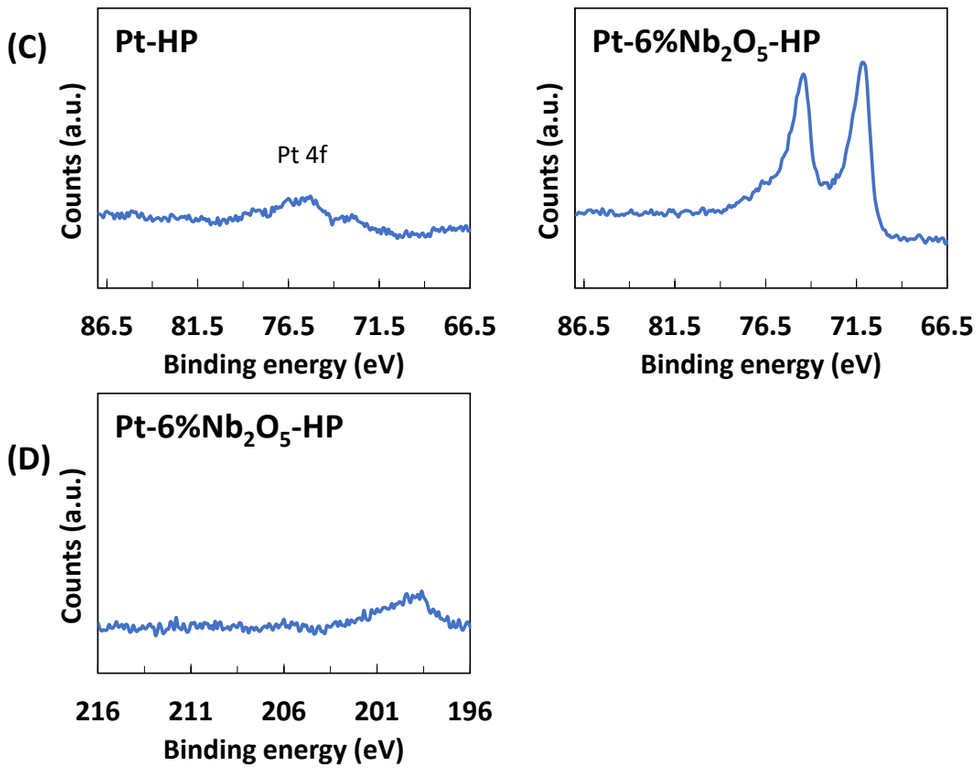

Figure 4-I.10. High resolution XPS spectra of (A) Ti 2p, (B) O 1s, (C) Pt 4f, and (D) Nb 3d peaks

4-I.3.12 Electron paramagnetic resonance (EPR) spectroscopy

The EPR spectra of the Pt-HP and Pt-6%Nb_2O_5-HP (Figure 4-I.11A) show no EPR signal, indicating that the photocatalysts cannot generate free electrons and oxygen vacancies under illumination. In the presence of DMPO/MeOH (Figure 4-I.11B), no EPR signal can be detected in the experiments performed in the dark, indicating that the photocatalysts cannot generate radicals in the absence of illumination. When the photocatalysts are irradiated, the EPR spectra show the characteristic paramagnetic resonance absorption of the DMPO-$^{\bullet}O_2^-$ adduct [295]. This result indicates that both photocatalysts can thermodynamically generate superoxide anion radicals ($^{\bullet}O_2^-$) under illumination. The EPR spectrum of the Pt-6%Nb_2O_5-HP sample shows higher intensity peaks, indicating stronger formation of the oxygen radicals, which is probably due to the more effective charge separation in the presence of Nb_2O_5. For Pt-HP samples suspended in water in the dark and in the presence of DMPO and H_2O_2 (Figure 4-I.11C), no EPR signals are detected, while the signals just mentioned are visible in the presence of Nb_2O_5. Upon irradiation, the EPR spectra lead to the characteristic paramagnetic resonance absorption of the DMPO-$^{\bullet}OH$ adduct only for the sample Pt-6%Nb_2O_5-HP. Therefore, only this sample can thermodynamically generate hydroxyl radicals ($^{\bullet}OH$) under illumination.

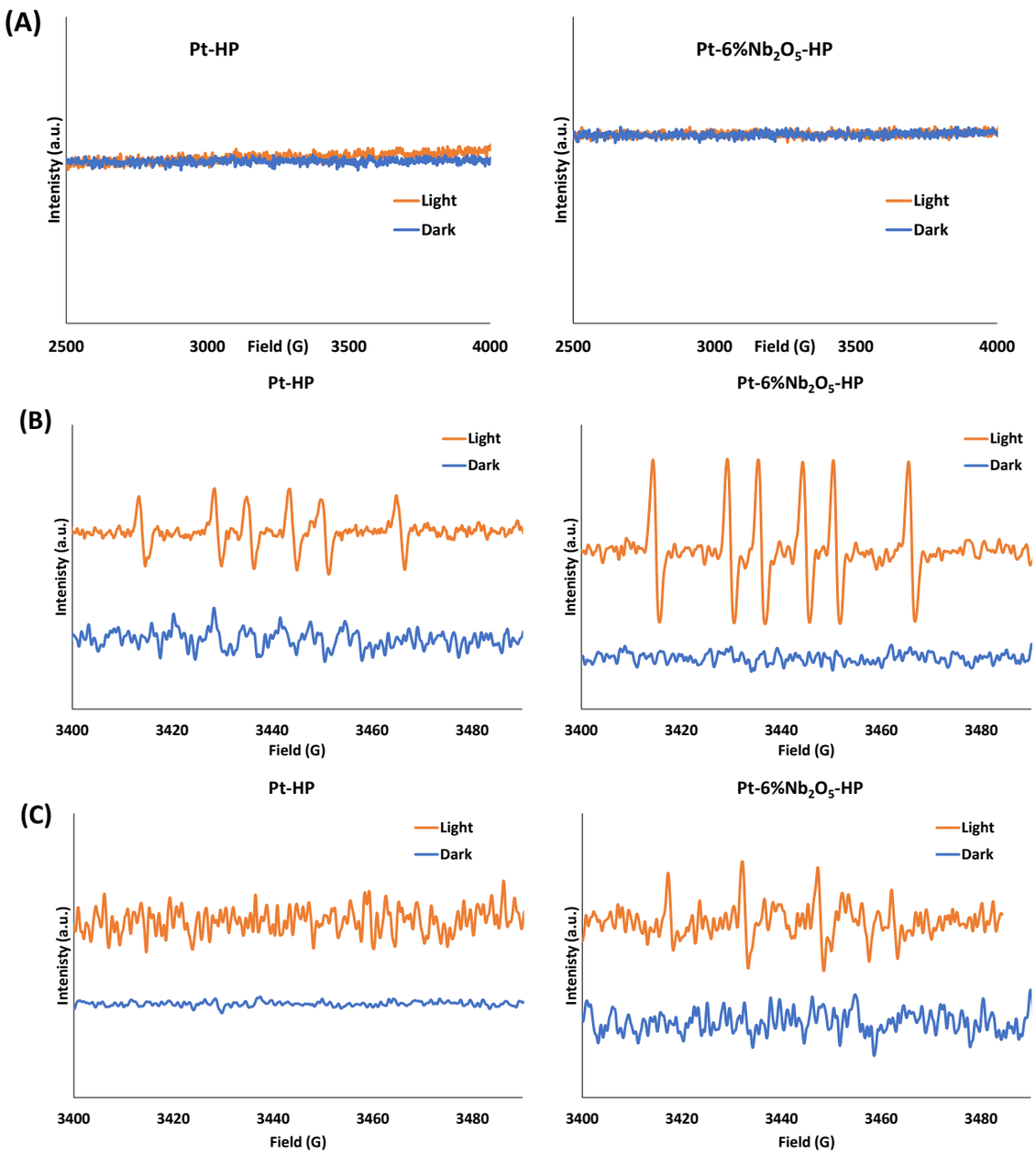

Figure 4-I.11 EPR spectra of (A) powder samples Pt-HP and Pt-6%Nb_2O_5-HP under dark and light irradiation, (B) samples suspended in H_2O/DMPO/MeOH solution, and (C) samples suspended in H_2O/DMPO/H_2O_2 solution

4-I.4 Photocatalytic activity

All TiO_2-based photocatalysts were used for the photo-reforming of aqueous glucose and fructose solutions under irradiation with near-UV light under anaerobic conditions. The obtained results were compared to relate the reactivity to some catalyst features. The presence of Pt nanoparticles on the catalyst surface increased the photoactivity thanks to their role in reducing the recombination rate of photogenerated e^-/h^+ pairs (in agreement with the results of solid-state PL analysis) and was essential for H_2 production, since in its absence only compounds from partial oxidation of the starting substrates and CO_2 from mineralization were observed (Tables 4-I.4 and 4-I.5). The different samples showed different conversions for both substrates, and the main partial oxidation products in the liquid phase were gluconic acid, arabinose, formic acid, erythrose, and fructose. In addition, H_2 and CO_2 were found in the gas phase in the headspace of the photoreactor.

Figure 4-I.12 shows the concentration values of the two substrates and their intermediates as a function of irradiation time for the series of experiments performed with the different Nb_2O_5-modified photocatalysts. All the catalysts produced the same compounds, suggesting very similar

reaction mechanisms [31]; only a different degree of conversion, distribution of intermediates and H_2 production were observed for the different photocatalysts for both substrates. The different activity of the photocatalysts used depended on the electronic and physico-chemical properties of the different TiO_2-based solids, such as the recombination rate of the photogenerated charges, the acidity and/or basicity of the surface, the number of active sites per surface unit (a parameter also related to the specific surface area) and so on. When the substrate was glucose, fructose was formed by isomerization, and both could form gluconic acid by oxidation of the anomeric C1 centre, converting the aldehyde group to the carboxyl group. A parallel mechanism consisted of α-cleavage, in which arabinose was formed in the first step and erythrose together with formic acid and hydrogen in the second step [31, 296].

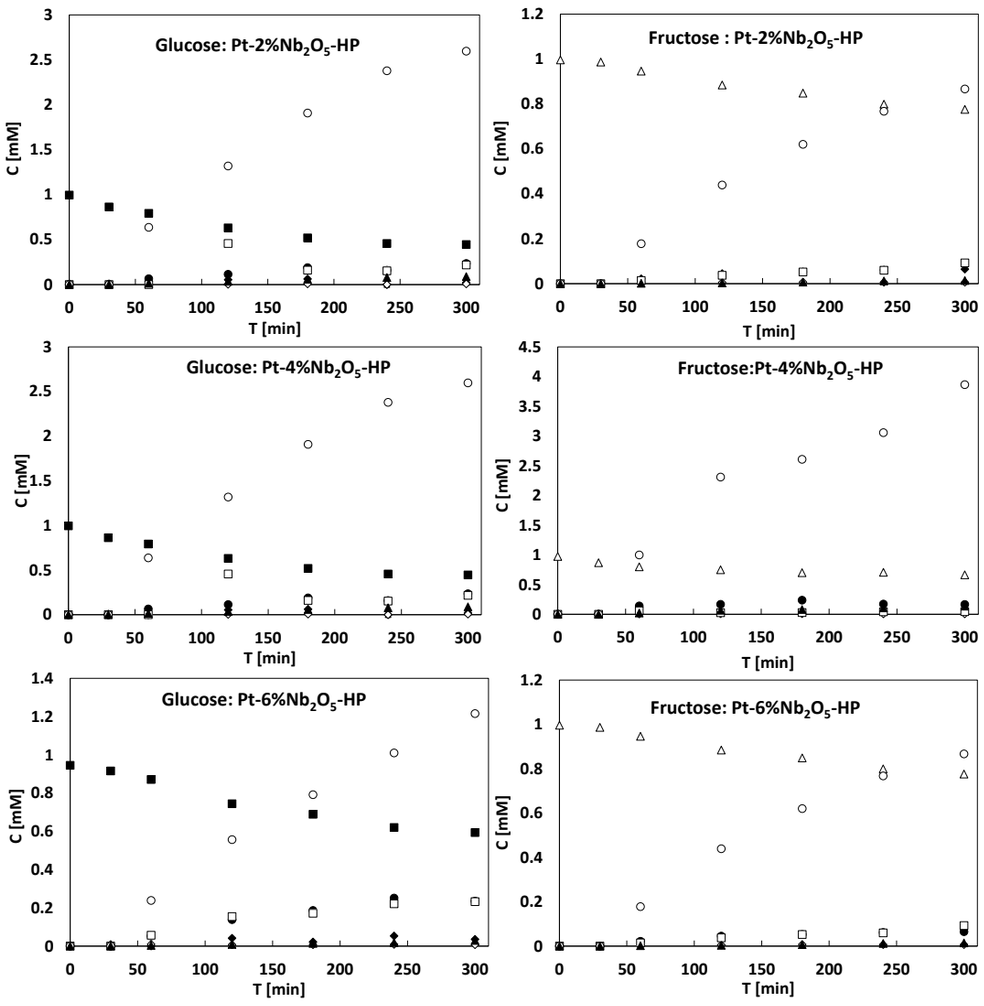

Figure 4-I.12 Concentrations of the two substrates and their products versus irradiation time for runs carried out by using Nb_2O_5 modified photocatalysts. Legend: ■ glucose, Δ fructose, ● arabinose, ◇ gluconic acid, □ formic acid, ○ hydrogen, ▲ CO_2

Tables 4-I.4 and 4-I.5 show the conversion, selectivity, and amounts of H_2 and CO_2 for the runs starting from glucose and fructose, respectively, using the different photocatalysts. Notably, in some cases, the sum of the selectivity of the different intermediates exceeds 100% because some compounds are progressive transformed in the other ones (formic acid is formed both from the cleavage of glucose and arabinose). In particular, it has been shown that a Pt-P25 sample used for comparison purposes generally performs less well than some HP-modified samples (with Pt and Nb_2O_5). The Pt-HP catalyst showed good conversion and selectivity towards arabinose with both glucose and fructose as starting substrates. As far as glucose is concerned, the highest conversion was obtained with the sample Pt-2%Nb_2O_5-HP, while a lower degree of conversion was observed in the exclusive presence of Nb_2O_5, suggesting that the surface acidity (the sample 4%Nb_2O_5-HP

showed the most intense DRIFT peaks in the presence of adsorbed pyridine) had an adverse effect. In this case, the increased amount of superoxide and hydroxyl radicals in the Nb_2O_5-containing samples (see EPR results) had no positive effect on the oxidation capacity of TiO_2. Fructose was formed practically only with the Pt-HP sample, since the increase in surface basicity (Table 4-I.2) due to the simultaneous presence of Pt and Nb_2O_5 was detrimental to the isomerization of glucose to fructose, in agreement with the literature [297]. The selectivity towards arabinose was favoured by Nb_2O_5, and in agreement with the α-cleavage mechanism, practically almost the same amount of arabinose and formic acid were obtained [31, 296]. As far as fructose is concerned, low amounts of Nb_2O_5 had no significant effect on the conversion, while the highest amounts had a negative effect. Moreover, the lowest amounts of Nb_2O_5 favoured the formation of arabinose.

The best photocatalyst for H_2 production under the operating and reaction conditions used was Pt-4%Nb_2O_5-HP in the presence of both substrates. The trend in terms of Nb_2O_5 content increased up to 4%, then H_2 production decreased.

Table 4-I.4 Glucose conversion, selectivity towards the main products, and H_2 and CO_2 amounts obtained after 5 h of irradiation

Sample	Conversion (%)	Selectivity (%)					H_2 (mM)	CO_2 (mM)
		Fructose	Gluconic acid	Arabinose	Formic acid	Erythrose		
Pt-HP	40	27	2.6	45	44	-	1.9	0.14
Pt-2%Nb_2O_5-HP	56	4	1.2	42	39	3.5	2.6	0.09
Pt-4%Nb_2O_5-HP	43	-	1.0	54	39	5.0	3.4	0.10
Pt-6%Nb_2O_5-HP	41	-	1.8	58	57	9.0	1.2	0.03
4%Nb_2O_5-HP	22	-	3.4	53	44	-	-	0.01
Pt-P25	32	31	4.6	41	31		1.9	0.07

Table 4-I.5 Fructose conversion, selectivity towards the main products, and H_2 and CO_2 amounts obtained after 5 h of irradiation

Sample	Conversion (%)	Selectivity (%)				H_2 (mM)	CO_2 (mM)
		Gluconic acid	Arabinose	Formic acid	Erythrose		
Pt-HP	40	4.5	-	6	7.5	3.2	0.12
Pt-2%Nb_2O_5-HP	39	2.2	75	15	9	1.9	0.07
Pt-4%Nb_2O_5-HP	40	2.0	42	11	9	3.8	0.14
Pt-6%Nb_2O_5-HP	22	3.0	-	41	29	0.9	0.01
4%Nb_2O_5-HP	13	4.2	-	24	-	-	0.01
Pt-P25	25	9		12		3.13	0.10

4-I.5 Conclusions

0.5 wt% Pt loaded home-prepared bare and Nb_2O_5-TiO_2 photocatalysts with different Nb_2O_5 content were prepared to evaluate their activity in the reforming of glucose and fructose. The photocatalytic results confirm that the photoactivity does not depend on a single parameter but is a compromise between several factors. The sample Pt-2%Nb_2O_5-HP proved to be the most oxidizing catalyst, but the solid Pt-4%Nb_2O_5-HP was the most efficient in terms of partial oxidation products and H_2 formation. Neither sample exhibited a property that could affect either type of photoactivity relative to the other, but had intermediate values for PZC, number of basic sites, oxygen vacancies, and photoluminescence effects (see PL spectra).

The samples were characterized by using different techniques to investigate the effects of Pt and Nb_2O_5 on the properties of the catalyst. Pt not only acted as an electron trap and improved the efficiency of e^-/h^+ separation, as reported in the literature, but surprisingly also changed the acid-base properties of the surface by increasing the number of basic sites. Nb_2O_5 alone increased the acidity of the TiO_2 surface, while stronger basic sites were formed compared to the bare host when Pt was also present. The increase in surface basicity due to the simultaneous presence of Pt and Nb_2O_5 adversely affected the isomerization of glucose to fructose. The formation of $O_2^{\bullet-}$ and $^{\bullet}OH$ radicals in the samples containing Nb_2O_5 did not have a positive effect on the oxidizing power of TiO_2 but favoured partial oxidation reactions and the formation of H_2. The home-prepared samples outperformed the well-known commercial TiO_2 P25.

CHAPTER 4-II

Investigating the activity of modified TiO_2 photocatalysts used for the photoreforming of biomass derivatives

In this chapter, text is adapted from the following publication.

Muhammad Umair, Vittorio Loddo, Leonardo Palmisano, Albin Pintar, Gregor Žerjav, Giovanni Palmisano, Samar Al Jitan, Marianna Bellardita. Investigating the activity of modified TiO_2 photocatalysts used for the photoreforming of biomass derivatives. *Journal of Photochemistry and Photobiology A: Chemistry* 2024, 453, 115654. https://doi.org/10.1016/j.jphotochem.2024.115654

CHAPTER 4-II

Investigating the activity of modified TiO_2 photocatalysts used for the photoreforming of biomass derivatives

4-II.1 Abstract

Different commercial and homemade TiO_2-based photocatalysts modified with metal species (Pt, Cu_2O, Nb) have been compared for the photo-reforming of glucose and fructose with the aim of linking the photoactivity to some structural and surface characteristics. The photocatalysts were characterized by different surface, structural and textural techniques. Each photocatalyst was tested under anaerobic conditions in aqueous medium, at room temperature and pressure, under near-UV light irradiation. The formation of different valuable compounds in liquid phase, as gluconic acid, formic acid, fructose, arabinose and erythrose was observed, whilst CO_2 and H_2 were found in the gas phase. A different degree of conversion, distribution of intermediates and H_2 production were detected with the different photocatalysts. Moreover, the results obtained with the same catalysts were slightly different with the two substrates, highlighting the importance of the interaction between the catalyst surface and the organic compound. Bare TiO_2 was inactive towards H_2 production, Cu_2O was effective in replacing Pt for hydrogen generation, and the presence of Pt/Nb was beneficial for both H_2 production and selective oxidation. Moreover, Pt also modifies the surface acid-base properties of catalysts as revealed by DRIFT and TDP measurements in the presence of probe molecules.

4-II.2 Photocatalysts preparation

4-II.2.1 Brookite

Brookite was prepared through hydrothermal hydrolysis. 210 mL of distilled water, 80 mL of HCl (concentrated) and 5 mL of $TiCl_4$ were added in a 500 mL beaker under stirring. After ca. 2 h the mixture was shifted into a Pyrex bottle and heated at 373 K in an oven for 48 h. The resulting powder was a mixture of brookite and rutile. Pure brookite nanoparticles (identified as Brookite) were recovered in the supernatant by peptizing with water at different times, and rutile phase was present as a precipitate.

Niobium (Nb) loading has been carried out by adding $NbCl_5$ to the solution obtained by dissolution of $TiCl_4$. Nb1-brookite was the code used for this sample where 1 indicates the nominal weight percentage of Nb with respect to TiO_2. Nb was chosen both because it enhances the photoactivity of TiO_2 [298, 299] and because it modifies its surface acid properties [300].

4-II.2.2 Home prepared TiO_2 (HP)

The preparation method has already been discussed in section 4-1.2.1.

4-II.2.3 Cu_2O-TiO_2 samples

Some Cu_2O (3 wt%)-TiO_2 coupled samples were prepared by mixing the two oxides by a Retsch Ball Mills, type PM100 ball milling. The powders were mixed for 2 hours at 150 rpm, reversing the sense of the rotation after 1 hour and 10 minutes of pause. The Cu_2O percentage was chosen considering the results obtained in a previous paper [301].

4-II.2.4 Pt-loaded samples

Samples were prepared through a similar method as discussed in section 4-1.2.3.

4-II.3 Results and discussions

4-II.3.1 X-ray diffraction (XRD)

Figure 4-II.1 shows the XRD patterns of all prepared photocatalysts. The three main polymorphs (anatase, rutile and brookite) of TiO_2 are indicated as A, R, B, respectively. The commercial TiO_2 BDH consists of only anatase phase, whereas P25 contains both the anatase and rutile phases. HP contains mainly anatase phase and also traces of rutile, pure brookite was home prepared. The commercial samples (P25 and BDH) show more intense and narrow peaks compared to those of the home prepared ones indicating a better crystallinity, due to their preparation at high temperature on industrial scale. Moreover, no diffraction peaks related to foreign species are present, probably due to the high degree of the dispersion and the low amount of these species with respect to TiO_2.

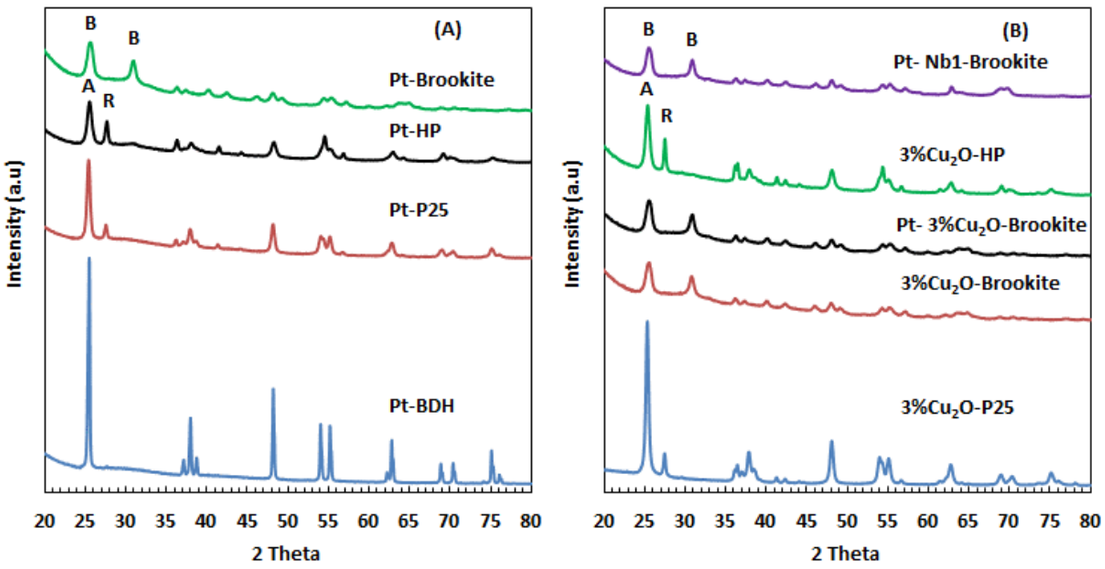

Figure 4-II.1 XRD patterns of: (A) Pt-BDH, Pt-P25, Pt-HP, and Pt-Brookite; (B) 3%Cu_2O-P25, 3%Cu_2O-Brookite, Pt-3% Cu_2O-Brookite, 3%Cu_2O-HP, and Pt-Nb1-Brookite samples. A = Anatase, B = Brookite, R = Rutile

4-II.3.2 Specific surface area (SSA)

The crystalline phase and specific surface area (SSA) of all the samples are listed in Table 4-II.1. Commercial samples exhibit lower SSA as compared to that of home prepared photocatalysts, being 48 $m^2 \cdot g^{-1}$ for 3%Cu_2O-P25 and 69 $m^2 \cdot g^{-1}$ for 3%Cu_2O-HP, respectively. Brookite samples display higher SSA ranging between 90 and 98 $m^2 \cdot g^{-1}$, whilst Pt-BDH shows the lowest SSA of 10 $m^2 \cdot g^{-1}$.

Table 4-II.1 Some physical-chemical properties of the investigated photocatalysts: composition (A = Anatase, R = Rutile, B = Brookite), band-gap, SSA and TPD results (amount and density of acid sites of catalysts and the corresponding temperatures of pyridine desorption)

Catalyst	Phase	Band gap (eV)	SSA (m^2/g)	Quantity of acid sites (mmol/g)	Density of acid sites (mmol/m^2)	Temperature of pyridine desorption (°C)
BDH	A	3.24	10	0.0095	0.0010	289
Pt-BDH	A	3.26	10	0.0091	0.0009	[a]N.D.
P25	A+R	3.18	50	0.1194	0.0024	289
Pt-P25	A+R	3.09	50	0.0944	0.0019	323, 388
3%Cu_2O-P25	A+R	3.08	48	0.1253	0.0026	264, 342
Brookite	B	3.34	98	0.2721	0.0028	406
Pt-Brookite	B	3.32	98	0.4836	0.0049	235, 408
Pt-Nb1-Brookite	B	3.27	90	0.2669	0.0030	402
3%Cu_2O-Brookite	B	3.33	91	0.2237	0.0025	290, 413
Pt-3%Cu_2O-Brookite	B	3.33	94	0.2669	0.0028	290, 403
HP	A+R	2.96	78	0.1605	0.0021	310
Pt-HP	A+R	3.01	78	0.1137	0.0015	375
3%Cu_2O-HP	A+R	3.05	69	0.1537	0.0022	261, 350
Cu_2O	Cu_2O	1.97	1	0.0009	0.0009	428

[a]N.D.: Not determined because no pyridine desorption peak was observed in the measured temperature range (see Figure 4-II.15).

4-II.3.3 Scanning electron microscopy (SEM)

SEM images of all prepared samples are displayed in Figure 4-II.2. All samples are formed by aggregates of irregular roundish particles whose size range is 30-130 nm. Due to the lower synthesis temperature, the particle sizes of homemade samples are smaller than those of commercial samples.

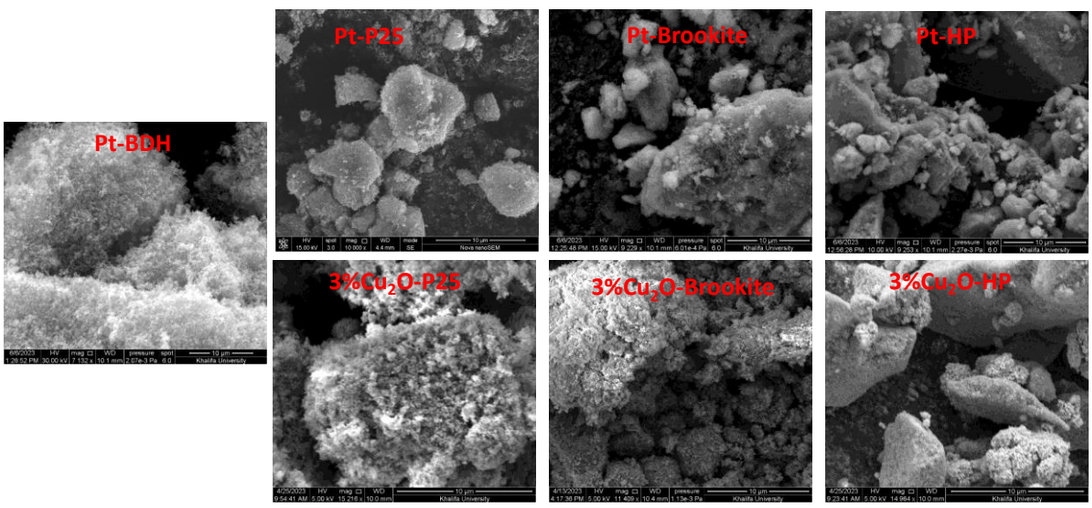

Figure 4-II.2 SEM images of the investigated samples

4-II.3.4 UV-Vis Diffuse reflectance spectroscopy (DRS)

Diffuse reflectance spectra (DRS) of the different TiO_2-based samples are shown in Figure 4-II.3. All the photocatalysts absorb light in the UV–visible range. The BDH and Brookite samples (Figure 4-II.3A) show an absorption band in the high energy region ($\lambda < 360$ nm), whilst all other samples exhibit a slight shift in absorption towards longer wavelengths. Pt presence and copper loading (Figure 4-II.3B) enhance the absorption at $\lambda > 420$ nm and slightly shift the absorption edge towards the visible part of the spectrum.

Band gap values of all samples, measured by plotting the modified Kubelka-Munk function, $[F(R'_\infty)h\nu]^{½}$, against the energy of the stimulating light, are reported in Table 4-II.1. All the powders exhibit band gap values in the range of 2.96-3.33 eV being the lowest value found for HP and highest figures observed for brookite based samples. No relevant variation with respect to pristine TiO_2 samples were observed in the presence of foreign species.

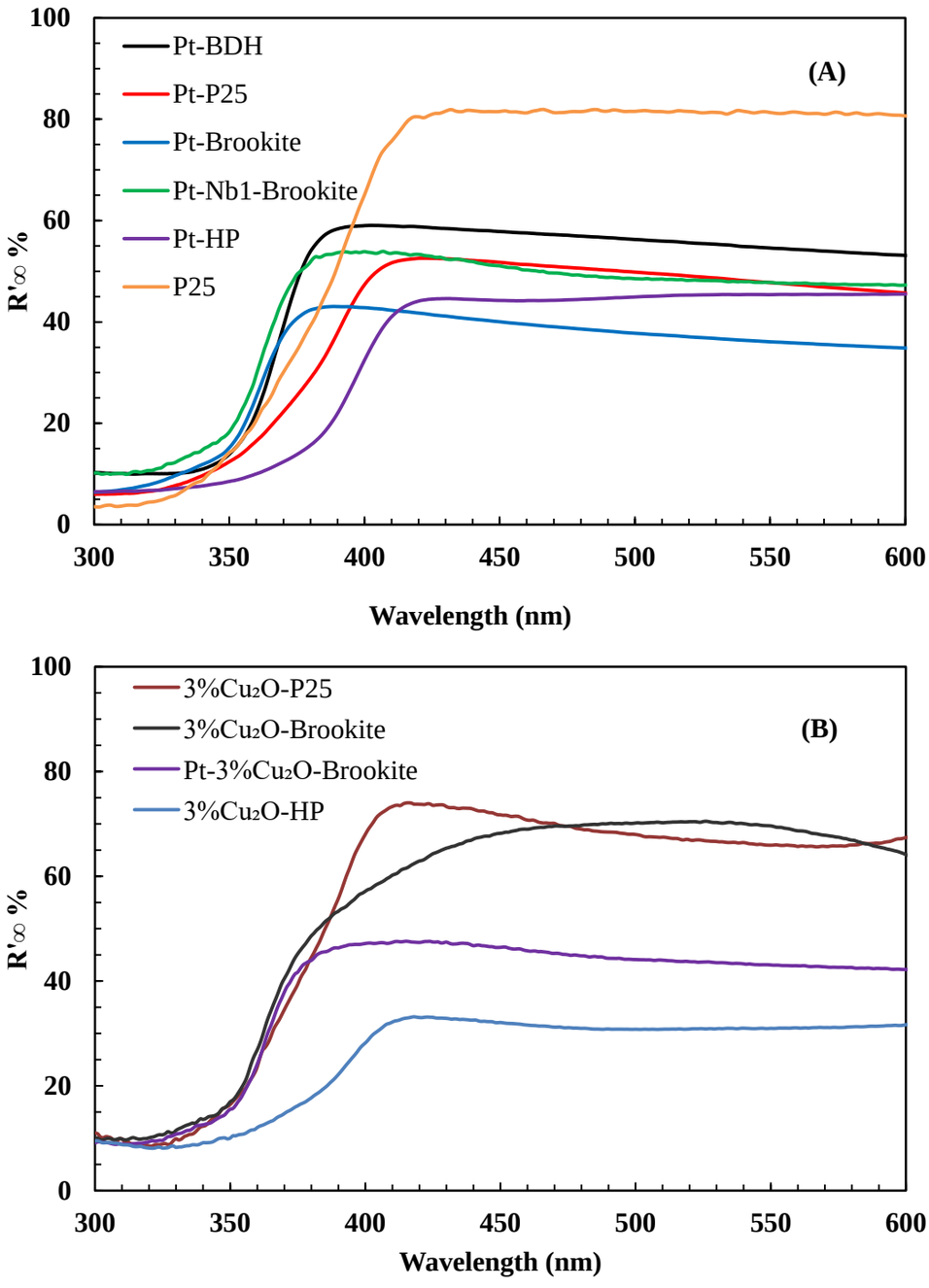

Figure 4-II.3 UV-Vis DRS spectra of the samples: (A) Pt-BDH, Pt-P25, Pt-Brookite, Pt-NB1-Brookite, and Pt-HP; (B) 3%Cu_2O-P25, 3%Cu_2O-Brookite, Pt-3%Cu_2O-Brookite, and 3%Cu_2O-HP

4-II.3.5 Raman spectroscopy

Figure 4-II.4 shows the Raman spectra of TiO_2 based composites. Raman bands at 144 cm^{-1} (E_g), 197 cm^{-1} (E_g), 396 cm^{-1} (B_{1g}), 514 cm^{-1} (A_{1g}), and 637 cm^{-1} (B_{1g}) are characteristic of anatase phase, whilst those at 446 cm^{-1} and 613 cm^{-1} are related to the rutile one. In P25 and HP based samples, being anatase the main component, the presence of rutile can be detected by enlarging the figures while there are no peaks relating to Cu_2O due to probably its small amount and dispersion within the TiO_2 matrix. In Figure 4-II.4B the bands at 126 cm^{-1}, 152 cm^{-1}, 212 cm^{-1}, 247 cm^{-1}, 322 cm^{-1}, 364 cm^{-1}, 409 cm^{-1}, 456 cm^{-1}, 498 cm^{-1}, 543 cm^{-1}, 582 cm^{-1} and 632 cm^{-1} are characteristic of brookite. In brookite-containing samples, the addition of the metal caused a decrease of the band intensity that can be attributed to the greater surface disorder due to the presence of Pt on the TiO_2 surface. There were no identifiable peaks of Pt, and this is consistent with the observation that this metal is not present within the TiO_2 lattice but only on the surface. Also in this case, no Cu_2O peaks were detectable.

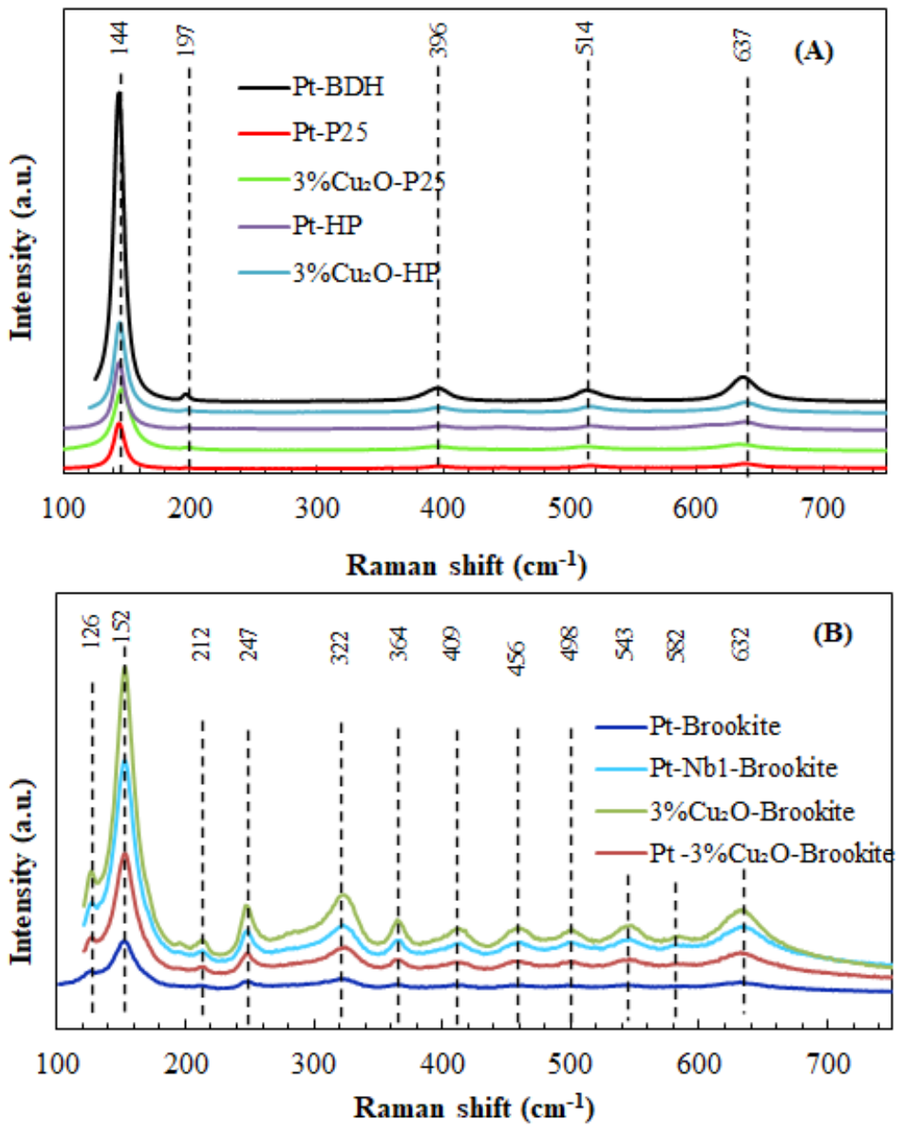

Figure 4-II.4 Raman spectra of samples: (A) Pt-BDH, Pt-P25, 3%Cu_2O-P25, Pt-HP, and 3%Cu_2O-HP; (B) Pt-Brookite, Pt-Nb1-Brookite, 3%Cu_2O-Brookite, and Pt-3% Cu_2O-Brookite

4-II.3.6 Zeta potential measurements

Figure 4-II.5 displays the zeta potential versus pH curves of some Pt-TiO_2 samples. The IEP (isoelectric point, i.e. the pH value at which the net charge on the catalyst surface is zero)

values are 4.23 for Pt-BDH, 4.45 for Pt-HP, 5.00 for Pt-P25 and 5.63 for Pt-Brookite. The above findings imply that at pH 5 (pH at which the photocatalytic runs were carried out) the catalyst's surface is negatively charged for Pt-BDH and Pt-HP, neutral for Pt-P25 and positively charged for Pt-Brookite. Then different coulombic interactions can take place between the species in the reaction mixture and the surface of the various TiO_2 powders [288].

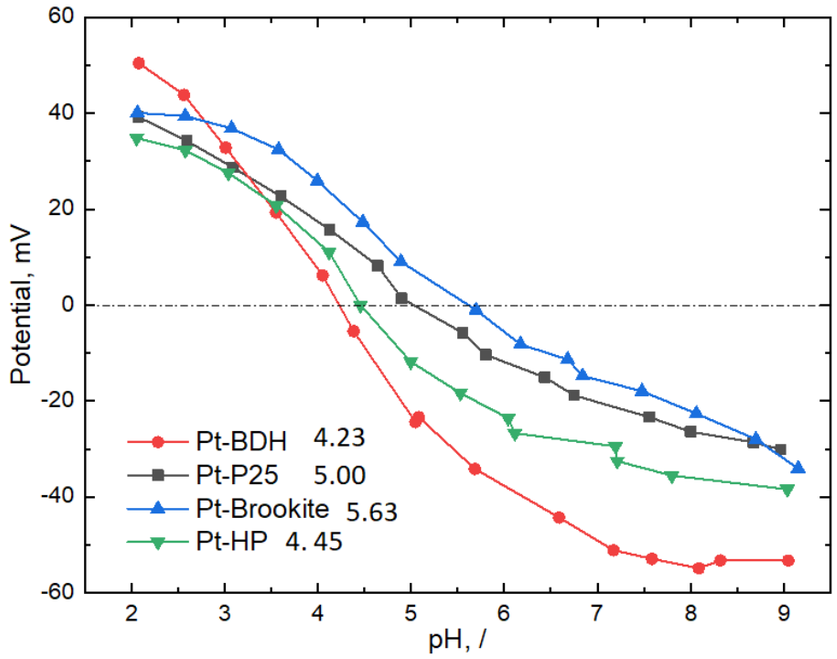

Figure 4-II.5 Results of the pH-related zeta potential measurements

4-II.3.7 Photoluminescence spectroscopy (PL)

The presence of noble metals such as Pt has been reported to be effective for the visible-light activation and the enhancement of the TiO_2 performance [302]. In fact, the Fermi levels of noble metals are lower than that of TiO_2, and this results in the transfer of the photogenerated electrons from the conduction band of TiO_2 to metal particles [303]. This process reduces the electron–hole recombination rate as can be seen from the decrease of the intensity of the photoluminescence bands in the presence of Pt (Figure 4-II.6) [304]. For all the samples, except for BDH which displays a peak at 380 nm, the main emission bands are at ca. 423 nm and this can be attributed to the band-to-band indirect transition of electrons in TiO_2 in accordance with the band gap values. The signals at higher wavelength can be assigned to a non-radiative recombination of the excited electrons towards lattice defects [291, 305]. A significant decrease in the PL intensity can be noticed after the coupling with Cu_2O and the addition of Nb due to the lower recombination rate of the photogenerated charges [301].

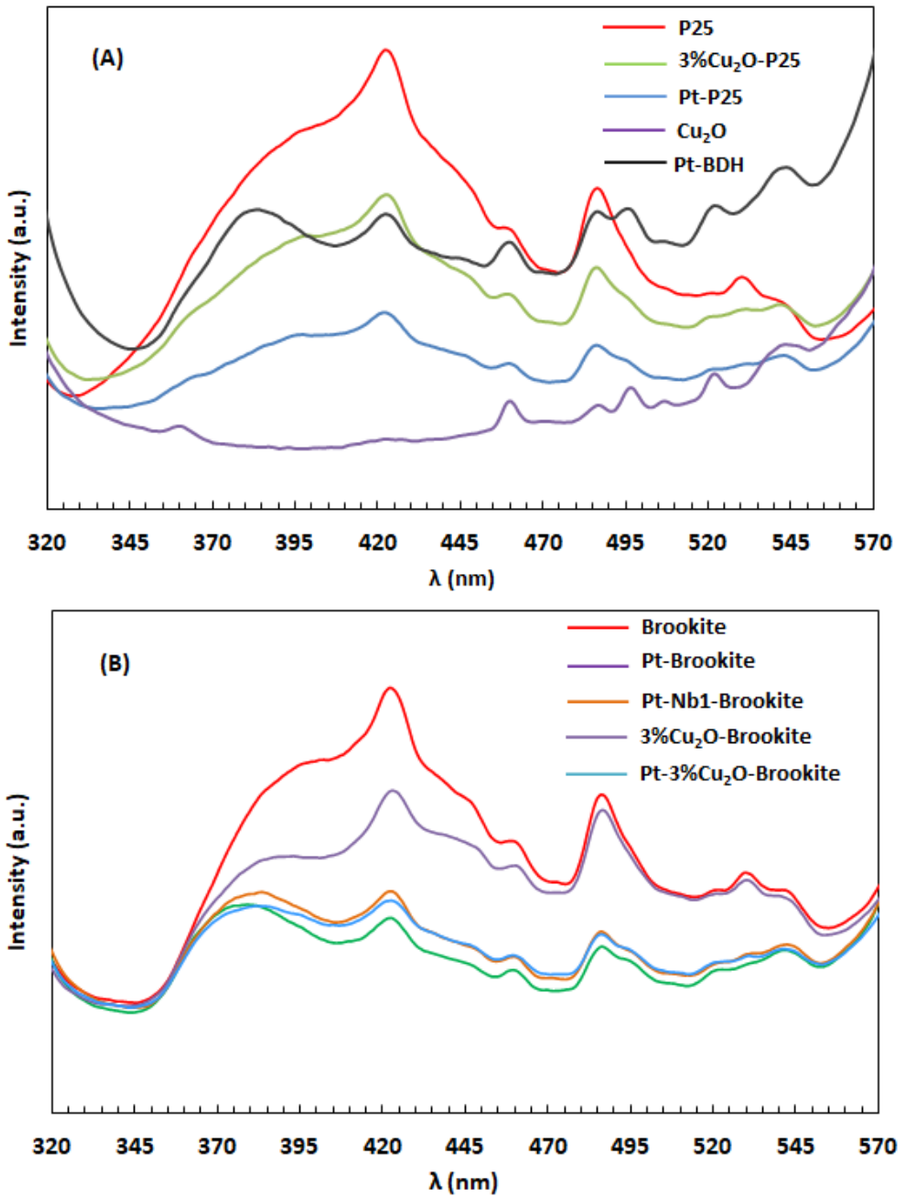

Figure 4-II.6 Photoluminescence spectra of the different samples

4-II.3.8 Transmission electron microscopy (TEM)

TEM images of the different samples were acquired to investigate the morphology, the particles dimension, and the distribution of the different components. Some selected images are reported in Figure 4-II.7, images of other samples are given in Figure 4-II.8. TEM images of the sample Pt-P25 (Figure 4-II.7A) reveal that Pt nanoparticles (represented by small dark spheres) are uniformly dispersed across the P25 surface confirming the effectiveness of the photodeposition method. The size of Pt nanoparticles is approximately 2 to 3 nm while the size of P25 particles (anatase and rutile) ranges between 10 to 20 nm. By zooming in on the image, it is possible to distinguish two lattice fringes of ca. 0.35 nm and 0.32 nm, characteristic of the (1 0 1) anatase and (1 1 0) rutile planes, respectively [221]. SAED (selected-area electron diffraction) patterns consisting of concentric rings indexed as the various planes of rutile and anatase, confirmed the biphasic structure of P25. On the other hand, in the HP sample (Figure 4-II.7B), Pt nanoparticles are clustered into one area on the TiO_2 surface. The size of TiO_2 particles ranges between 5 to 25 nm, which is a slightly larger range compared to the Pt-P25 sample, and the size of Pt nanoparticles is ca. 1 to 2 nm that is slightly smaller than that found in the Pt-P25 sample. Also, in this case an intimate contact between anatase and rutile can be observed.

Brookite consists of rod-shaped particles which size ranges between 10 to 30 nm (Figure 4-II.7C). Pt nanoparticles (dimensions ca. 2-3 nm) are concentrated in some areas whilst Nb

particles are not distinguishable due to their low quantity and high degree of dispersion in the TiO_2 matrix. In the Cu_2O/TiO_2 composite samples a good contact between the two components can be clearly seen in the images reported in Figure 4-II.8. The sizes of Cu_2O particles range between 5 to 10 nm, which are smaller than those of TiO_2 particles.

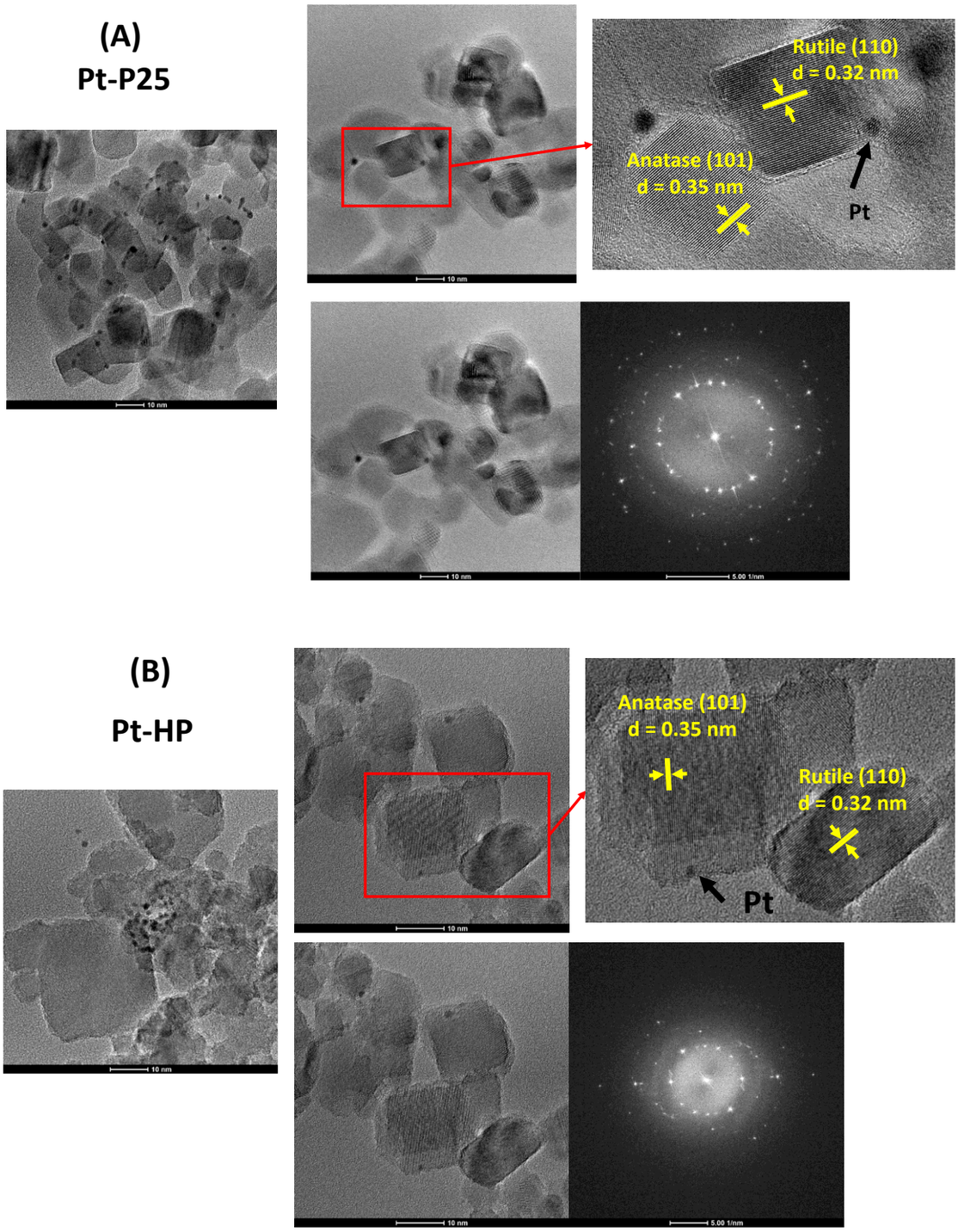

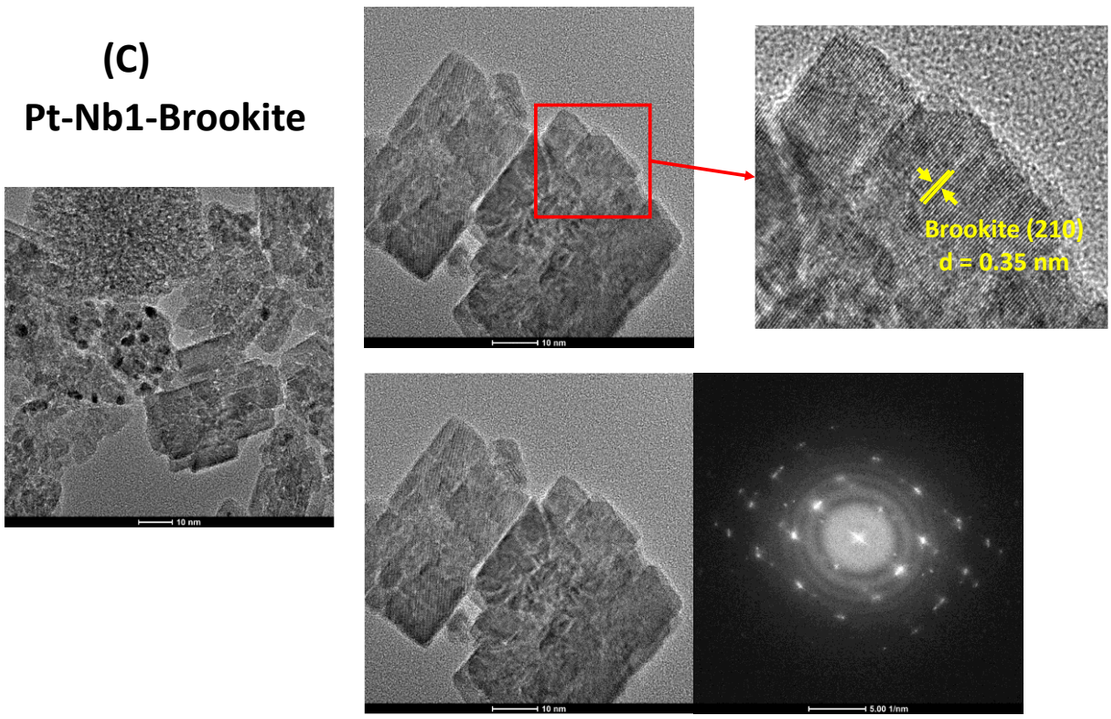

Figure 4-II.7 TEM images of the samples: (A) Pt-P25, (B) Pt-HP, and (C) Pt-NB1-Brookite

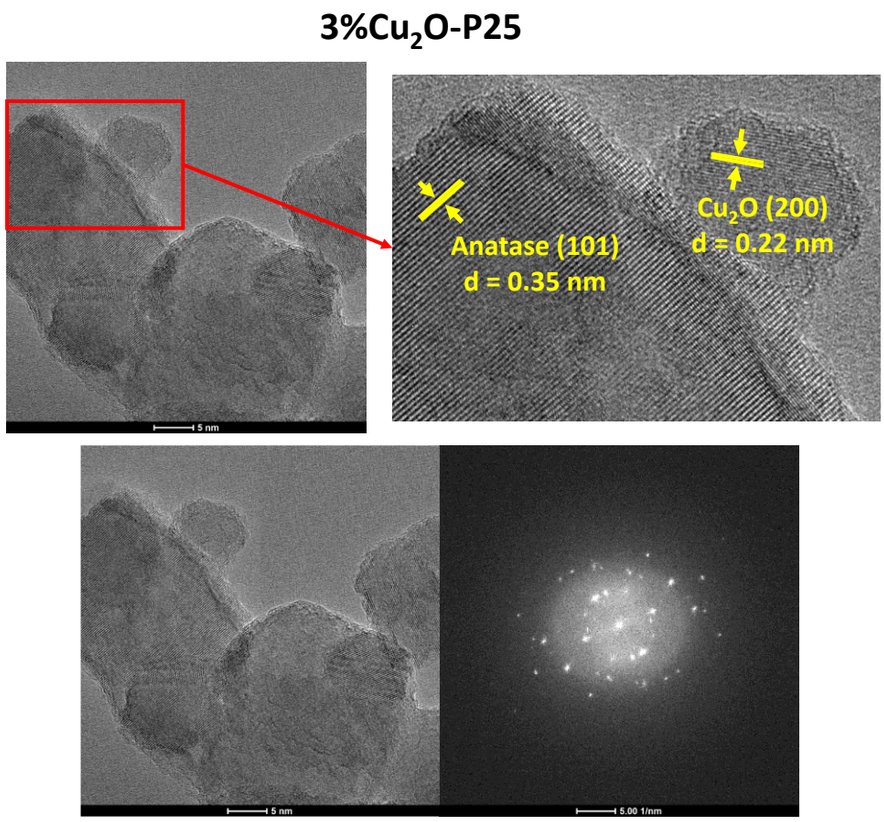

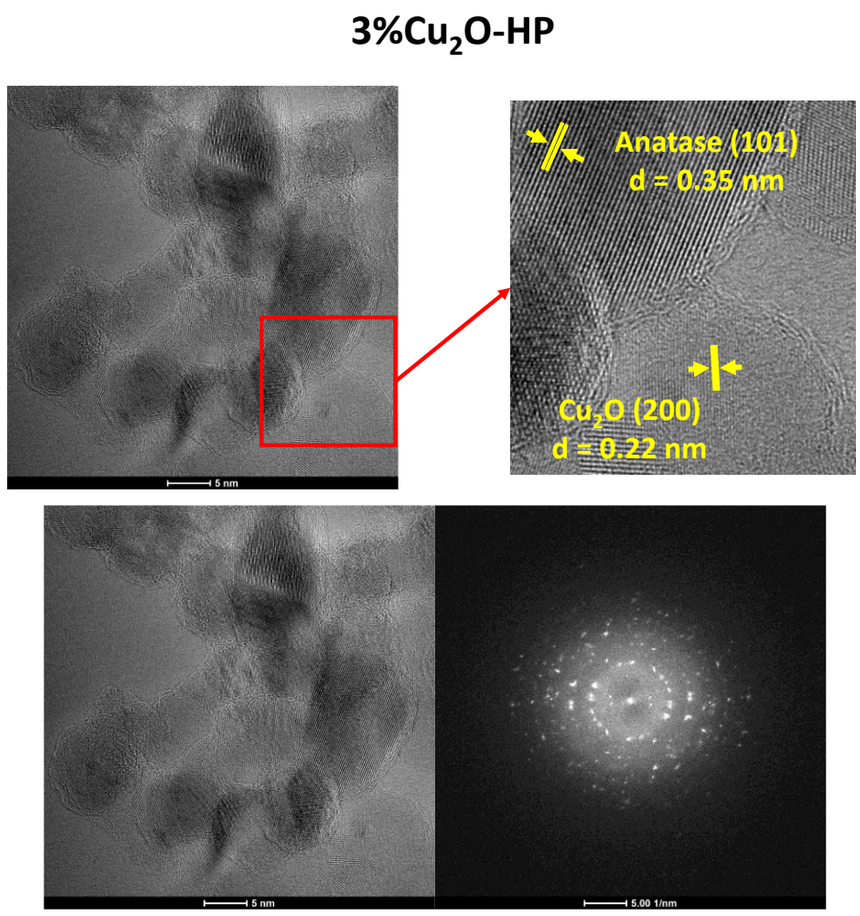

Figure 4-II.8 TEM images of the Cu_2O-TiO_2 samples

4-II.3.9 X-ray photoelectron spectroscopy (XPS)

XPS measurements of some selected samples were carried out to examine the surface composition and the oxidation states of the different species. In Figure 4-II.9 the XPS survey spectrum of the samples with the various species indicated is presented. Peaks for Pt (not shown in XPS survey) were barely detected due to its small atomic concentration. Cl, as residual species deriving from $TiCl_4$, $PtCl_4$ and $NbCl_5$ precursors, was also detected. When both present, Cl and Nb are not clearly distinguishable because their peaks almost overlap. The high resolution XPS spectra of the Ti 2p peaks are reported in Figure 4-II.10A. In Pt-P25 sample the two peaks of Ti $2p_{3/2}$ at 459.5 eV and Ti $2p_{1/2}$ at 465.3 eV with a binding energy distance of 5.8 eV are characteristic of Ti^{4+} in TiO_2 [292]. The Ti $2p_{3/2}$ shoulder peak at 461.4 eV which is visible only for the 3%Cu_2O-P25 sample is characteristic of Ti^{3+}. This indicates that in this sample Ti is present in two oxidation states (+3 and +4) due to an electron transfer from Cu_2O to P25. The high-resolution O 1s spectra are shown in Figure 4-II.10B. For almost all of the samples the main peak is that at ca. 530.7 eV, assigned to O^{2-} ions of the TiO_2 crystalline lattice. The peak at ca. 533.0 eV, related to -OH groups [306], is negligible in Pt-Nb1-Brookite, small in Pt-P25, more evident in 3%Cu_2O-P25 and comparable to that at higher energy for 3%Cu_2O-HP. The presence of Cu_2O seems to favour the formation of surface hydroxyl groups. The main Pt peak at ca. 76 eV (Figure 4-II.10C) corresponds to Pt^0, the less intense peaks at lower binding energy are characteristic of partially oxidized Pt species [294].

High resolution XPS spectra of Cu 2p are reported in Figure 4-II.10D. For the P25 sample, the binding energy of the Cu $2p_{3/2}$ peak at 955.4 eV and of $2p_{1/2}$ at 933.2 eV are characteristic of Cu(I) oxide. For the HP sample the presence of a shakeup satellite peak between the main two Cu 2p peaks is characteristic of Cu^{2+} ions. The Nb 3d spectrum (Figure 4-II.10E) displays two peaks at 209.9 eV and 207.1 eV (binding energy distance of 2.8 eV) characteristic of Nb_2O_5 [74]. The

other two peaks at lower binding energies are those of Cl 2p. In Table 4-II.2 the atomic concentrations of the different species obtained by XPS investigations are reported.

Table 4-II.2 Relative atomic concentrations obtained from the XPS composition analysis

Catalyst	Ti	O	Pt	Cu	Nb
Pt-P25	16.82	48.79	0.21	-	-
3%Cu_2O-P25	18.35	53.59	-	0.42	-
Pt-Nb1-Brookite	18.65	56.83	0.12	-	0.28
Pt-HP	21.62	60.68	0.10	-	-
3%Cu_2O-HP	25.62	64.90	-	1.31	-

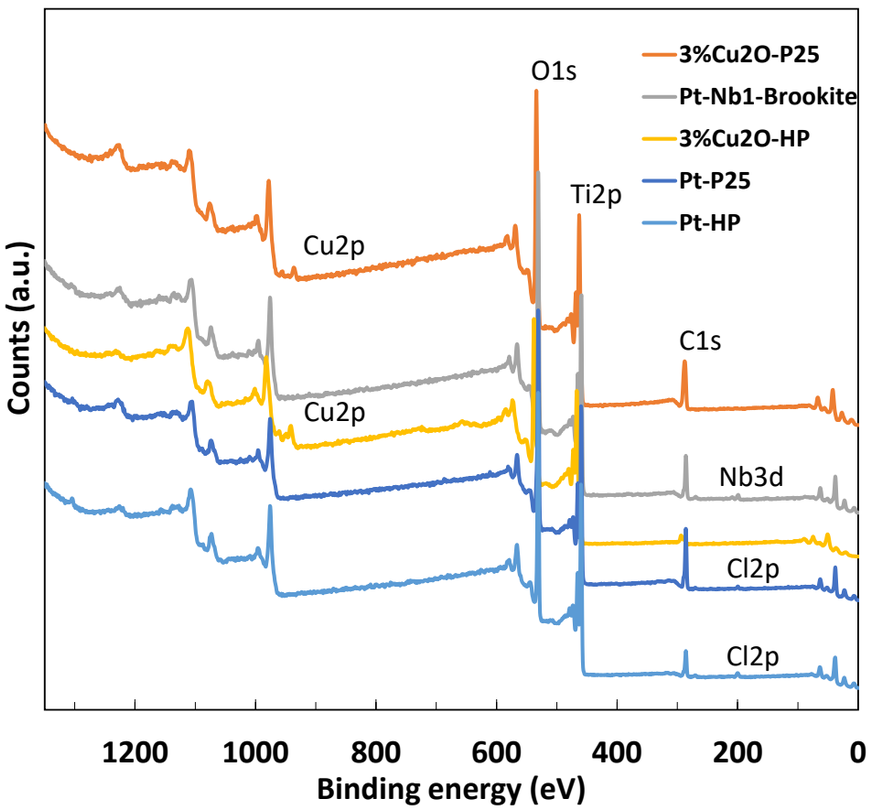

Figure 4-II.9 XPS survey of the different samples

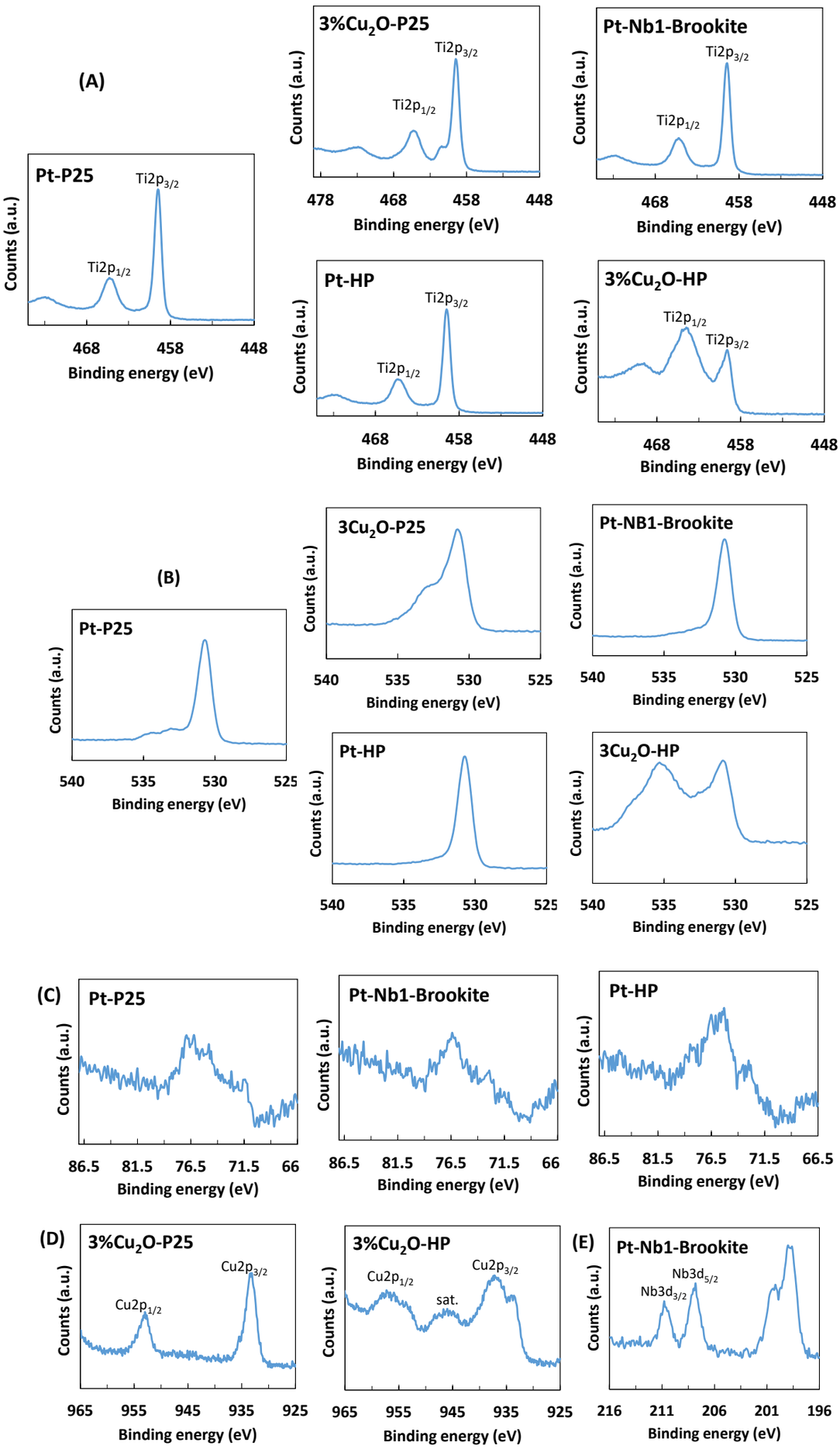

Figure 4-II.10 High resolution XPS spectra of: (A) Ti 2p, (B) O 1s, (C) Pt 4f, (D) Cu 2p, and (E) Nb 3d

4-II.3.10 Electron paramagnetic resonance (EPR) spectroscopy

As illustrated in Figure 4-II.11, the EPR spectra of the powdered samples 3%Cu_2O-P25, 3%Cu_2O-HP and Pt-3%Cu_2O-Brookite show a broad signal at g = 1.999 which can be assigned to Ti^{3+} ions on the surface [307]. The experiments carried out with samples containing Nb did not show any EPR signal, pointing out that the photocatalysts are unable to generate free electrons and oxygen vacancies under illumination. The Pt-3%Cu_2O-Brookite sample shows the highest intensity peaks indicating stronger presence of free electrons and oxygen vacancies, probably because the electrons are transferred to Pt and trapped therein. Conversely, the 3%Cu_2O-P25 solid showed the lowest EPR peak intensity. In the presence of DMPO/MeOH solutions (Figure 4-II.12), the experiments carried out in the dark did not detect any EPR signal, indicating that the photocatalysts are unable to generate radicals in absence of illumination. When the photocatalysts is exposed to light, the EPR spectra give rise to the characteristic paramagnetic resonance absorption of the adducts of DMPO-$^{\bullet}O_2^-$. This result indicates that all the photocatalysts can thermodynamically produce superoxide anion radicals ($\bullet O_2^-$) under illumination.

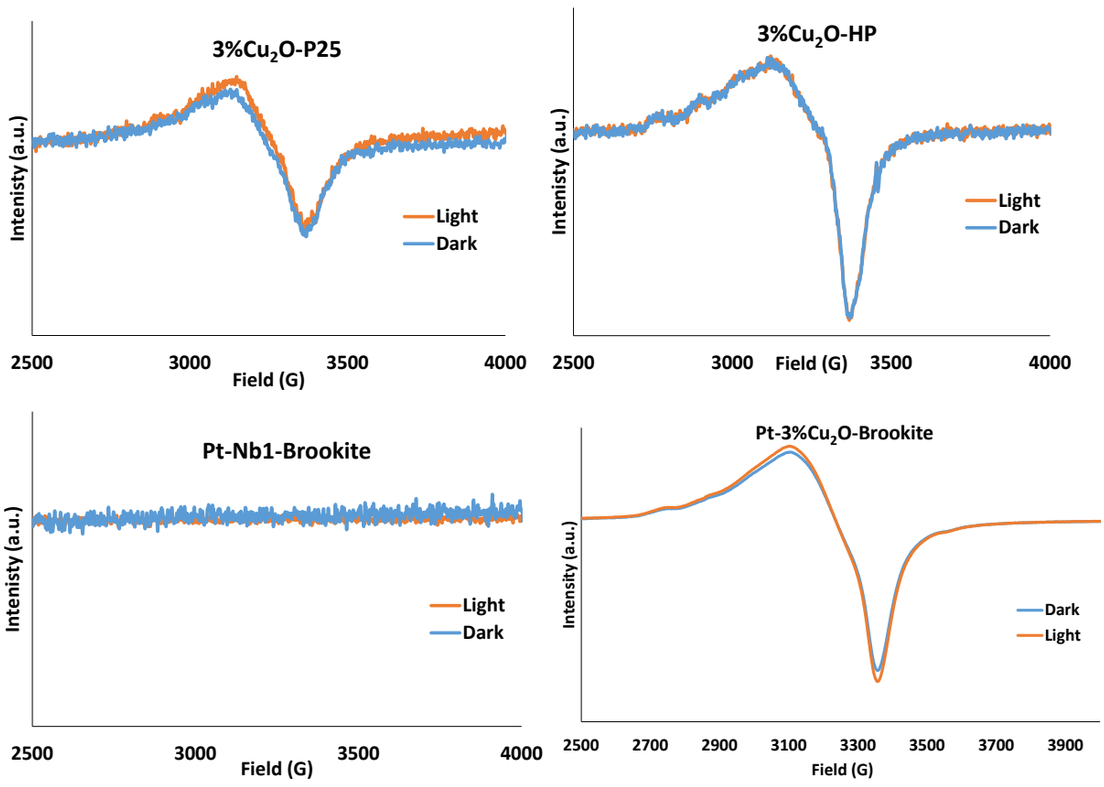

Figure 4-II.11 EPR spectra of different TiO_2 powder samples under dark and light irradiation

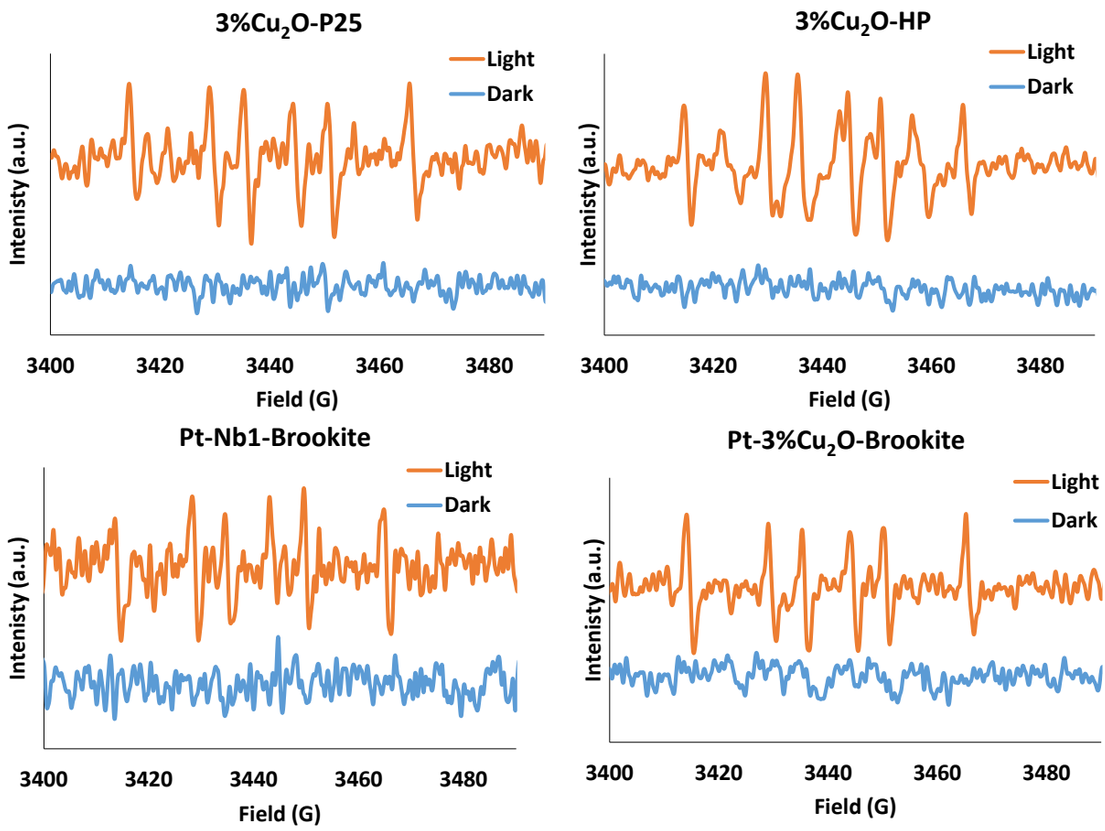

Figure 4-II.12 EPR spectra of MeOH suspended samples in the presence of DMPO

For DMPO/H_2O_2/water suspended samples (Figure 4-II.13), in the dark, no EPR signal is detected. Under irradiation, the EPR spectra give rise to the characteristic paramagnetic resonance absorption of the adducts of DMPO-•OH. Results indicate that only 3%Cu_2O-P25 and 3%Cu_2O-HP samples can thermodynamically produce hydroxyl (•OH) radicals under illumination. Samples with brookite phase TiO_2 were unable to produce •OH radicals under light. Although brookite TiO_2 can still exhibit some photocatalytic activity, it is often less efficient at generating hydroxyl radicals under light than anatase and rutile. This is due probably to the variations in the electronic structure, band gap, and surface properties among the different TiO_2 phases. The P25 sample showed the highest intensity peaks indicating strongest formation of the hydroxyl radicals.

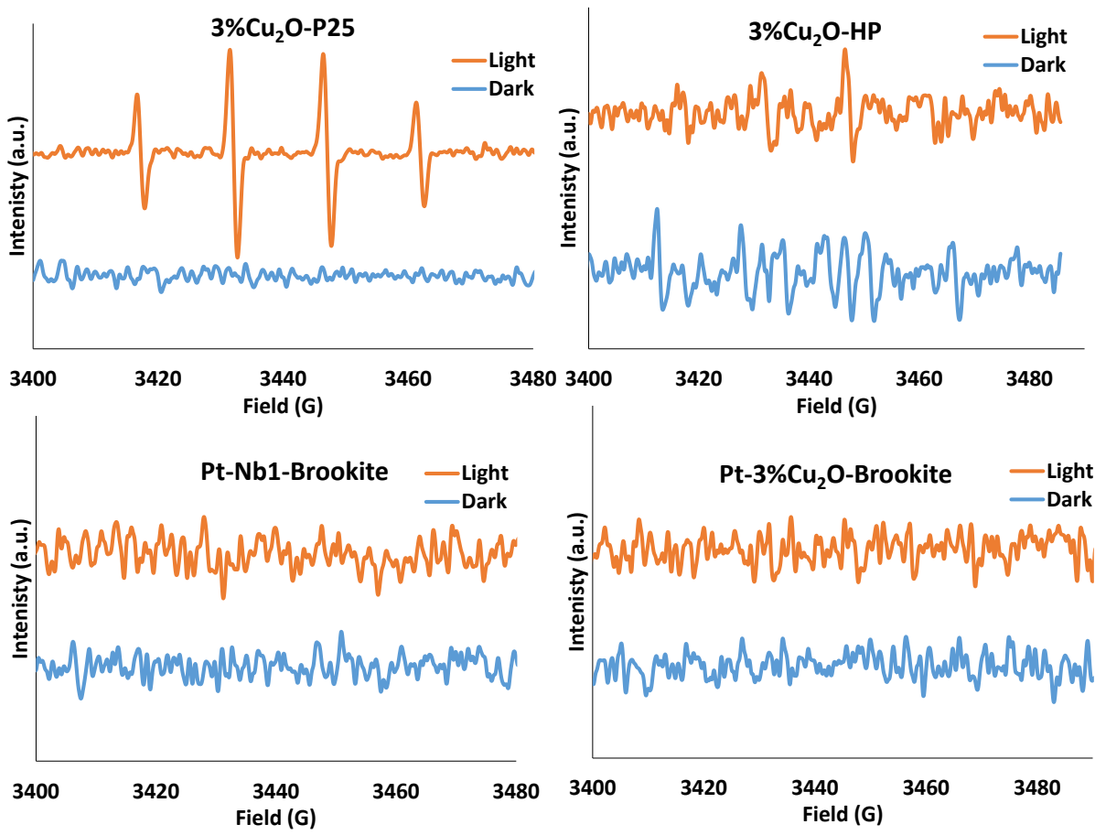

Figure 4-II.13 EPR spectra of water suspended samples in the presence of DMPO and H_2O_2

4-II.3.11 Diffuse reflectance infrared Fourier transform spectroscopy (DRIFTS)

In situ DRIFTS of adsorbed pyridine was used to identify the nature and the density of surface acid sites. In Figure 4-II.14 are illustrated the spectra related to bare and different Pt-loaded TiO_2 samples. The peaks at 1445 cm^{-1}, 1486 cm^{-1}, 1574 cm^{-1} and 1604 cm^{-1} are related to the pyridine ring coordinated to surface Lewis acid sites, whilst those at 1545 cm^{-1} and 1635 cm^{-1} correspond to the Brønsted acid sites on which the pyridinium ions are adsorbed [297, 308-311]. A clear predominance of acidic Lewis sites is detectable in all the samples; in addition, these spectra show the presence of both protonated pyridine (1545 and 1635 cm^{-1}) and co-ordinated pyridine (at 1604 and 1445 cm^{-1}). The peak at 1574 cm^{-1} is ascribable to a weak interaction of pyridine with the acid sites on the catalyst surface. Sharp and intense peaks are present for commercial P25 and home prepared HP samples, moderate for brookite and very weak for BDH solids. Although these spectra essentially give qualitative information, we can roughly say that a higher intensity corresponds to a higher concentration of acid sites, consequently the BDH sample exhibits the lowest concentration of surface acid sites, while P25 and HP solids the largest. Pt loading causes a decrease in the intensity of the bands for P25 (Figure 4-II.14A) and HP (Figure 4-II.14C) samples, a little increase for BDH solid (Figure 4-II.14B) and a significant rise for Brookite sample (Figure 4-II.14D). The different effects of Pt on the various solids can probably be due to the diverse TiO_2 phases. Shifts to higher wavenumbers of the peaks at 1604 and 1445 cm^{-1} observed in Figures 4-II.14B and 4-II.14D for the spectra of Pt-BDH and Pt-Brookite samples could be due to electronic effects of Pt ensembles on the pyridine ring coordinated to Lewis acid sites on the surface.

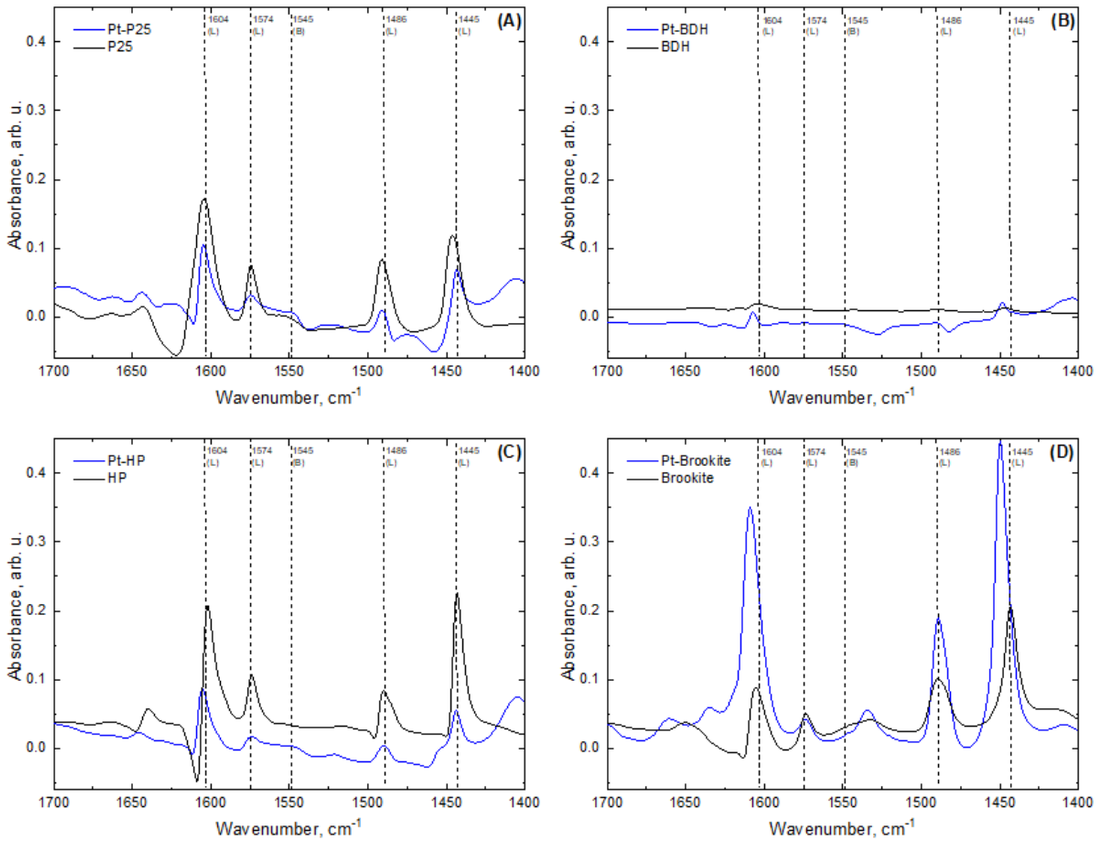

Figure 4-II.14 DRIFTS spectra of pyridine adsorbed on the surface of investigated materials; (A) P25 based solids, (B) BDH based samples, (C) HP based materials, and (D) brookite based photocatalysts

4-II.3.12 Temperature programmed desorption (TPD) spectroscopy

In Table 4-II.1 are also reported the quantitative results related to pyridine TPD measurements in terms of amount and density of acid sites present on the surface of different catalysts, and the corresponding temperatures of pyridine desorption. Pyridine TPD profiles are shown in Figure 4-II.15.

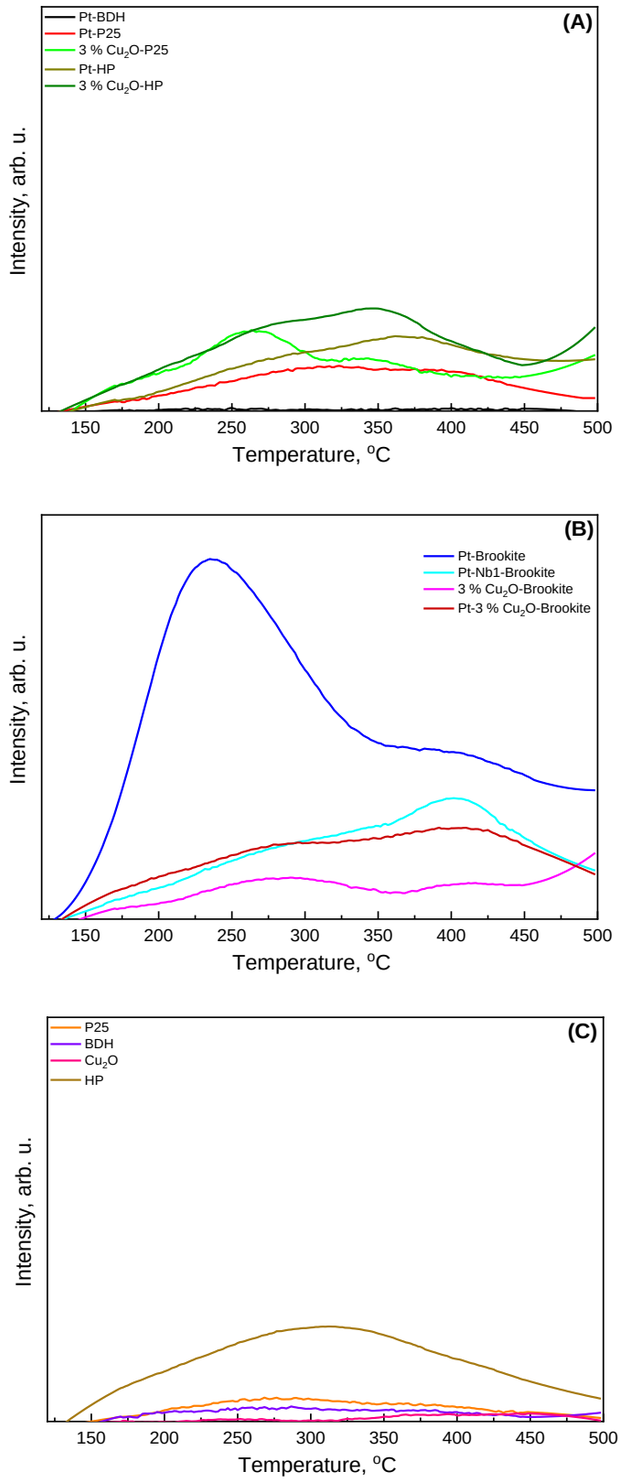

Figure 4-II.15 Pyridine TPD profiles for different photocatalysts

Comparing the pristine TiO_2 samples, Brookite and BDH solids display the highest and the lowest amount of acid sites, respectively; P25 sample shows less than half with respect to Brookite sample and HP solid has an intermediate amount. After Pt deposition it can be noted a decrease of the quantity of acid sites in all the TiO_2 bare samples, except for Brookite solid, and the appearance of a second desorption peak except for HP sample. Moreover, a general increase in the temperature of pyridine desorption can be observed in the presence of Pt, which implies a rise in the acid strength of the sites. The coupling with Cu_2O commonly reduces the desorption temperature and has different effects on the quantity of acid sites present on the various samples. In particular, it has a little effect on the amount of acid sites in P25 and HP samples, whilst a decrease is observed in Brookite sample. The latter is the only sample in which, in the presence of Cu_2O, the desorption temperature of the pyridine is practically equal to that of the bare sample. Moreover, a second

desorption peak at higher temperature is visible. In the Pt-Nb1-Brookite sample, the addition of Nb reduces the amount of acid sites with respect to Pt-Brookite sample and has not influence on the temperature of pyridine desorption.

The TPD technique after CO_2 adsorption on TiO_2 surface allows to study the basic surface properties of the different catalysts. In Figure 4-II.16 are shown the CO_2-TPD profiles of the investigated samples and in Table 4-II.3 are reported the amounts of basic sites. The peaks between 323-423 K are ascribed to the desorption of molecular CO_2, whilst those at higher temperatures to HCO_3^- or carboxylate deriving from the interaction of CO_2 with the TiO_2 surface hydroxyl groups [312]. The presence of peaks at higher temperatures indicates the existence of a stronger adsorption of CO_2 on the catalysts.

The observation of Table 4-II.3 related to pristine TiO_2 reveals that pure anatase (BDH sample) exhibits the least number of basic sites, the mixtures of anatase and rutile (P25 and HP solids) have the same middle amount, whilst brookite possesses the highest quantity. After the Pt addition, an increase, except for BDH sample, can be noted and Pt-P25 solid displays the largest amount of basic sites in the high temperature range.

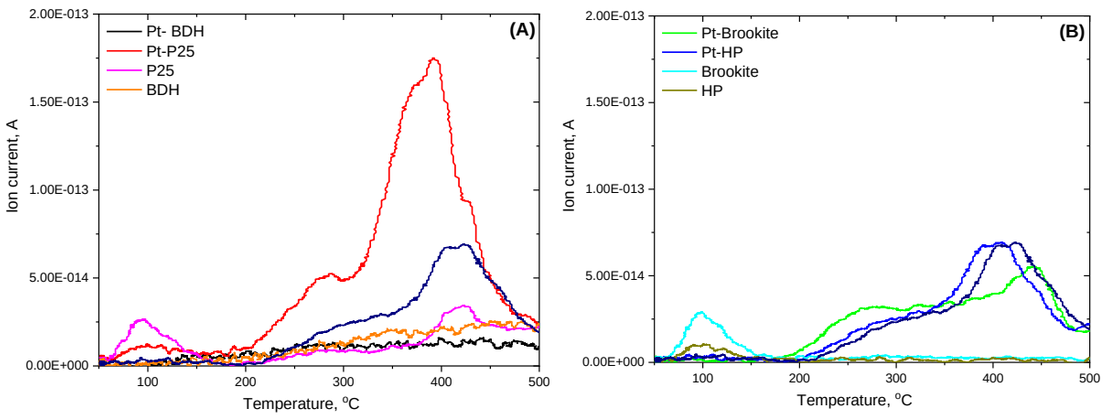

Figure 4-II.16 CO_2 TPD profiles of investigated materials

Table 4-II.3 Amount and density of basic sites on the surface of investigated materials

Sample	Mass of catalyst (g)	Peak area (A s)	Amount of basic sites (µmol/g)	Density of basic sites (µmol/m^2)
BDH	0.0447	2.95 E^{-11}	8.14	0.814
Pt-BDH	0.0521	2.09 E^{-11}	8.05	0.805
P25	0.0507	3.688 E^{-11}	12.1	0.242
Pt-P25	0.0518	1.287 E^{-10}	81.7	1.634
Brookite	0.0518	1.85 E^{-11}	28.3	0.288
Pt-Brookite	0.0502	5.75 E^{-11}	74.7	0.762
HP	0.0499	7.38 E^{-12}	12.8	0.164
Pt-HP	0.0520	5.74 E^{-11}	53.6	0.687

4-II.4 Photocatalytic activity

All the TiO_2 based samples were compared for glucose and fructose aqueous photo-reforming under UV light irradiation in anaerobic conditions with the aim to link the reactivity to some catalyst's features. The photocatalytic results obtained with the two substrates are reported in Tables 4-II.4 and 4-II.5. Pt enhances the photoactivity thanks to its role in the reduction of the recombination rate (in accordance with the PL results) and it is essential for H_2 production, as only compounds deriving from the partial oxidation of the starting substrates and CO_2 originating from mineralization were observed in the presence of naked TiO_2 [122]. The main identified intermediates in the liquid phase deriving from the partial oxidation of the starting substrates are arabinose, erythrose, gluconic acid, glucaric acid, fructose (starting from glucose) and formic acid (Figure 4-II.17), whereas H_2 and CO_2 are measured in the gaseous phase present in the head space of the photoreactor. In Figure 4-II.18 are reported the concentration of glucose, fructose, the molecules obtained from their oxidation in liquid phase and those in the head space, CO_2 and H_2, versus irradiation time in the presence of the most active photocatalysts. All the samples give rise to the same compounds highlighting the same reaction mechanism (Figure 4-II.17), but a different conversion degree, distribution of intermediates and H_2 production were observed with the different photocatalysts for both the substrates (Tables 4-II.4 and 4-II.5). The electronic and physico-chemical features of the different TiO_2 based materials, such as recombination rate of the photogenerated charges, polymorphic form, hydroxylation degree, crystallinity percentages, surface acidity, are the causes of their different photocatalytic behaviours.

Starting from glucose as substrate, fructose is formed by isomerization, and both can form gluconic acid by the oxidation of the anomeric C_1 center converting the aldehydic group to the carboxylic one. All the catalysts give rise to low amounts of glucaric acid starting both from glucose and fructose. A parallel mechanism consists in the α-scission of the carbohydrates giving rise to arabinose in the first step and erythrose in the second one along with formic acid and hydrogen [296, 122, 313]. In our experiment, starting from glucose, arabinose was the main product and traces of erythrose were observed with some catalysts, whilst starting from fructose, erythrose was essentially formed, confirming the breaking of the chain at the carbon bonded to carbonyl.

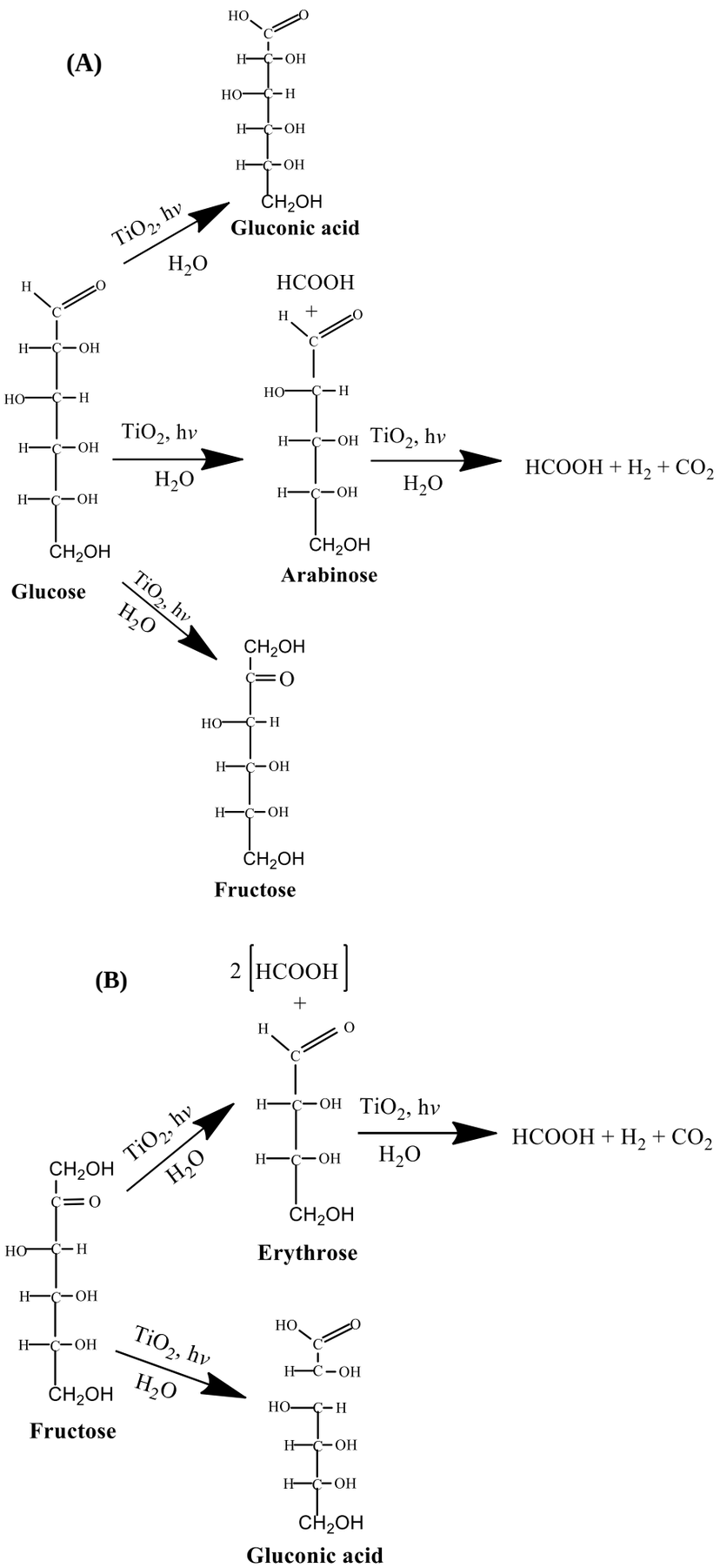

Figure 4-II.17 Hypothesized reaction mechanism of photo-reforming of (A) glucose and (B) fructose

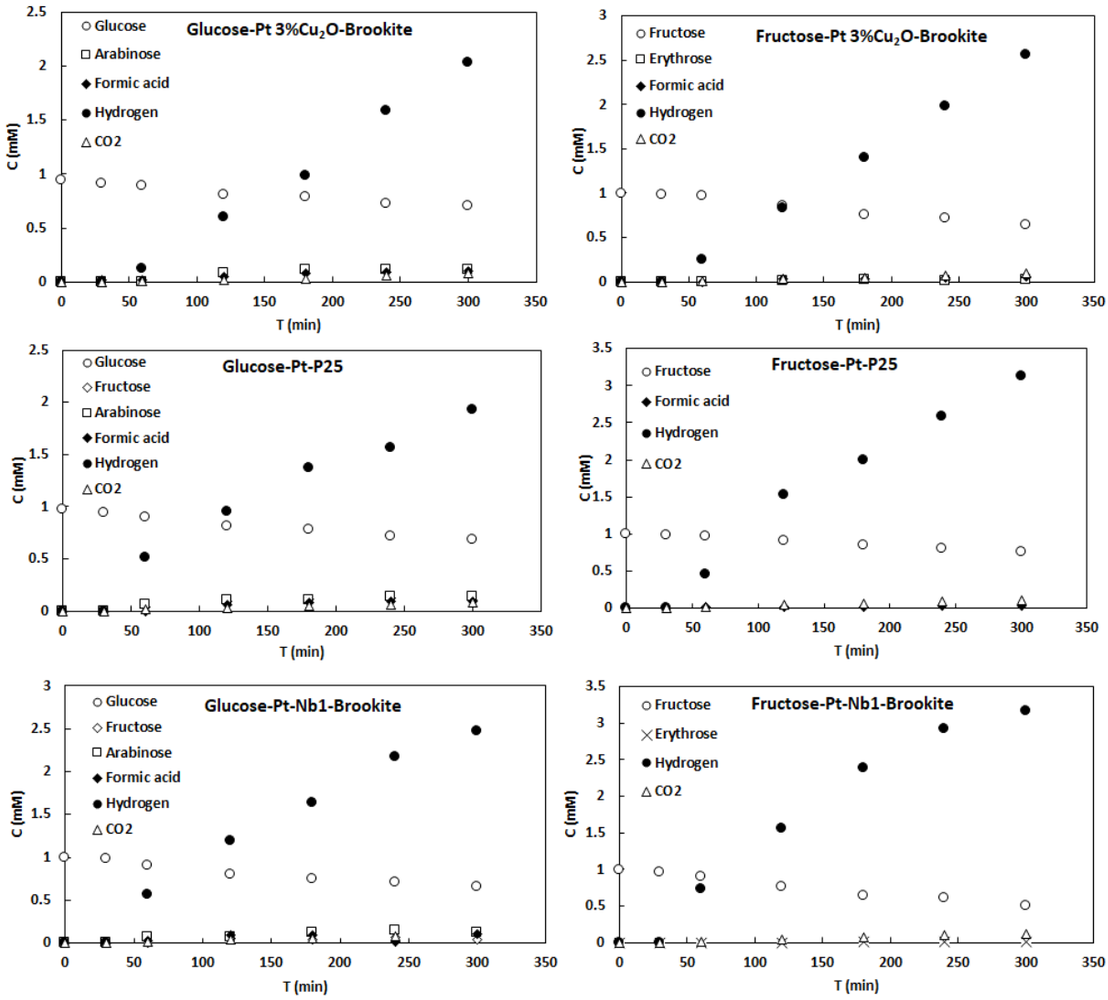

Figure 4-II.18 Concentration of (○) glucose, (◊) fructose, (□) arabinose, (x) erythrose, (♦) formic acid, (●) H_2, and (Δ) CO_2 versus irradiation time in the presence of various photocatalysts after 5 h of irradiation

Negligible amounts of H_2 were formed by using the pristine TiO_2 samples and the largely used Pt was essential to obtain satisfactory amounts. The coupling of TiO_2 with Cu_2O was beneficial both for conversion and selectivity for P25 sample, whilst it exhibited a slightly negative effect on Brookite and HP solids, in any cases was effective in replacing Pt for H_2 formation, avoiding the use of noble metal species.

Home prepared samples were competitive with the commercial ones being more active than the benchmark P25 solid. The commercial samples afforded less photocatalytic conversion for glucose and fructose than the home prepared ones. The highest glucose conversion (40%) was obtained with Pt-HP samples, whilst the most oxidant sample for fructose is Pt-Nb1-Brookite (conversion 50%). With the sample Pt-HP, almost the same degree of conversion was reached with the two substrates, while for fructose lower selectivity values but greater quantities of H_2 compared to glucose were obtained.

With glucose, Pt-Brookite based samples showed a little increase in the conversion, a generally decrease in the fructose selectivity and an enhanced H_2 formation. By using Pt-Brookite and Pt-Nb1-Brookite samples, the conversion of glucose was similar, the Nb addition enhanced H_2 formation and the selectivity towards the intermediates and fructose was also formed. HP based powders exhibited the highest conversion percentages and arabinose selectivity. The maximum hydrogen concentration was obtained with the Pt-Brookite photocatalyst that displayed the highest amount of acidic cites. Among the Pt-containing samples, Pt-BDH solid exhibited the lowest glucose conversion and formic acid selectivity, the highest fructose selectivity and no arabinose formation indicating a different reaction pathway [122, 296]. This finding is different from the

results of Román-Leshkov et al. [314] who attributed the isomerization of glucose to fructose by using tin-containing zeolite Sn-Beta as catalyst to the presence of Lewis acidic sites. In our case the solid with the lowest number of acidic sites (Table 4-II.1 and DRIFT measurements) gave rise to the highest fructose formation. Probably other features as catalyst type (we use TiO_2 instead of zeolite-based catalyst) and preparation method played a fundamental role.

By using fructose as substrate, a lower selectivity towards the partial oxidation compounds was obtained with respect to glucose. The most efficient catalysts were Pt-Brookite and Pt-Nb1-Brookite both for conversion and production of H_2.

Table 4-II.4 Glucose conversion, selectivity towards fructose, gluconic acid, arabinose and formic acid, and H_2 and CO_2 production. The listed values were obtained after 5 h of irradiation

Photocatalyst	Conversion (%)	Selectivities (%)				H_2 [mM]	CO_2 [mM]
		Fructose	Gluconic acid	Arabinose	Formic acid		
P25	12	22	1.5	38	29	-	0.03
Pt-P25	32	31	4.6	41	31	1.93	0.07
3%Cu_2O-P25	28	19	8.0	30	32	1.25	0.06
Pt-BDH	21	58	4.9	-	13	1.44	0.03
Pt-Brookite	33	-	2.5	27	40	2.71	0.09
Pt-Nb1-Brookite	35	12	3.7	32	31	2.40	0.09
3%Cu_2O-Brookite	26	20	3.0	36	25	1.20	0.08
Pt-3%Cu_2O-Brookite	30	-	3.1	37	34	2.03	0.08
Pt-HP	40	27	2.6	45	44	1.89	0.14
3%Cu_2O-HP	37	-	3.0	49	37	1.51	0.07

Table 4-II.5 Fructose conversion, selectivity towards gluconic acid, formic acid, erythrose, and H_2 and CO_2 production. The listed values were obtained after 5 h of irradiation

Photocatalyst	Conversion (%)	Selectivities (%)			H_2 [mM]	CO_2 [mM]
		Gluconic acid	Formic acid	Erythrose		
Pt-P25	25	9.0	12	-	3.13	0.11
3%Cu_2O-P25	35	5.0	5	-	1.80	0.08
Pt-BDH	28	4.1	7	-	1.34	0.02
Pt-Brookite	42	2.7	12	3.80	3.20	0.12
Pt-Nb1-Brookite	50	2.0	11	2.68	3.16	0.11
3%Cu_2O-Brookite	32	2.2	11	-	1.65	0.09
Pt-3%Cu_2O-Brookite	35	0.5	25	5.27	2.55	0.09
Pt-HP	40	4.5	6	7.47	3.26	0.12
3%Cu_2O-HP	35	6.2	17	7.60	1.70	0.09

4-II.5 Conclusions

In conclusion, the activity of various commercial and home prepared modified TiO_2 photocatalysts was compared for the photo-reforming of two biomass derivatives (glucose and fructose) selected as probe molecules. Numerous structural and surface characterizations have highlighted the different properties of the samples used and some of them have been related to the photocatalytic activity, although a direct correlation to a specific property was not found. This confirms the dependence of photoactivity on a number of parameters. Importantly, the home-prepared catalysts were more active than the commercial catalysts both in hydrogen generation and in the formation of partial oxidation compounds.

CHAPTER 5

Visible-light photoreforming of biomass derivatives through MBi_2O_4-P25 heterostructures: Study of the influence of metals (M= Cu, Ni, Zn, Co)

In this chapter, text is adapted from the following publication.

Muhammad Umair, Ahmed Malek Djaballah, Marianna Bellardita, Radia Bagtache, Leonardo Palmisano, Mohamed Trari. Visible-Light Photoreforming of Biomass Derivatives through MBi_2O_4-P25 Heterostructures: Study of the Influence of Metals (M= Cu, Ni, Zn, Co). *Advanced Sustainable Systems* 2024, 8(5), 2400298. https://doi.org/10.1002/adsu.202400298

CHAPTER 5

Visible-light photoreforming of biomass derivatives through MBi_2O_4-P25 heterostructures: Study of the influence of metals (M= Cu, Ni, Zn, Co)

5.1 Abstract

MBi_2O_4-P25 (M = Cu, Ni, Co, Zn) composites were successfully synthesized by a simple ball milling method by varying some parameters (rotation speed, rotation time, metal/TiO_2 ratio) to optimize the preparation conditions. The noble metal free TiO_2 based photocatalysts were used to carry out the partial oxidation of glucose and glycerol with the simultaneous H_2 production under simulated solar light irradiation. Starting from glucose, 2.6 mmol of H_2 were obtained with a conversion of 34%, along with arabinose, formic acid and gluconic acid as main intermediates. By using glycerol, 3.2 mmol of H_2 were produced, with 17% conversion and the production of dihydroxyacetone and glycolic acid. The composites exhibited higher activity than pure P25 and $CuBi_2O_4$ (CBO). The produced H_2 amount was comparable to that reported in the literature by using Pt-TiO_2 photocatalysts. This study offers a paradigm for the future design of bifunctional photocatalysts for simultaneous noble metal free H_2 production and biomass valorisation under environmentally friendly conditions with a possible scale up of the process.

5.2 Photocatalysts preparation

5.2.1 Synthesis of MBi_2O_4 with M= Cu, Ni, Zn, Co

$CuBi_2O_4$ (CBO) was synthesized by a very facile co-precipitation method following the nitrate route. $Cu(NO_3)_2 \cdot 3H_2O$ and $Bi(NO_3)_3 \cdot 5H_2O$ were added in stoichiometric proportions to 50 ml distilled water. The mixture was air-heated at 140°C for 48 hours after adjusting the pH at 12.20 with KOH. The solid obtained was recovered by filtration, washed with water and dried at 60°C. This synthesis is different from that reported by many Authors who used complexing agents in organic solvents and high temperature treatments [315-318]. $NiBi_2O_4$, $ZnBi_2O_4$, $CoBi_2O_4$, were synthesized by sol–gel route using $M(NO_3)_2 \cdot 3H_2O$ salts (M = Ni, Zn, Co) and Bi $(NO_3)_3 \cdot 5H_2O$ dissolved in stoichiometric proportions in water with a 5% excess of citric acid added. The solution was gradually evaporated on a hot plate and the amorphous powdered solid obtained was homogenized in an agate mortar and calcined at 800°C in a programmed furnace (5 °C min^{-1}).

5.2.2 Synthesis of MBi_2O_4 -P25 heterostructures

All the MBi_2O_4 heterosystems with different metals (M= Cu, Ni, Zn, Co) and P25 were obtained by mixing the two components in a planetary ball mill (PM 100, Retsch-Allee 1-5, 42781 Haan, Germany) instrument. The combined powders were prepared by placing the powders inside a chrome steel jar coated with zirconium oxide filled with six zirconium oxide balls.

To optimize the synthesis conditions, $CuBi_2O_4$ -P25 composites were prepared at three different rotation speeds (100, 150 and 200 rpm) and rotation times (1, 2 and 3 hours) in different weight ratios, such as 2, 3, and 4 % of CBO with respect to P25. The codes used for the samples were X%MBO-P25@s rpm & th where X is the spinel percentage (2, 3, 4%), M the metal species (in particular, C = copper, N = nickel, Z= zinc and Co = cobalt), s the rotation speed (100, 150 or 200 rpm) and t the rotation time (1, 2 or 3 hours).

5.3 Results and discussions

$CuBi_2O_4$ (p-type semiconductor) has an optimal band gap in the range 1.5-1.8 eV, suitable for solar light activation and for water splitting reaction due to its more negative redox potential of its conduction band than that of H^+/H_2 [315-318]. The doping of TiO_2 with metals (i.e., Nb, Cu, Co, Ni, Au) has been reported in literature to be effective in the reduction of the recombination rate of photoexcited electron-hole pairs and modification of some surface features [19, 76b-f, 105].

5.3.1 X-ray diffraction (XRD)

The diffractograms of the different samples are reported in Figure 5.1. The bare P25 sample shows both anatase and rutile characteristic peaks (anatase JCPDS NO. 99-0008, rutile JCPDS NO. 99-0090, respectively). The diffraction peaks related to the spinel ABi_2O_4 (A= Cu, Ni, Zn or Co) were not detected in the composites due to the low content of the latter in the heterosystems and its uniform dispersion in the TiO_2 matrix.

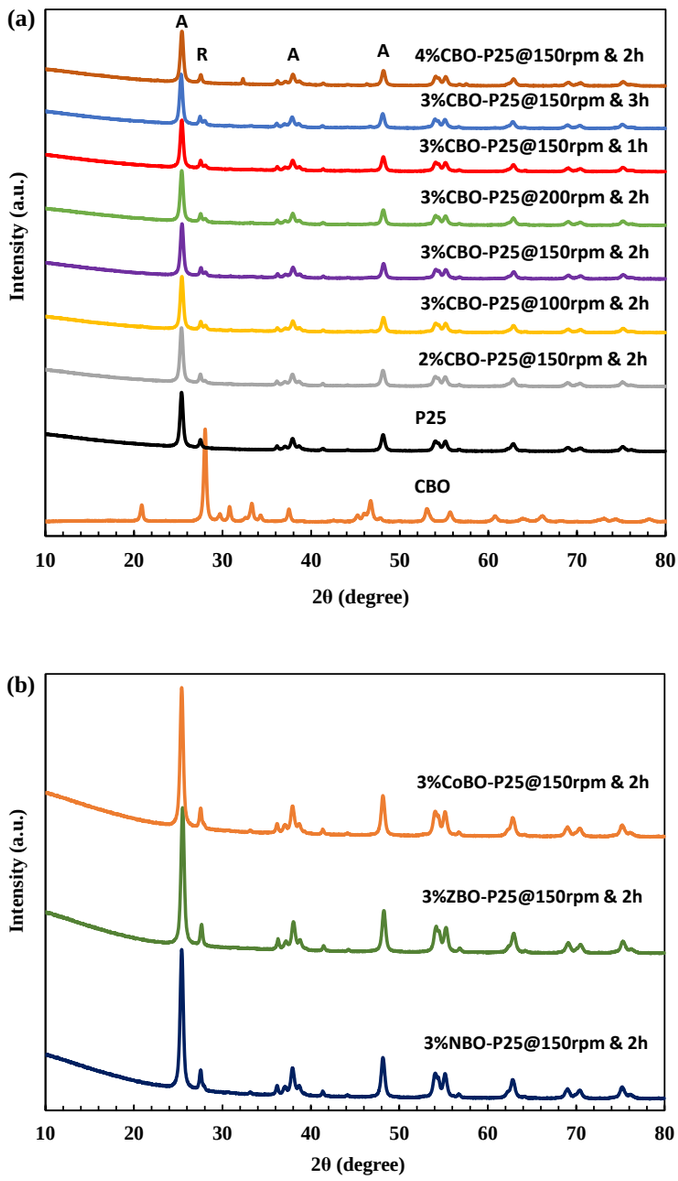

Figure 5.1 XRD patterns of (a) CBO, P25 and CBO-P25 coupled samples prepared in different experimental conditions; (b) MBO with M (Zn, Co and Ni)-P25 coupled samples. A = anatase and R= rutile

The size of nanocrystallites (D = 14.9 nm) was calculated by using the Williamson Hall equation ($\beta\cos\theta = k\lambda/D + 4\varepsilon \sin\theta$) [319] (Figure 5.2) from the full width at half maxima (β) of the strongest TiO_2 peaks. No substantial differences were noticed in the coupled samples.

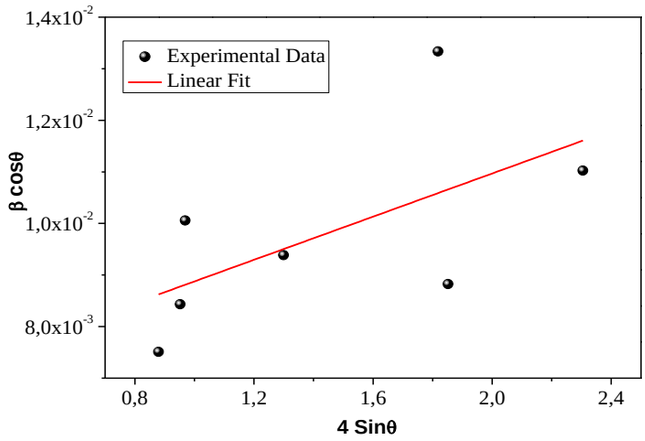

Figure 5.2 The crystallite size determined from the Williamson–Hall plot of 3% CBO-P25@150rpm & 2h

5.3.2 Raman spectroscopy

Raman spectroscopy was used to examine the structural characteristics of P25-based photocatalysts. The Raman spectrum of CBO (Figure 5.3a) shows seven active bands at 76, 122, 128, 186, 258, 400 and 581 cm^{-1}. The B_{2g} mode of the in-plane bending vibration of the Bi polyhedral is correlated with the peak at 76 cm^{-1}. The peaks at 122 and 128 cm^{-1} are attributed to the translational vibration of the CuO_4 plane along the Z axis with the A_{1g} mode [320]. The peak at 186 cm^{-1} corresponds to the E_g mode of the Cu-Cu vibration, while the band at 258 cm^{-1} is attributed to the rotation of two CuO_4 squares stacked in opposite directions [321]. The band at 400 cm^{-1} highlights the A_{1g} mode of the Bi-O stretching vibration while the A_{1g} mode of the in-plane respiration of the CuO_4 squares is due to the band at 581 cm^{-1}. These observations are consistent with previous studies and support the tetragonal crystal structure of CBO. For P25 based photocatalysts (Figures 5.3b, 5.3c and 5.3d), a total of five characteristic Raman active modes with frequencies around 141, 193, 387, 505 and 626 cm^{-1} were obtained, belonging to the anatase Raman bands. No signal related to spinel oxides of Cu, Co, Ni can be observed (Figure 5.3d), due to their low quantity and high degree of dispersion on the TiO_2 surface according to the XRD results. The enlargement of the anatase main peak at ca. 144 cm^{-1} (inset Figures 5.3b, 5.3c and 5.3d) reveals a slight shift towards lower wavenumber in the coupled samples. By considering that this vibrational mode is related to the O-Ti-O vibration, probably the presence of spinels causes a bond distortion that is reflected in a shift of the band.

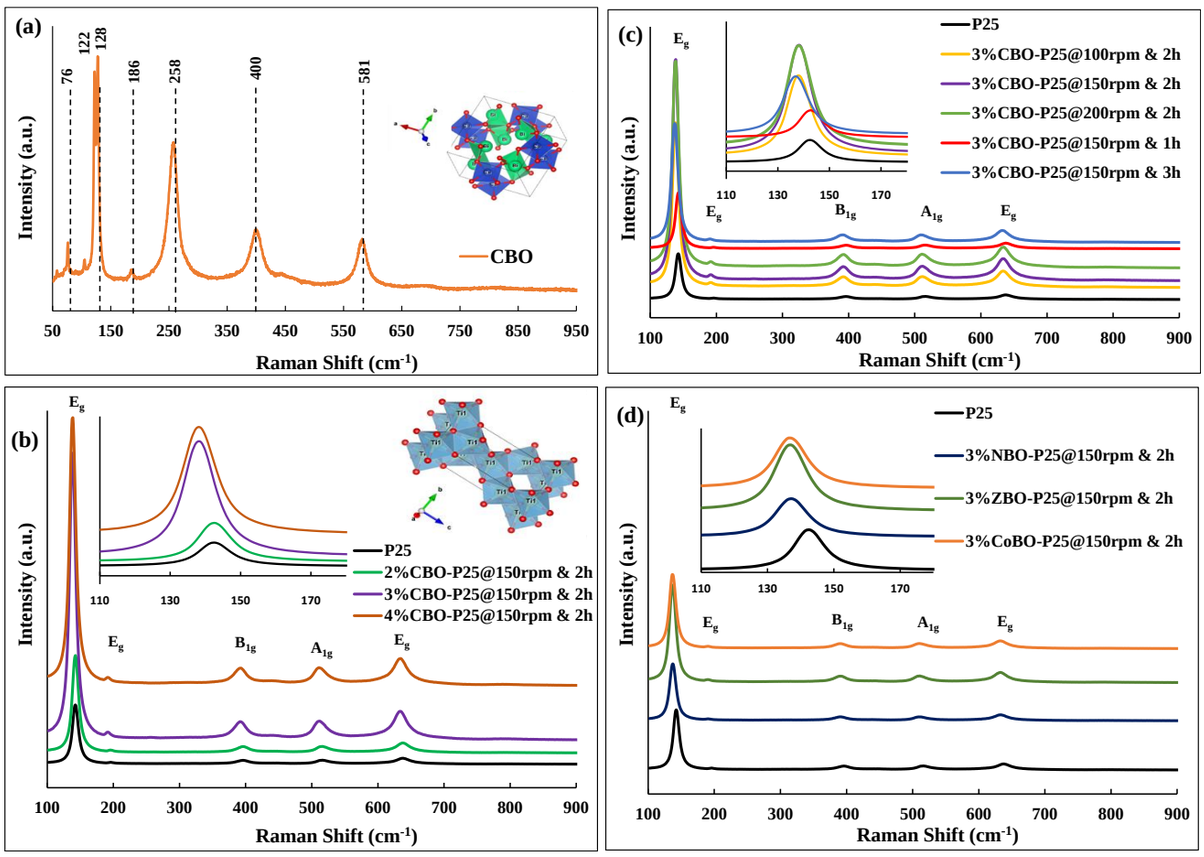

Figure 5.3. Raman spectra of the different samples

5.3.3 UV-Vis Diffuse reflectance spectroscopy (DRS)

The optical characteristics of the photocatalysts were investigated by the UV–Vis diffuse reflectance spectra (DRS). Figure 5.4a, shows the DRS of different samples. The commercial P25 has an absorption beginning at 350 nm, which corresponds to the typical band-gap of anatase-rutile mixture. Due to its brown colour and small bandgap, CBO exhibits an absorption edge in the visible range between 620 and 800 nm.

The coupled MBi_2O_4 with M (Cu, Co, Ni, Zn) and TiO_2 systems show an enhancement in light absorption capacity in the visible region which is maximum in the sample containing the highest CBO percentage. Notably, another absorption edge at about 600 nm can be noticed in the composite samples. In accordance with the literature, the presence of these two absorption edges is typical of the formation of a heterostructure between the spinel and TiO_2 [322]. Formation of all heterosystems between MBi_2O_4 and TiO_2 is expected to improve the light absorption capacity in terms of the photoactivation role of MBi_2O_4 responsible for electron transfer to TiO_2.

The band gap of samples was calculated from the Tauc plots (Figure 5.4b) accordingly to the following equation 5.1 [319]:

$$(\alpha h\nu)^{1/n} = K \times (h\nu - E_g) \quad (5.1)$$

where α, hν, and E_g are the absorption coefficient, the light energy of photon, and the band gap, respectively: K is a proportionality constant, while the exponent n indicates the transition nature, and it is equal to 2 and 0.5 for indirect and direct transition, respectively.

Band gap values of the used samples are reported in Table 5.1. P25 shows a band gap value of 3.17 eV, typical of an anatase–rutile mixture while bare CBO showed absorption of visible light and band gap of 1.88 eV. For the heterostructures, values are slightly lower than that of P25 indicating that the interaction with spinel does not substantially modify the electronic structure of TiO_2.

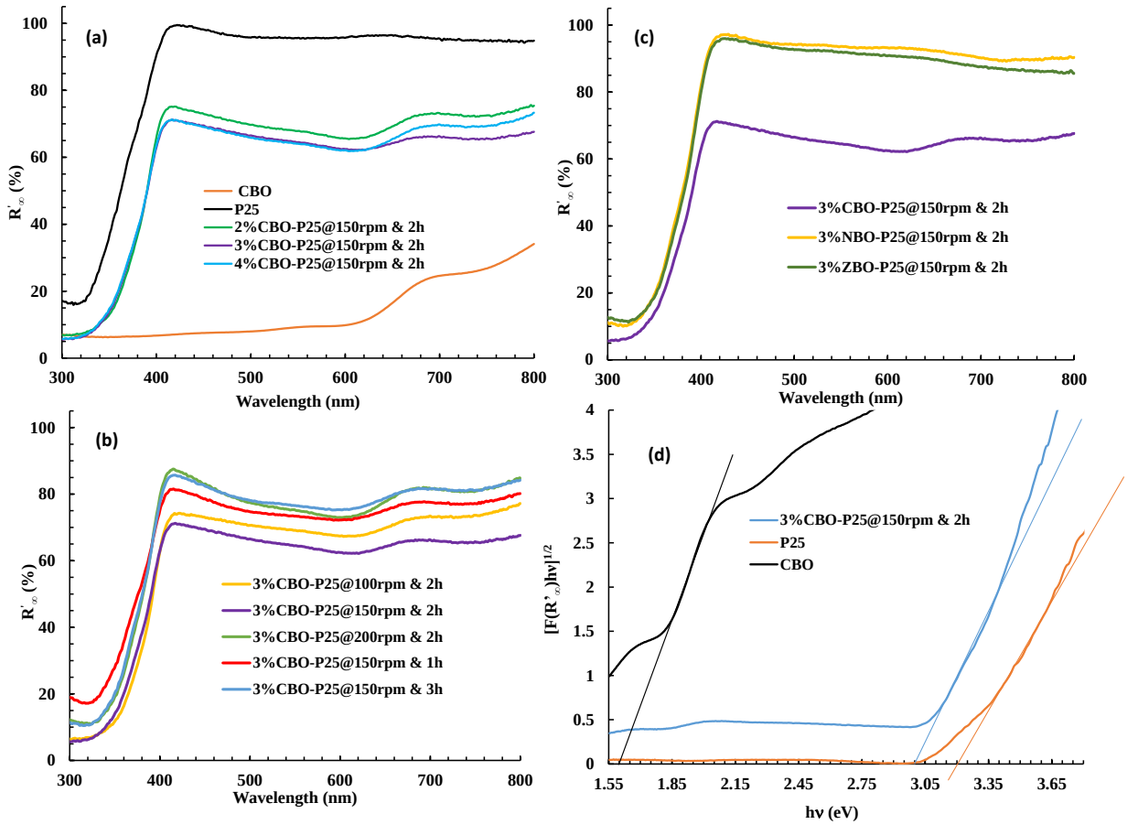

Figure 5.4. UV–Vis diffuse reflectance spectra of the different samples (a), (b), (c); band gap energy calculation of P25, bare CBO, and the 3%CBO-P25@150rpm & 2h composite sample (d)

5.3.4 Specific surface area (SSA)

P25 presents a specific surface area (SSA) of 50 m^2g^{-1} while that of bare CBO is very low (2 $m^2 g^{-1}$). All the coupled samples showed almost the same values as bare P25 due the low spinel amounts. Moreover, variations of rotation speed, CBO percentage and treatment time in ball milling do not influence the SSA values of the composites with respect to P25. 3%ZBO-P25 sample shows a slightly higher value of 62 $m^2 g^{-1}$.

Table 5.1 S.S.A. and band gap values of the different samples

Sample	S.S.A ($m^2 g^{-1}$)	Band-Gap (eV)
P25	50	3.17
CBO	2	1.88
2%CBO-P25@150rpm & 2h	53	3.10
3%CBO-P25@100rpm & 2h	48	3.10
3%CBO-P25@150rpm & 2h	46	3.05
3%CBO-P25@150rpm & 1h	45	3.12
3%CBO-P25 @200rpm & 2h	52	3.11
3%CBO-P25@150rpm & 3h	49	3.12
4%CBO-P25@150rpm & 2h	50	3.11
3%NBO-P25@150rpm & 2h	45	3.12
3%CoBO-P25@150rpm & 2h	46	3.13
3%ZBO-P25@150rpm & 2h	62	3.12

5.3.5 Fourier-transform infrared spectroscopy (FTIR)

Figure 5.5 shows a sequence of FTIR spectra for P25, bare CBO and 3% CBO-P25@150rpm & 2h samples. The spectrum of P25 clearly shows four bands. The broad band centred around 3500 cm^{-1}, corresponding to the stretching vibration of the hydroxyl -OH groups of the P25 surface [323], is the broadest one. The band at around 1630 cm^{-1} corresponds to HOH bending mode of undissociated water molecules adsorbed on TiO_2 surface [324, 325]; the peak at 1243 cm^{-1} could be attributed to carboxyl groups derived from adventitious residual organic species [326]. The band at ca. 731 cm^{-1} might be ascribed to the antisymmetric Ti-O stretching mode of the Ti-O-Ti [325]. According to previous findings [327], CBO exhibits two prominent peaks at 1386 and 554 cm^{-1} resulting from the stretching vibration of the Bi–O and Cu–O bonds, respectively.

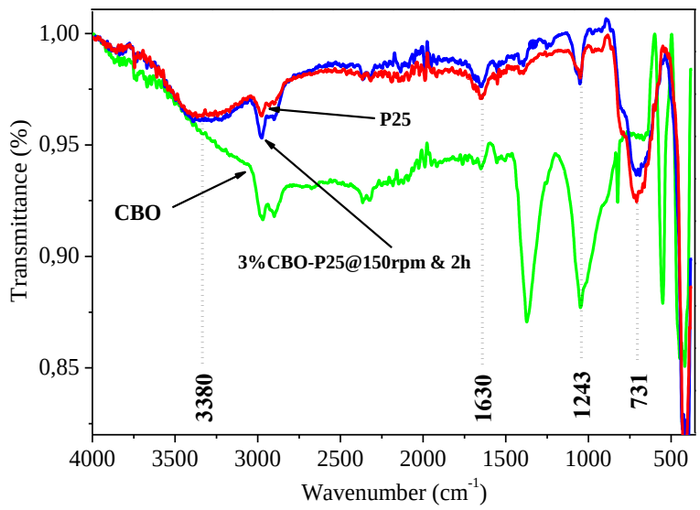

Figure 5.5 FTIR spectra of TiO_2, CBO, and 3%CBO-P25@150rpm & 2h49

5.3.6 X-ray photoelectron spectroscopy (XPS)

X-ray photo spectroscopy was used to study the surface chemical composition and the electronic core levels of the composite samples. The XPS survey spectrum of the sample 3%CBO-P25@150rpm & 2h (Figure 5.6a) confirms the presence of C, O, Cu and Ti in the CBO-P25 coupled samples and the results are consistent with EDS element distribution determinations. The C signal observed at 284.6 eV originates from the amorphous carbon applied to calibrate the binding energy scale.

Figure 5.6b, shows high-resolution XPS analysis of the Ti 2p region. The two peaks at 458.13 eV and 463.83 eV correspond to $2p_{3/2}$ and $2p_{1/2}$ binding energies of Ti^{4+} arranged in the anatase tetragonal structure [307, 328]. As shown in Figure 5.6c, the peaks at 529.23 eV and 529.93 eV are related to O 1s binding energies and indicate the existence of two chemical states of oxygen in all catalysts: crystal lattice oxygen and off-lattice oxygen surface hydroxyl groups, respectively. Additionally, the high binding energy peak at 532.7 eV can be ascribed to weakly adsorbed organic oxygen or to surface defects [322, 329]. The Cu 2p central level spectrum is displayed in Figure 5.6d. The main peak at ca. 933 eV and the shake-up satellite peaks with higher binding energy (ca. 941 and 943 eV) are assigned to Cu^{2+} [330], whereas the peak at ca. 953.5 eV can be attributed to the binding energy of Cu^{+} [331].

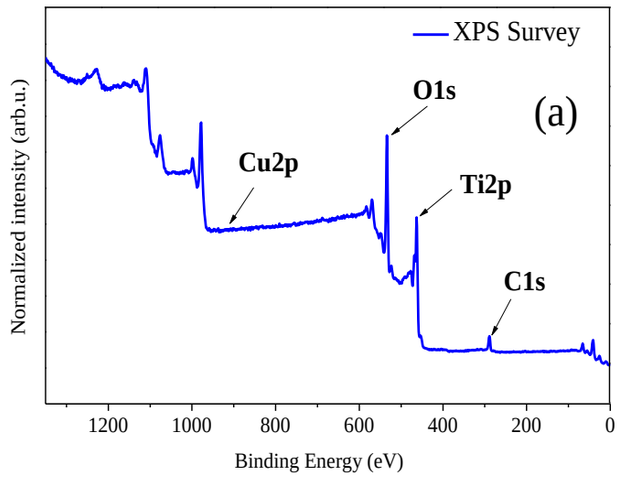
XPS Survey
O1s
(a)
Cu2p
Ti2p
C1s
Normalized intensity (arb.u.)
1200
1000
800
600
400
200
0
Binding Energy (eV)

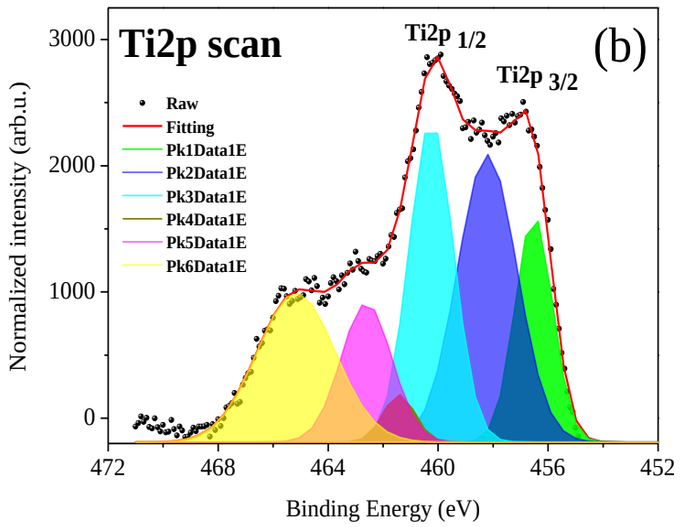
Ti2p scan
Ti2p 1/2
Ti2p 3/2
(b)
Raw
Fitting
Pk1Data1E
Pk2Data1E
Pk3Data1E
Pk4Data1E
Pk5Data1E
Pk6Data1E
Normalized intensity (arb.u.)
3000
2000
1000
0
472
468
464
460
456
452
Binding Energy (eV)

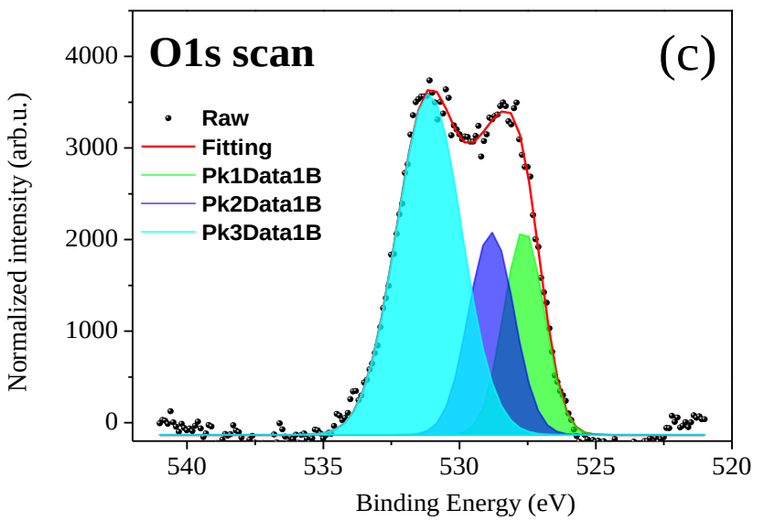
O1s scan
(c)
Raw
Fitting
Pk1Data1B
Pk2Data1B
Pk3Data1B
Normalized intensity (arb.u.)
4000
3000
2000
1000
0
540
535
530
525
520
Binding Energy (eV)

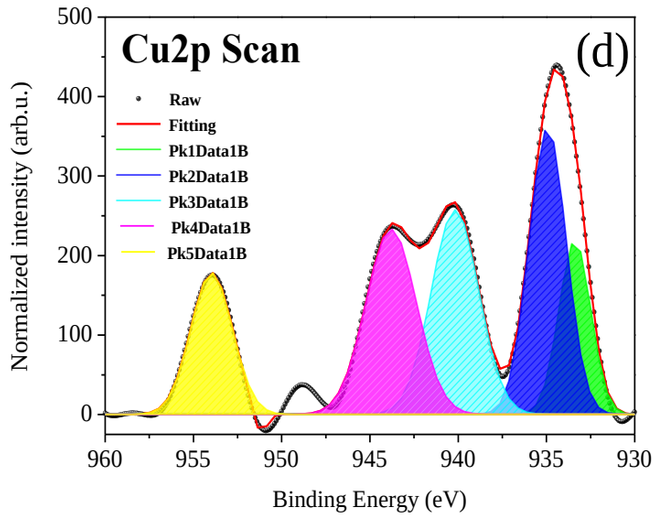

Figure 5.6 XPS spectra survey of 3%CBO-P25@150rpm & 2h (a) and Ti 2p (b), O 1s (c), Cu 2p (d) spectra

5.3.7 Scanning electron microscopy (SEM)

The morphology of the most active sample 3%CBO-P25@150rpm & 2h (Tables 5.2 and 5.3) was explored by SEM analysis (Figure 5.7). The distribution of the particles is uniform and irregular, and shaped agglomerates are present indicating a good mixing of the two components. The energy dispersion spectrum (EDS), in accordance with XPS measurements, confirms the presence of O, Ti, Cu and Bi (Figure 5.7a**)**, and Cu and Bi are present in small amounts in the coupled systems. Furthermore, the EDS elemental mapping images (Figure 5.7b) reveals the homogeneous distribution of the different elements supporting the successful formation of a heterostructure between CBO and P25.

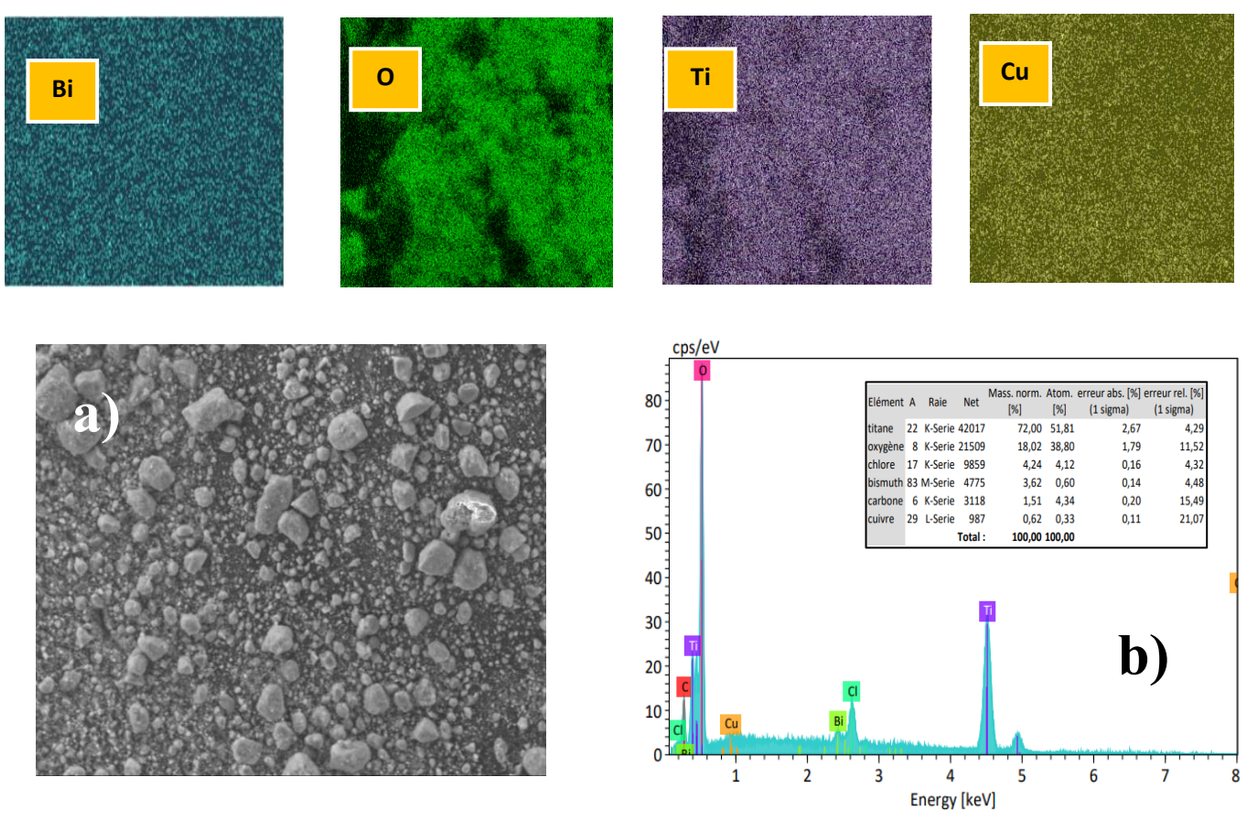

Figure 5.7 SEM image of 3% CBO-P25@150rpm & 2h (a); Mapping Analysis using EDX (b)

5.4 Photocatalytic activity

MBi_2O_4-P25 photocatalysts containing different metal species were used for the photoreforming of both glucose and glycerol substrates in aqueous solution. Concentrations of species formed in the liquid phase (arabinose, gluconic acid, formic acid) and gaseous phase (H_2 and CO_2) during the partial oxidation of glucose versus irradiation time in the presence of selected catalysts are reported in Figure 5.8. Figure 5.9 reports, on the contrary, the concentrations of glyceraldehyde, dihydroxyacetone, glycolic acid and H_2 and CO_2 derived from glycerol. The concentration of the two substrates gradually decreases while that of the compounds deriving from their partial oxidation and of the products in the gaseous phase increases. P25 resulted in the formation of arabinose, gluconic acid and formic acid from glucose reforming while the products deriving from glycerol were dihydroxyacetone, glyceraldehyde and glycolic acid. For both substrates no H_2 was obtained in the presence of the bare P25 photocatalyst and CO_2, deriving from substrates mineralization, was formed only in low quantities. Bare CBO displayed a negligible activity both towards glucose and glycerol. The behaviour of the composite samples was like that of P25 giving rise to the same compounds but with a different distribution and higher conversion of the two substrates. The amount of converted glucose and fructose in the presence of the coupled systems is higher than that of bare P25 highlighting a more effective charges separation probably due to the formation of an effective heterojunction [322]. Notably, from perusal of Table 5.2 and 5.3 can be observed that the two bare photocatalysts are inefficient for H_2 production whilst it is formed in the presence of the heterostructures. This finding is very interesting because the valuable energy carrier is produced without the addition of noble metal species as Pt. The optimization of preparation conditions (CBO percentages, different rotation speed and treatment time) allowed to enhance the efficiency both towards H_2 production and high value-added compounds formation.

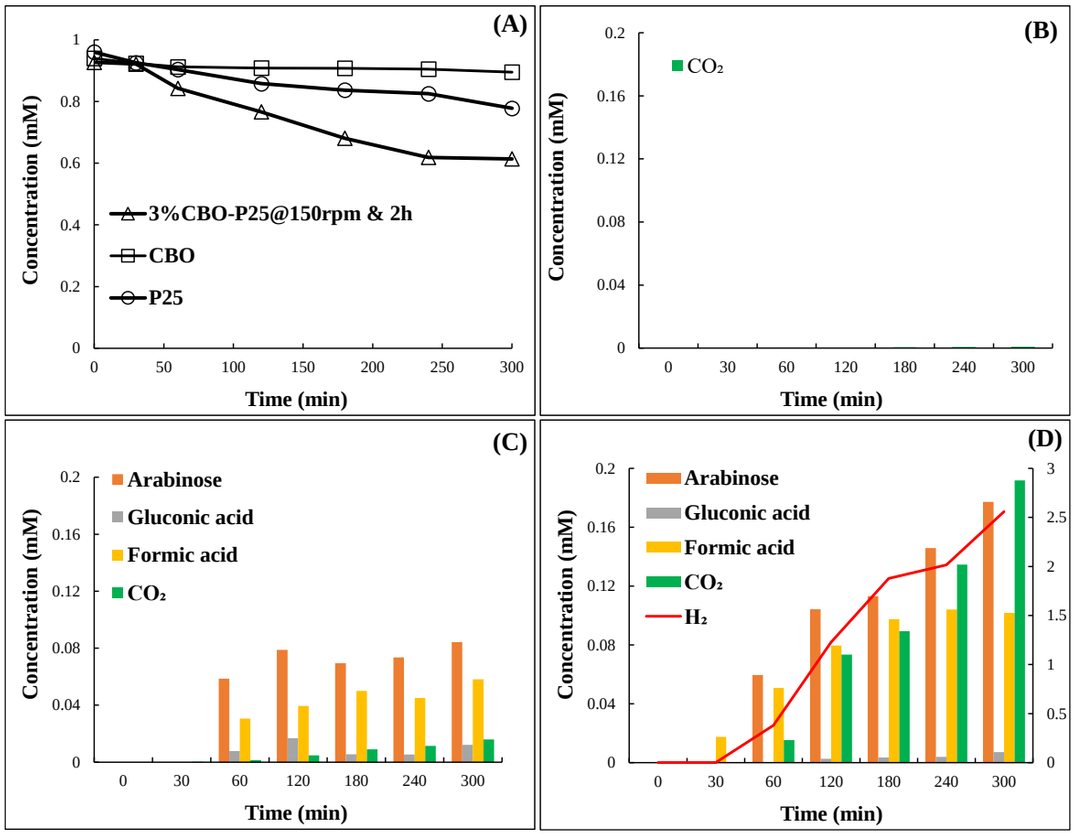

Figure 5.8 Variation of glucose concentration under irradiation (A), concentrations of liquid and gaseous species versus irradiation time in the presence of CBO (B), P25 (C) and 3%CBO-P25@150rpm & 2h (D) (H_2: right side y-axis))

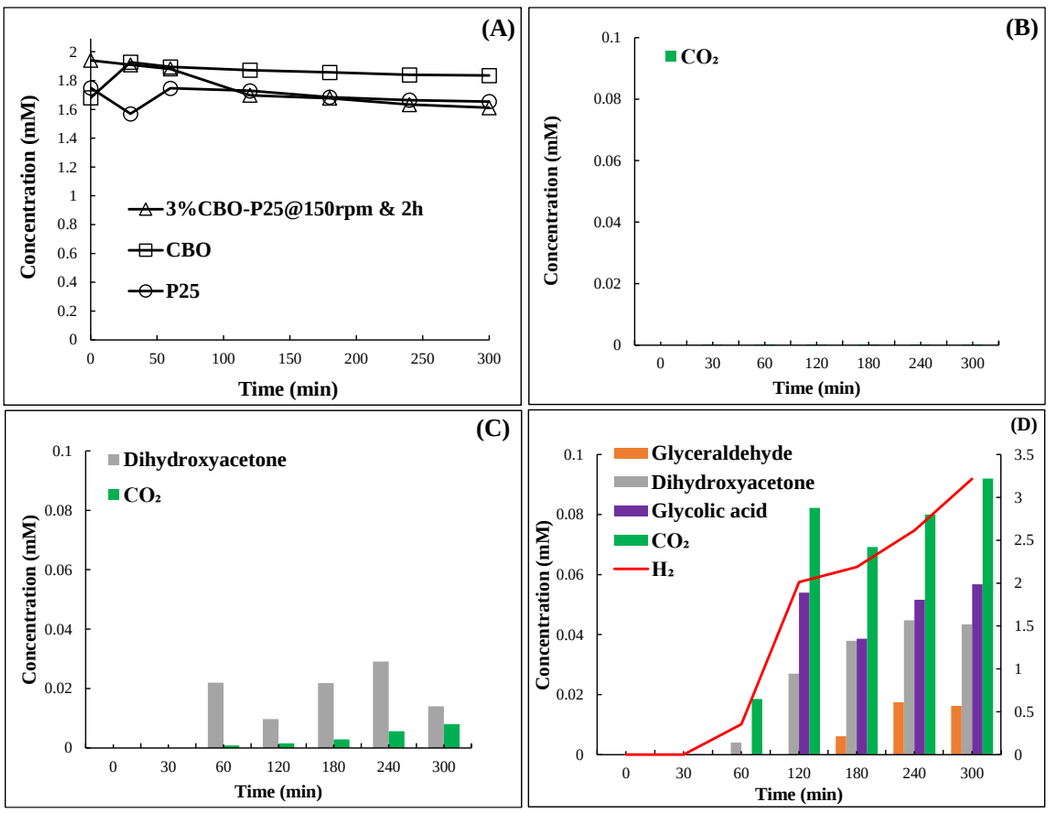

Figure 5.9 Variation of glycerol concentration under irradiation in the presence of different photoctalysts (A), concentrations of liquid and gaseous species versus irradiation time in the presence of CBO (B), P25 (C) and 3%CBO-P25@150rpm & 2h (D) (H_2: right side y-axis))

3%CBO-P25 samples (the CBO percentage with respect to TiO_2 was chosen considering previous results [301, 328]) was selected to study how the rotation speed and time of ball milling treatment influence the photoactivity. The samples were prepared by mixing the two components at three different ball milling rpm (Table 5.2 entries 3-5) for 2h. It can be noticed that higher the rotation speed from 100 to 150 rpm, 36% higher the glucose conversion with the contemporary slight enhancement in the selectivity and a 73% increase in H_2 concentration. The further increase of the rotation speed to 200 rpm did not more increase the performance of the catalyst, obtaining almost the same conversion, a small increase in selectivity towards arabinose and a lower production of H_2. Probably at 150 rpm an optimal mixing of the two components can be obtained. Therefore, set the rotation speed at 150 rpm, 3%CBO-P25 heterostructures were prepared by varying the treatment time in the ball milling from 1 to 3 hours. The best samples resulted 3%CBO-P25@200 rpm & 2h as 3%CBO-P25@200 rpm & 1h and 3%CBO-P25@200 rpm & 3h samples showed a lower glucose conversion (ca. 27%) and H_2 and CO_2 production. The same trend, although with different conversion, selectivity and H_2 production values, was obtained with glycerol (Table 5.3), confirming the importance of organic compound-catalyst interaction in addressing the activity. In fact, with glycerol, lower conversion and selectivity values but generally slightly higher H_2 amounts were formed. By varying the CBO amount the best value was found to be 3%. For glucose reforming, the catalysts named 2%CBO-P25@150 rpm & 2h and 4%CBO-P25@150rpm & 2h showed conversion of 33 and 36%, respectively and the amount of H_2 was 0.81 and 1.1 mM, respectively. The sample 2%CBO-P25@150 rpm & 2h produced more arabinose and formic acid. When glycerol was the substrate, the three catalysts prepared at 150 rpm for 2h, showed almost the same conversion, higher selectivity with 2 and 4% of CBO and the highest H_2 amount with the 3%CBO-P25@150 rpm & 2h sample.

The 3%CBO-P25@150 rpm & 2h sample proved to be the most effective sample towards H_2 formation using both glucose and glycerol as substrates. In fact, in its presence, H_2 was produced in concentrations of 2.6 mM starting from glucose and 3.21 mM in the presence of glycerol. The addition of CBO to P25 promoted the formation of an effective heterojunction

enhancing both H_2 production and the formation of high added value compounds and 3%CBO revealed to be the best combination. Higher amounts of CBO, probably prevents the TiO_2 surface from participating in the reactive process due to high surface coverage which causes poor light penetration.

To compare the effect of the presence of different metal species, some composites containing Ni, Co and Zn as metal species were prepared under the same conditions as the best 3%CBO-P25@150 rpm & 2h photocatalyst, i.e. 150 rpm and 2 hours of milling, and their behaviour was compared with that sample for the photoreforming of glucose and glycerol.

All these composites afforded comparatively lower glucose conversion and H_2 and CO_2 amount than those containing CBO. No arabinose was found but the amount of gluconic acid was greater with the 3%CoBO-P25@150 rpm & 2h. Among these composites, 3%ZBO-P25@150 rpm & 2h showed high conversion and a significant amount of H_2, although the corresponding copper-containing composite performed better. It is not easy to fully explain why the presence of copper gives better results than other metals. It is known that the Cu^{2+}/Cu^{+} couple present in photocatalysts [301, 332] such as TiO_2 and others, favours many oxidative and reductive processes (see for example the photoreduction of CO_2 and the oxidation of polluting organic molecules) [19]. This work has indicated that even in more complex composite materials, it is likely that the versatility of copper to acquire electrons and lose them during irradiation facilitates some intermediate stages of the described reactions, the mechanism of which certainly deserves to be explored in more depth in subsequent works.

As for the reaction with glycerol, only the 3%ZBO-P25@150 rpm & 2h sample was tested. The latter gave rise to a higher conversion (29% compared to 17%, with respect to the best copper-containing sample) i.e. 3%CBO-P25@150 rpm & 2h, but less selectivity towards the major identified products and H_2 production.

Table 5.2 Glucose conversion, selectivity towards different high value-added compounds and H_2 and CO_2 production

Samples	X (%)	$S_{Arabinose}$ (%)	S_{GluA} (%)	S_{FA} (%)	H_2 [mM]	CO_2 [mM]
P25	19	46	6.7	32	-	0.02
CBO	4.7	-	-	-	-	negligible
3%CBO-P25@100rpm & 2h	25	51	2.8	28	1.50	0.18
3%CBO-P25@150rpm & 2h	34	57	2.3	32	2.60	0.19
3%CBO-P25@200rpm & 2h	36	46	3.1	35	1.08	0.13
3%CBO-P25@150 pm & 1h	27	35	2.5	44	0.15	0.02
3%CBO-P25@150rpm & 3h	26	48	2.4	46	0.12	0.04
2%CBO-P25@150rpm & 2h	33	63	1.9	55	0.81	0.12
4%CBO-P25@150pm & 2h	36	45	2.0	43	1.10	0.14
3%NBO-P25@150rpm & 2h	19	18	3.0	54	0.09	0.01
3%CoBO-P25@150rpm & 2h	20	-	9.4	40	0.11	0.01
3%ZBO-P25@150rpm & 2h	27	46	1.2	49	1.37	0.10

Table 5.3 Glycerol conversion, selectivity towards dihydroxyacetone and H_2 and CO_2 production

Samples	X (%)	S_{GAld} (%)	S_{DHA} (%)	S_{GAcid} (%)	H_2 [mM]	CO_2 [mM]
P25	5	-	15.0	-	-	negligible
CBO	5	-	-	-	-	negligible
2%CBO-P25@150rpm & 2h	15	23.3	23.5	30.5	1.57	0.07
3%CBO-P25@100rpm & 2h	11	5.5	20.7	27.3	1.67	0.07
3%CBO-P25@150rpm & 2h	17	4.9	13.2	17.2	3.21	0.09
3%CBO-P25@200rpm & 2h	25	5.0	13.7	13.7	1.45	0.05
3%CBO-P25@150rpm & 1h	23	4.4	17.1	11.3	1.32	0.04
3%CBO-P25@150rpm & 3h	35	3.1	5.3	6.4	0.49	0.02
4%CBO-P25@150rpm & 2h	16	6.2	20.3	28.0	1.17	0.04
3%ZBO-P25@150rpm & 2h	29	3.3	6.1	12.4	1.34	0.05

In Figure 5.10a the hypothesized reaction pathway of glucose selective conversion is reported: the oxidation of the carbonyl to the carboxylic group lead to the formation of gluconic acid, whilst the formation of arabinose occurs after breaking of the C1-C2 (α-scission) carbon bond with the contemporary formation of H_2 and HCOOH [122, 296]. The main intermediates observed during glycerol conversion are 1,3 dihydroxyacetone, glyceraldehyde and glycolic acid. The first two compounds are formed by partial oxidation of the hydroxy group in position 1 or 2 to the carbonyl one, while the formation of glycolic acid arises from the C–C bond cleavage [296].

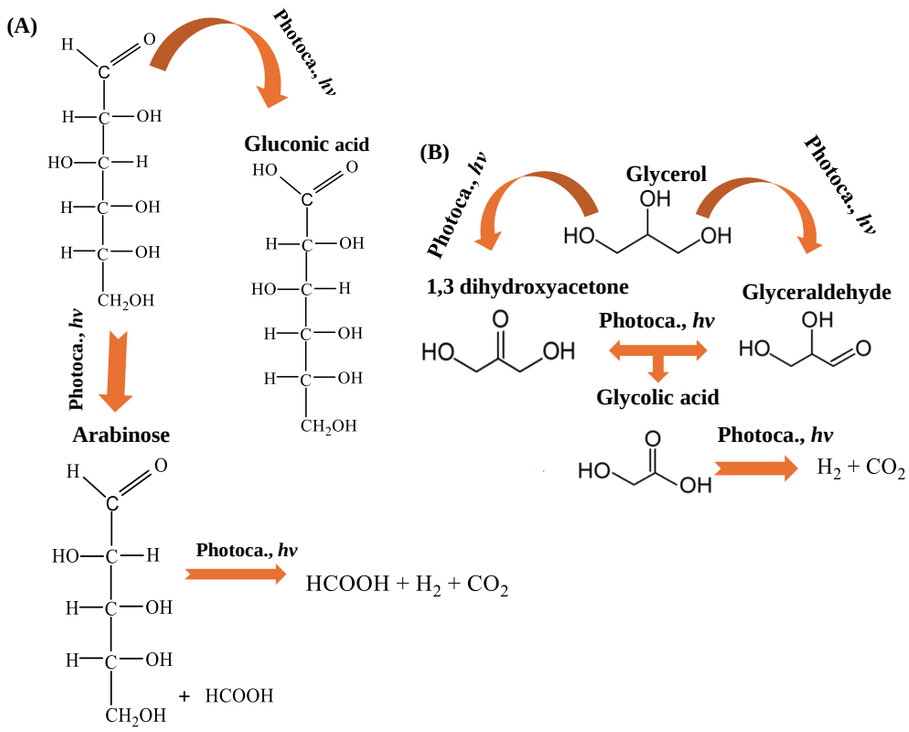

Figure 5.10 Hypothesized reaction routes of glucose (A) and glycerol (B)

5.5 Conclusions

MBi_2O_4-P25 coupled samples with M (Cu, Ni, Zn, Co) were successfully synthesized by a simple mechanical ball milling. The photocatalytic performance under simulated solar irradiation towards the production of H_2 and the partial oxidation of glycerol and glucose improved compared to unmixed solids. The enhanced photocatalytic activity was attributed to the improved absorption of visible light, the efficient separation of photogenerated electrons and holes and their rapid transfer to the reacting species due to the formation of an effective heterostructure. The most efficient catalyst was 3%CBO-P25@150rpm & 2h with a glucose conversion of 34% and H_2 production of 2.6 mM after 5 h. Moreover, arabinose and formic acid were the main products with selectivity values of 57 and 32% respectively. During glycerol photoreforming, a good H_2 production, similar to literature results related to Pt-P25 and different Pt-TiO_2 photocatalysts [301, 333], with the contemporary production of high added value compounds, has been obtained using the composite sample 3%CBO-P25@150 rpm & 2h.

This study suggests the possibility of replacing noble metals using a simple and easily applicable method in terms of scale-up for the preparation of active photocatalysts not only to produce H_2, but also co-products with high added value.

CHAPTER 6

Comparison between the efficiency of bare and Pt-loaded TiO_2 and $ZnIn_2S_4$ for H_2 production in the presence of triethanolamine, methanol, furfuryl alcohol used as sacrificial agents

In this chapter, text is adapted from the following publication.

Muhammad Umair, Leonardo Palmisano, Vittorio Loddo, Marianna Bellardita. Comparison between the efficiency of bare and Pt-loaded TiO_2 and $ZnIn_2S_4$ for H_2 production in the presence of triethanolamine, methanol, furfuryl alcohol used as sacrificial agents. *Inorganic Chemistry Communications*. Under review.

CHAPTER 6

Comparison between the efficiency of bare and Pt-loaded TiO_2 and $ZnIn_2S_4$ for H_2 production in the presence of triethanolamine, methanol, furfuryl alcohol used as sacrificial agents

6.1 Abstract

The worldwide increase in energy demand, global warming and the depletion of fossil fuel reserves, push scientific research towards the search for alternative sources of green energy. In this context, the production of H_2 from water via photocatalysis is proposed as an effective and alternative process especially if sunlight is used as a source of irradiation. To avoid or reduce the recombination of photo-generated charges that is deleterious for the occurrence of photocatalytic reactions, aqueous solutions containing sacrificial species that function as scavengers of the holes have been used. Sacrificial agents including triethanolamine and methanol are often employed although they trap the holes without turning into valuable partial oxidation products. The use of biomass derivatives such as furfuryl alcohol allows, instead, the simultaneous production of H_2 and high value-added compounds. In this work, the photocatalytic performance under simulated sunlight irradiation of $ZnIn_2S_4$, a photocatalyst which is relatively new and active under solar irradiation, was compared with that of TiO_2 (P25), the most widely used material, in the absence and presence of photodeposited Pt. The bare $ZnIn_2S_4$ was found to be more active than Pt-P25 for both H_2 and furfural production in the presence of furfuryl alcohol, giving rise to about 22 μmol g^{-1} h^{-1} of H_2 along with a furfuryl alcohol conversion and furfural selectivity of about 49% and 81%, respectively.

6.2 Photocatalysts preparation

6.2.1 $ZnIn_2S_4$

$ZnIn_2S_4$ was prepared through a hydrothermal method. In a beaker of 250 ml containing ethanol and deionized water, 0.4 mmol of $Zn(CH_3COO)_2 \cdot H_2O$ and 0.8 mmol of $InCl_3$ were added After stirring for 30 minutes, 3.2 mmol of thiourea was added and until the clear suspension, the mixture was continued stirring. After that, mixture was added into a stainless-steel autoclave and heated for 24h at 180 ºC. After drying at 65 ºC, the resulting powder was named $ZnIn_2S_4$. The synthetic route of $ZnIn_2S_4$ has been shown in Figure 6.1.

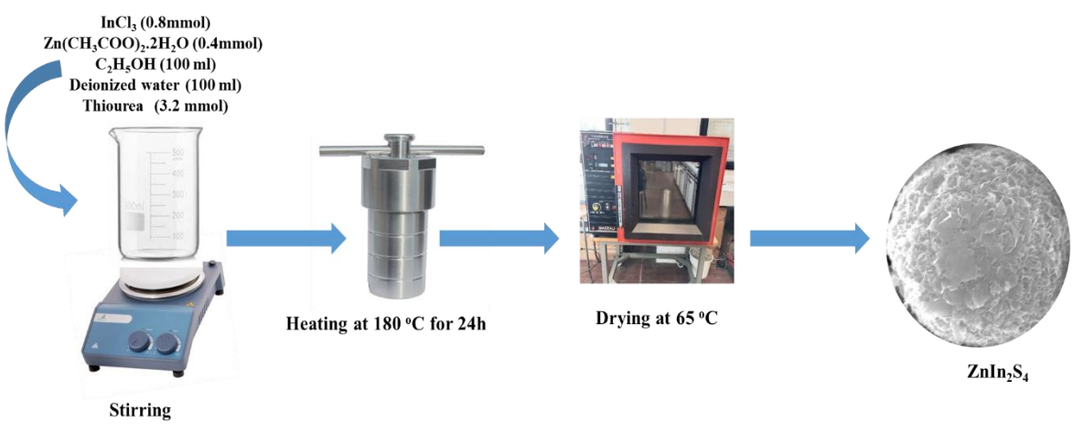

Figure 6.1 Synthetic route of the $ZnIn_2S_4$

6.2.2 Pt-$ZnIn_2S_4$

$ZnIn_2S_4$ was loaded with 0.5% Pt by a photo deposition method. Typically, $ZnIn_2S_4$ (2 g), ethanol (100 mL), distilled water (400 mL) and $PtCl_4$ (10 mL) were added into an 800 mL photoreactor and stirred in the dark with nitrogen (N_2) bubbling for 30 minutes. After that, the mixture was irradiated with a UV lamp (125 W) with continuously bubbling of N_2 for 8 h. The obtained mixture was filtered, washed with distilled water and dried in an oven for 7-8 h. The obtained sample was named Pt-$ZnIn_2S_4$. In the same way, the Pt-P25 was also prepared.

6.3 Results and discussions

6.3.1 X-ray diffraction (XRD)

XRD patterns of $ZnIn_2S_4$ and P25 are shown in Figure 6.2a. The peaks of $ZnIn_2S_4$ at 2θ values 21.6°, 27.7°, 39.5°, 44.2°, and 47.9° correspond to (006), (102), (108), (110), and (116) crystalline planes and are attributed to the hexagonal phase (JCPDS, card no. 65-2023). P25 contains both anatase (2θ values at 25.7°, 38.1°, 48.1°, 54.7°) and rutile (2θ values at 27.6°, 36.7°, 41.4°, 54.2°, 56.5°) phases. The presence of Pt (diffractograms not reported for the sake of clarity), does not modify the patterns in accordance with previous investigations [75, 334].

6.3.2 UV-Vis diffuse reflectance spectroscopy (DRS)

UV-Vis DRS spectra of P25, $ZnIn_2S_4$, Pt-$ZnIn_2S_4$ and Pt-P25 are reported in Figure 6.2b. P25 shows the typical anatase (being the major component) TiO_2 shape with a transition at ca. 380 nm; in the presence of Pt the band gap remains substantially unchanged but the absorption in the visible part of the spectrum increases. $ZnIn_2S_4$ is active under visible light displaying a transition edge at 415 nm; 50% decrease in reflectance following the Pt addition is due to presence of grayish color Pt loaded through the photodeposition method onto the catalysts surface. The band gaps of the used catalysts were determined by plotting the modified Kubelka-Munk function $[F(R'_\infty)h\nu]^{1/2}$ against the energy of the exciting light. $ZnIn_2S_4$ showed a band gap value of 2.36 eV while a larger value was found for P25 based samples, in accordance with the values reported in literature [31, 166] considering the reflectance shape of Pt- $ZnIn_2S_4$ it is not possible to estimate its band gap energy. Band gap and specific surface area values of the used samples are given in Table 6.1. SSA of $ZnIn_2S_4$ is lower than that of P25.

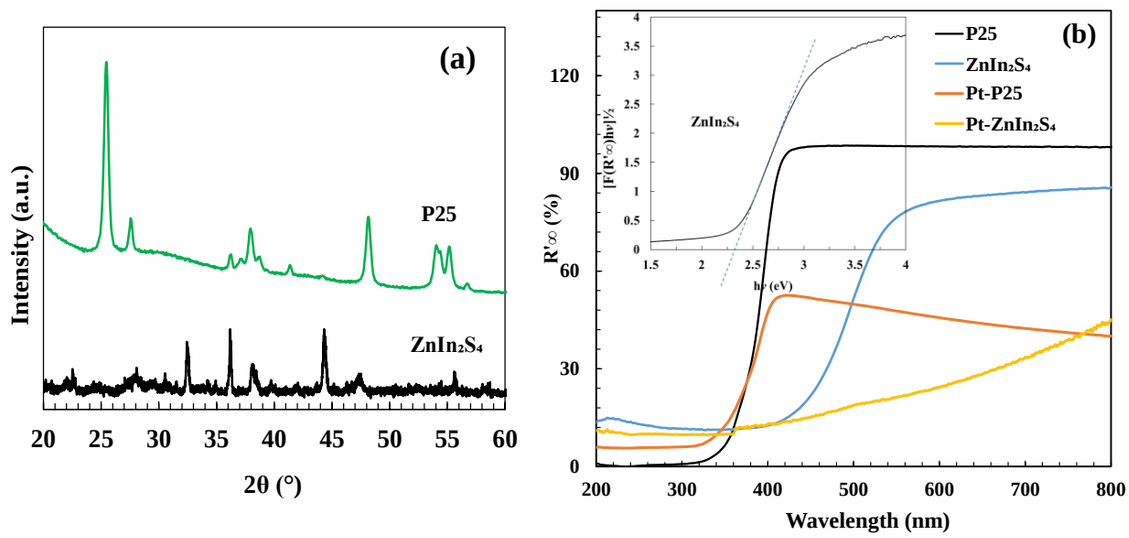

Figure 6.2 (a) XRD patterns of P25 and $ZnIn_2S_4$; (b) UV-Vis DRS spectra of P25, $ZnIn_2S_4$, Pt-$ZnIn_2S_4$ and Pt-P25

Table 6.1 Band gap values of the used photocatalysts

Catalyst	Band gap (eV)	SSA (m^2/g)
$ZnIn_2S_4$	2.36	7.4
Pt- $ZnIn_2S_4$	-	7.3
P25	3.20	50
Pt-P25	3.18	50

6.3.3 Scanning electron microscopy (SEM)

Figure 6.3 shows SEM images of $ZnIn_2S_4$ and P25. $ZnIn_2S_4$ has a marigold-like spherical superstructure and is composed of numerous microspheres with an average diameter of about 3-10 µm. P25 showed agglomerates formed by roundish particles with the size ranging between 18 and 130 nm. As reported before, the Pt presence[56, 334, 335] doesn't change the morphology.

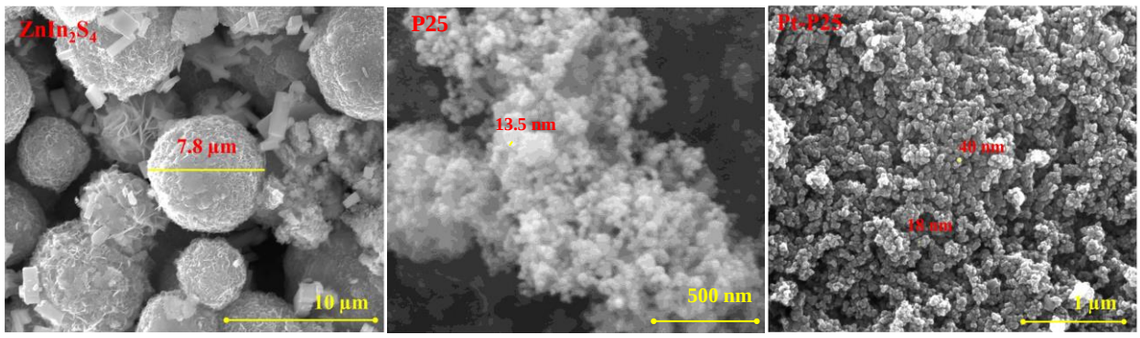

Figure 6.3 Scanning electron microscopy image of $ZnIn_2S_4$, P25, and Pt-P25

6.4 Photocatalytic activity

In Table 6.2 the results obtained during the runs carried out in the presence of different substrates by using $ZnIn_2S_4$, P25, Pt- $ZnIn_2S_4$ and Pt-P25 as photocatalysts are reported. In particular, three different sacrificial agents, namely TEOA, methanol and furfuryl alcohol, were used under anaerobic conditions to verify the efficacy of bare $ZnIn_2S_4$ for H_2 production.

It has been widely demonstrated that photocatalytic water splitting is an energy-intensive reaction, and the addition of a sacrificial molecule decreases the free energy of the reaction [336, 337]. Methanol and TEOA are two of the most widely used organic compounds due to the high amount of H_2 that is obtained in their presence during a photocatalytic process, especially in the presence of photocatalysts containing noble metals such as Pt that act as electron sinks [144, 165, 336, 338-340]. However, although in their presence a good production of H_2 is obtained, the photocatalytic process is not fully exploited since no valuable products are obtained from their partial oxidation. Photoreforming of aromatic alcohols instead allows the use of photogenerated holes to obtain high added value aldehydes together with the formation of H_2 [341-343], and for this purpose, furfuryl alcohol was chosen as another sacrificial agent [56, 344-346].

Furthermore, it should be remembered that generally only a sacrificial agent is chosen in specific studies where comparisons of H_2 production obtained with different photocatalysts and under different experimental conditions are presented. However, as it has been demonstrated in the case of partial oxidation reactions [346], also in the photoreforming process the intrinsic characteristics of a photocatalyst should be considered for the choice of the appropriate sacrificial agent [336], although this is often difficult.

The results reported in Table 6.2 reveal that no H_2 was produced when the TEOA-containing solution was irradiated in the absence of a photocatalyst, highlighting that the interaction of the starting substrate with the charges generated on the photocatalyst surface by irradiation is necessary. Using bare P25, no H_2 was obtained, which was surprisingly formed in the presence of bare $ZnIn_2S_4$ with a concentration of 0.88 mM that increased up to 1.7 mM for the Pt-$ZnIn_2S_4$ sample. In the presence of Pt-P25 instead of bare TiO_2 the H_2 concentration was 1.22 mM, instead of zero, confirming, as expected, the beneficial role of the noble metal. Furthermore, the Pt-P25 sample was found in this case to be less effective in generating H_2 than the Pt-$ZnIn_2S_4$. It is worth noting that TiO_2 samples with Pt on the surface are used with great success in the literature. A comparable CO_2 amount was measured with the two samples containing Pt (0.0004 versus 0.0003 mM). In the absence of organic substances, no water splitting occurred with the best Pt-$ZnIn_2S_4$ sample, confirming their positive role in H_2 formation via photoreforming and the difficulty of "pure" water splitting.

As for methanol, P25 gave rise to a small amount of H_2 in its presence, $ZnIn_2S_4$ and Pt-$ZnIn_2S_4$ a slightly higher H_2 concentration (0.11 versus 0.14 mM) whilst Pt-P25 a significantly higher amount (9.65 mM). The amount of CO_2 was also the highest in the presence of Pt-P25.

Using furfuryl alcohol, P25 did not produce H_2 and with the other three photocatalysts practically the same amount of H_2 was observed, but a higher degree of mineralization was found for Pt-P25, indicating its higher oxidizing power. This behaviour can be explained by the fact that the sites existing on TiO_2 surface, despite the presence of Pt, allow more easily the occurrence of successive steps of adsorption and desorption after successive attacks of oxidizing radical species that allow a complete degradation of the initial molecule up to CO_2, compared to those present on the surface of bare $ZnIn_2S_4$.

All the samples used were found to be active in the conversion of furfuryl alcohol with conversion values ranging from approximately 32 to 49%, the highest amount being recorded in the presence of bare $ZnIn_2S_4$. The selectivity towards furfural, the main intermediate identified, was low with P25 and higher with the $ZnIn_2S_4$-based catalysts. In particular, with bare $ZnIn_2S_4$ a selectivity value higher than 81% was obtained despite the significant conversion degree of furfuryl alcohol (48.6%). It has been reported that generally low selectivity values are obtained when the conversion of alcohol in water is high [347, 348]. Trace amounts (selectivity ≤1%) of 2-furoic acid were also found in the reaction mixture in the presence of all samples. The high selectivity to furfural obtained with bare $ZnIn_2S_4$ can be mainly attributed to its narrow band gap and band edge energy suitable for partial oxidation of furfuryl alcohol [348].

H_2 production from aqueous solutions containing the three sacrificial agents follows the order methanol>TEOA>furfuryl alcohol using Pt-P25, while TEOA>furfuryl alcohol>methanol for $ZnIn_2S_4$ and TEOA>methanol>furfuryl alcohol for Pt-$ZnIn_2S_4$. It should be noticed, however, that the differences between the presence of methanol and furfuryl alcohol are not very high in the case of the $ZnIn_2S_4$ (0.11 versus 0.16 mM) and Pt-$ZnIn_2S_4$ (0.14 versus 0.13 mM) samples, but the presence of furfuryl alcohol obviously allows the simultaneous formation of furfural.

In the presence of bare $ZnIn_2S_4$ it is possible to produce H_2 under green conditions since no metal species are present, water can be used as the solvent and sunlight as irradiation source. Furthermore, although the amount of H_2 obtained from furfuryl alcohol is lower than that formed with the other substrates, as mentioned before a particularly high amount of furfural can be obtained in the presence of pure $ZnIn_2S_4$. These results appear promising in view of the application of photocatalytic technology to organic synthesis considering that high conversion and selectivity values in H_2O (the green solvent par excellence) are obtained.

As regards the existing literature, Wang et al. [349] used layered titanate $H_{1.4}Ti_{1.65}O_4 \cdot H_2O$ as a photocatalyst obtaining a selectivity to furfural of 32.3% with a conversion of 95.9% of the alcohol but in acetonitrile used as solvent. The selectivity was 99% after a 54% conversion using benzotrifluoride, but obviously without H_2 evolution. TiO_2 allowed a fair conversion of furfuryl

alcohol, but a low selectivity to aldehyde was observed, indicating the unsuitability of the material for this reaction [56].

Table 6.2 H_2 and CO_2 production during TEOA, methanol and furfuryl alcohol reforming and furfuryl alcohol conversion (X) and selectivity (S) towards furfural and 2-furoic acid after 5h simulated solar light irradiation

Catalyst	Sacrificial agents	H_2 (mM)	CO_2 (mM)	X (%)	$S_{Furfural}$ (%)
No catalyst	TEOA	-	-	-	-
P25	TEOA	0.00	0.0140	-	-
Pt-P25	TEOA	1.22	0.0004	-	-
$ZnIn_2S_4$	TEOA	0.88	-	-	-
Pt-$ZnIn_2S_4$	TEOA	1.70	0.0003	-	-
Pt-$ZnIn_2S_4$	None (water)	-	-	-	-
P25	Methanol	0.05	0.0025	-	-
Pt-P25	Methanol	9.65	0.0591	-	-
$ZnIn_2S_4$	Methanol	0.11	0.0047	-	-
Pt- $ZnIn_2S_4$	Methanol	0.14	0.0031	-	-
P25	Furfuryl Alcohol	-	0.0145	34.1	5.10
Pt-P25	Furfuryl Alcohol	0.12	0.0251	32.2	7.90
$ZnIn_2S_4$	Furfuryl Alcohol	0.16	0.0084	48.6	81.4
Pt- $ZnIn_2S_4$	Furfuryl Alcohol	0.13	0.0026	37.3	56.0

In Figure 6.4 is reported the concentration of furfuryl alcohol, furfural, H_2 and CO_2 versus irradiation time by using bare $ZnIn_2S_4$, Pt- $ZnIn_2S_4$ and Pt-P25. While the concentration of alcohol progressively decreases, that of the formed species increases. $ZnIn_2S_4$ proved to be the most performing photocatalyst for both alcohol conversion and H_2 and furfural production.

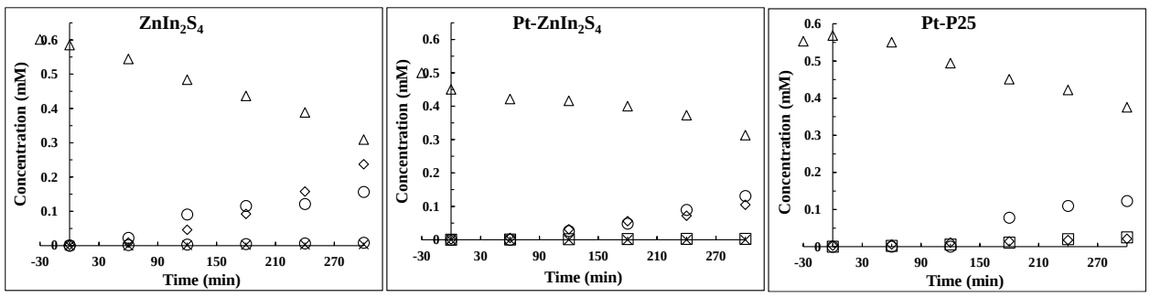

Figure 6.4 Concentrations of liquid and gaseous species versus irradiation time in the presence of $ZnIn_2S_4$ during furfuryl alcohol photoreforming. Furfuryl alcohol (△), furfural (◇), H_2 (○) and CO_2 (□)

In order to find a possible explanation for the different behaviour of P25 and $ZnIn_2S_4$ towards furfuryl alcohol, dark adsorption tests of the alcohol and the corresponding furfuryl aldehyde were performed (Table 6.3). As for alcohol, a poor adsorption was observed, estimated at about 1% mol on P25, while it was 24% mol on $ZnIn_2S_4$. This would lead to think that the occurrence of a higher conversion in the presence of $ZnIn_2S_4$ could be due at least in part to a greater adsorption of the alcohol on the latter catalyst. In this case, a more significant

mineralization would be expected since the molecule would be found in proximity to the sites where the oxidizing radical species are produced under irradiation. Therefore, the formation of a greater quantity of CO_2 and a lower selectivity towards the partial oxidation products would be favoured, in agreement with previous studies [350]. Surprisingly, however, a lower mineralization (Table 6.2) was detected with $ZnIn_2S_4$ compared to P25 and a consequent higher selectivity towards the aldehyde. Furfural adsorption, on the other hand, was practically the same on the two powders, and therefore the higher selectivity towards furfural detected with $ZnIn_2S_4$ cannot be due to its lower adsorption on the surface of this catalyst [350, 351] but to a higher productivity probably due to a lower oxidizing power of the $ZnIn_2S_4$ surface compared to that of P25 as far as the number of radicals is concerned, in addition to the favorable narrow band gap and band edge energy. As the potential energy of holes in $ZnIn_2S_4$ is more negative than that of the $H_2O/^{\bullet}OH$ couple, the photogenerated h^+ have no capability to generate the highly oxidant $^{\bullet}OH$ radicals, and therefore the oxidation of furfuryl alcohol will occur directly through the holes. The milder oxidizing power of $ZnIn_2S_4$, in fact, would reduce the succession of different oxidative steps that would lead to complete mineralization of the alcohol on P25. It should be noticed, however, that dark adsorption studies, often reported in literature to explain the photocatalytic activity of particular photocatalysts towards many molecules, although very useful, only give an indication of the tendency of the molecules to adsorb on the surface of a given solid. In fact, it is not easy to study the physical phenomena of photoadsorption-photodesorption experimentally in a quantitative way, since when they occur the irradiated photocatalyst begins to produce active species that simultaneously trigger the reaction, decreasing the quantity of the substance under examination.

Table 6.3. Adsorption runs in the dark of furfuryl alcohol and furfural on P25 and $ZnIn_2S_4$ surfaces

	Adsorption (mol%)	
Catalyst	**Furfuryl alcohol**	**Furfural**
P25	1	29
$ZnIn_2S_4$	24	31

Figures 6.5a show the degradation of furfuryl alcohol by irradiation in the presence of P25 and $ZnIn_2S_4$ and specific scavengers. The photoactivity of P25 underwent a slight variation (Figure 6.5b) following the addition of tert-butanol and sodium oxalate that trap $^{\bullet}OH$ and h^+, respectively. This implies that $^{\bullet}OH$ and h^+ play a minor role in the degradation of the alcohol. It can be noticed, instead, that after the addition of $AgNO_3$ and benzoquinone the photocatalytic activity increases. It can be assumed, therefore, that the reduction of the amount of e^- is beneficial on the photoactivity. In fact, more holes are available for the oxidation of furfuryl alcohol by trapping electrons.

By using $ZnIn_2S_4$ as photocatalyst, a slight decrease in the photoactivity was noticed in the presence of tert-butanol and $Na_2C_2O_4$, highlighting that $^{\bullet}OH$ and h^+ played a small role in the conversion of furfuryl alcohol; a slightly more significant effect has been noticed after $AgNO_3$ addition, highlighting a greater effect of e^-. The presence of scavengers naturally also influenced the H_2 production. In the case of P25, H_2 was never found, confirming the results obtained with pure TiO_2; by using $ZnIn_2S_4$, on the other hand, positive or negative variations were observed. In particular, a slight increase was recorded following the addition of $Na_2C_2O_4$ since, by consuming holes, there are a greater number of electrons available for the reduction of H^+ ions. Hydrogen was not formed in the presence of $AgNO_3$ because Ag^+ consumed electrons instead of H^+; following the elimination of hydroxyl radicals (in the presence of tert-butanol) there is a greater quantity of holes that can recombine with electrons while when benzoquinone was added, no H_2 was obtained,

because in anaerobic conditions, benzoquinone captured electrons [352]. This behaviour is confirmed by the fact that the addition of benzoquinone had the same effect as the addition of $AgNO_3$ (see Figure 6.5b).

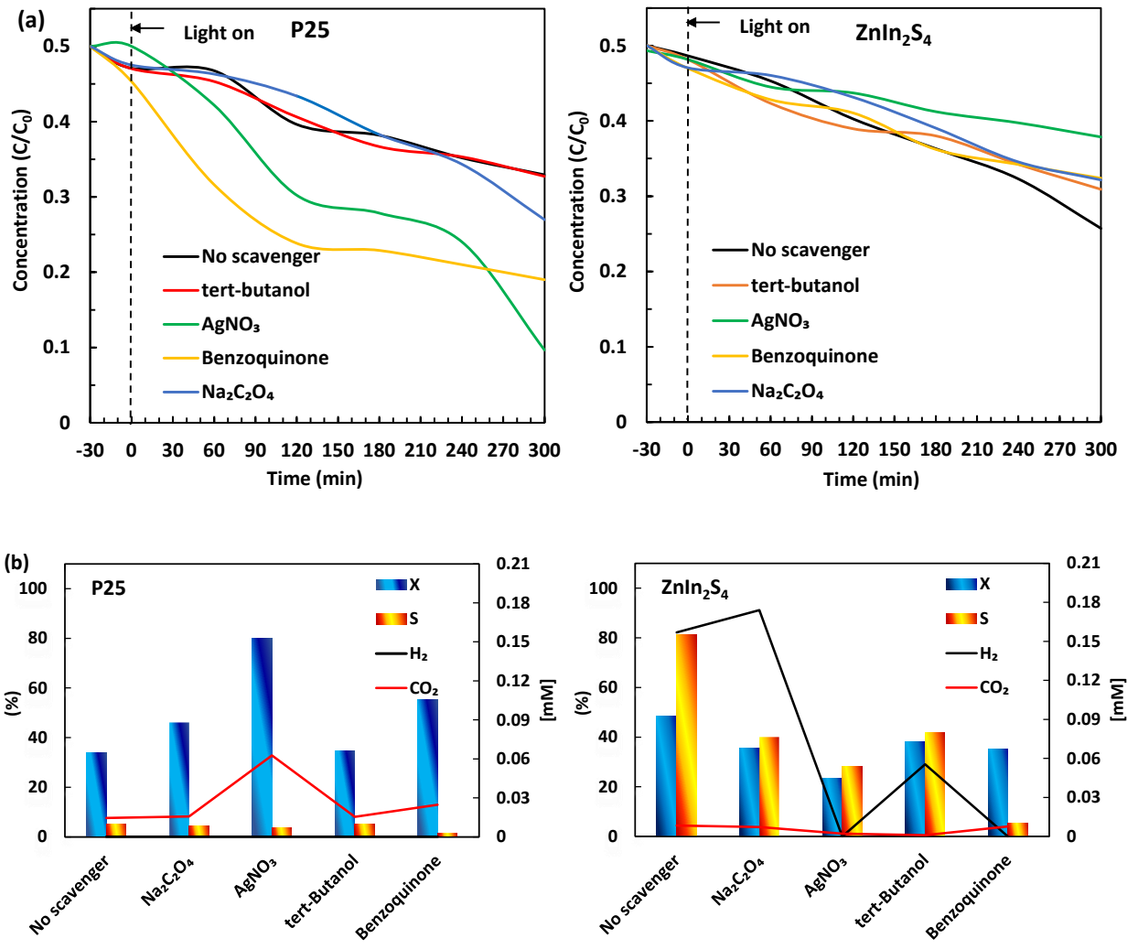

Figure 6.5. (a) Variation of furfuryl alcohol concentration *vs*. irradiation time and (b) furfuryl alcohol conversion (X), furfural selectivity (S), H_2 and CO_2 concentration after 5h of irradiation by using P25 and $ZnIn_2S_4$ in the absence and presence of scavenging species

The possible reaction scheme for the partial oxidation of furfuryl alcohol is represented in Figure 6.6. Under irradiation, holes in the valence band or $^{\bullet}OH$ react with the furfuryl alcohol and lead to the formation of furfural, which can be further oxidized to 2-furoic acid and H_2 and CO_2.

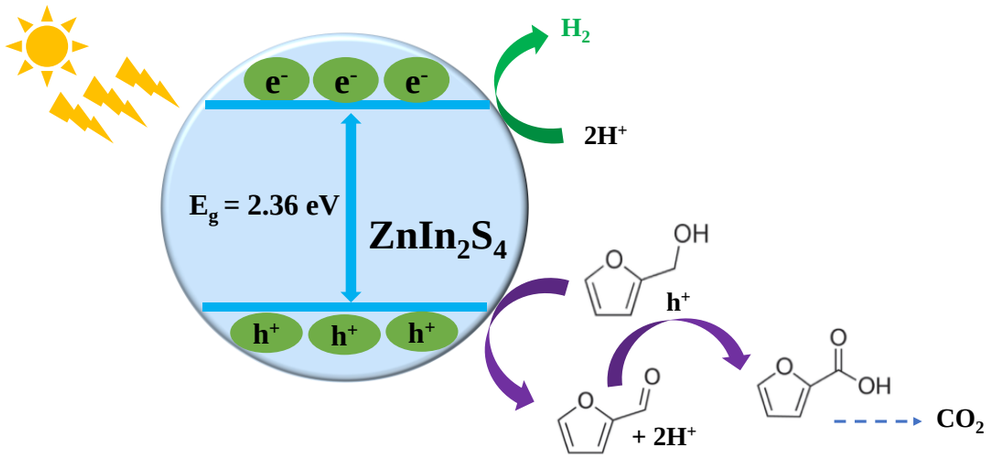

Figure 6.6. Possible simple reaction scheme for the partial oxidation of furfuryl alcohol

6.5 Conclusions

The photocatalytic activity under simulated solar light irradiation of $ZnIn_2S_4$, obtained by a simple hydrothermal method, was investigated for H_2 production from aqueous solutions containing three sacrificial agents: triethanolamine, methanol and furfuryl alcohol. High value furfural was also obtained from the partial oxidation of the last compounds. Commercial TiO_2 (P25) was used as the sake of comparison and the effect of Pt was also evaluated. Pt-P25 gave the highest H_2 production by using methanol as sacrificial agent while bare $ZnIn_2S_4$ exhibited the highest activity towards furfuryl alcohol partial oxidation affording ca. 49% and 81% conversion and furfural selectivity, respectively, along with H_2 production. These results are promising by considering the wide annual production and market price of furfural and the possible implementation of the system of the process. In fact, the high selectivity decreases the cost of extra purification allowing the use of the process on a large scale.

CHAPTER 7-I

Biomass derivatives photoreforming in pilot plant scale to obtain H_2 under green conditions by using ball milling Cu_2O-TiO_2 P25 photocatalysts

In this chapter, text is adapted from the following publication.

Muhammad Umair, Alba Ruiz-Aguirre, Ilaria Berruti, Sixto Malato Rodríguez, Leonardo Palmisano, Vittorio Loddo, Marianna Bellardita. Biomass derivatives photoreforming in pilot plant scale to obtain H_2 under green conditions by using ball milling Cu_2O-TiO_2 P25 photocatalysts. *Chemical Engineering Journal* 2025, 504, 158585. https://doi.org/10.1016/j.cej.2024.158585

CHAPTER 7-I

Biomass derivatives photoreforming in pilot plant scale to obtain H_2 under green conditions by using ball milling Cu_2O-TiO_2 P25 photocatalysts

7-I.1 Abstract

In this work the photocatalytic activity of Cu_2O-TiO_2 (P25) composites prepared by a facile ball milling method, was evaluated for solar-to-hydrogen (STH) conversion in real condition in a pilot plant scale reactor. Samples containing various Cu_2O amounts were obtained under different experimental conditions (ball milling time and rotation speed) to optimize the synthesis parameters and characterized by X-ray diffraction, scanning and transmission electron microscopy, BET specific surface area measurements and diffuse reflectance, Raman and photoluminescence spectroscopy. The composites obtained by ball milling displayed higher activity than bare TiO_2 being Cu_2O effective in replacing noble metals for H_2 production and glycerol, ethanol and glucose were used as examples of biomass derivatives. The best results were obtained by using glycerol as sacrificial agent and the sample 3%Cu_2O-P25 @150rpm **&** 2h as photocatalyst prepared by ball milling (solar-to-hydrogen, STH, conversion 1.71%). To prove the effectiveness of the ball milling method, a 3% Cu_2O-P25 sample was prepared simply by hand mixing and showed to be much less efficient.

7-I.2 Photocatalysts preparation

7-1.2.1 x%Cu_2O-P25@ y rpm & zh

The preparation method of Cu_2O-P25 has been already discussed in section 4-II.2.3.

7-I.3 Results and discussions

7-I.3.1 UV-VIS diffuse reflectance spectroscopy (DRS)

The UV-Vis DRS spectra of the bare P25 and Cu_2O samples and the coupled samples are reported in Figure 7-I.1. For bare P25, an absorbance edge is visible in the UV region at about 360 nm, which corresponds to the band gap of anatase (rutile, in fact, is present in smaller amounts), while Cu_2O which is active under visible light shows an absorption edge at about 620 nm. It can be seen that the coupled samples show almost the same shape. The addition of Cu_2O to TiO_2 resulted in low reflectance (i.e., increased absorption of visible light), demonstrating the effectiveness of the coupling strategy.

Considering the values reported in Table 7-I.1, it can be stated that the presence of Cu_2O does not influence the band gap values of the heterostructures which are similar to that of P25, being the latter the major component, but an absorbance edge between 600-650 nm attributable to Cu_2O can be observed [353]. In agreement with previous studies [301, 322] this result suggests the formation of a heterojunction between the two components.

Increasing the amount of Cu_2O % in P25 up to a certain limit (Figure 7-I.1a) and the ball mill rotation speed (Figure 7-I.1b) improves the absorbance in the visible region, while only small variations are recorded when varying the rotation time (Figure 7-I.1c). The band gap decreases with increasing ball mill speed, probably due to a better dispersion of Cu_2O in the TiO_2 matrix, but does not seem to be influenced by the ball mill mixing time.

Table 7-I.1 Band gap values of different samples used

Catalyst	Band gap (eV)
P25	3.15
Cu_2O	1.99
1%Cu_2O-P25@150rpm & 2h	3.09
2%Cu_2O-P25@150rpm & 2h	3.08
3%Cu_2O-P25@100rpm & 2h	3.18
3%Cu_2O-P25@150rpm & 2h	3.14
3%Cu_2O-P25@200rpm & 2h	3.12
3%Cu_2O-P25@150rpm & 1h	3.14
3%Cu_2O-P25@150rpm & 3h	3.14
4%Cu_2O-P25@150rpm & 2h	3.17
5%Cu_2O-P25@150rpm & 2h	3.15

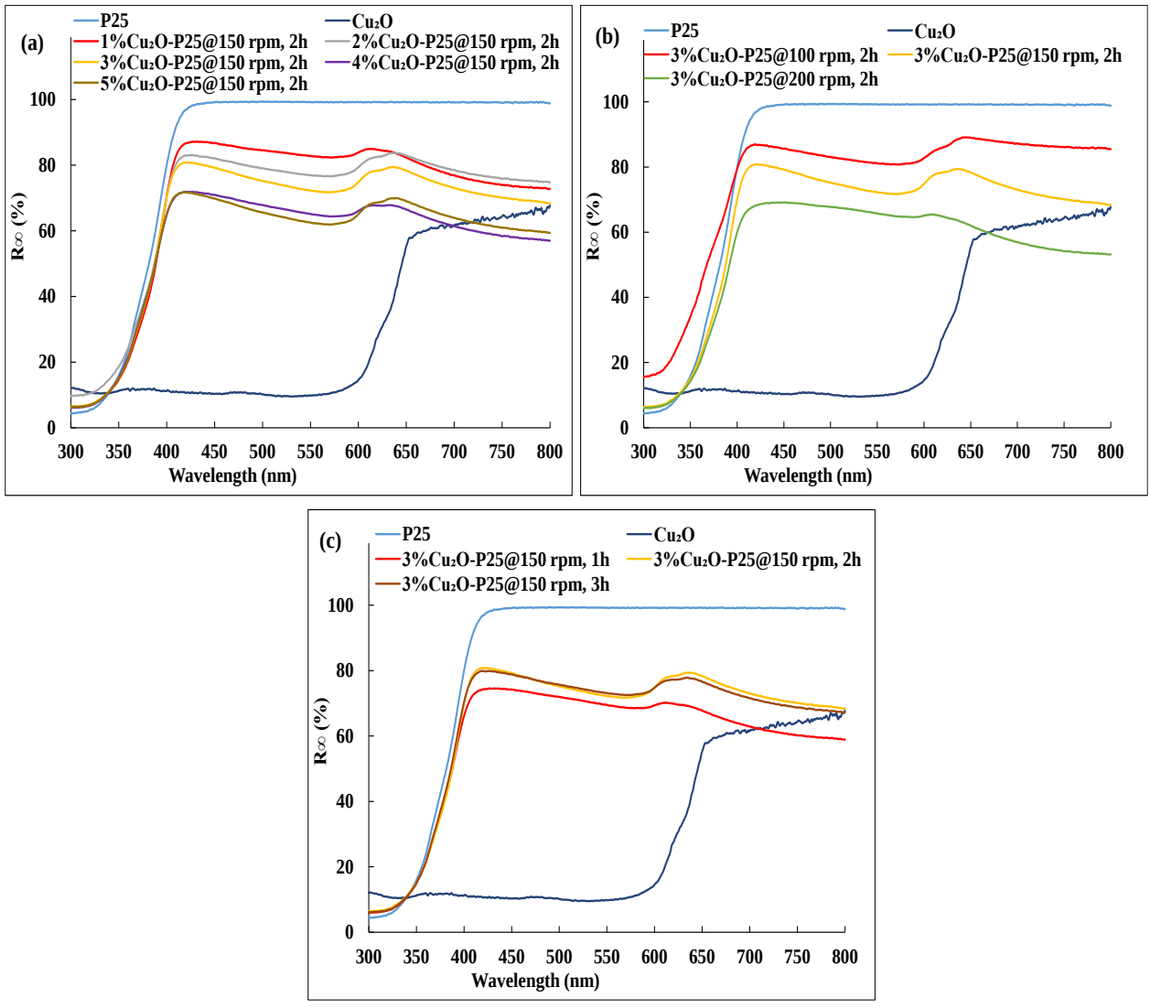

Figure 7-I.1 UV-Vis DRS spectra of the used samples

7-I.3.2 Specific surface area (SSA)

For samples P25 and 3%Cu_2O-P25@150rpm &2h, specific surface area (SSA) observed was 50 and 48 $m^2 \cdot g^{-1}$ respectively, which means the addition of small quantity of Cu_2O into TiO_2 did not modify the SSA.

7-I.3.3 X-ray diffraction (XRD)

Figure 7-I.2 shows the XRD patterns of some selected samples. The commercial P25 displays the typical peaks ascribed to anatase (at 2θ = 25.7°, 38.1°, 48.1°, 54.7°) and rutile (at 2θ = 27.6°, 36.7°, 41.4°, 54.2°, 56.5°) phases. A small peak of Cu_2O was also identified for the coupled samples at 2θ = 36.2° showing the formation of the Cu_2O-TiO_2 heterostructures.

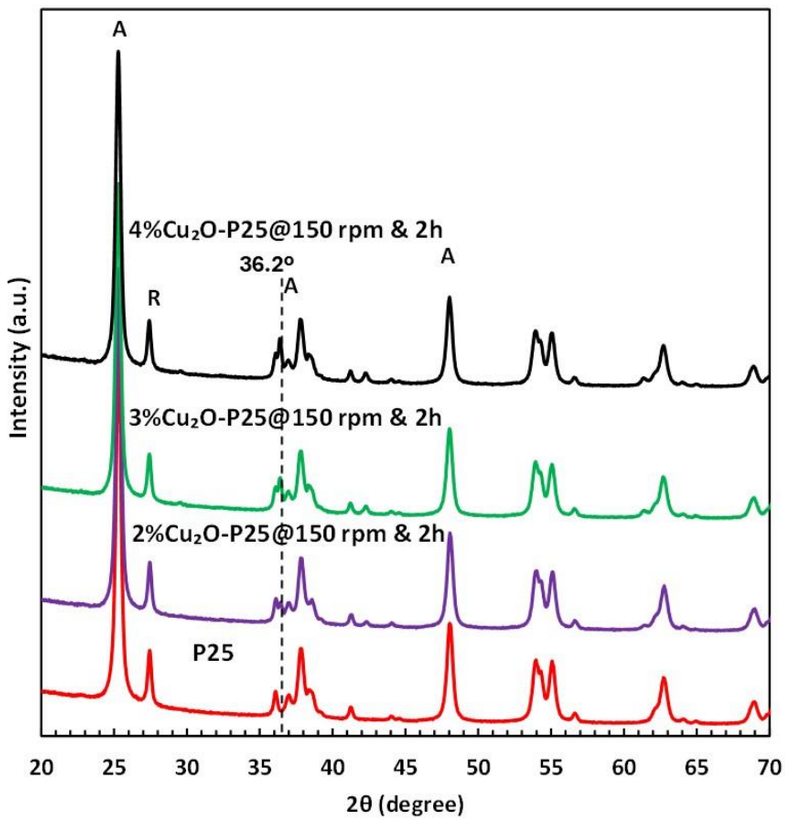

Figure 7-I.2 XRD patterns of some selected samples

7-I.3.4 Raman spectroscopy

To further investigate the powder structure, Raman spectra of some selected samples were recorded. In Figure 7-I.3, the Raman bands at 144 cm^{-1}, 197 cm^{-1}, 396 cm^{-1}, 514 cm^{-1}, and 637 cm^{-1} belong to the anatase phase, while no bands related to the rutile phase are detectable due to its lower amount compared to anatase. By increasing the amount of Cu_2O in P25, the intensity of the anatase band decreases. However, no peaks attributable to Cu_2O are observed due to its low amount and high degree of dispersion on the TiO_2 surface [73].

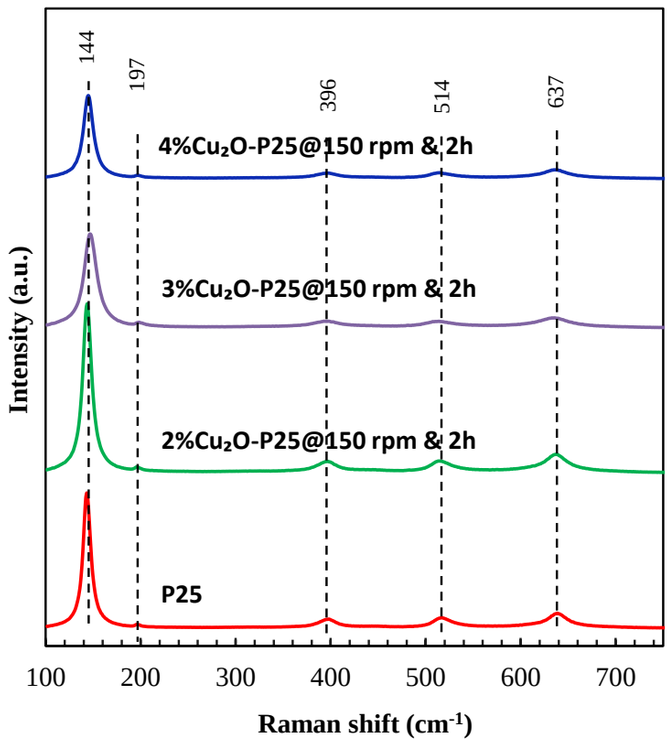

Figure 7-I.3 Raman spectra of some selected samples

7-I.3.5 Photoluminescence spectroscopy (PL)

Figure 7-I.4 shows the photoluminescence spectra of P25 and 3%Cu_2O-P25@150rpm, 2h. P25 showed the typical TiO_2 transition, at ca. 400 nm ascribed to the band-to-band emission, and between 410 and 480 nm due to a non-radiative recombination of the photo-promoted electrons towards defect levels [301]. After the addition of Cu_2O into TiO_2, a decrease in intensity can be observed, due to a lower recombination rate of photogenerated electron-hole pairs that leads to enhanced efficiency towards H_2 generation [289]. Moreover, in the presence of Cu_2O the peaks are shifted towards higher wavelengths due to the enhanced absorption in the visible range. The band at ca. 540 nm is attributable to the band-to-band emission of Cu_2O.

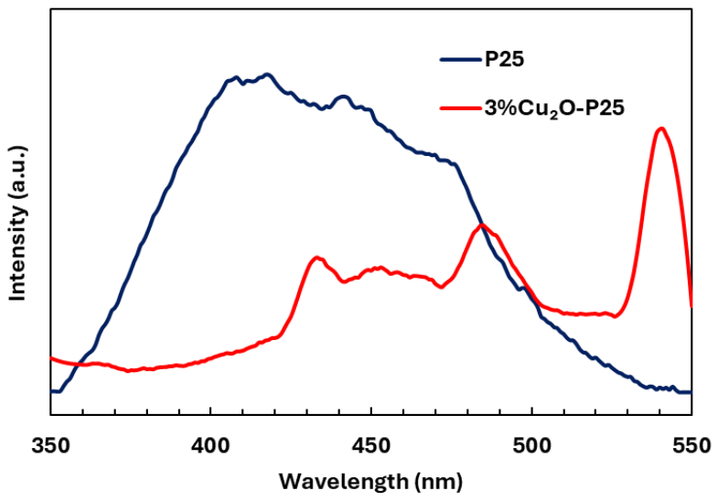

Figure 7-I.4 Photoluminescence spectra of P25 and 3%Cu_2O-P25@150rpm, 2h

7-I.3.6 Morphology

To study the morphology and distribution of different oxides and particle sizes, SEM and TEM images were acquired. Figure 7-I.5 (a, b) shows the SEM images of P25 and 3%Cu_2O-P25@150rpm, 2h. These samples display aggregates of irregular roundish shapes with sizes in the

20-130 nm range. The morphology of 3%Cu_2O-P25@150rpm, 2h is very similar to that of P25 due to the low amount of Cu_2O and good mixing in the TiO_2 matrix by ball milling.

In Figure 7-I.5(c), the TEM image of 3%Cu2O-P25@150rpm indicates the presence of Cu_2O as black spheres on the TiO_2 surface, confirming the effectiveness of the ball milling method in forming heterostructured samples. The particle sizes of Cu_2O are in the range of 5–10 nm, while those of TiO_2 are in the range of 5–25 nm.

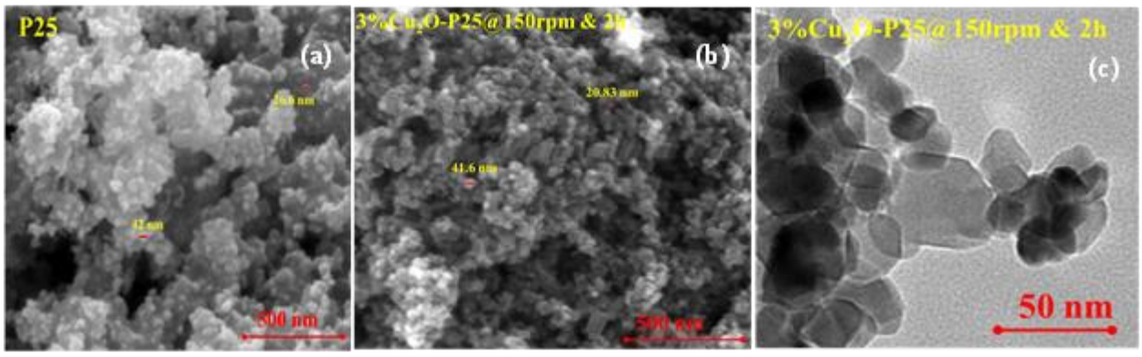

Figure 7-I.5 SEM images of (a) P25, and (b) 3%Cu_2O-P25@150rpm, 2h and (c) TEM image of 3%Cu_2O-P25@150rpm

7-I.4 Photocatalytic activity

The effect of the addition of Cu_2O to TiO_2 photocatalyst was tested for different loading of this metal oxide (from 1 to 5 %). Table 7-I.2 shows the H_2 production (mmol) for each percentage of copper oxide for a H_{UV} of 440 $\pm$ 10 $kJ \cdot m^{-2}$. H_2 production increased between 69% and 84% compared to using TiO_2 alone as can also be seen by observing the results reported in Table 7-I.2. At higher H_{UV} (H_{UV} of 760 $kJ \cdot m^{-2}$, Figure 7-I.6a) the maximum H_2 production, obtained with the sample 3%Cu_2O-P25@150rpm & 2h, was approximately 94 mmol which was 6 times greater than that of pure P25. Loading values above 3% could prevent light radiation from reaching the outer surface of the TiO_2 and thus the absorption of photons which is crucial for the high-energy reactions. In other words, excessive Cu_2O loading reduces the available active sites on the TiO_2 surface and may increase the number of Cu^o species. This makes e^-/h^+ transfer more difficult, favouring their recombination.

The production rate of H_2 under UV-visible light irradiation is negatively affected by the variation of ball milling parameters. By setting the optimum ratio of 3%Cu_2O-P25, the catalysts were prepared at different speeds ranging from 100 to 200 rpm and time intervals of 1 and 3 h to study the influence of these parameters on the H_2 production (Table 7-I.2). The H_2 formation at 150 rpm was about 1.3 and 2 times greater than the samples prepared at 100 rpm (STH of 1.4%) and 200 rpm (STH of 0.89%), respectively. Thus, the optimum speed found in this study considering the range from 100 rpm to 200 rpm was 150 rpm.

The milling speed influences the efficiency of photocatalysts because the mechanical forces exerted on the material vary and consequently some important characteristics of photocatalysts such as particle size, surface area, defect formation, crystallinity and homogeneity are affected. In particular, an increase in speed causes more intense collisions that can give rise to particle aggregation with consequent lower efficiency at maximum rpm. Too low speed would instead result in a lower photocatalytic efficiency since the mechanical forces may not be sufficient to induce a reduction in particle size which is generally always beneficial for photoactivity due to the increase in surface area, all other things being equal.

As for the number of defects and crystallinity, higher speeds can induce the formation of defects in lattice structure of photocatalysts such as dislocations and grain boundaries. However, the number of defects should be optimized since some defects have a beneficial effect that

increases the activity by trapping electrons-holes and reducing their recombination, while an excess of them decreases the crystallinity and electron mobility, causing the contrary detrimental effect of decreased efficiency. A lower milling speed, although it preserves crystallinity, does not favour the formation of a sufficient number of defects and consequently the charge separation is reduced.

Another factor influenced by speed is the homogeneity of the photocatalysts used. Higher speeds lead to a more uniform distribution of the active sites, which is advantageous, while lower speeds have an adverse effect that can lead to incomplete incorporation of the active phases.

Therefore, it can be inferred from the above that the ball milling speed should be optimized to achieve a balance between the discussed parameters and properties. In this study, the intermediate speed was found to be the optimal speed. Although the ball milling time parameter was found to be less important than the milling speed, Table 7-I.2 shows that even for the time, the intermediate one was the best option. For example, 3%Cu_2O-P25 samples prepared at the same ball milling speed, i.e., 150 rpm, but at varying mixing times of 1 h (STH of 1.45%) and 3 h (STH of 1.56%) showed almost the same activity, but this was lower than that shown by the sample prepared with an intermediate time of 2 h. The 3%Cu_2O-P25 sample prepared in 2 h showed 16% and 9% higher photoactivity than the samples prepared in 1 h and 3 h, respectively. The milling time has an influence on the same parameters as the speed, following the same trend. That is, excessively long milling may cause agglomeration of the material with a reduction in surface area, while too short times may be insufficient to reduce the particle size negatively affecting the presence of active sites. However, optimal milling times lead to an appropriate decrease in particle size with the achievement of a surface area where more active sites are present to interact with light.

Amorphization can also be induced by ball milling time. When the ball milling time is too long, the crystalline structure can become amorphous, and the material's ability to absorb light effectively is reduced. The number of defects can also be controlled by the ball milling time. They act as active sites, improving efficiency, but too many defects, as mentioned before, could act as electron-hole recombination centers, causing the opposite effect. Therefore, finding an optimal ball milling time is crucial because one must limit the reduction in particle size, while preserving the crystalline structure, but also prevent excessive agglomeration by maintaining a sufficient number of active sites.

Table 7-I.2 Comparison of H_2 production with different sacrificial agents and catalysts used for H_{UV} of 440 + 10 kJ·m^2 (100 mg·L^{-1} photocatalyst)

Sample	Sacrificial agent	Initial Concentration (M)	H_2 (mmol)
P25	Glycerol	0.075	9.28
Effect of Cu_2O %			
1%Cu_2O-P25@150rpm & 2h	Glycerol	0.075	29.87
2%Cu_2O-P25@150rpm & 2h	Glycerol	0.075	36.80
3%Cu_2O-P25@150rpm & 2h	**Glycerol**	**0.075**	**56.59**
3%Cu_2O-P25@150rpm & 2h	Glycerol	0.05	39.2
4%Cu_2O-P25@150rpm & 2h	Glycerol	0.075	45.78
5%Cu_2O-P25@150rpm & 2h	Glycerol	0.075	42.70
Effect of ball milling parameters			
3%Cu_2O-P25@100rpm & 2h	Glycerol	0.075	44.18
3%Cu_2O-P25@200rpm & 2h	Glycerol	0.075	27.91
3%Cu_2O-P25@150rpm & 1h	Glycerol	0.075	47.54
3%Cu_2O-P25@150rpm & 3h	Glycerol	0.075	51.31
3%Cu_2O-P25 (Hand mixing)	Glycerol	0.075	32.56
Effect of sacrificial agents			
3%Cu_2O-P25@150rpm & 2h	Glycerol	**0.075**	**56.59**
3%Cu_2O-P25@150rpm & 2h	Ethanol	0.1125	17.63
3%Cu_2O-P25@150rpm & 2h	Glucose	0.0375	20.96

Finally, the efficiency of the ball milling method in the preparation of coupled photocatalysts was verified by comparing the activity of 3%Cu_2O-P25 prepared at 150 rpm for 2 h with that of a photocatalyst based on the same material, i.e., Cu_2O and TiO_2 with 3% copper(I) oxide, but simply mixed by hand.

Figure 7-I.6(a) shows that the H_2 production obtained with the ball-milled photocatalyst is about 42% higher than that with the hand-mixed photocatalyst. As mentioned above, the mechanical forces generated during the ball-milling treatment can be useful to create a situation where the lattice defects, surface area, crystallinity and homogeneity of the photocatalysts are optimal for the reaction of interest, at least in the chosen range of experimental conditions. Furthermore, the higher activity of the manually mixed 3%Cu_2O-P25 sample compared to bare P25 (see Fig. 7.2a) indicates that deep contact between Cu_2O and TiO_2 can be created by a simple manual mixing procedure, but a vigorous mechanical ball milling allows to obtain significantly higher H_2 production.

It should be noted that the best photocatalyst found in this study, i.e. 3%Cu_2O-P25@150 rpm & 2h, so far shows a higher H_2 production than the hand-mixed TiO_2-CuO based photocatalysts presented in the literature [354]. The lower activity of CuO-TiO_2 composites can be attributed to the CB energy of CuO which is less negative than that of TiO_2 and, consequently, energetically less favorable for H_2 production [301, 355].

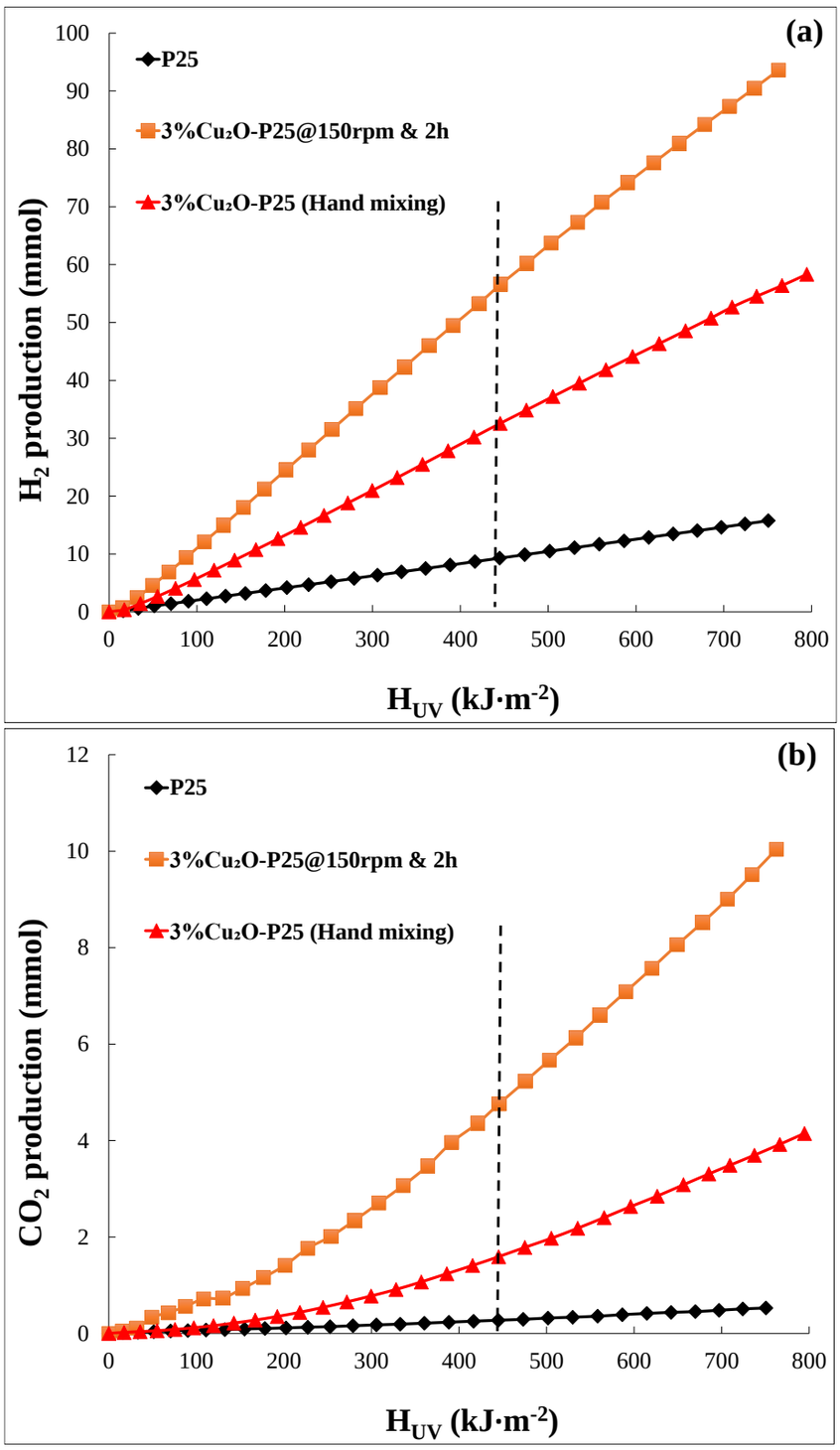

Figure 7-I.6 Production of (a) H_2 (b) CO_2 with P25, 3%Cu_2O-P25@150 rpm, 2h, and 3%Cu_2O-P25 (hand mixing) (Glycerol 0.075 M, 100 mg·L^{-1} photocatalyst)

Furthermore, the best sample (3%Cu_2O-P25@150 rpm and 2h) was tested with a lower concentration of glycerol (0.05 M) to study the effect of sacrificial agent concentration on H_2 production. Table 7-I.2 shows that lowering the glycerol concentration also reduced the amount of H_2 produced and the relative STH (1.26%, that was 31% less than STH obtained starting from 0.075 M of glycerol).

It is also useful to evaluate the influence of different sacrificial agents on H_2 production. In this regard, the best photocatalyst, 3%Cu_2O-P25@150 rpm & 2h, was used for the photoreforming of two alcohols, i.e., glycerol and ethanol and a monosaccharide, i.e., glucose. The concentrations of other substrates were determined by considering the total number of carbon atoms present in 0.075M of glycerol solution.

The H_2 production after 5 hs of solar irradiation in the presence of the different sacrificial agents was in the following order (see Table 7-I.2): glycerol (56.59 mmol) > glucose (20.96 mmol) > ethanol (17.63 mmol).

It is not easy to explain, even qualitatively, the differences in photoactivity between different organic molecules. It must be considered in general terms that their reactivity with the holes generated by solar light is influenced both by the nucleophilicity of the groups present in their molecular structure and by their adsorption capacity on the catalyst surface.

Glycerol has some characteristics that may make it a better option as a sacrificial agent. One of these is its low redox potential, which indicates its high tendency, greater than that of glucose and ethanol, to release electrons and undergo oxidation to CO_2.

Compared to glucose, glycerol has a simpler chemical structure that also favours its oxidation, resulting in a faster transfer of electrons to be used in the reduction of protons to produce H_2. Glucose, on the other hand, has a more complicated oxidation pathway, which slows down the reactions. In fact, the hydroxyl groups present in the glycerol molecule are easily oxidized, accelerating the rate of H_2 production. The complexity of the glucose molecule, on the other hand, gives rise to intermediates that can adsorb on the catalyst surface, blocking its active sites. In the case of ethanol, only one hydroxyl group is present, while in glycerol there are three groups. This can justify the higher H_2 production.

Additionally, for each experiment, liquid samples from the reaction mixture were also analyzed and showed the formation of short chain carboxylic acids or their anionic conjugate base (Figure 7-I.7), i.e., formic acid from photoreforming of glycerol before complete mineralization in CO_2, glycolate and formate from glucose and acetate (no formate was detected in water) from ethanol. The concentration of carboxylic acids versus H_{UV} resulting from photoreforming of different sacrificial agents in the presence of 3%Cu_2O-P25@150 rpm & 2h as photocatalyst is shown in Figure 7-I.7.

It can be said that the formed intermediates rapidly transform into formic acid, and the CO_2 evolved during the reaction (Figure 7-I.6b) indicates the occurrence of a certain degree of mineralization of the sacrificial agents. The CO_2 evolved in the presence of 3%Cu_2O-P25@150 rpm & 2h, 3%Cu_2O-P25 (hand mixing) and P25 at 440 kJ·m^2 was 4.8 mmol, 1.6 mmol and 0.3 mmol, respectively, starting from an inzial glycerol concentration of 0.075 M.

During the reaction, dissolved organic carbon (DOC) decreased (e.g. in the case of glucose, the initial and final values were 663 and 615 mg L^{-1}). The initial pH of the reaction mixture was about 6, and after 5 h of reaction it decreased to about 3, suggesting the degradation of the initial substrates into carboxylic acids.

The temperature inside the reactor increased from about 22.1 ºC (1st, 10:30 AM) to about 45 ºC (after 5 h, 03:30 PM). Although the temperature increase is not high, a catalytic effect on photoactivity cannot be ruled out. However, a more detailed study of the influence of temperature is beyond the scope of the present work, which aims mainly to highlight the effectiveness of cheap, easy-to-prepare, noble-metal-free photocatalysts in green H_2 production in pilot-scale reactors under solar irradiation.

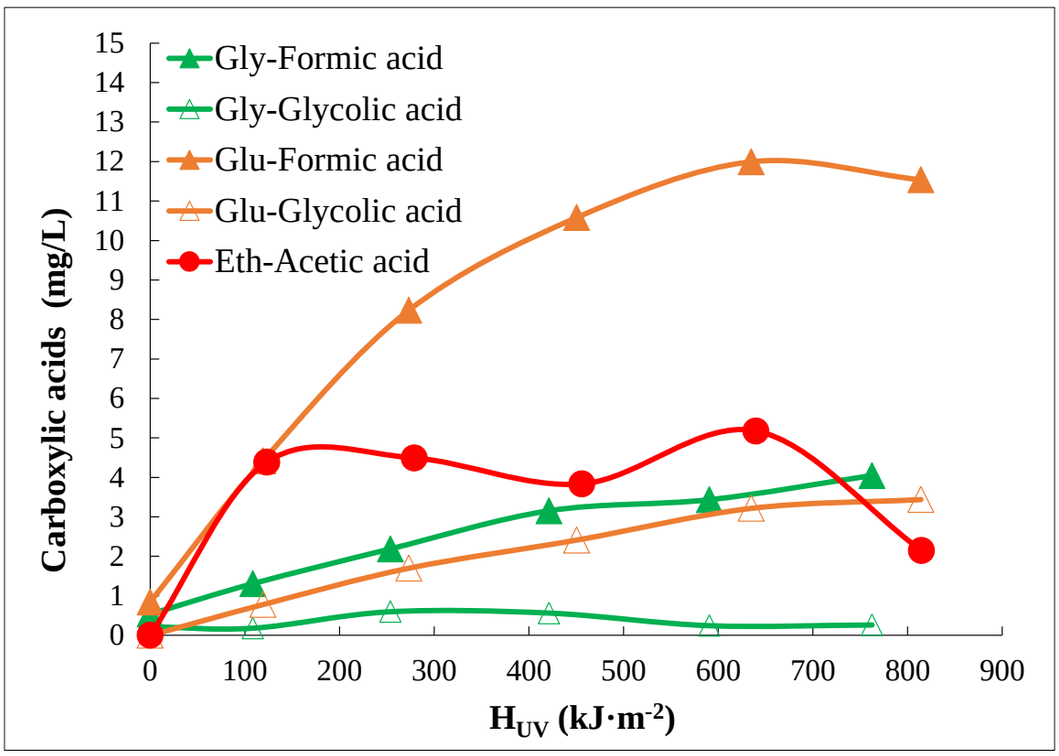

Figure 7-I.7 Formation of carboxylic acids by photoreforming of different sacrificial agents with 3%Cu_2O-P25@150 rpm & 2h. (Legend: Gly= glycerol, Glu= glucose, Eth= ethanol)

Table 7-I.3 shows the copper species leaching results at the first hour and an average value for the last 4 h of reaction time with ball-milled samples (3%Cu_2O-P25@100 rpm & 2h) and simply mixed by hand. The production of organic acids during the photoreforming reaction of glycerol can facilitate the partial dissolution of copper oxides [356]. During the photocatalytic reaction, Cu_2O probably acts as an electron sink that causes the reduction reaction by promoting significant Cu species leaching. With the ball mill sample, the copper leaching was 2 times higher than with the simply mixed catalyst, probably due to higher activity than the hand-mixed sample and consequently the higher amount of reduced copper. This research would be considered as an initial roadmap because metal leaching is a critical problem that should be avoided during large-scale applications through the preparation of catalysts with good stability.

Table 7-I.3 Cu leached % during the photocatalytic reaction

Time (h)	**3 % Cu_2O-P25 @150rpm and 2h %**	**3 % Cu_2O-P25 (Hand mixing) %**
	(0.05 M Glycerol)	(0.075 M Glycerol)
1	22.57	11.21
4-5	48.09	25.35

7-I.5 Proposed reaction mechanism

The reaction mechanism proposed in Figure 7-I.8 takes into account the existence of a Cu_2O-TiO_2 p-n heterojunction where Cu_2O plays the role of an energetic antenna due to its ability to absorb energy only in the visible region [357]. Both the CB and the VB of Cu_2O are energetically positioned above the CB and the VB of TiO_2, respectively. Under solar irradiation both semiconductors are activated (Equations 7-I.1 and 7-I.2) to produce electrons and holes, and after their generation electrons transfer from the CB of Cu_2O to the CB of TiO_2 and are subsequently captured by adsorbed protons that transform into H_2 (reduction reaction) (Equation 7-I.3).

At the same time, the holes formed in the VB of TiO_2 transfer to the VB of Cu_2O and react with the adsorbed organic species to produce by-products and protons (Equation 7-I.4) (oxidation reaction) [358]. It cannot be excluded that some of the electrons in the CB of TiO_2 recombine with the holes in the VB of Cu_2O via a Z-scheme mechanism [301] and holes react with H_2O to produce hydroxyl radicals and H^+ (Equation 7-I.5) that contribute to H_2 formation, in accordance with literature [333, 359].

$$Cu_2O + hv \rightarrow h^+ + e^- \quad (7\text{-I.1})$$

$$TiO_2 + hv \rightarrow h^+ + e^- \quad (7\text{-I.2})$$

$$2H^+ + 2e^- \rightarrow H_2 \quad \text{(Reduction)} \quad (7\text{-I.3})$$

$$Sacrificial\ agent + h^+ \rightarrow Byproduct + H^+ \quad \text{(Oxidation)} \quad (7\text{-I.4})$$

$$H_2O + h^+ \rightarrow {}^{\cdot}OH + H^+ \quad \text{(Oxidation)} \quad (7\text{-I.5})$$

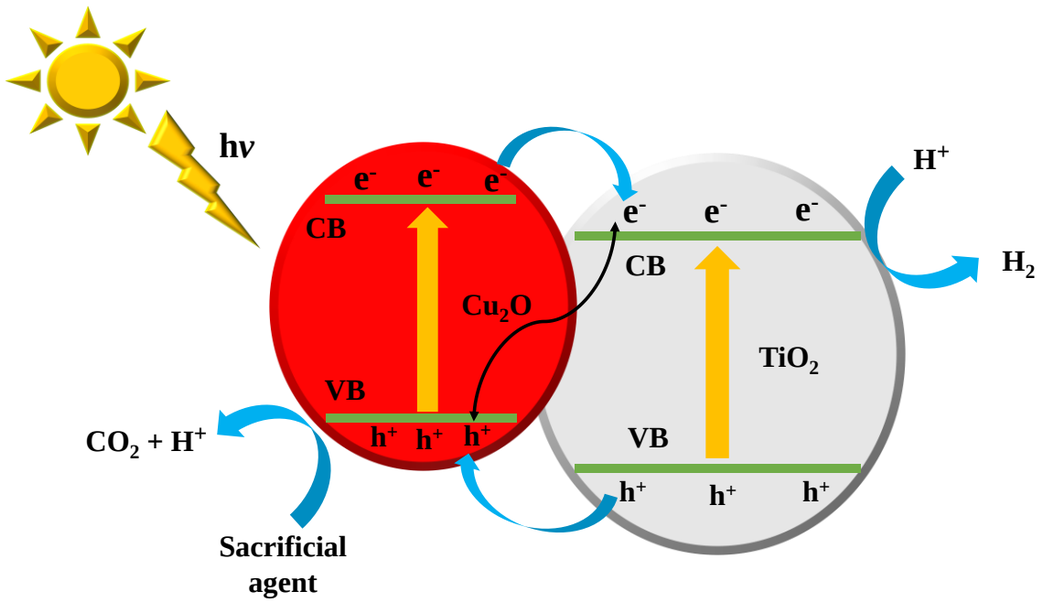

Figure 7-I.8 Proposed reaction mechanism for H_2 production under direct sun light through p-n heterojunction Cu_2O-TiO_2

7-I.6 Conclusions

The coupled Cu_2O-TiO_2 photocatalysts were prepared by a simple ball milling procedure under different experimental conditions: different weight ratios, ball mill rotation rates and rotation times. The photocatalytic activity of the samples was evaluated under sunlight irradiation in a pilot-scale reactor for photoreforming different sacrificial agents, namely glycerol, glucose and ethanol. The ball milling method was shown to be a cost-effective and efficient method for the preparation of active Cu_2O-TiO_2 heterostructures for H_2 production.

Cu_2O was effective in shifting the absorption of photocatalysts into the solar wavelength range. This material allows to replace noble metals in the solar-to-hydrogen (STH) conversion process. Optimization of the synthesis parameters allowed to obtain very active samples. The best photocatalyst was 3% Cu_2O-P25 @150rpm & 2h in the presence of glycerol as sacrificial agent, which showed a H_2 production of about 94 mmol (STH of 1.7%) at H_{UV} of 760 $kJ \cdot m^{-2}$ in 5 h. This amount was about 6 times higher than that obtained in the presence of bare P25 under the same experimental conditions.

CHAPTER 7-II

Investigating the photoactivity of Cu_2O-TiO_2 (Home Prepared) composites for H_2 production by photoreforming under natural solar light in a pilot plant photoreactor

In this chapter, text is adapted from the following publication.

Muhammad Umair, Alba Ruiz Aguirre, Ilaria Berruti, Leonardo Palmisano, Sixto Malato Rodríguez, Vittorio Loddo, Marianna Bellardita. Investigating the photoactivity of Cu_2O-TiO_2 (Home Prepared) composites for H_2 production by photoreforming under natural solar light in a pilot plant photoreactor. *Internation Journal of Hydrogen Energy*. Under review.

CHAPTER 7-II

Investigating the photoactivity of Cu_2O-TiO_2 (Home Prepared) composites for H_2 production by photoreforming under natural solar light in a pilot plant photoreactor

7-II.1 Abstract

In this work TiO_2 constituted of an anatase/rutile mixture was synthesized by a precipitation method and coupled with different Cu_2O amounts by a simple ball method technique. The samples were characterized by UV-Vis diffuse spectroscopy (DRS), specific surface area (SSA) determination, photoluminescence (PL) and Raman spectra, X-ray diffraction (XRD), scanning electron microscopy (SEM), transmission electron microscopy (TEM), and X-ray photoelectron spectroscopy (XPS). The photocatalytic activity was studied for H_2 production under natural solar light irradiation in a pilot plant reactor in the presence of different sacrificial agents (formic acid, glucose, ethanol, glycerol). The results showed that the coupled samples were photoactive and an effective heterojunction, that enhanced the charges transfer processes, was formed between the components. 3%Cu_2O-TiO_2 was the most active photocatalyst and the presence of Cu_2O (instead of the noble metals generally used) was efficient for H_2 production with 62 mmol obtained after 5h of solar irradiation starting from glycerol, which yielded the highest H_2 amount with respect to the other sacrificial agents.Copper was present in different oxidation states and a certain amount of leaching of Cu species was observed. Holes, $OH^{\bullet}$ and $O_2^{\bullet-}$ radicals were the main active species for glycerol degradation while a higher availability of photoproduced electrons was beneficial for H_2 production.

7-II.2 Photocatalysts preparation

7-II.2.1 TiO_2 HP

The preparation method of TiO_2 HP has been discussed in section 4-I.2.1.

7-II.2.2 Cu_2O-TiO_2 HP

The preparation method of Cu_2O- TiO_2 HP has been already discussed in section 4-II.2.3.

7-II.3 Results and discussions

7-II.3.1 UV-VIS diffuse reflectance spectroscopy (DRS)

Figure 7-II.1A shows the UV-Vis DRS spectra of the samples used. Cu_2O showed absorbance only in the visible range while HP-TiO_2 sample is active in the UV-Vis region with a transition edge at ca. 340 nm and a significant light absorption in the range 400-650 nm, ascribable to the presence of oxygen vacancies In the composite samples, an increase in absorbance by increasing Cu_2O from 1 to 5%, samples showed an increased light absorption at higher wavelengths and a second absorption edge associated to Cu_2O. The band gap values of the samples were determined by plotting the modified Kubelka-Munk function, $[F(R'_\infty)h\nu]^{½}$, versus the energy of the exciting light ($h\nu$) (Figure 7-II.1B). Cu_2O showed a band gap of 1.97 eV while in the presence of Cu_2O the TiO_2 band gap remained unchanged and a transition, coincident with the hosted oxide, can be observed. The presence of the two edges suggests the formation of a heterostructure between the two oxides [301, 322].

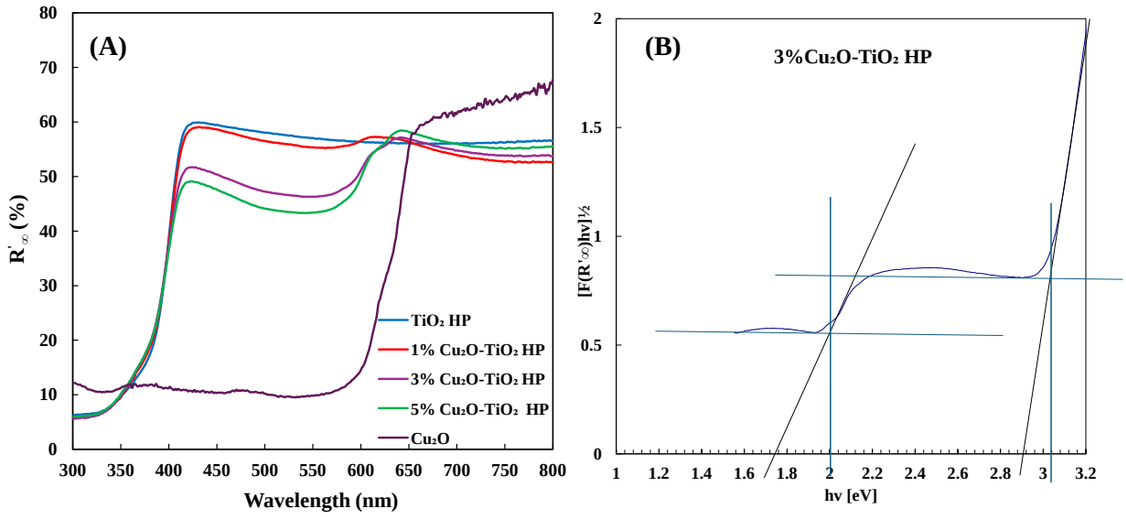

Figure 7-II.1 UV-Vis DRS spectra of the used samples (A); band bap determination (B)

7-II.3.2 Specific surface area (SSA)

Table 7-II.1 shows the band gap values and SSA of the used samples. SAA of TiO_2 HP was 78 $m^2 \cdot g^{-1}$ and with 3%Cu_2O-TiO_2 HP decreased to 69 $m^2 \cdot g^{-1}$.

Table 7-II.1 Band gap values and SSA of the used photocatalysts

Samples	Band gap (eV)	SSA ($m^2 \cdot g^{-1}$)
TiO_2 HP	3.03	78
1%Cu_2O-TiO_2 HP	3.02	72
3%Cu_2O-TiO_2 HP	3.02	69
5%Cu_2O-TiO_2 HP	3.03	68
Cu_2O	1.97	1

7-II.3.3 X-ray diffraction (XRD)

Figure 7-II.2A represents the XRD diffractograms of TiO_2 HP and 3%Cu_2O-TiO_2 HP. TiO_2 HP consists of a mixture of anatase (main peak at 2θ = 25.28◦) and rutile (main peak at 2θ = 27.53 ◦). After the addition of Cu_2O, two peaks were also recorded at 2θ = 36.5° and 42.4° corresponding to the crystal planes of (111) and (200) of Cu_2O respectively, in agreement with the literature [360].

7-II.3.4 Raman spectroscopy

In Figure 7-II.2B the Raman spectra of bare TiO_2 and its composite with 3%Cu_2O are reported. In the TiO_2 sample, only the characteristic anatase bands at 144 cm^{-1}, 197 cm^{-1}, 396 cm^{-1}, 514 cm^{-1} and 637 cm^{-1} are visible, whilst no band attributable to rutile are present due to its lower content with respect to anatase. In 3%Cu_2O-TiO_2 HP no peaks of Cu_2O were observed, probably due to the low amount and high degree of dispersion on TiO_2 surface. However, by enlarging the main anatase peak associated with the O-Ti-O vibration (inset of Figure 7-II.2B), a slight red shift, attributable to a bond distortion into the TiO_2 lattice, can be noticed [361]. This finding confirms an interaction between TiO_2 and Cu_2O in the composite samples.

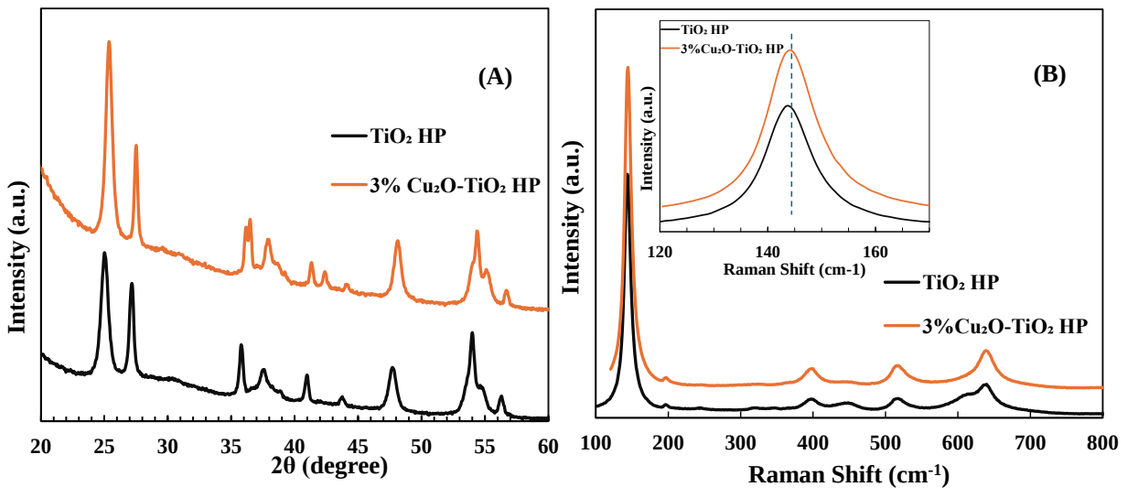

Figure 7-II.2 XRD patterns (A) and Raman spectra (B) of TiO_2 HP and 3%Cu_2O-TiO_2 HP samples.

7-II.3.5 Photoluminescence spectroscopy (PL)

In Figure 7-II.3 the photoluminescence spectra of selected samples are reported. TiO_2 presents different emission peaks: the one at ca. 420 nm derives from to the band-to-band emission, the peaks at higher wavelengths are ascribed to the non-radiative recombination of the photo-promoted electrons towards defect levels [291]. The coupling with Cu_2O causes a reduction in the photoluminescence intensity due to a decrease in the recombination rate of the photogenerated charges [301].

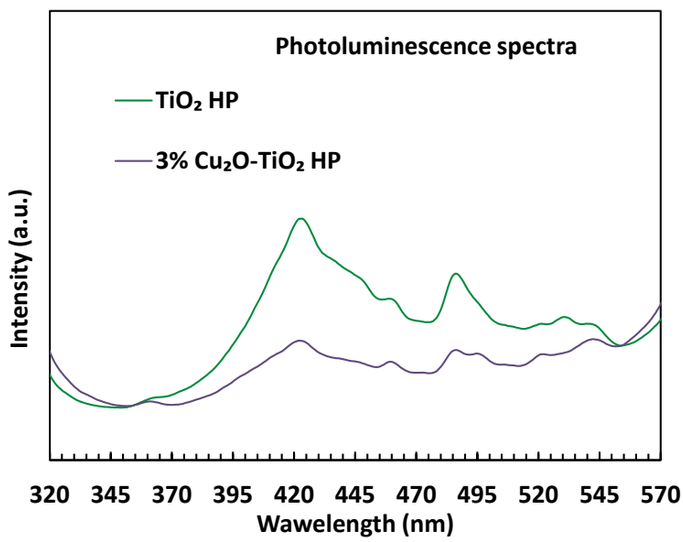

Figure 7-II.3 Photoluminescence spectra of TiO_2 HP and 3%Cu_2O-TiO_2 HP powders

7-II.3.6 Morphology

Figure 7-II.4 (A, B) shows the SEM images of TiO_2 and 3%Cu_2O-TiO_2 HP powders. Irregular roundish shaped aggregates with a size ranging from 20 to 130 nm were observed in TiO_2 and, no change in morphology was observed after the addition of Cu_2O, probably due to the low amount and proper mixing into TiO_2 matrix. TEM image was also acquired to study the distribution of components and particles dimensions. In Figure 7-II.4 (C), Cu_2O showed particle size ranges between 5 and 10 nm while size of TiO_2 HP (anatase) ranged between 5 and 25 nm. The lattice fringes of the (101) plane of TiO_2 HP (anatase) are ca. 0.35 nm while those of Cu_2O (200) plane are ca. 0.22 nm.

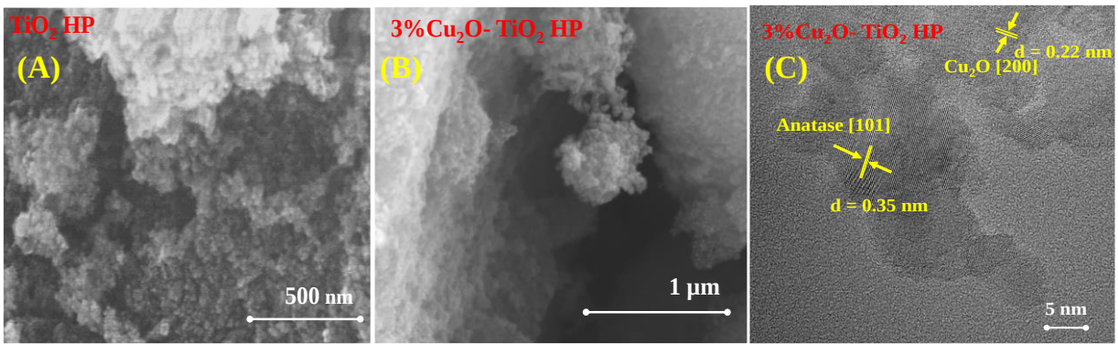

Figure 7-II.4 SEM images of TiO_2 HP (A), 3%Cu_2O-TiO_2 HP (B) and TEM image of 3%Cu_2O-TiO_2 HP (C)

7-II.4 Photocatalytic activity

The experiments were carried out in a pilot plant CPC photoreactor under direct sunlight and at the natural pH of the systems containing the photocatalysts and the different sacrificial compounds. The optimal amount of the catalyst was found to be 100 $mg \cdot L^{-1}$ and glycerol concentration 0.075M. The influence of different Cu_2O percentages in TiO_2 was evaluated by the photoreforming of glycerol, and then under the best conditions, the photoactivity between the other sacrificial agents such as formic acid, ethanol, and glucose was compared. Glycerol was chosen because of its low redox potential and wide availability. Bare TiO_2 is inactive for H_2 generation, thus Cu_2O was introduced to improve photoactivity. In Figure 7-II.5, the amount of produced hydrogen is plotted versus the radiant energy received by the photoreactor surface. No H_2 formation was observed with the two bare photocatalysts; in the presence of 1%Cu_2O-TiO_2 HP a H_2 generation of 42.2 mmol (STH of 0.86%) was obtained, suggesting the effectiveness of Cu_2O-TiO_2 heterostructure [301]. The increase of Cu_2O loading into TiO_2 has a positive effect on H_2 generation. Indeed, the amount of H_2 generated with a 3%Cu_2O-TiO_2 HP sample was 53.1 mmol (STH of 1.10%), 26% higher than that of 1%Cu_2O-TiO_2 HP. By further increasing the amount of Cu_2O into TiO_2, however, H_2 production decreased, being the H_2 amount generated with 5%Cu_2O-TiO_2 HP 48.3 mmol (STH of 0.99%) as shown in Figure 7-II.5. Therefore, an optimal ratio between the two components is essential to have high efficiency. It can be noticed that at a lower percentage, there were not enough Cu_2O nanoparticles to improve photocatalytic activity by providing active sites. It seemed that 3% Cu_2O proved to be the optimal amount to provide a balance between surface area and active sites of Cu_2O interacting with TiO_2 and ultimately increased H_2 generation. However, with a further increase of Cu_2O, particles started to form agglomerates and Cu_2O-TiO_2 heterojunction became less effective. Also, excessive Cu_2O can inhibit the absorption of light by the TiO_2 surface reducing its ability to generate electron-hole pairs and increases the recombination rate of photogenerated electron-hole pairs.

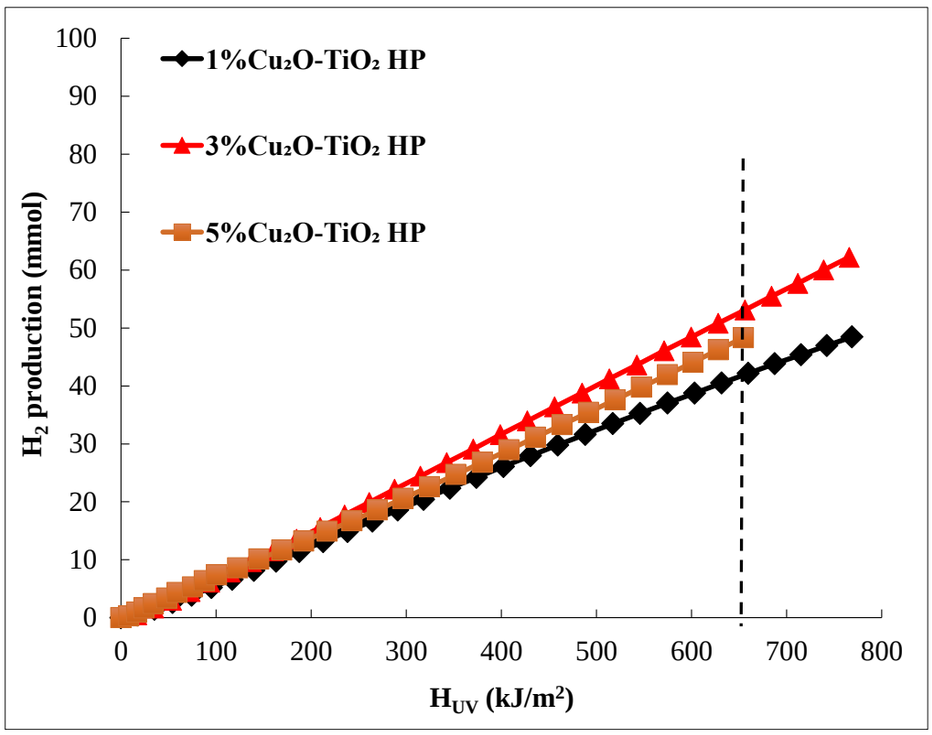

Figure 7-II.5 H_2 generation with 1%Cu_2O-TiO_2 HP, 3%Cu_2O-TiO_2 HP, and 5%Cu_2O-TiO_2 HP (Glycerol 0.075 M, 100 mg/L photocatalyst)

H_2 generation through the Cu_2O-TiO_2 HP catalysts follows a Z-scheme charge transfer (Figure 7-II.6). Under solar irradiation, photoexcited electrons are produced in both Cu_2O and TiO_2, but Cu_2O absorbs both UV and visible light while TiO_2 absorbs only UV light. The conduction band (CB) of Cu_2O is more negative than that of TiO_2 and electrons move from CB of Cu_2O to the CB of TiO_2 and can reduce protons to generate H_2. At the same time holes move from valence band (VB) of TiO_2 to that of Cu_2O thus enhancing the charge separation. Finally, the electrons at CB of TiO_2 can recombine with holes at VB of Cu_2O. Holes with high oxidation ability at VB of TiO_2 start to move toward the particle surface, where they react with the sacrificial agent, and generate oxidation products, as shown in Figure 7-II.6. Under irradiation, the color of CPC tubes was turned into garnet-purple, this means that electrons at CB of TiO_2 were generated and accumulated before they transferred to the VB of Cu_2O. The contact between Cu_2O and TiO_2 allows the formation of a Z-scheme, reduces the recombination rate of intra-photogenerated electron-hole pairs, removes holes from Cu_2O and electrons from TiO_2, and improves photocatalytic H_2 generation.

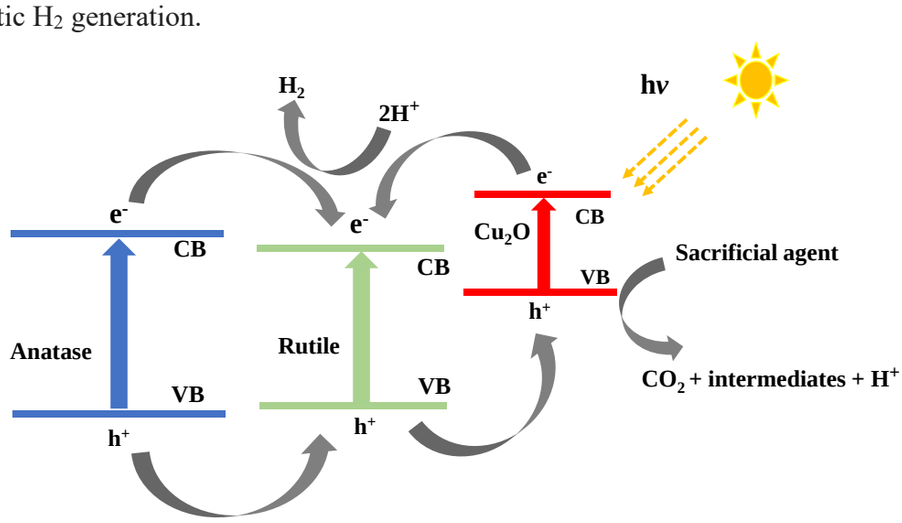

Figure 7-II.6 Proposed reaction mechanism for H_2 generation in the presence of Cu_2O-TiO_2 HP

To further evaluate the effect of different sacrificial on H_2 generation other species such as formic acid, ethanol, and glucose were used in the presence of the best sample (3%Cu_2O-TiO_2 HP). These sacrificial agents were selected due to their low splitting energy demand of 32.9, 29, and 46.7 kJ mol^{-1} respectively, compared to 237.13 kJ mol^{-1} for pure water. Moreover, the suitable position of their redox potential and the position of the semiconductor valence band make them suitable for trapping the photo-generated holes capable of oxidizing organics. Ethanol is produced through the fermentation of sugars. It can be converted into H_2 fuel instead of being used in a combustion engine that has comparatively low efficiency and causes serious environmental pollution [362]. Moreover, glucose produced from renewable biomass is also a rich source and thermodynamically favorable for H_2 production and can be scaled up for practical applications.

The initial concentrations of these substrates were calculated with respect to the total number of carbons present in the respective molecules while the concentration of glycerol (0.075M) was used as a reference. The amount of H_2 generated with formic acid (Figure 7-II.7) was 33.9 mmol (STH of 1.05%), similar to that of glycerol (STH of 1.07%). Formic acid has the simplest molecular structure that undergoes straightforward reactions yielding H_2 and CO_2. The single carboxylic group in formic acid provides a highly efficient route for electrons donation favoring the H_2 generation mechanism. Glycerol contains multiple hydroxyl groups, is easy to oxidize, and provides more reactive sites for H_2 generation. The use of sacrificial agents such as ethanol and glucose resulted in poor H_2 generation, yielding 4.1 mmol (STH of 0.13%) and 3.4 mmol (STH of 0.11%) respectively, as shown in Figure 7-II.7. Ethanol contains a single hydroxyl group, providing less reactive sites for oxidation reactions causing poor H_2 yield. On the other hand, glucose has a complex molecular structure and may require more energy to break down into H_2 and other intermediates resulting in lower efficiency. The difference in H_2 yield with the different sacrificial agents can also be ascribed to faster charge movement compared to the recombination rate of photogenerated electron-hole pairs. The primary features such as several hydroxyl groups, the length of the carbon chain, and dehydrogenation characteristics of sacrificial agents have a direct effect on H_2 generation [336]. Additionally, some other characteristics of the sacrificial species including the polarity, the ability to be adsorbed by the surface of the photocatalyst, the production of byproducts, and the selectivity with generated holes could all have a significant impact on H_2 production efficiency and intermediate products [363, 364].

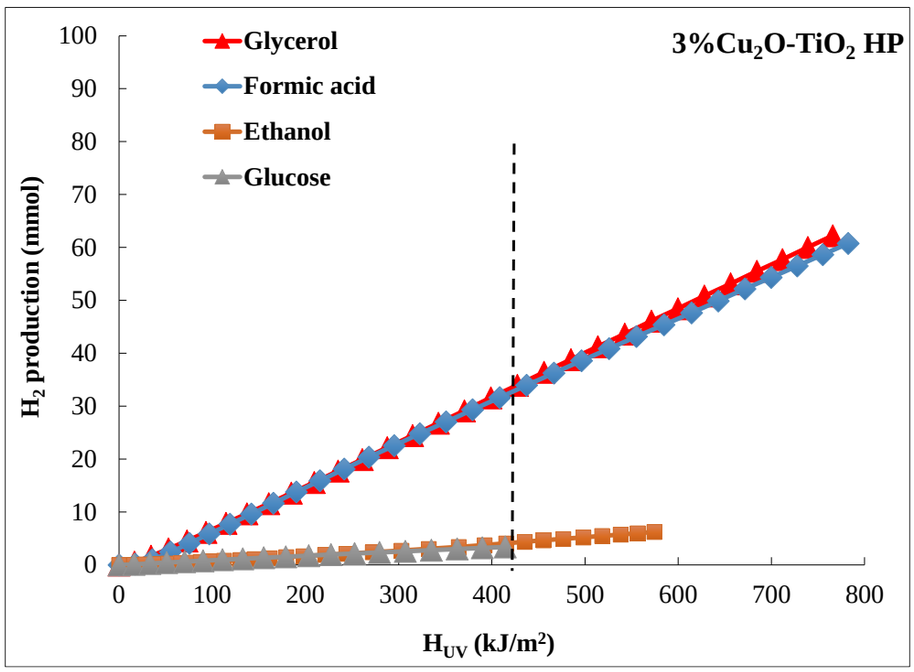

Figure 7-II.7 H_2 generation with glycerol, formic acid, ethanol, and glucose in the presence of 3%Cu_2O-TiO_2 HP

During the photoreforming, the evolution of CO_2 was observed by GC and the formation of short-chain carboxylic acids (Figure 7-II.8) was monitored by ionic chromatography. Figure 7-II.8a shows that during the photoreforming of glycerol, formic acid (FA) was the main product along with traces of glycolic acid (GA). However, it can also be assumed that other reaction intermediates could be formed but rapidly transformed into formic acid. The partial oxidation of the initial substrate was faster than the mineralization of formic acid. FA is the main intermediates obtained from glucose (Figure 7-II.8b) along with low amounts of GA; in the presence of ethanol, in addition to FA and GA, traces of acetic acid (AA) were also identified.

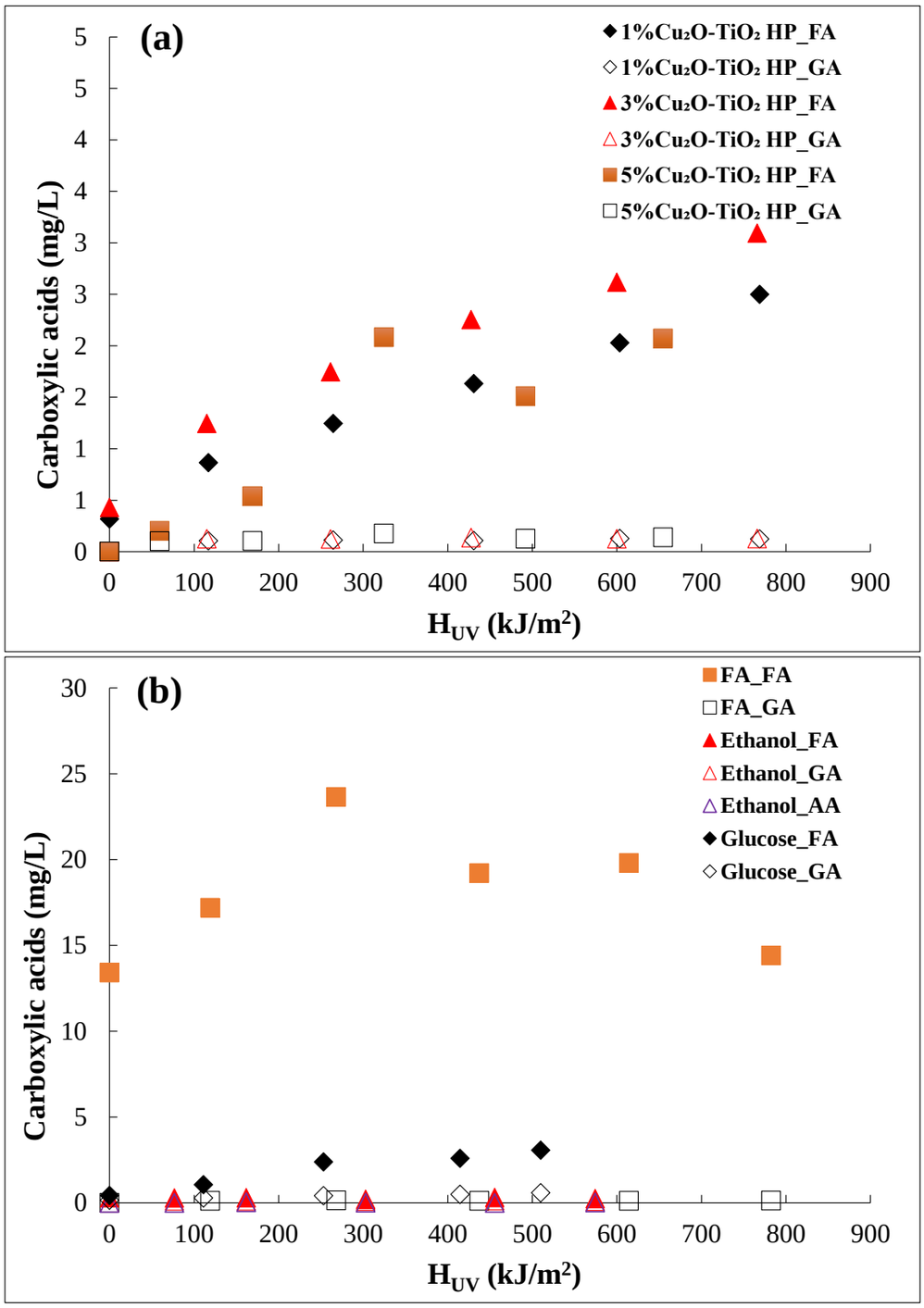

Figure 7-II.8 (a) Formation of formic acid (FA), glycolic acid (GA) with different catalysts in the presence of glycerol as a sacrificial agent (b) Formation of FA, GA, and acetic acid (AA) with ethanol and glucose as sacrificial agents in the presence 3%Cu_2O-TiO_2 HP

During the reaction, with the exception of formic acid, a decrease in pH from ~7.5 to ~4.5 was observed. This is due to a decrease in the initial concentration of sacrificial agents and the

formation of short-chain carboxylic acids. In the case of formic acid, the pH remained almost unchanged at ~3.3 due to its acidic properties. During each run, the temperature rose from ~29°C to ~52°C, however, the temperature has no effect on H_2 generation as discussed in the literature [365]. Dissolved organic carbon (DOC) was also determined by TOC analyses. DOC values decreased during the reaction, in particular, in the case of ethanol. Starting and final DOC concentrations were 2466 and 2300 $mg \cdot L^{-1}$ respectively, which is in agreement with the conversion to short-chain carboxylic acids and finally to CO_2.

7-II.5 Cu leaching

The leaching of non-noble metals during the photocatalytic reaction is important in accessing catalyst stability. During the photoreforming, the formation of organic acids could support the considerable dissolution of Cu oxides causing photo-corrosion [366]. The progressive decrease in the pH could also favour this phenomenon. Cu leaching was studied by ICP-MS under the best experimental conditions, i.e, with 3%Cu_2O-TiO_2 HP and glycerol. During the irradiation, the Cu content in the solution increased, and the leaching before the irradiation and after 5 hours of reaction was 0.32 and 2.16 $mg \cdot L^{-1}$ respectively. Cu leaching is a negative behaviour, however this work can be considered as an initial study demonstrating the efficacy of noble metal-free photocatalytic systems towards hydrogen production at pilot scale. Further efforts are needed to make these photocatalysts more stable.

7-II.6 Conclusions

Home prepared TiO_2 was modified with Cu_2O through a facile ball milling method towards improving photocatalytic H_2 production on a pilot plant scale photorecator. Initially, the effect of Cu_2O percentages on H_2 production was evaluated in the presence of glycerol as a sacrificial agent. The amount of H_2 produced was 53.1 mmol (STH of 1.10%) in the presence of 3%Cu_2O-TiO_2 HP. The catalyst 3%Cu_2O-TiO_2 HP was proved to be a best candidate and then it was further tested to determine the effect of different sacrificial agents such ethanol, glucose and formic acid on H_2 production.

CHAPTER 8

Efficient photocatalytic partial oxidation of aromatic alcohols by using $ZnIn_2S_4$ under green conditions

In this chapter, text is adapted from the following publication.

Muhammad Umair, Claudio Maria Pecoraro, Francesco Di Franco, Monica Santamaria, Leonardo Palmisano, Vittorio Loddo, Marianna Bellardita. Efficient Photocatalytic Partial Oxidation of Aromatic Alcohols by Using $ZnIn_2S_4$ under Green Conditions. *ChemSusChem* **2024**, e202400404. https://doi.org/10.1002/cssc.202400404

CHAPTER 8

Efficient photocatalytic partial oxidation of aromatic alcohols by using $ZnIn_2S_4$ under green conditions

8.1 Abstract

The ternary chalcogenide $ZnIn_2S_4$ (ZIS) has been synthesized by a simple hydrothermal method in which the carcinogenic thiacetamide, universally used as a precursor, has been, for the first time, replaced successfully with the harmless thiourea. This material has been used as photocatalyst for the partial oxidation of different aromatic alcohols to their corresponding aldehyde in aqueous solution, under ambient conditions and simulated solar light irradiation. The photocatalytic performances of $ZnIn_2S_4$, compared in similar experimental conditions with those of the Aeroxide TiO_2 P25 widely used in the literature, showed a significantly higher efficiency than the latter photocatalyst. In fact, 4-methoxybenzyl alcohol (4MBA), piperonyl alcohol (PA), and benzyl alcohol (BA), among the alcohols tested, showed a selectivity towards the corresponding aldehyde of 99% for a conversion of 46%, 75% for a conversion of 81%, and 87% for a conversion of 25%, respectively, in the presence of ZIS. The same alcohols showed a selectivity of 19% for a conversion of 41%, 19% for a conversion of 13%, and 16% for a conversion of 26%, in the presence of Aeroxide TiO_2 P25.

8.2 Photocatalyst preparation

8.2.1 $ZnIn_2S_4$

Thiourea was used to the best of our knowledge for the first time as a sulfur precursor to synthesize $ZnIn_2S_4$ instead of the carcinogenic thioacetamide.

Typically, 261.12 mg of $ZnCl_2$, 848.64 mg of $InCl_3$, and 584.56 mg of thiourea were dissolved in 200 ml absolute ethanol. The mixture was stirred for 30 minutes until the formation of a clear solution and then it was heated at 80 °C for 2h. Subsequently, the resulting solution was transferred to a stainless-steel autoclave and heated at 180 °C for 18h. After that, the autoclave was cooled down to ambient temperature and the resulted solid was recovered. The synthetic route of the preparation of $ZnIn_2S_4$ (ZIS) powder is shown in Figure 8.1.

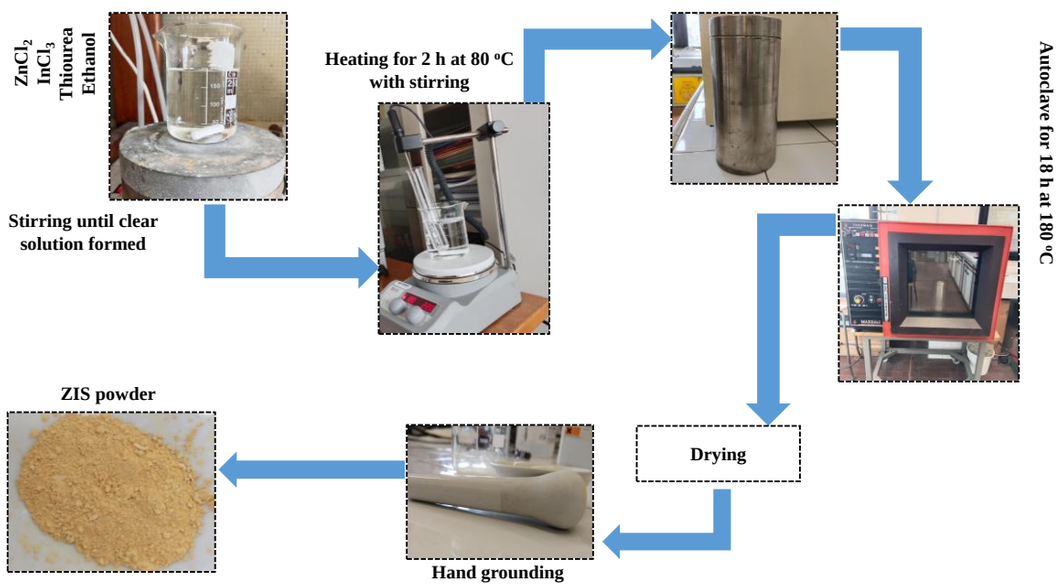

Figure 8.1 Synthetic route of ZIS powder

8.3 Photoelectrochemical measurements

Photoelectrochemical measurements were carried out by using a three-electrode configuration cell in a 0.1 M aqueous solution of ammonium pentaborate (ABE) at a pH of approximately 9. The ZIS photocatalyst was immersed in the ABE solution after drop-casting onto a carbon paper support (Toray 40% wet Proofed-E-Tek). A platinum wire was the counter electrode, while a silver/silver chloride (Ag/AgCl/sat. KCl) electrode was used as the reference one (0 V vs Ag/AgCl = 0.197 V vs SHE). The photocurrent spectra were obtained by irradiating the samples through the quartz window of the cell using a 450 W UV-VIS xenon lamp and a monochromator, by changing the wavelength at a fixed potential. The electrode potential was controlled by using a potentiostat, and the signal corresponding to the measured current was sent to a two-phase lock-in amplifier to isolate the photocurrent from the overall cell current. A mechanical chopper was employed to interrupt the irradiation at a known frequency (specifically, 13 Hz). The flat bland potential was determined by plotting the photocurrent versus the applied potential at a fixed wavelength.

8.4 Results and discussions

8.4.1 UV-VIS diffuse reflectance spectroscopy (DRS)

The UV-vis diffuse reflectance spectrum of the $ZnIn_2S_4$ photocatalyst is reported in Figure 8.2. The spectrum indicates the occurrence of a significant light absorption in the visible range with a steep absorption edge between 420 and 500 nm corresponding to the band-to-band transition of the material [367]. The optical band gap of $ZnIn_2S_4$ is 2.58 eV and was calculated, considering it as an indirect semiconductor, by plotting the modified Kubelka-Munk function, $[F(R`\infty)h\nu]^{½}$, versus the energy of the exciting light (inset of Figure 8.2).

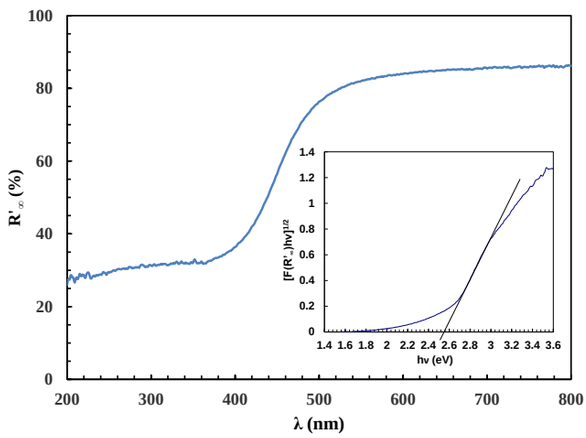

Figure 8.2 UV-vis diffuse reflectance spectra of $ZnIn_2S_4$ photocatalyst. Inset: Tauc plot for band-gap determination

8.4.2 X-ray diffraction (XRD)

Figure 8.3 shows the XRD pattern of the $ZnIn_2S_4$ sample. All the diffraction peaks are consistent with the hexagonal phase of $ZnIn_2S_4$ (JCPDS No. 65-2023) [368]. The BET surface area of the powders resulted to be 1 $m^2\ g^{-1}$.

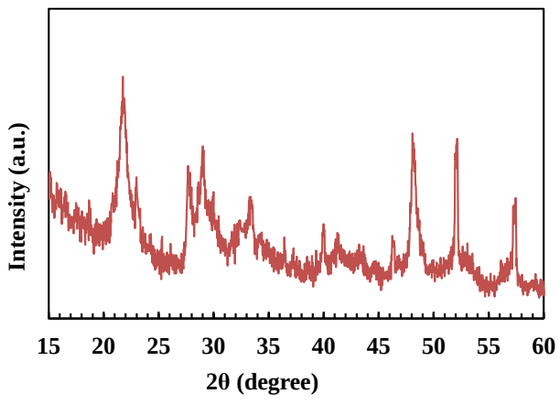

Figure 8.3 XRD pattern of the sample $ZnIn_2S_4$

8.4.3 Scanning electron microscopy (SEM)

The SEM images of the sample (Figure 8.4 a,b,c) show the formation of numerous flower-shaped microspheres with a diameter between 3 and 6 µm similarly to what is reported in the literature for ZIS prepared from thioacetamide [369]. An enlargement of the surface highlights the formation of several flaked layers. EDS mapping demonstrates the presence of Zn, In and S and their uniform distribution. The atomic percentage of the elements was found to be 8%, 23% and 36% for Zn, In and S, respectively, in good accordance with the ZIS molecular composition.

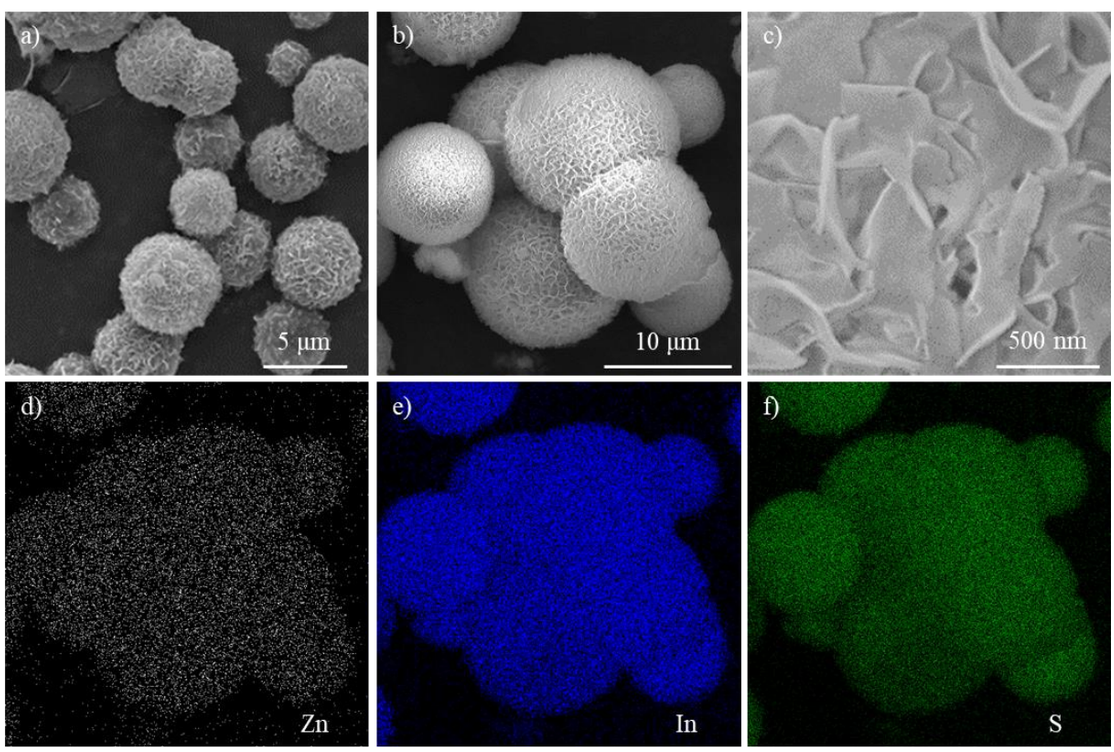

Figure 8.4 SEM images of the sample $ZnIn_2S_4$ at different magnifications (a,b,c), and EDS mapping images related to Zn (d), In (e) and S (f)

8.4.4 Electrochemical measurement

The electrochemical characterizations were performed to obtain more information on the intrinsic electronic properties of the photocatalyst. Figure 8.5a shows the photocurrent spectrum, recorded in a 0.1 M ABE solution by polarizing the ZIS supported on carbon paper (see experimental section) at the open-circuit potential measured in this electrolyte (i.e. 0.35 V versus Ag/AgCl).

The following Equation 8.1 was employed to estimate the optical band gap (E_g) of the material:

$$(Q_{ph} \cdot hv)^n \propto hv - Eg \quad (8.1)$$

where hν represents the energy of the photon, n = 0.5 because the occurrence of a non-direct optical transition is assumed, and Q_{ph} is the photocurrent yield [370, 371]. The latter is the measured photocurrent adjusted for the lamp efficiency and it is proportional to the light absorption coefficient at a photon energy close to that of the band gap. As depicted in Figure 8.5b, the optical band gap was estimated by extrapolating the $(Q_{ph} \cdot hν)^{0.5}$ vs hν plot to zero. E_g ~ 2.7 eV was estimated, in agreement with the other results reported in the literature [346] and with the experimental results obtained from diffuse reflectance spectroscopy (DRS). In order to determine the flat band potential of ZIS, the dependence of I_{ph} on potential was studied under constant irradiating wavelength (see Figure 8.5c). The photocurrent decreases as soon as the potential decreases, as expected for n-type semiconducting material, and I_{ph} = 0 at ~ 0.25 V vs Ag/AgCl, thus suggesting a flat band potential (E_{fb}) around this value.

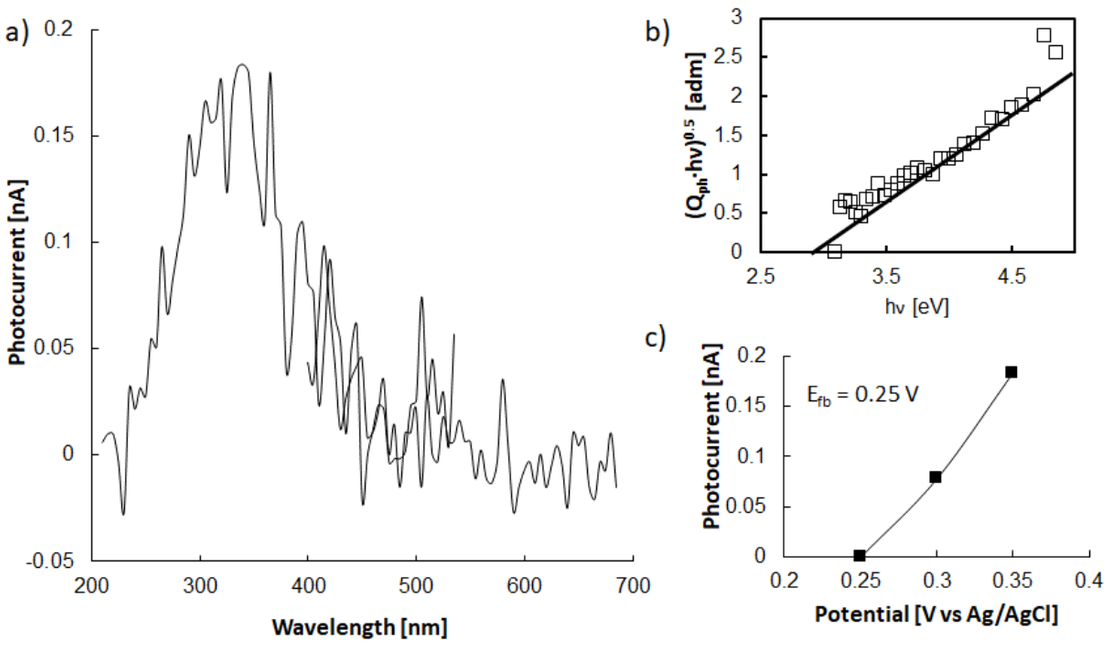

Figure 8.5 a) Photocurrent spectra of $ZnIn_2S_4$ recorded in 0.1 M ABE and Open Circuit Potential of 0.35 V vs Ag/AgCl. The respective $(Q_{ph} \cdot hν)^{0.5}$ vs hν is shown in b). Photocurrent vs potential recorded at 345 nm is reported in c)

8.5 Photocatalytic activity

The results of the photoactivity runs with different substrates i.e., benzyl alcohol (BA), furfuryl alcohol (FA), piperonyl alcohol (PA), cinnamyl alcohol (CA), vanillyl alcohol (VA), 4-methoxybenzyl alcohol (4MBA), 4-nitrobenzyl alcohol (4NBA), 4-hydroxybenzyl alcohol (4HBA), and 2-hydroxybenzyl alcohol (2HBA) are reported in Figure 8.6, in which the evolution of the concentrations of the different alcohols and corresponding aldehydes and acids are plotted versus irradiation time.

For the various alcohols a different amount of converted substrate and formed intermediates can be observed, confirming the finding that for each catalyst an absolute photocatalytic activity must not be considered but it must always be contextualized to the individual substrate [367, 372]. It should be taken into account, of course, the specific interactions

between the photocatalyst and the organic compounds (both the chemical structure of the aromatic alcohols and of the formed compounds) [351, 372-374].

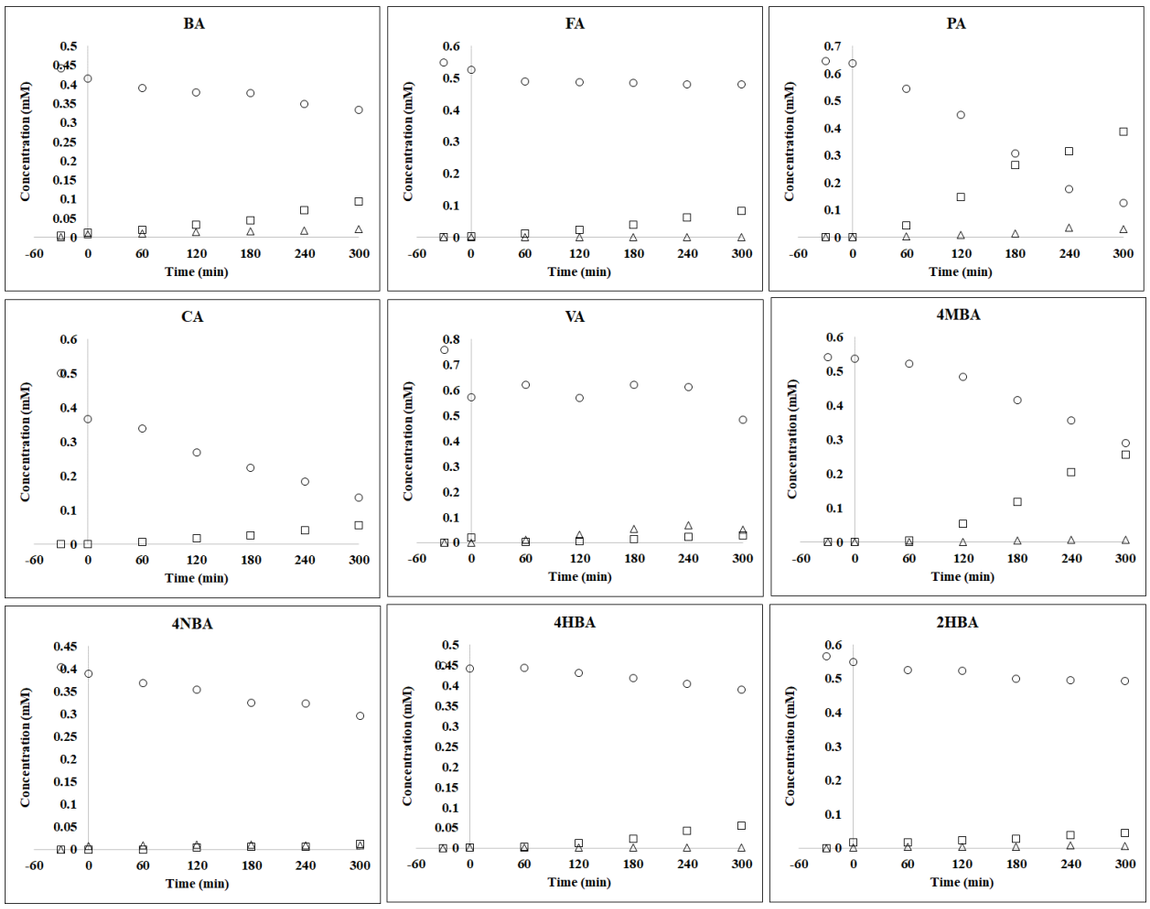

Figure 8.6 Evolution of the concentration vs. time for different alcohols with ZIS (Alcohol ○, aldehyde □ and acid Δ) under simulated solar light irradiation

In Table 8.1 are reported the values of alcohols conversion (X) (Equation 8.2), selectivity (S) (Equation 8.3) and yield (Y) (Equation 8.4) towards the main intermediates, after 5h of irradiation. The following equations were used for the determination of X, S and Y:

$$X = \frac{[Alcohol]i - [Alcohol]t}{[Alcohol]i} * 100 \quad (8.2)$$

$$S = \frac{[P]t}{[Alcohol]i - [Alcohol]t} * 100 \quad (8.3)$$

$$Y = \frac{[P]t}{[Alcohol]i} * 100 \quad (8.4)$$

where: [Alcohol]i and [Alcohol]t indicate the initial molar concentration and molar concentration at time t of the different alcohols, respectively. [P]t is the molar concentration of the obtained product (aldehyde or acid) at time t.

It is worth mentioning that ZIS photocatalyst was active under solar light irradiation for the selective partial oxidation of all the used alcohols and the obtained products were principally aldehydes and trace amounts of acids. Furthermore, the photocatalyst proved to be (photo)stable because after three tests carried out after its recovery at the end of the tests no significant decrease in photoactivity was found.

After 5h of irradiation, the conversion degree ranges between 13 and 81% being the lowest figures obtained with FA and the two OH-substituted benzyl alcohols (4HBA and 2HBA) whereas

the highest one with PA. High selectivity values were obtained with almost all the substrates except for 4NBA, CA and VA.

Previous literature data in the presence of TiO_2 based photocatalysts have shown that selectivity is high when the conversion is low, and its increase corresponds to a decrease in selectivity [347]. By using ZIS photocatalyst high values of both conversion and selectivity were achieved for many substrates. These results appear very satisfactory considering that the reactions have been carried out in pure water and under simulated solar light irradiation, contrarily to what is often reported in the literature [249]. Under these conditions the photocatalysts performance is generally lower than in the presence of organic co-solvents and UV light irradiation [335, 375]. Furthermore, it must also be considered that when using organic solvents, the runs are carried out with small reaction volumes (1.5 mL) and a high catalyst amount (5.3 g L^{-1}) [249, 376].

For BA, after 5h of irradiation the conversion was 25% while the selectivity reached 87%. An electron donating substituent group as -O-CH_3 in *para* position (4MBA) induced higher conversion (46%), and selectivity (99%), in accordance with literature [377]. In fact, being an ortho-para orienting group, the methoxy group in the para position favours the attack on the benzyl group in the para position by the oxidizing species in the conversion of alcohol into aldehyde [375]. Furthermore, the inductive and delocalization effects hinder a subsequent oxidizing action towards the aromatic ring, avoiding its significant mineralization and therefore essentially favoring the partial oxidation reaction. Notably, by using ZIS as the photocatalyst both conversion and selectivity were improved with respect to TiO_2 based samples [377, 378]. By starting from 4NBA the conversion was 27% and the selectivity 11%. In accordance with Yurdakal et al. [374] the presence of –NO_2 group in the *para*-position of the aromatic ring, being an electron withdrawing group, had a detrimental effect on the selectivity while the conversion was substantially the same to that of BA.

For the 4HBA and 2HBA substrates the ZIS photocatalyst showed the same low conversion (only 13%) while the selectivity towards the corresponding aldehyde starting from 4HBA was higher than that which occurred in the presence of 2HBA, confirming that the selectivity is greater when the substituent is in the para position compared to the ortho position [246]. As was previously demonstrated by using TiO_2 photocatalysts [351], this result can be attributed to the lower adsorption of 4-hydroxybelzaldehyde compared to 2-hydroxybelzaldehyde also on the surface of the ZIS photocatalyst. Adsorption tests in the dark of the two aldehydes confirmed this hypothesis being negligible the amount 4-hydroxybelzaldehyde adsorbed onto ZIS surface after 2h of stirring and 65% the percentage of adsorbed 2-hydroxybelzaldehyde. By increasing the irradiation time up to 7h a higher conversion and a lower selectivity has been noticed.

For FA a low degree of both conversion and selectivity was obtained contrarily to what was observed using UV light with TiO_2 photocatalysts for which high selectivity values were obtained at low conversion values [56]. The percentage of adsorbed furfuryl aldehyde after 2h adsorption on the dark was 35%, and this data can justify the low selectivity. Irradiation for longer times (7.5h instead of 5h) showed a conversion increase up to 36% with the same selectivity value.

ZIS showed a high activity towards the partial oxidation of PA (conversion 81%) to piperonal (selectivity 75%) being the yield after 5 hours of 60%, while starting from CA a high conversion and low selectivity was noticed. For VA the conversion and selectivity were 36% and 10%, respectively with a low degree of adsorption of the aldehyde (8%) on the catalyst surface. The results reached in the presence of PA are very satisfactory by considering the results obtained with TiO_2 and C_3N_4 photocatalysts under both UV and simulated solar light irradiation [375, 379].

Table 8.1 Conversion (X) of different alcohols, selectivity (S) and yield values towards the corresponding aldehydes and acids after 5h of irradiation by using the home prepared $ZnIn_2S_4$. In the green boxes, runs conducted for more than 5 hours

Substrates	Chemical structure	X	S_{Ald}	S_{Acid}	Y_{Ald}	Y_{Acid}
BA	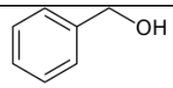	25	87	19	21	5
4MBA	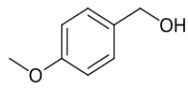	46	99	negligible	47	negligible
4NBA	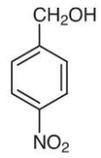	27	11	9	3	2
4HBA	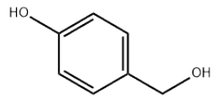	13	93	3	12	negligible
4HBA		28 (7h)	14	1.5	4	negligible
2HBA	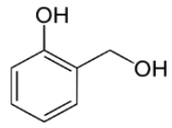	13	60	7	8	1
2HBA		28 (7.5h)	9	negligible	2	negligible
FA	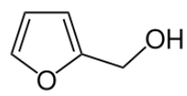	13	32	1.5	15	0
FA		36 (7.5h)	31	negligible	11	negligible
PA	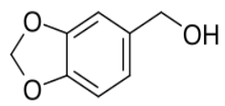	81	75	6	60	5
CA	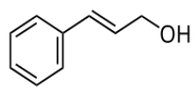	73	15	0	11	0
VA	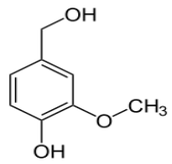	36	10	19	4	7

Overall, the results obtained by using ZIS for the selective synthesis of valuable chemicals such as aldehydes under green conditions are encouraging. In fact, in many cases high selectivity values combined with high conversions have been obtained.

In Table 8.2 are reported the conversion and selectivity values related to the different alcohols obtained with the commercial widely used TiO_2 P25 in the same experimental conditions of ZIS. For the sake of comparison, the different alcohols show similar conversion degrees as those reported in Table 8.2 and the corresponding irradiation times, t, necessary to reach that conversion degree. As can be seen, with the exception of 4NBA, higher selectivity values at the same alcohols

conversion degree were always obtained with ZIS. The results showed in Table 8.2 confirm that TiO_2 generally have a higher oxidant power than ZIS (Table 8.1), being the same conversion reached in less time and the selectivity values lower.

Table 8.2 Conversion (X) of different alcohols, time (t) necessary to reach the reported conversion, selectivity (S) and yield values (Y) towards the corresponding aldehydes and acids in the presence of commercial TiO_2 P25

Substrates	**X**	**t**	**S_{Ald}**	**S_{Acid}**	**Y_{Ald}**
BA	26	2.5h	16	7	4.3
4MBA	41	4h	19	-	7.0
4NBA	22	4h	18	11	4.0
4HBA	13	4h	10	-	1.8
2HBA	13	5h	23	-	3.0
FA	13	1.5h	13	1	1.5
PA	13	3h	19	-	2.5
CA	65	8h	8	-	5.8
VA	35	5h	9	35	3.3

Figure 8.7a shows the degradation of piperonyl alcohol under irradiation in the presence of ZIS and various scavengers. The results indicate that the main active species in PA degradation are e^- since the lowest photoactivity is observed after the addition of $AgNO_3$. Also in the presence of benzoquinone a significant reduction in photoactivity is noted which highlights the important role of $^{\bullet}O_2^-$ radicals. These results are in agreement with each other considering that under irradiation the $^{\bullet}O_2^-$ radicals are formed from the reaction between O_2 and the photogenerated e^-. The presence of $AgNO_3$ reduces the amount of e^- available, and therefore decreases the production of $^{\bullet}O_2^-$. A less pronounced decrease in activity can be noted in the presence of $Na_2C_2O_4$ and tert-butanol indicating a minor role of holes and hydroxyl radicals.

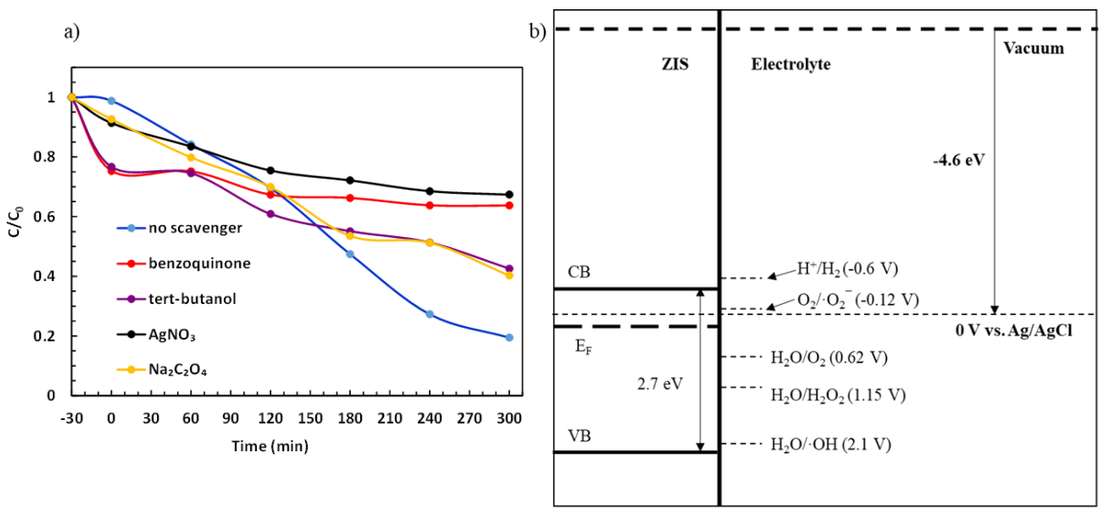

Figure 8.7 a) Photocatalytic degradation of PA with ZIS in the presence of different scavengers and b) energetic sketch of the semiconductor/electrolyte interface

These experimental findings can be also supported by the energetics of the ZIS/electrolyte interface reported in Figure 8.7b, drawn by considering the electrochemical measurements. The VB edge of the material is located at –6.85 eV in agreement with the results reported in ref. [380], thus allowing to locate the CB edge at ~ -4.1 eV (the optical band gap being ~ 2.7 eV). The band edge energy location is consistent with the estimated flat band potential (see Figure 8.6b) and with the reactivity of the photocatalyst under irradiation. Indeed, the generated holes are noble enough to produce hydroxyl radicals, while the photogenerated electrons can induce oxygen reduction to produce $^{\bullet}O_2^-$. It is also worth mentioning that the conduction band edge energy location suggests that hydrogen evolution is not thermodynamically possible. This statement is supported experimentally by gas chromatographic analyses, carried out during the partial oxidation of FA, since hydrogen is not revealed up to 5 h of irradiation.

In Figure 8.8 is proposed a reaction scheme drawn in accordance with the above reported results. The photoexcited electrons and holes migrate towards the ZIS surface. These results agree with each other because the electrons react with molecular oxygen to form the superoxide radical ($^{\bullet}O_2^-$) and these, together with holes, attack the aromatic alcohols transforming them into the corresponding aldehydes.

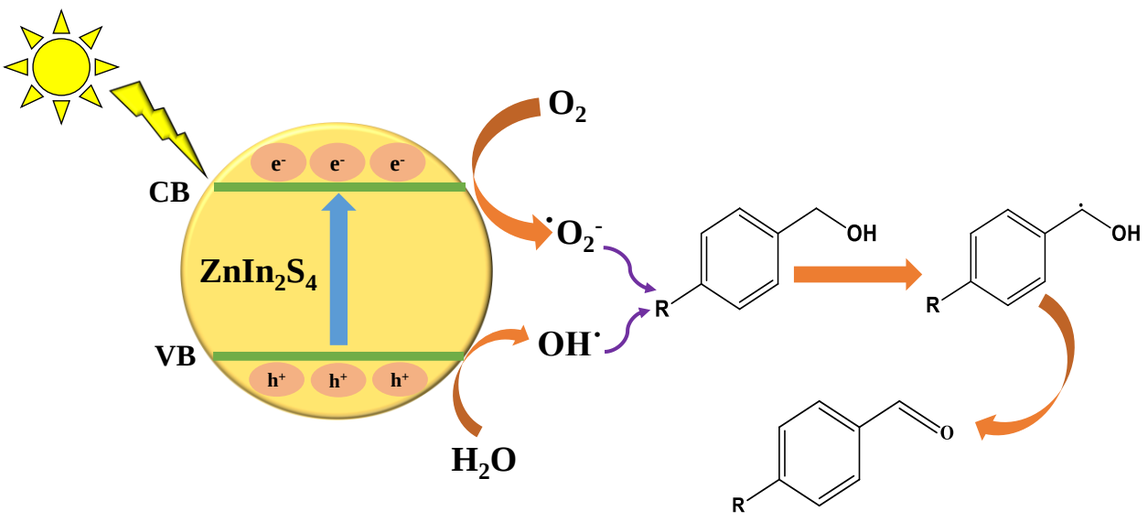

Figure 8.8 Hypothesized reaction pathway

8.6 Conclusions

$ZnIn_2S_4$ photocatalyst synthesized by a facile hydrothermal method exhibited high photoactivity for the selective partial oxidation of different aromatic alcohols to their corresponding valuable aldehydes under green conditions. The performance of ZIS was higher than that of the benchmark TiO_2 P25 highlighting the use of this new catalyst as a very effective substitute for TiO_2 in selective syntheses under sunlight irradiation and aqueous medium. Furthermore, in this case one of the disadvantages of synthetic photocatalysis is also overcome, namely the low conversion of the substrate to obtain high selectivity. In fact, it has been seen that for many alcohols it has been possible to obtain high selectivity values with good degrees of conversion of the different substrates. Therefore, this can be considered a preliminary fundamental study, precisely to verify the efficiency of the process. A subsequent development could include the coupling with an aldehyde separation system, for example the use of selective membranes, which allow maximizing both conversion and yield, even if it is not easy to select a suitable membrane both from the engineering and chemical point of view for molecules that are too similar

CHAPTER 9

Enhanced aqueous photocatalytic selective oxidation of HMF: comparison of the performance of different photocatalysts

In this chapter, text is adapted from the following publication.
Muhammad Umair, Claudio Maria Pecoraro, Francesco Di Franco, Monica Santamaria, Leonardo Palmisano, Vittorio Loddo, Marianna Bellardita. Enhanced aqueous photocatalytic selective oxidation of HMF using simulated sunlight: comparison of the performance of different photocatalysts. *Sustainable Materials and Technologies* 2025, 43, e01188. https://doi.org/10.1016/j.susmat.2024.e01188

CHAPTER 9

Enhanced aqueous photocatalytic selective oxidation of HMF using simulated sunlight: Comparison of the performance of different photocatalysts

9.1 Abstract

Selective conversion of biomass derivatives to valuable compounds is an effective and sustainable route to fulfill the industrial request of chemicals. In this paper the partial oxidation of the lignocellulose derivative 5-hydroxymethyl-2-furfural (HMF) to high value compounds in green conditions has been studied in the presence of different photocatalysts and irradiation sources. In particular, TiO_2 based and alternative TiO_2 photocatalysts (Bi_2O_3, Cu_2O, C_3N_4, $ZnIn_2S_4$) were studied with the aim to increase the activity and selectivity in HMF partial oxidation under environmental friend conditions. $ZnIn_2S_4$ showed to be the best photocatalyst under simulated solar light irradiation with a HMF conversion of 43% and a 68% selectivity towards 2,5-diformylfuran. Electrochemical measurements and experimental runs in the presence of various scavengers (tert-butanol, $AgNO_3$, benzoquinone, $Na_2C_2O_4$) revealed that e^- and $^{\bullet}O_2^-$ radicals play a key role in the selective conversion of HMF. A kinetic study was carried out and the kinetic parameters were determined by using the Langmuir-Hinshelwood model.

9.2 Photocatalysts preparation

9.2.1 Pt-BDH

Pt-BDH prepared through photodeposition method has already been discussed in section 4-II.2.4.

9.2.2 3%Nb_2O_5-BDH

3%Nb_2O_5-BDH was prepared through a similar method as of x%Nb_2O_5-HP (Section 4-1.2.2).

9.2.3 HP05 (TiO_2)

Bare TiO_2 was prepared through the gradual addition of $TiCl_4$ to distilled water (1:10, v/v) at room temperature. The mixture was stirred continuously for 12 h to obtain a clear suspension that was boiled for 30 minutes under stirring. The resulting white milky suspension was dried under vacuum at 60 ºC to recovery the powder.

9.2.4 C_3N_4

10 g of melamine, placed in a ceramic crucible covered with a lid, were heated to 520 °C in a muffle furnace at a rate of 3°C/min; bulk graphitic carbon nitride powder was produced. Then, 5 g of obtained powder was dispersed in the bottom of a ceramic bowl and subjected to another heat treatment to obtain the thermo-exfoliated sample (the sample was heated in static air at a rate of 3 °C/min to 520 °C and calcined for 4h).

9.2.5 Bi_2O_3

5 g of $Bi(NO_3)_3$ $5H_2O$ was added into 80 mL of a 1.5 M HNO_3 solution under stirring. After, KOH was added until pH 13 was reached. The suspension was heated for 2 h at 80 °C and the obtained precipitate was filtered and washed with water until the natural pH of the water was reached. The wet powder was dried in an oven overnight at 120°C. The solid was first calcined at 300°C for 6h with a ramp of 3.5°C/min and 4.5°C/min for heating and cooling respectively and

successively sintered at 500°C for 6 h with a ramp of 3.5°C/min and 4.5°C/min for heating and cooling respectively.

9.2.6 $ZnIn_2S_4$-1

The preparation method has been discussed in section 8.2.1.

9.2.7 $ZnIn_2S_4$-2

The preparation method has been discussed in section 6.2.1.

9.3 Results and discussions

9.3.1 UV-VIS diffuse reflectance spectroscopy (DRS)

UV-Vis diffuse reflectance spectra of the different samples are shown in Figure 9.1 (A and B). Band gap values determined by plotting the modified Kubelka-Munk function, $[F(R'_\infty)h\nu]^{1/2}$, vs the energy of the exciting light hν are reported in Table 9.1. The used photocatalysts are all active under UV–visible light irradiation showing band gap values ranging from 2.54 to 3.26 eV.

Commercial bare TiO_2 BDH (Figure 9.1A) shows an absorption band at ca. 360 nm ascribed to the band-to-band transition typical of anatase phase (E_g= 3.25 eV) while the home prepared TiO_2 exhibits a little red shift highlighting activation at higher wavelengths (E_g= 3.00 eV). The loading of Pt on the BDH surface, allowed an increase of the absorption in the visible region as compared to bare BDH without any variation in the absorption edge (E_g= 3.26 eV). In the presence of 3%Nb_2O_5 the spectrum is practically superimposable to that of pristine BDH and also the band gap values are the same; bare Nb_2O_5 presents an absorption edge at slightly lower wavelength (E_g= 3.12 eV). The C_3N_4 spectrum shows a red shift towards higher wavelengths with a wider absorption from 400 to 550 nm resulting from the electrons transition from the valence to the conduction band with E_g= 2.81 eV. Bare Bi_2O_3 (Figure 9.1B) presents an absorption edge at ca. 430 nm (E_g= 2.79 eV) while Cu_2O is active in the orange region of visible light spectrum (E_g= 1.94 eV) with a step edge at ca. 630 nm and a higher absorption up to 800 nm. The two differently prepared $ZnIn_2S_4$ samples can be activated by solar light irradiation exhibiting an absorption edge in the range 380-460 nm which corresponds to a band gap of 2.54 eV and 2.30 eV for $ZnIn_2S_4$-1 and $ZnIn_2S_4$-2, respectively.

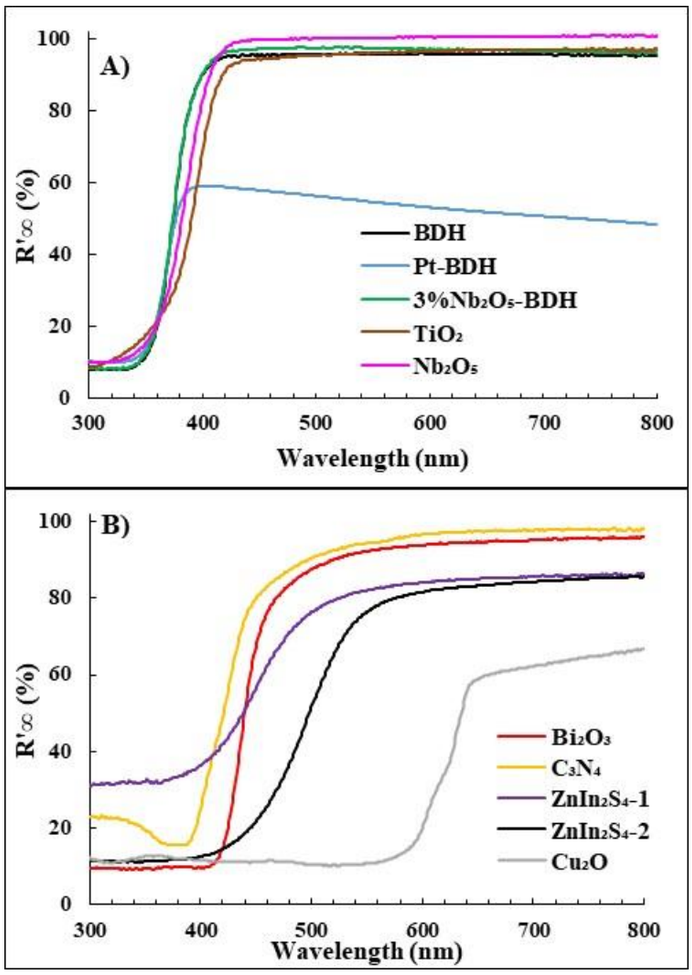

Figure 9.1 UV-Vis diffuse reflectance spectra of the used samples

9.3.2 Specific surface area (SSA)

The various samples have different specific surface areas (Table 9.1) ranging from ca. 1 m^2 g^{-1} for Bi_2O_3 and $ZnIn_2S_4$-1, up to values close to 10 m^2 g^{-1} for BDH, 3%Nb_2O_5-BDH and $ZnIn_2S_4$-2, to 16 m^2 g^{-1} for Nb_2O_5 and to 102 m^2 g^{-1} for home prepared TiO_2 and 150 m^2 g^{-1} for C_3N_4.

Table 9.1 Band gap and Specific Surface Area values of the different catalysts

Samples	Band gap (eV)	S.S.A. (m^2 g^{-1})
BDH	3.25	10
Pt-BDH	3.26	10
Nb_2O_5	3.12	16
3%Nb_2O_5-BDH	3.24	9
Bi_2O_3	2.79	1
Cu_2O	1.94	1
TiO_2	3.00	102
C_3N_4	2.81	150
$ZnIn_2S_4$-1	2.54	1
$ZnIn_2S_4$-2	2.30	8

9.3.3 Raman spectroscopy

In Figure 9.2A the Raman spectra of BDH based powders are reported. The spectra of all the samples are virtually the same and the characteristic modes of TiO_2 anatase at 144, 196, 397, 513 and 639 cm^{-1} [381] are indicated. No significant differences can be observed in the presence of 0.5%Pt or 3%Nb_2O_5 because of their low amount and uniform distribution on TiO_2. Home prepared TiO_2 (Figure 9.2B) presents the same peaks of commercial anatase (BDH) but with lower intensities probably due to the low preparation temperature. The spectrum of Bi_2O_3 shows the characteristic bands of α-Bi_2O_3 in accordance with the pertinent literature [382, 383]. The peaks at 139 and 153 cm^{-1} are related to the displacements of Bi and O atoms in the α-Bi_2O_3 lattice [384]. The Raman modes at 184, 212, 283, 317, 416, 447, and 534 cm^{-1} are assigned to the displacements of the O atoms [384]. For carbon nitride, peaks at 470, 707, 771, 984, 1130, 1165, 1211, 1237 and 1318 cm^{-1} have been found and they can be assigned to the vibration modes of CN heterocycles [385, 386].

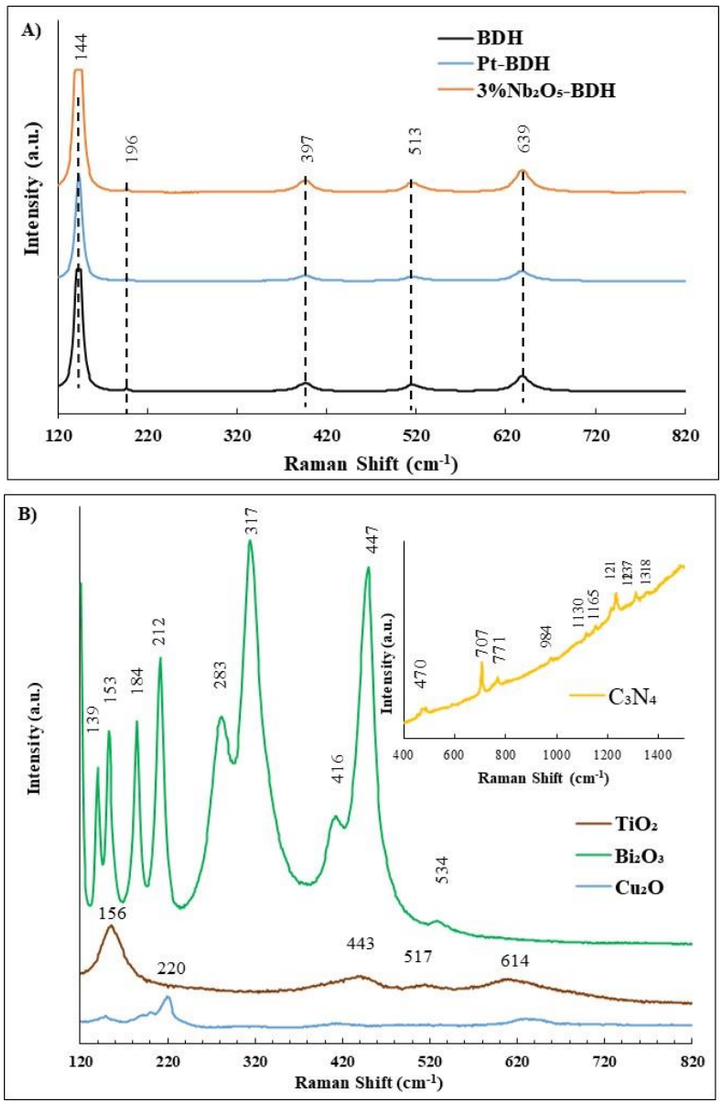

Figure 9.2 Raman spectra of the used samples

9.3.4 X-ray diffraction (XRD)

The XRD patterns of the $ZnIn_2S_4$ powders are presented in Figure 9.3. The diffractogram of $ZnIn_2S_4$-1 shows the peaks at 14.4°, 27.8°, 44.2°and 47.4° which are characteristic of (111), (311), (511) and (440) crystal planes of cubic $ZnIn_2S_4$ (JCPDS, 00-048-1778) [387, 388]. For $ZnIn_2S_4$-2, however, peaks are noticed at 21.6°, 27.7°, 39.5°, 44.2°, and 47.9°, attributable to the

(006), (102), (108), (110), and (116) crystalline planes of hexagonal $ZnIn_2S_4$ [387], [388] (JCPDS card No. 65-2023).

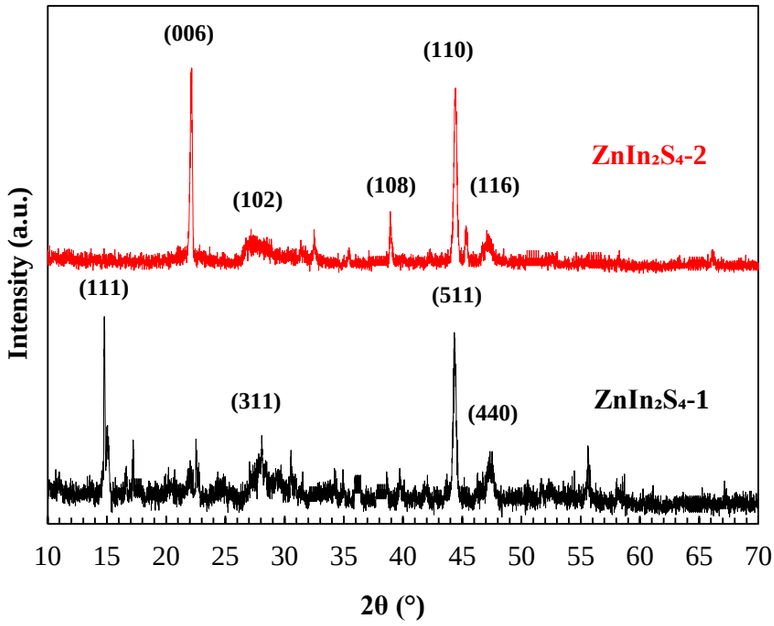

Figure 9.3 XRD patterns of $ZnIn_2S_4$ samples with the indication of the main peaks

9.3.5 Scanning electron microscopy (SEM)

The morphology of the used photocatalysts has been investigated by SEM analysis and it is shown in Figure 9.4A. Home prepared TiO_2 consists of irregular shaped roundish aggregates whose dimensions vary from a few nanometers to ca. 500 nm. Bi_2O_3 exhibits a rod-like morphology, similar to that reported in literature for α-Bi_2O_3 [389], with a length ranging between a few microns to approximately 10 μm and a diameter of about 1.5 μm. Pt-BDH is constituted by aggregates of spherical particles with dimensions varying from 100 to 400 nm; its morphology is like to pristine BDH [390] as Pt is photodeposited onto TiO_2 surface at room temperature. In the composite 3%Nb_2O_5-BDH sample no particles related to Nb_2O_5 are distinguishable, due the low amount ad high dispersion degree within TiO_2. C_3N_4 shows a lamellar multi-layered structure in accordance with literature [375]. $ZnIn_2S_4$ powders (Figure 9.4B) consist of flowerlike microspheres with diameter ranging from ca. 5 to 9 μm, very similar to those observed in samples prepared by different methods [346, 391, 392].

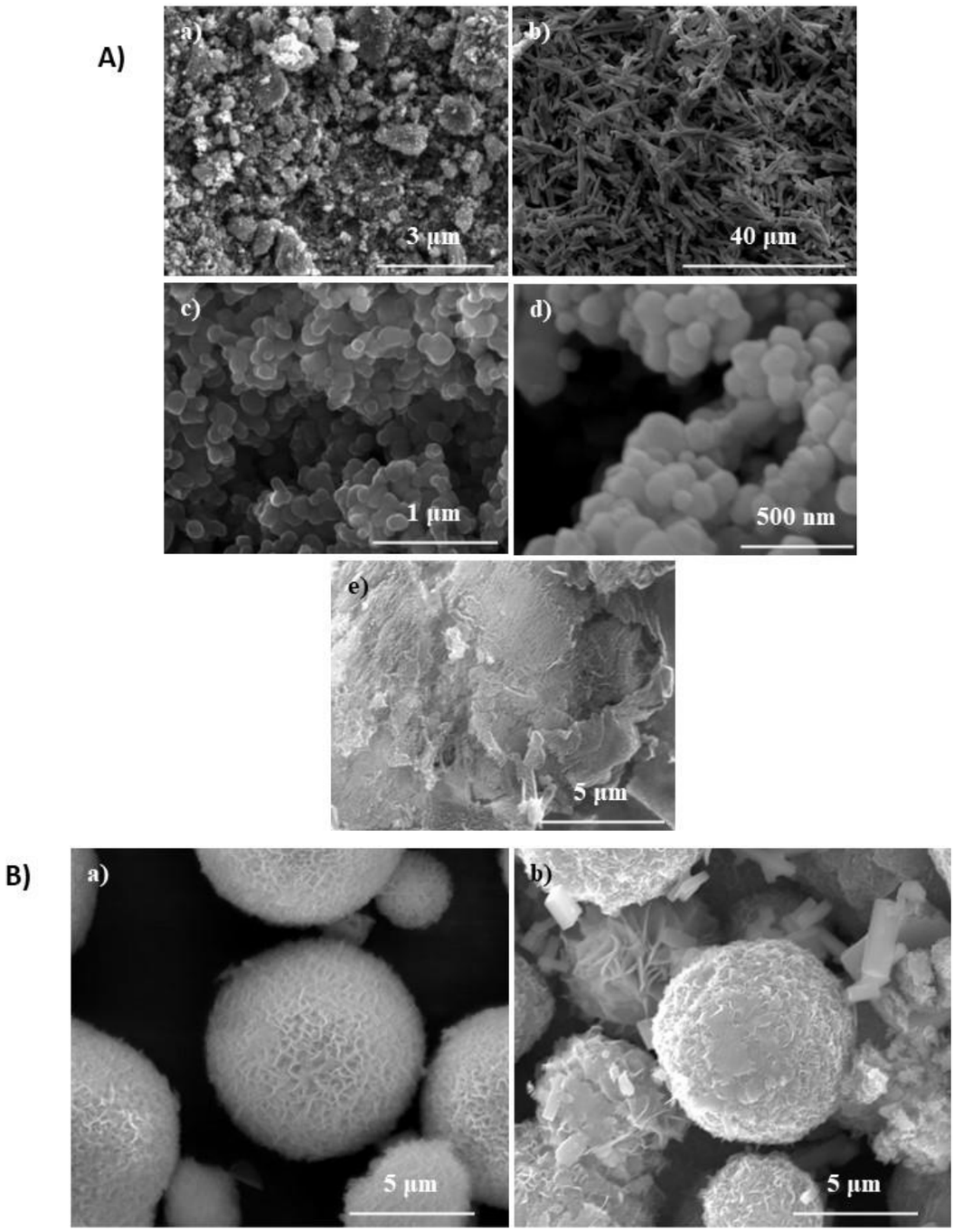

Figure 9.4 SEM images of the samples: (A) a) TiO_2, b) Bi_2O_3, c) Pt-BDH, d) 3%Nb_2O_5-BDH e) C_3N_4; (B) a) $ZnIn_2S_4$-1, b) $ZnIn_2S_4$-2

9.3.6 Electrochemical measurement

Photoelectrochemical measures were carried out on $ZnIn_2S_4$-2 sample which is the most active photocatalyst. Figure 9.5A shows the effect of light irradiation at 450 nm and 360 nm on the Open Circuit Potential (OCP). Soon after irradiation OCP shifts towards the negative direction, as expected for n-type semiconductor. The shift is more pronounced when the sample is irradiated at 360 nm light with respect to 450 nm. The n-type semiconductor behaviour is also confirmed by the photocurrent transient reported in Figure 9.5B recorded under monochromatic irradiation (λ = 360 nm) at various constant potentials and showing the presence of an anodic photocurrent. The photocurrent was measured by manually stopping the irradiation at applied potential ranging from 0.5 V to - 0.3 V vs Ag/AgCl (see Figure 9.5B). The anodic photocurrent reached the value of zero at ~ - 0.2 V vs Ag/AgCl, which can be considered as an estimate of the flat band potential (V_{FB}).

To examine the electronic properties of the photocatalysts, the photocurrent spectrum recorded at 0.5 V vs Ag/AgCl was obtained. Figure 9.5C shows the curve of photocurrent values versus wavelength and it can be noticed a peak at approximately 360 nm. Assuming a non-direct

optical transitions, it was possible to estimate the optical band gap value (E_g) by extrapolating to zero $(Q_{ph} \cdot h\nu)^{0.5}$ versus hν plot (Figure 9.5D). An E_g of ~ 2.3 eV was determined, in accordance with findings in the literature [393].

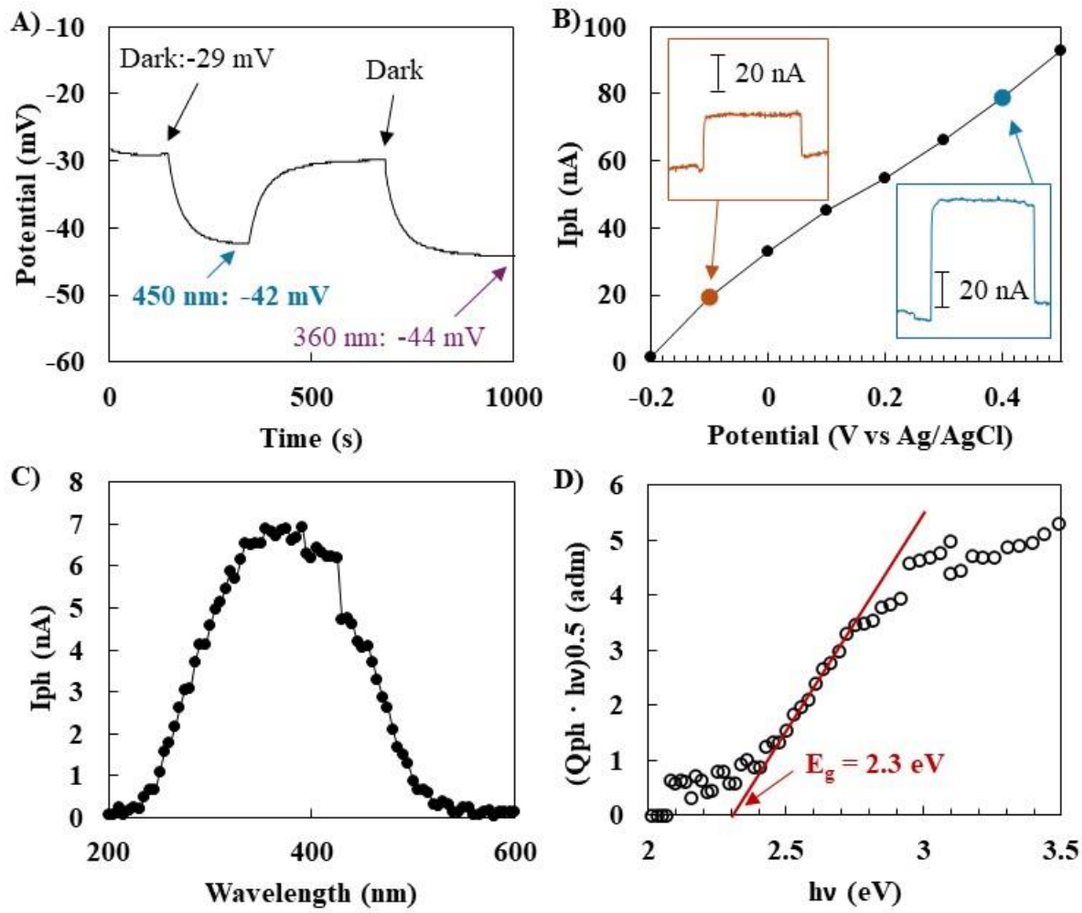

Figure 9.5 A) $ZnIn_2S_4$-2 photopotential recorded both under dark and by irradiation at 450 nm and 360 nm. Photocurrent transient under monochromatic light recorded at 360 nm and applied potential from 0.5V to -0.3V vs Ag/AgCl with a step of 0.1 V are reported in B), the respective photocurrent vs time plots recorded at 0.4 V and -0.2 V vs Ag/AgCl are reported in the inset. C) Photocurrent spectra recorded at 0.5 V vs Ag/AgCl, the respective $(Q_{ph} \cdot h\nu)^{0.5}$ vs hν plot is shown in D)

The energetic sketch was built by using for the band energy level the values obtained from the photoelectrochemical characterizations, and it is showed in Figure 9.8B to illustrate the possible photoelectrocatalytic mechanism. The preferential formation of FFCA from HMF can be attributed to the hindered H_2 production while the photocatalyst facilitates the formation of the super oxide radical ($\cdot O_2^-$) and hydrogen peroxide (H_2O_2) which can further oxidate HMF. Moreover, the $ZnIn_2S_4$ energy level of the VB suppresses the generation of hydroxyl radicals ($^{\cdot}OH$). As a result, the degradation of HMF through C-C cleavage is prevented [394, 395] leading to an increased formation of partial oxidation products such as FFCA. In summary, the energy diagram highlights the effectiveness of $ZnIn_2S_4$ in influencing the reaction pathway and selectivity of HMF partial oxidation.

9.4 Photocatalytic activity

The following equations 9.1-9.3 were used for the calculations of HMF conversion, selectivity, and yield towards the main intermediates:

$$X = \frac{(C)_i - (C)_t}{(C)_i} * 100 \quad (9.1)$$

$$S = \frac{(P)_t}{(C)_i - (C)_t} * 100 \quad (9.2)$$

$$Y = \frac{(P)_t}{(C)_i} * 100 \quad (9.3)$$

where: $(C)_i$ and $(C)_t$ represent the initial molar concentration and the molar concentration at time t of HMF. $(P)_t$ represents the molar concentration of the products obtained at t irradiation time.

As showed in the scheme of Figure 9.6, HMF can be partially oxidized to different furanic compounds as 2,5-diformylfuran (FDC), 5-formyl-2-furancarboxylic acid (FCA) and 5-hydroxymethyl-2-furan carboxylic acid (HMFCA) by following different reaction pathways [396-398] depending on the catalyst electronic features. FDC (path I) is formed through the oxidation of alcoholic group of HMF to the carbonyl one whereas (path II) HMFCA is obtained through the oxidation of the carbonyl functional group of HMF to the carboxylic one; both these compounds can form FCA [399].

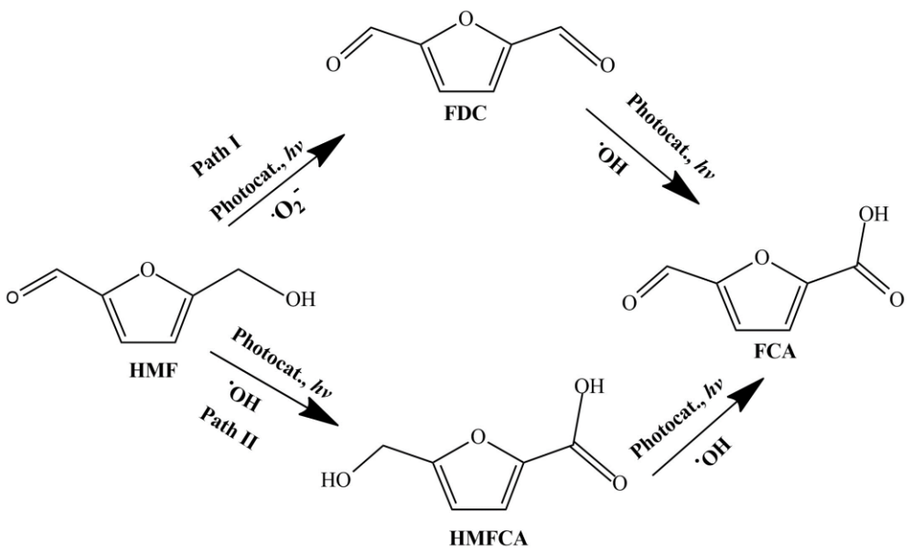

Figure 9.6 Possible reaction scheme related to the photocatalytic HMF partial oxidation

In Table 9.2 the results of some preliminary tests carried out under UV light irradiation are reported. Initially, the photocatalytic runs in the presence of commercial TiO_2 BDH (bare and with photodeposited Pt) were carried out under different experimental conditions to determine the best ones. By bubbling pure oxygen, Pt-BDH completely oxidized HMF within the first hour of irradiation and negligible amounts of oxidized compounds were formed. In order to work in less oxidant conditions, both Pt-BDH and naked BDH were used in the presence of atmospheric air instead of pure O_2. HMF was completely converted after 4h but, also in this case, the selectivity towards the formed intermediates was very low confirming previous results [400, 401]. Pt-BDH was tested under anaerobic conditions to check the possibility of H_2 evolution (as during photoreforming processes naked TiO_2 was not effective [122]) but no hydrogen was observed and, although the HMF conversion after 5h of irradiation decreased down to 77%, negligible selectivity values were found. For this reason, the subsequent tests were carried out in the reactor open to atmospheric air by using photocatalysts with less oxidant power. The home-prepared TiO_2 was tested because it showed a low oxidizing activity for 4-methoxybenzyl alcohol but a high selectivity in the partial oxidation of the same to 4-methoxybenzaldehyde [347]. By using HMF as the substrate, however, the conversion was ca. 79% with low selectivity towards FDC. These preliminary results suggested that TiO_2 based catalysts are not suitable for HMF partial oxidations

probably due to the formation of surface highly oxidative hydroxyl radicals under UV light irradiation. Alternative photocatalysts as Bi_2O_3 and Cu_2O exhibited low oxidant power, being the HMF conversion equal to 43% and 39%, respectively, but also low selectivity.

Table 9.2 HMF conversion and selectivity towards the identified intermediates during 0.5 mM HMF oxidation after 5h UV irradiation

Conditions	Samples	X_{HMF} (%)	S_{FDC} (%)	S_{FCA} (%)	S_{HMFCA} (%)
O_2 bubbled (results after 1h irradiation)	Pt-BDH	100	negligible	negligible	2.1
Atmospheric air	Pt-BDH	100	negligible	negligible	-
	BDH	100	negligible	negligible	1.2
	TiO_2	79	2.1	-	-
	Bi_2O_3	43	1.7	negligible	3.9
	Cu_2O	39	negligible	negligible	4.6
He bubbled in closed reactor	Pt-BDH	77	negligible	negligible	1.8

With the aim to decrease the oxidant power of the system and explore the possibility to increase the selectivity towards the partial oxidation compounds, runs with selected photocatalysts were carried out by employing a 150 W halogen lamp (simulating the solar light irradiation) (Table 9.3) as it has been done in previous investigations [335]. As expected, the conversion decreased but the selectivity slightly increased compared with the data reported in Table 9.2 but, in any case, they were very low, in some cases negligible. For this reason, the photocatalysts TiO_2 based were substituted with $ZnIn_2S_4$-1, a photocatalyst which has recently attracted great attention [402-405] and displayed high activity in partial oxidation reactions [406] found in previous investigations [335]. HMF conversion after 5h of irradiation was ca. 60% and the selectivity values towards FDC, FCA and HMFCA were 5.5, 4 and 4.4 %, respectively.

Table 9.3 Conversion and selectivity values during the partial oxidation of 0.5 mM HMF after 5h using a 150 W halogen lamp irradiation in the reactor opened to atmospheric air

Samples	X_{HMF} (%)	S_{FDC} (%)	S_{FCA} (%)	S_{HMFCA} (%)
BDH	98	negligible	negligible	1.3
Nb_2O_5	13	6.3	negligible	11.2
3%Nb_2O_5-BDH	94	-	negligible	2.1
Bi_2O_3	18	1.5	5.4	20.4
$ZnIn_2S_4$-1	60	5.5	4.0	4.4

Considering that HMF was easily oxidized under 150 W halogen lamp irradiation (Table 9.3), a series of tests were carried out by using a 50 W halogen lamp (Table 9.4). Bare BDH samples showed good activity for HMF oxidation (conversion ca. 54%) but low selectivity towards oxidation products such as FDC and FCA. Bare Nb_2O_5 and Bi_2O_3 displayed a negligible activity

whilst the composite 3%Nb_2O_5-BDH afforded 46% of conversion and low selectivity towards the partial oxidation compounds. TiO_2 was also used for the sake of comparison and the obtained conversion was ca. 14%, while the selectivity towards FDC and HMFCA were ca. 46 and 9%, respectively. C_3N_4, instead, exhibited a conversion of only 8% with selectivity towards FDC, FCA and HMFCA of 44%, 3% and 16%, respectively.

$ZnIn_2S_4$ photocatalysts were the most active samples. In particular $ZnIn_2S_4$-1 afforded 27% of conversion and 58.2, 1.9 and 4.2% of selectivity towards FDC, FCA and HMFCA, respectively, by using the oxygen present in atmospheric air. Conversely, by bubbling pure oxygen the conversion increased up to 64%, and the selectivity decreased, but the yield to FDC was virtually the same. In the presence of $ZnIn_2S_4$-2 the conversion raised up to 43% and the selectivity towards FDC and FCA was 68 and 3.2%, respectively. Notably, a high selectivity (yield ca. 30%) was achieved despite the high conversion. Indeed, a decrease in selectivity generally has been noticed in correspondence with an increase in conversion. This finding highlighted that the properties of a photocatalysts are not only related to the specific semiconductor but also to the preparation conditions. To verify the possible formation of H_2 with $ZnIn_2S_4$-2, a run has been carried out under anaerobic conditions (last line Table 9.4) [122]. The HMF conversion was lower than that obtained in the open to air reactor due to the less presence of O_2 in solution and the presence of H_2 was not detected. This is in agreement both with the tests carried out in the presence of scavengers (Figure 9.8A) and with the results of the electrochemical characterizations which showed that the potential of the conduction band is not compatible with H_2 formation (Figure 9.8B). It can be noticed that H_2 evolution coupled with HMF partial oxidation has been reported in the presence of C_3N_4 containing Pt [407] whilst by using $ZnIn_2S_4$ based photocatalysts (Pt- $ZnIn_2S_4$ [392] or Ni- $ZnIn_2S_4$ [408]) H_2 was obtained by using triethanolamine as scavenger.

Table 9.4 Conversion, selectivity and yield (Y) values during 0.5 mM HMF oxidation under 50 W halogen lamp irradiation in an open-air reactor after 5h of irradiation

Samples	X_{HMF} (%)	S_{FDC} (%)	S_{FCA} (%)	S_{HMFCA} (%)	Y_{FDC} (%)
BDH	53.6	4.8	0.9	-	2.6
Nb_2O_5	negligible	-	-	-	-
3% Nb_2O_5-BDH	46	6.8	1.0	6.9	3.2
Bi_2O_3	negligible	-	-	-	-
Cu_2O	negligible	-	-	-	-
TiO_2	14	46.1	negligible	9.2	6.3
C_3N_4	8	43.8	2.5	16.4	3.7
$ZnIn_2S_4$-1	27	58.2	1.9	4.2	15.5
$ZnIn_2S_4$-1 (O_2 bubbled)	64	23.7	2.1	1.4	15.0
$ZnIn_2S_4$-2	43	68.0	3.2	negligible	29.8
$ZnIn_2S_4$-2 (closed reactor)	23	47.1	1.6	3.4	11.1

Figure 9.7 shows the trends of the concentration of HMF and that of the main reaction intermediates as a function of the irradiation time by using the 50 W halogen lamp, in the presence of some selected photocatalysts. A progressive decrease in HMF conversion and increase in partial oxidation compounds can be noticed. With the various samples, a different amount of converted substrate and formed intermediates can be observed, and the highest FDC amount is obtained with

$ZnIn_2S_4$ based catalysts. These last are very promising photocatalysts in the field of selective oxidation of biomass derivatives under solar light irradiation in aqueous solution.

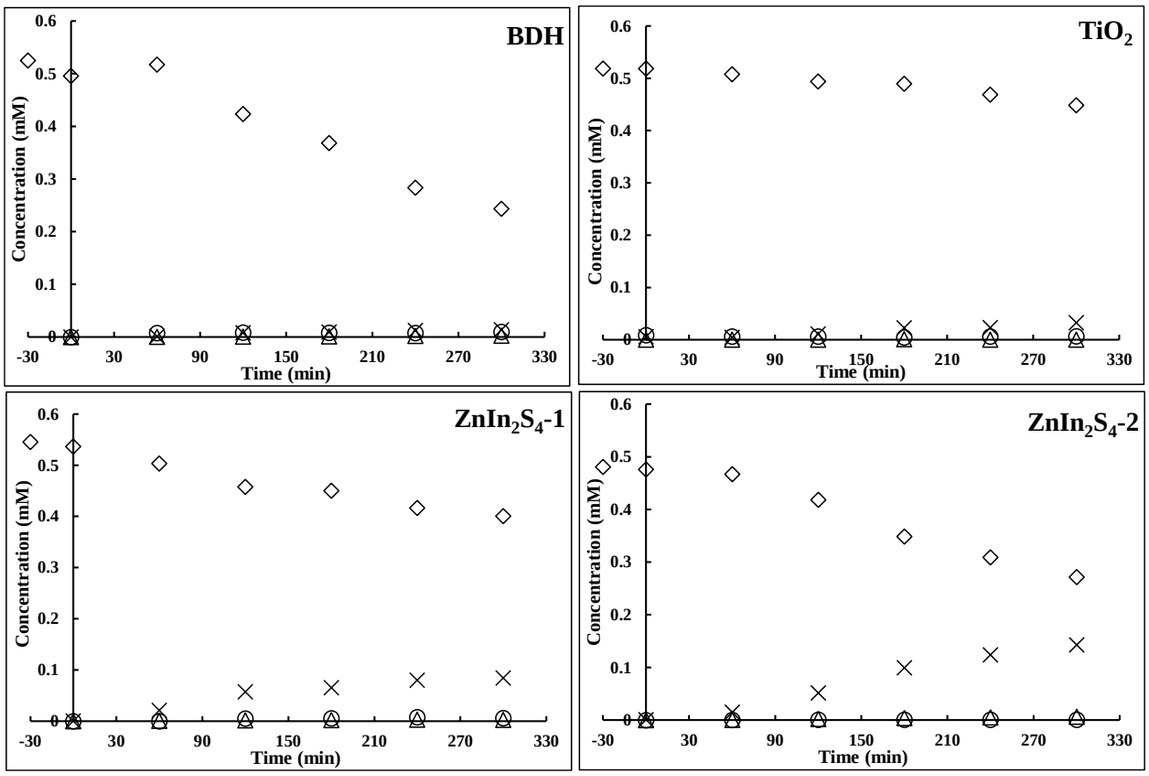

Figure 9.7 Concentrations of HMF (◊), FDC (x), FCA (○) and HMFCA (Δ) in the presence of some photocatalysts under 50 W halogen lamp irradiation

Figure 9.8A shows the variation of the concentration of HMF under simulated solar light irradiation in the presence of $ZnIn_2S_4$-2 as photocatalyst and the different scavengers. The results highlight that the dominant active species are e^- and $^{\bullet}O_2^-$ radicals since the lowest photoactivity is observed after the addition of $AgNO_3$ and benzoquinone. These findings, moreover, indicate the significant role of photogenerated e^- in the activation of O_2 to form $^{\bullet}O_2^-$ radicals. On the contrary, holes and hydroxyl radicals do not participate in the oxidation of HMF as no significant variations in the activity are observed after the addition of $Na_2C_2O_4$ and tert-butanol scavengers.

The energetic sketch reported in Figure 9.8B, related to the $ZnIn_2S_4$/electrolyte interface, was built by using the energetic levels obtained from the photoelectrochemical characterizations and it was used to confirm the photocatalytic mechanism. The Fermi level is found to be at ca. -0.2V, the CB energy is located at -0.4 V and by adding the band gap value to this one, the edge of the VB is found to be 1.9 V. By considering the potentials of the different redox couples involved in the photocatalytic process, the $ZnIn_2S_4$ energy level of the VB suppresses the generation of $^{\bullet}OH$ radicals whilst that of CB allows the generation of $^{\bullet}O_2^-$ radicals and hinders the H^+ reduction. As a result, the overoxidation of HMF through C-C cleavage is prevented [394, 395] leading to an increased formation of partial oxidation products and no H_2 is produced. In accordance with the reaction scheme reported in Figure 9.6, photogenerated electrons may react with O_2 to produce superoxide radicals that allows the preferential formation of FDC. In summary, the energy diagram highlights the effectiveness of $ZnIn_2S_4$ towards the HMF partial oxidation and the formation of specific valuable compounds.

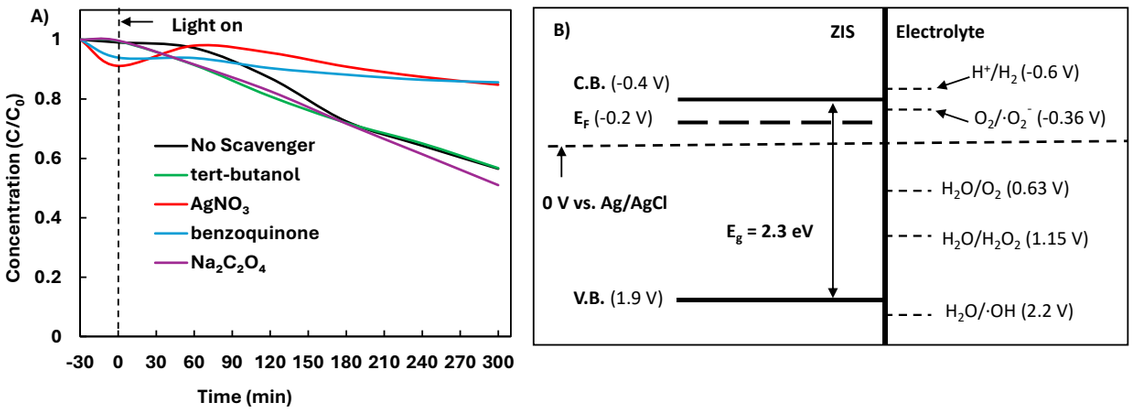

Figure 9.8 A) Concentrations of HMF during the runs carried out under 50 W halogen lamp irradiation in the presence of different scavengers and $ZnIn_2S_4$-2 as photocatalyst; B) Sketch of the energetic levels of the photocatalyst/electrolyte interface at pH=7

9.5 Mechanistic aspects

As far as the kinetics study is concerned, runs starting from different initial HMF concentrations were carried out by using $ZnIn_2S_4$-1 as the photocatalyst (Table 9.5). It showed that by increasing the substrate concentration, conversion decreased, and selectivity increased, in accordance with literature.

Table 9.5 Conversion and selectivity values and observed kinetic constants during HMF oxidation under 50 W halogen lamp irradiation in an open-air reactor after 5h of irradiation in the presence of $ZnIn_2S_4$-1

HMF (mM)	X_{HMF} (%)	S_{FDC} (%)	S_{FCA} (%)	S_{HMFCA} (%)	r ($M\ s^{-1}$)
0.1	42	29.8	1.7	13.0	$2.38E^{-09}$
0.5	27	58.1	1.9	4.2	$6.87E^{-09}$
0.7	17	56.0	2.8	9.1	$6.89E^{-09}$
1	15	65.6	1.3	4.7	$9.78E^{-09}$

In a photocatalytic process the primary step is the absorption of a radiation of suitable energy by the semiconductor with the formation of electron-hole pairs which must be trapped to avoid recombination. The experimental results carried out by using $ZnIn_2S_4$ as the photocatalyst, allow us to hypothesise the following mechanism:

$$ZnIn_2S_4 \xrightarrow{h\nu} ZnIn_2S_4 + h^+_{VB} + e^-_{CB} \quad (9.4)$$

Generally, holes are trapped by hydroxyl group with the formation of hydroxyl radicals, whereas electrons are trapped by adsorbed oxygen species according with the following reactions:

$$ZnIn_2S_{4(substrate)} - OH^-_S + h^+ \rightarrow ZnIn_2S_{4(substrate)} - OH^{\bullet}_{Ads} \quad (9.5)$$

$$O_{2(Ads)} + e^- \rightarrow {}^{\bullet}O^-_{2(Ads)} \quad (9.6)$$

As a consequence of the trapping of the photoproduced pairs, several species are produced and they could be involved in the reaction mechanism. By considering the results of the runs in the presence of the different scavengers, which indicate that the dominant active species are e^- and ${}^{\bullet}O_2^-$, the following reactions are hypothesised, in accordance with the scheme of Figure 9.6:

$$HMF + {}^{\bullet}O^{-}_{2(Ads)} \rightarrow FDC \tag{9.7}$$

$$FDC + OH^{\bullet}_{Ads} \rightarrow FCA \tag{9.8}$$

As the adsorbed oxygen acts as an electron trap thus hindering the electron–hole recombination, the radicals' concentration depends on the fractional sites' coverage by O_2. Assuming that two types of sites exist on the surface of the catalyst capable of adsorbing HMF and oxygen, respectively, the reaction rate for second-order surface oxidation of HMF may be written in terms of Langmuir–Hinshelwood kinetics as:

$$r = k'' \cdot \theta_{Ox} \cdot \theta_{HMF} \tag{9.9}$$

in which k'' is the second order rate constant and θ_{Ox} and θ_{HMF} are the fractional sites coverages by oxygen and HMF, respectively.

The fractional sites coverages are given by:

$$\theta_{Ox} = \frac{K_{Ox} C_{Ox}}{1 + K_{Ox} C_{Ox}} \tag{9.10}$$

$$\theta_{HMF} = \frac{K_{HMF} C_{HMF}}{1 + K_{HMF} C_{HMF}} \tag{9.11}$$

in which K_{Ox} and K_{HMF} are the equilibrium adsorption constant for oxygen and HMF, respectively and C_{Ox} and C_{HMF} the oxygen and HMF concentrations in liquid phase.

As all the experiments were carried out in a batch reactor open to the air, it may be assumed that the term θ_{Ox} remain constant during the HMF photooxidation. Equation 9.9 can therefore be written as:

$$r = k' \cdot \theta_{HMF} \tag{9.12}$$

in which k' is the pseudo-first order rate constant equal to $k'' \cdot \theta_{Ox}$.

By substituting equation 9.11 in equation 9.12 the following equation is obtained:

$$r = -\frac{dC_{HMF}}{dt} = k' \cdot \frac{K_{HMF} C_{HMF}}{1 + K_{HMF} C_{HMF}} \tag{9.13}$$

From the reactivity data reported in Figures 9.7, it may be noted that a straight line quite fits the data of concentration versus time indicating that the reaction is of pseudo zero order. Then we can write:

$$r = -\frac{dC_{HMF}}{dt} = k' \cdot \frac{K_{HMF} C_{HMF}}{1 + K_{HMF} C_{HMF}} = k_{obs} \tag{9.14}$$

in which k_{obs} is the observed kinetic constant determined by a regression procedure on the experimental data.

Figure 9.9 shows the values of r, determined from the experimental data, versus C_{HMF}. By applying a least-square best fitting procedure to the experimental data the values of k' ($k' = 1.83 \cdot 10^{-8}$ $M \cdot s^{-1}$) and K_{HMF} ($K_{HMF} = 1.1 \cdot 10^{3}$ M^{-1}) have been determined.

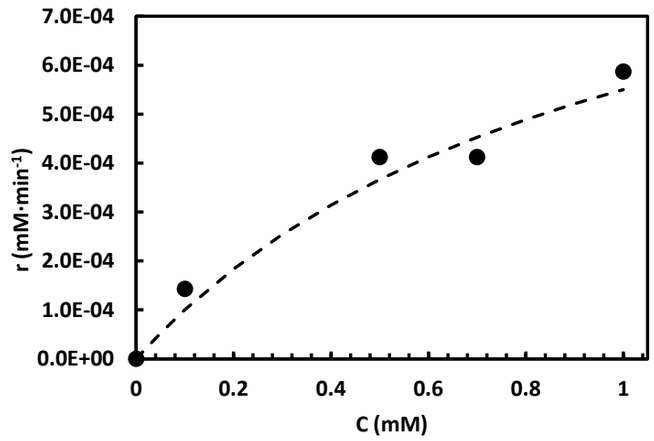

Figure 9.9 Experimental values of HMF reaction rate versus C_{HMF} (●). The dotted line represents the fitting of the model

A run was carried out by bubbling pure oxygen thus increasing the concentration of dissolving oxygen in the liquid phase. Figure 9.10 shows the data of reaction rate r versus the oxygen concentration C_{Ox} in presence of air (21% O_2) and in the presence of pure oxygen (100% O_2). A least square best fitting procedure allowed us to determine the K_{Ox} whose value is $9 \cdot 10^2$ M^{-1}. The value of k'' was determined from the value of k' and the fractional site coverage by oxygen under the operative conditions of the experimental runs (using air) and it is $1.95 \cdot 10^{-7}$ $M \cdot s^{-1}$. The obtained results are in accordance with the proposed kinetic model.

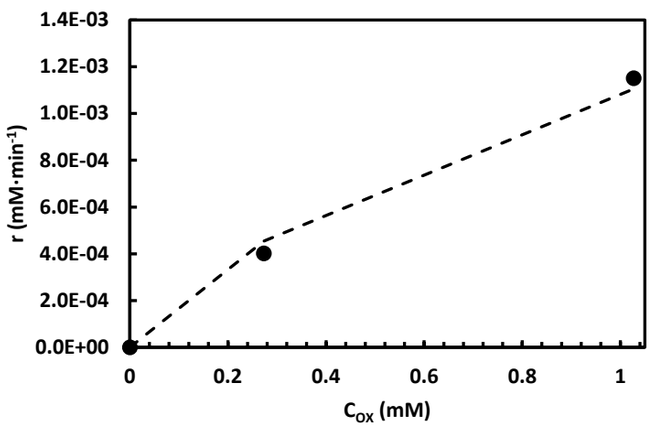

Figure 9.10 Experimental values of HMF reaction rate versus C_{Ox} (●). The dotted line represents the fitting of the model

9.6 Conclusions

This study reports an optimization of the experimental conditions during the partial oxidation of HMF in aqueous solution. Photocatalytic runs were carried out by varying the type and intensity of light radiation, the quantity of oxygen and the photocatalysts. As HMF is easily oxidized under the operative conditions used, the best results were obtained using low-power halogen lamps, atmospheric oxygen as the oxidant and catalysts alternative to TiO_2. $ZnIn_2S_4$ was the best performing photocatalyst affording both good HMF conversion and selectivity towards FDC. Electrochemical and mechanistic investigations revealed the dominant role of e^- and $^{\bullet}O_2^-$ radicals in the selective conversion of HMF. The experimental results confirmed that the kinetics follows the Langmuir-Hinshelwood model.

CHAPTER 10

Efficient photocatalytic removal of drugs in aqueous dispersions by using different TiO_2 based semiconductors

In this chapter, text is adapted from the following in preparation manuscript:
Muhammad Umair, Vittorio Loddo, Tayyaba Kanwal, Leonardo Palmisano, Marianna Bellardita. Efficient photocatalytic removal of drugs in aqueous dispersions by using different TiO_2 based semiconductors.

CHAPTER 10

Efficient photocatalytic removal of drugs in aqueous dispersions by using different TiO_2 based semiconductors

10.1 Abstract

Antibiotics are an important class of environmental pollutants. Due to their widespread use, low metabolism by organisms and persistence in the aquatic environment, they pose a serious risk to human health and environmental quality. The effective removal of pharmaceuticals and their metabolites from aqueous wastewater represents an audacious challenge for the scientific community. Heterogeneous photocatalysis has been applied as an effective technology for the removal of organic pollutants because it can induce their complete mineralization into CO_2, H_2O and inorganic species when heteroatoms are present in the degraded molecules without giving rise to the so-called secondary pollution.

This study is addressed to enhance the efficiency of differently modified commercial and home-prepared TiO_2 based photocatalysts towards some representative drugs (tetracycline, oxytetracycline and lincomycin). N-doped TiO_2 revealed high photocatalytic activity under both UV and simulated solar light irradiation, allowing not only the drugs removal but also a higher mineralization degree. $O_2^{\bullet-}$ radicals was found to be the main active species in the drugs degradation. Mechanistic investigations revealed a first order kinetics.

10.2 Photocatalysts preparation

10.2.1 Brookite/Rutile

The preparation method is already discussed in section 4-II.2.2 For comparison, prepared brookite was calcined at 450 °C and named as calcined brookite.

10.2.2 x%Cu_2O/WO_3–P25

The samples were prepared through a similar method as discussed in section 4-II.2.3

10.2.3 1:75 TiO_2 x%N

$TiCl_4$ and distilled water were added in a molar ratio of (1:75) in a beaker of 1000 mL and stirred until the formation of clear suspension. After that, different percentages of NH_4Cl were added to prepare N-doped photocatalysts. Then, the resulting mixture was placed in an oven at 100 °C for 48 h. The samples were identified as 1:75 for bare TiO_2 and 1:75 1%N, 1:75 2%N and 1:75 3%N for N-doped TiO_2.

10.2.4 1:75 TiO_2 HP

The preparation method is already discussed in section 4-I.2.1.

10.3 Results & discussions

10.3.1 Raman spectroscopy

Raman spectra of the used samples are reported in Figure 10.1. For single phase powder the main bands related to TiO_2 rutile (235.5, 445.8 and 609.5 cm^{-1}), anatase (144, 196, 397, 513 and 639 cm^{-1}) and brookite (153, 323, 366, 413, 459, 500, 545, 584 and 633 cm^{-1}) can be distinguished [381, 409, 410]. In the home made HP1 the bands characteristic of both anatase and rutile are observable whilst in the commercial TiO_2 P25 only the anatase peaks are visible. In the heterostructure no peaks corresponding to Cu_2O or WO_3 are observed, due to their low amount and uniform dispersion on P25 surface. Raman spectra of bare and N-doped HP2 powders reveal

the contemporary presence of anatase and brookite TiO_2 polymorphs, the addition of nitrogen doesn't modify the TiO_2 peaks position [411].

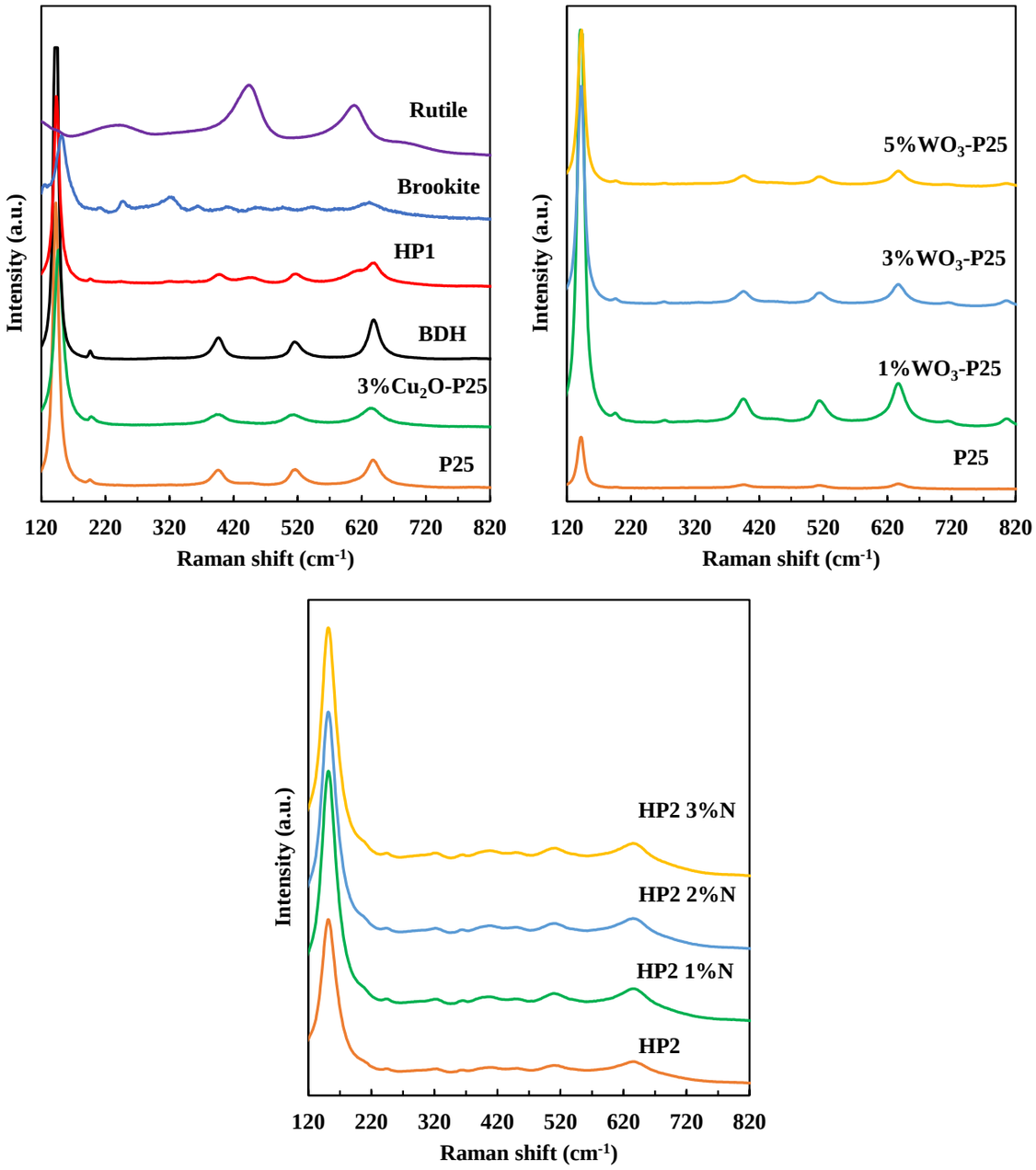

Figure 10.1 Raman spectra of the different samples

10.3.2 UV-Vis diffuse reflectance spectroscopy (DRS)

Figure 10.2 shows the UV-Vis DRS spectra of the different solids used. BDH and Brookite show an adsorption edge at ca. 360 nm corresponding to the typical anatase and brookite TiO_2 polymorphs band gap whilst a little shift towards higher wavelengths is presented by rutile and HP1, constituted by an anatase-rutile mixture. P25 displays a reflectance similar to that of anatase, being the main component; after coupling with Cu_2O a slight shift towards higher wavelengths along with an enhancement in the light absorption between 400 and 800 nm can be noticed. Moreover, the appearance of a second absorption edges attributable to the hosted oxide, confirming the formation of a heterostructure between the two components, is present [301, 412]. After the addition of WO_3, instead, only an increase in the light absorption at wavelengths higher than 400 nm is noticed for the higher WO_3 percentages. HP2 exhibits the typical reflectance shape of TiO_2 with a transition edge in the range of 360-390 nm. A slightly decrease in reflectance was observed in the presence of N. The band gap values of all photocatalysts were calculated by plotting the

modified Kubelka-Munk function, [F(R'∞)hν]½, versus the energy of the exciting light (Figure 10.2). The photocatalysts showed band gap values in the range of 2.96 to 3.26 eV.

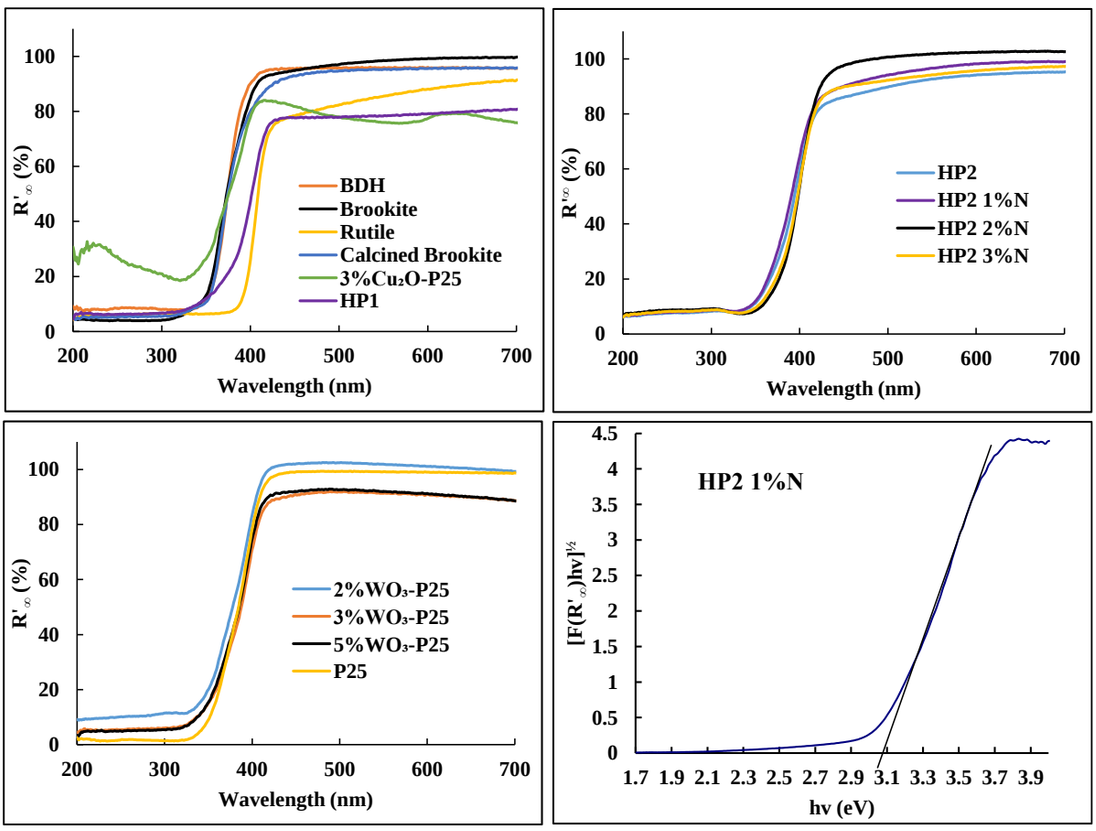

Figure 10.2 UV-Vis DRS spectra of different solids used and a [F(R'∞)hν]½ versus the energy of the exciting light for a selected catalyst

10.3.3 Specific surface area (SSA)

Table 10.1 shows the results of SSA and bad-gaps values determined for the used solids. The values very from 10 to 115 m^2 g^{-1} being the lower values showed by the commercial samples.

Table 10.1 Specific Surface Areas (SSA) and Band gap values of the different photocatalysts

Samples	TiO_2 Crystalline phase	SSA (m^2/g)	Band gap (eV)
BDH	A	10	3.17
Rutile	R	85	3.02
Brookite	B	88	3.26
Calcined Brookite	B	46	3.26
HP1	A, R	75	2.99
P25	A, R	48	3.18
3%Cu_2O-P25	A, R	48	3.08
2%WO_3-P25	A, R	33	3.09
3%WO_3-P25	A, R	36	3.09
5%WO_3-P25	A, R	34	3.11
HP2	A, R	115	3.03
HP2 1% N	A, R	113	3.04
HP2 2% N	A, R	81	3.02
HP2 3% N	A, R	87	3.03

10.3.4 Scanning electron microscopy (SEM)

Figure 10.3 SEM images of some selected samples used for drug degradation. All samples are formed by aggregates consisting of small particles of irregular shape with dimensions of the order of a few hundred nanometers. The presence of species other than TiO_2 is not observed, and these do not modify the morphology of the oxide that hosts them.

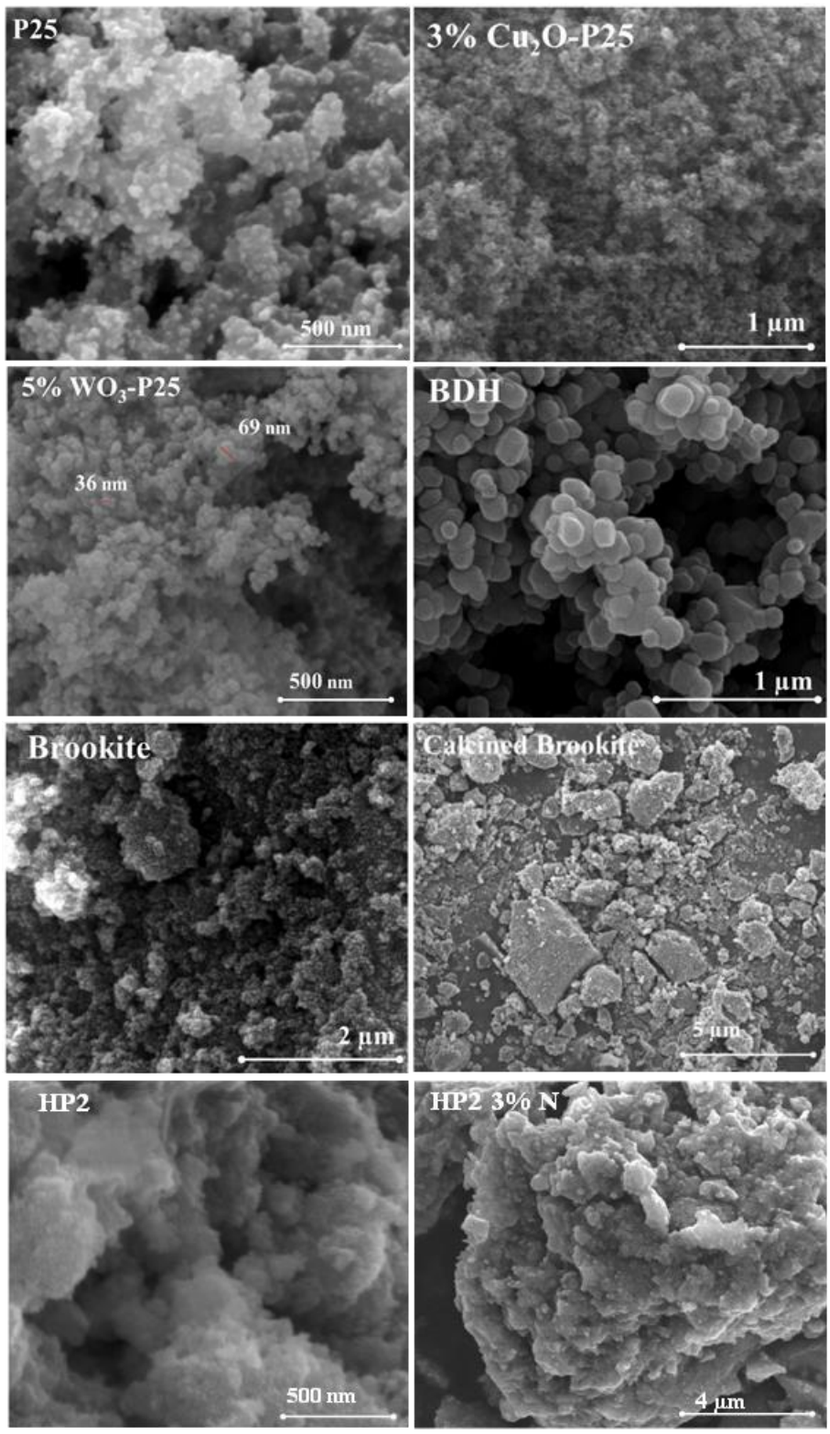

Figure 10.3 SEM images of the selected samples

10.4 Photocatalytic activity

Table 10.2 shows the results of the photocatalytic runs performed using the different photocatalysts in terms of pseudo first order constant and degree of mineralization after 4 h of irradiation. P25 was found to be active in the degradation of all drugs with degree of mineralization ranging from 33 to 77%. Commercial anatase (BDH) and home-made Brookite, Rutile and HP1

showed lower activity. For this reason, modified P25-based photocatalysts and a new nitrogen-modified TiO_2 photocatalyst (HP2), produced in the laboratory, were used. The coupling with 3% Cu_2O, unlike previous investigations related to glycerol photoreforming [301], was not advantageous in this case; only in the presence of LCM a slight improvement of the activity compared to pure P25 was obtained.

The addition of WO_3 to bare P25 caused an increase in the degree of mineralization of TC while it was deleterious in the degradation of drugs and in the mineralization of OTC and LCM. Using HP2, instead, a higher kinetic constant for TC and OTC was obtained together with a higher degree of mineralization of TC. Doping HP2 with 1%N an increase in the kinetic constant for TC and OTC was observed while the mineralization was maximum after the addition of 3% N reaching 81% after 4 h of irradiation. The performance of these samples was worse than that of bare P25 for LCM highlighting that it is not possible to establish in absolute terms which is the highest photoactivity but it should be attempted to correlate it to each single substrate considering the specific interactions between the latter and the surface of the photocatalyst [298, 351]. For complex molecules such as those studied in this work, however, this is not always easy. A very detailed analytical study would probably be necessary, in fact, to identify at least the main reaction intermediates for each of the three chosen substrates and verify which of these presents a higher photoreactivity on the surface of each of the photocatalysts used. However, this enormous analytical study is beyond the scope of this work.

Notably, the results reached in this study are valuable considering that, in the best experimental conditions, TC was completely degraded after 1h of irradiation and a TOC removal of 81% was obtained over 4h, with photocatalysts (N doped TiO_2) prepared in an easy and economical way.

In this work we will try to compare, using various characterization techniques, the various photocatalysts prepared with other commercial ones and understand which intrinsic electronic or chemical-physical surface characteristics can give indications on the observed behaviour. However, it must be clear to the reader that this is independent from the influence that the presence of different degradation intermediates for the three molecules can have on the observed photoreactivity. In fact, just as an example, very different photoabsorptions and photodesorptions phenomena and acidity of the intermediate species present during the reaction might significantly influence the interaction with the surface of the photocatalyst and therefore the reaction rate of the system both under UV and simulated solar irradiation.

Table 10.2 Pseudo first order rate constants and mineralization percentages determined by using the different photocatalysts with the used substrates

Sample	Tetracycline		Oxytetracycline		Lincomycin	
	Rate·10^4 [s^{-1}]	**Mineraliz. [%]**	**Rate·10^4 [s^{-1}]**	**Mineraliz. [%]**	**Rate·10^4 [s^{-1}]**	**Mineraliz. [%]**
No catalyst	0.6	5	negligible	negligible	0.04	negligible
P25	15.9	57	7.8	77	9.6	33
BDH	3.5	13	3.4	12	2.8	1
Brookite	7.5	45	4.6	51	2.5	10
Rutile	1.2	5	0.5	3	5.6	1
Calc. Brookite	4.5	34	3.8	19	8.7	4
3%Cu_2O-P25	6.8	55	8.4	44	10.9	32
HP1	5.5	41	6.7	55	2.1	11
2%WO_3-P25	4.1	60	3.9	40	3.2	13
3%WO_3-P25	6.0	75	5.4	36	3.8	30
5%WO_3-P25	3.1	61	3.3	25	3.5	10
HP2	17.7	77	10.6	59	2.3	11
HP2 1%N	22.5	75	9.4	61	3.7	16
HP2 2%N	1.2	76	7.7	69	1.8	13
HP2 3%N	6.7	81	9.0	78	2.5	10

To evaluate the efficiency of the prepared photocatalysts under real conditions, tests were carried out using a lamp simulating sunlight only in the presence of the most active samples. Figure 10.4 shows the TC concentration versus irradiation time in runs performed using P25 and HP2 1%N. The two powders were effective in converting TC in about 2 h and nitrogen-doped TiO_2 was more active than P25 for both conversion and drug mineralization which reached 70% after 4 h of irradiation with the home-made photocatalyst and 54% with P25. Probably, the presence of N in the TiO_2 lattice, although does not reduce its band gap, creates intermediate states close the valence band edge that enable the photocatalyst activation by visible light and reduce the electrons/holes recombination rate .

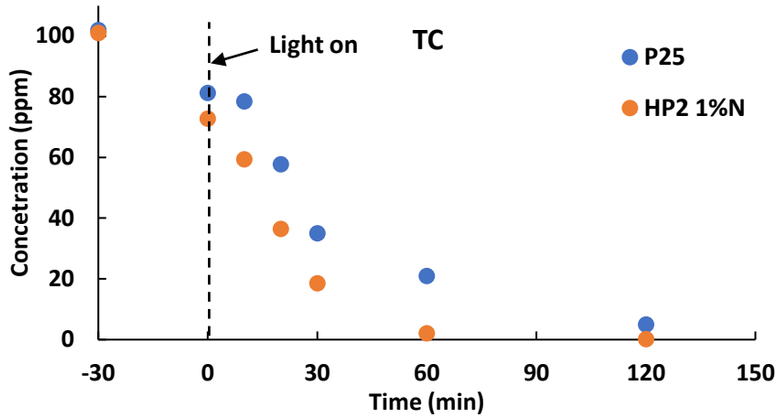

Figure 10.4 Photocatalytic degradation under simulated solar light irradiation of TC by using selected photocatalysts

10.5 Mechanistic aspects

All data fit pseudo first order kinetics very well. Table 10.2 shows the values of the observed pseudo-first order rate constants and the mineralization percentages determined using the different photocatalysts with the antibiotics used under UV irradiation. Figure 10.5 shows typical concentration versus time values for the runs carried out using the three drugs in the presence of HP2 3%N (the sample that gave the highest mineralization percentage for tetracycline (81%) and oxytetracycline (78%)). It can be seen that the exponential curves fit the data very well, thus confirming pseudo first order kinetics. The procedure for determining the kinetic parameters is described below.

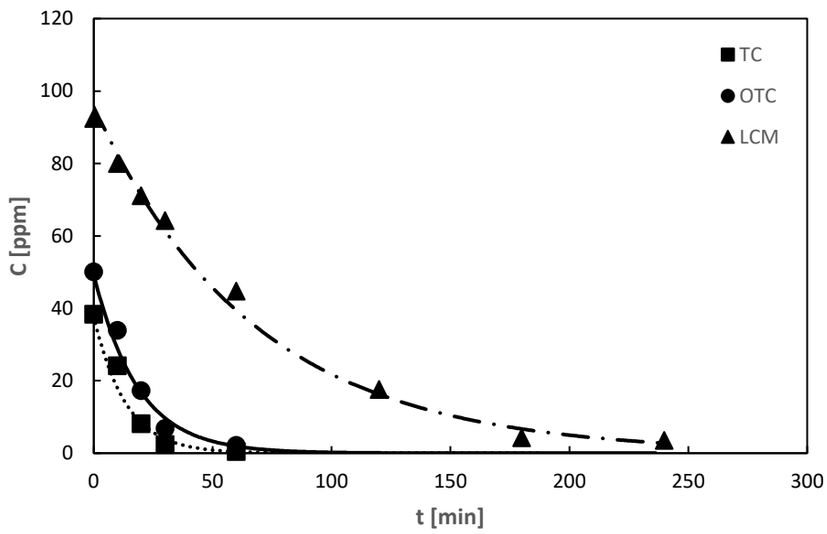

Figure 10.5 Concentration versus irradiation time for runs carried out with TiO_2 HP 3% N for the three drugs

Without solid catalyst, an appreciable photolytic degradation of tetracycline and oxytetracycline was observed, and about 70% of the first molecule disappeared in 4 hours. On the contrary, only 20% of lincomycin was destroyed at the same irradiation time.

This behaviour can be explained by comparing the absorption spectrum of the three molecules with the emission spectrum of the lamp (Figure 10.6). Both oxytetracycline and tetracycline reveal, in fact, absorption bands that partially overlap with the emission peaks of the lamp. Therefore, for these molecules it is necessary to take into account the simultaneous occurrence of two photolytic processes, one in the homogeneous phase and one in the adsorbed

phase (heterogeneous photocatalysis). For TC k_{obs} in homogeneous was 0.6 $\cdot 10^{-4}$ s^{-1} and only 5% of mineralization was observed. The photodegradation of lincomycin, which was found to be less significant than that observed for the other two molecules, can only be attributed to the photocatalytic reaction in the adsorbed phase as a very low degradation (k_{obs} = 4 $\cdot 10^{-6}$ s^{-1}) and a negligible mineralization degree was measured in homogeneous conditions, in accordance with its absorption spectrum (Figure 10.6).

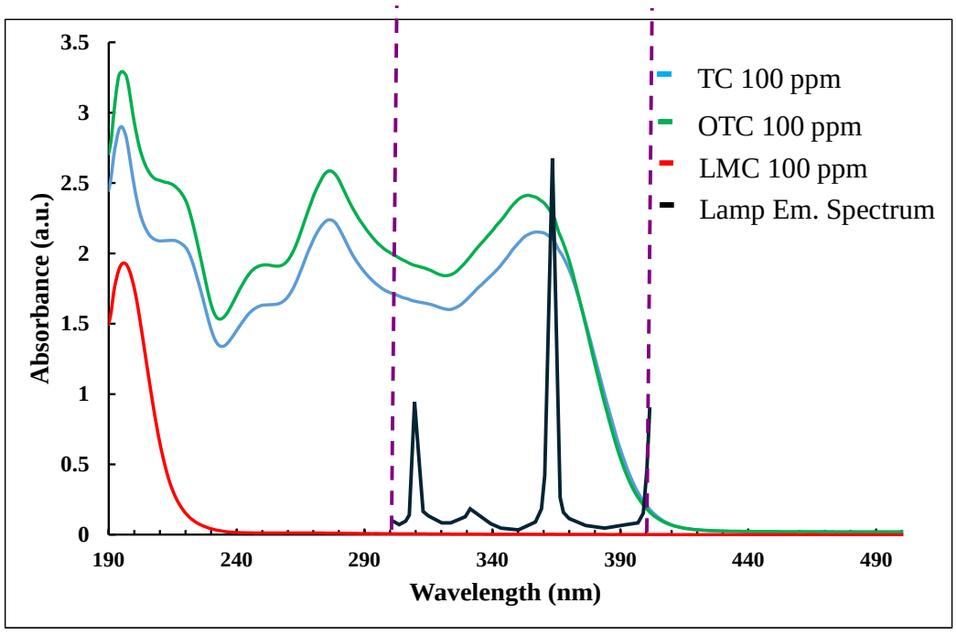

Figure 10.6 Absorption spectra of the substrates and emission spectrum of the medium pressure mercury lamp

The homogeneous photodegradation of an organic compound generally starts from an electronic excited state:

$$R \xrightarrow{h\nu} R^* \tag{10.1}$$

The excited R* species can undergo homolytic bond scission to form radicals that eventually react to give final products with or without the participation of molecular oxygen:

$$R^* \rightarrow R_1^\bullet + R_1^\bullet \rightarrow \text{products} \tag{10.2}$$

As far as the process of electronic transfer with oxygen molecules:

$$R^\bullet + O_2 \rightarrow R^{\bullet+} + O_2^{\bullet-} \tag{10.3}$$

Equation 10.3 is a typical quenching reaction. The radical cation, $R^{\cdot+}$, can undergo hydrolysis or mesolytic bond scission to low weight products, whereas the superoxide radical, $O_2^{\cdot-}$, is a very strong oxidant species able to degrade many aromatic species. Side-chain degradations by deamination, desulfuration and dealkylation are typical of many photolytic processes [413-416]. The homogeneous degradation of tetracycline can be attributed to a deamination of the molecule [253, 417, 418] which occurs when it is irradiated with near-UV light by producing dimethylamine (see Figure 10.7).

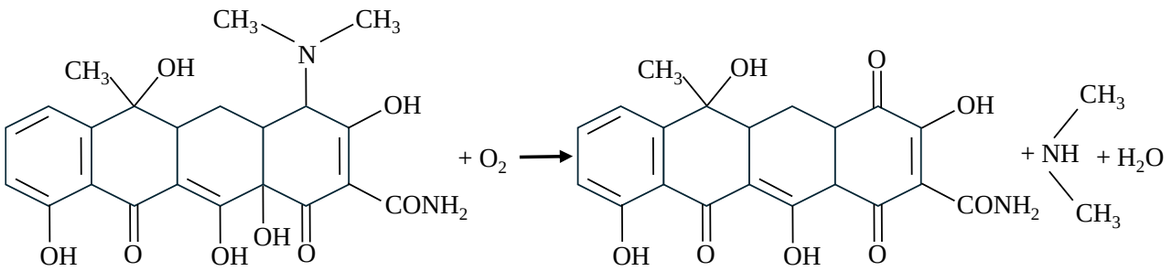

Figure 10.7 Scheme of homogeneous degradation of tetracycline in the presence of oxygen

The photochemical oxidation of lincomycin probably leads to the conversion of the thiomethyl group into sulfoxide and sulfone derivatives (see Figure 10.8).

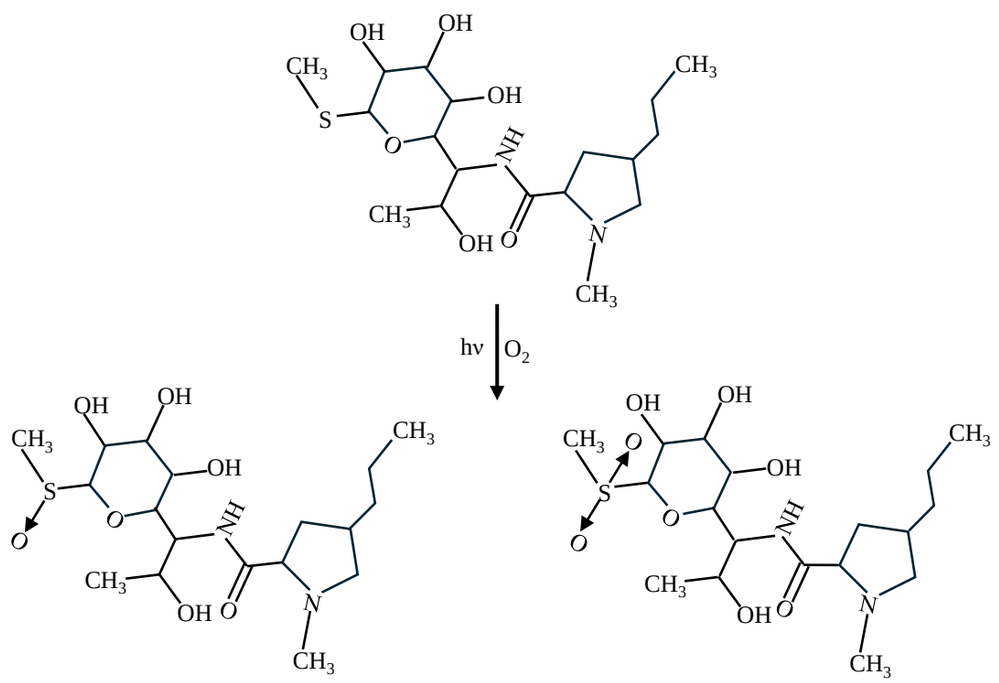

Figure 10.8 Scheme of photochemical degradation of lincomycin

As far as the mechanism of the heterogeneous photocatalytic reaction is concerned, the primary step is the generation of electrons and holes within the TiO_2 particle when it is irradiated by light of suitable energy.

$$TiO_2 \xrightarrow{h\nu} TiO_2 + e^-_{CB} + h^+_{VB} \quad (10.4)$$

Electrons and holes if properly separated can migrate to the surface of the particles where they can either recombine or participate in interfacial oxidation and reduction reactions. In aqueous solutions, the positive holes can react, with adsorbed water or with hydroxyl groups to form hydroxyl radicals $OH^{\cdot}$ which give rise to the oxidation reaction of a pollutant [419]:

$$H_2O + h^+_{VB} \rightarrow OH^{\bullet} + H^+ \quad (10.5)$$

$$OH^- + h^+_{VB} \rightarrow OH^{\bullet} \quad (10.6)$$

Hydroxyl radicals can also be formed by the photoproduced electrons via the following reactions:

$$O_2 + e^-_{CB} \rightarrow O_2^{\bullet -} \quad (10.7)$$

$$O_2^{\bullet -} + H_2O \rightarrow HO_2^{\bullet} + OH^- \quad (10.8)$$

$$HO_2^{\bullet} + H_2O \rightarrow H_2O_2 + OH^{\bullet} \quad (10.9)$$

To disclose the structural changes of TC during irradiation in the presence of HP2, the UV–Vis spectra recorded before and after the catalyst addition and under irradiation are reported in Figure 10.9. TC displays three main peaks at 200, 280 and 365 nm. The peak at 275 nm is related to the aromatic ring 1, the one at 365 nm derives from aromatic rings 2–4, including the chromophores groups. The progressive reduction of the last peak under irradiation indicates the fragmentation of phenolic groups linked to aromatic ring 2 while the reduction of absorbance at 280 nm is attributed to the formation of acylamino and hydroxyl groups.

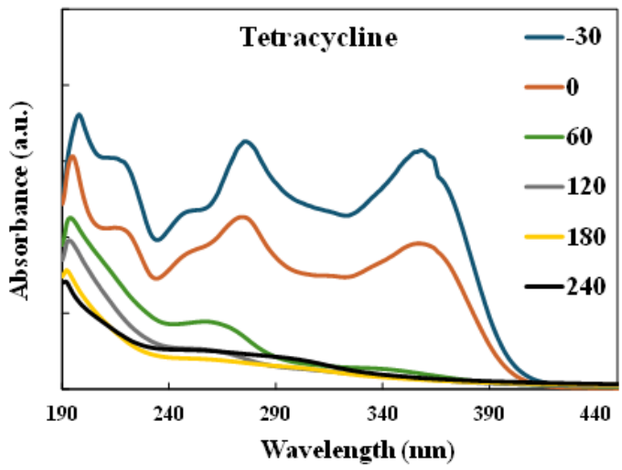

Figure 10.9 Absorption spectra of tetracycline under irradiation

In Figure 10.10 is reported the variation of concentration of TC and LCM under irradiation by using HP2 as photocatalyst in the absence and presence of various selected scavengers. The curves shown in the two graphs show the same trend, demonstrating that the photocatalyst behaves in the same way with the two drugs. Only after adding benzoquinone a decrease in the activity is observed indicating that $^{\bullet}O_2^-$ radicals are active species in the drugs degradation. On the contrary the removal of $^{\bullet}OH$ radicals, e^- and h^+ had a positive effect being the degradation enhanced in the presence of tert-butanol, $AgNO_3$ and $Na_2C_2O_4$, respectively. It can be assumed that the decrease in the amount of these species from the system, reduces the recombination rate of the photogenerated charges.

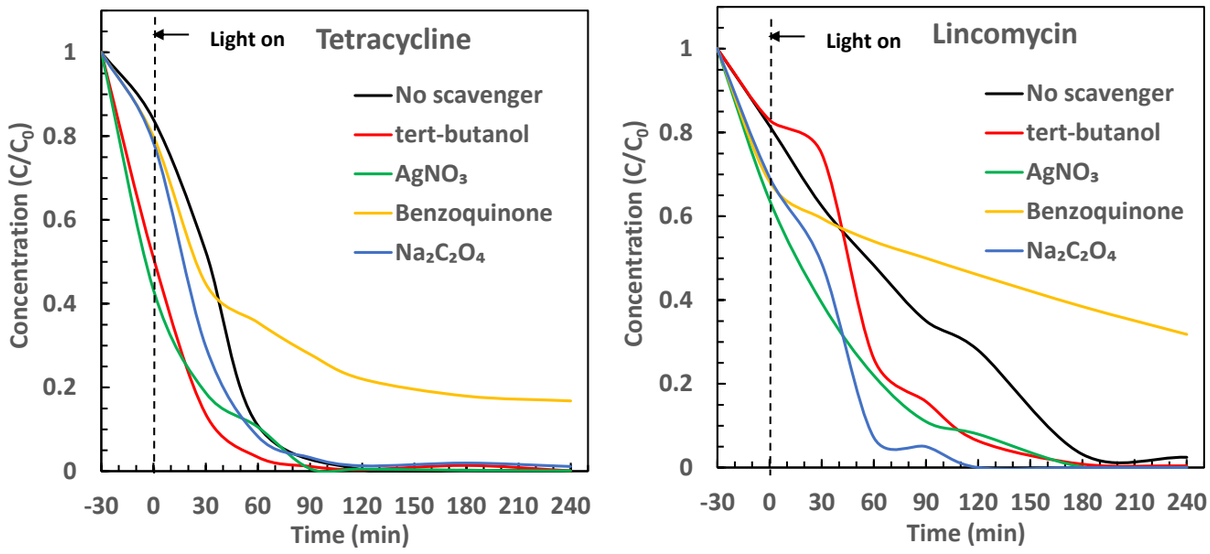

Figure 10.10 Concentration of TC and LCM versus irradiation time by using HP2 photocatalyst in the absence and presence of different scavenging species

10.6 Kinetic aspects

In the presence of an excess of molecular oxygen, the quenching of the excited state (Equation 10.3) is not a limiting step. By hypothesizing that the absorption of light is uniform in the reaction volume and the lifetimes of radicals and other reactive species are sufficiently long so that uniform concentrations throughout the reaction volume result from diffusion, it can be assumed that the rate of tetracycline degradation by homogeneous photochemical reaction, (r_{hom}), can be written as:

$$-r_{hom} = -\frac{1}{V}\frac{dN_D}{dt} = -\frac{dC_D}{dt} = k_{hom} I_a^n C_D^{\alpha} C_{Ox}^{\beta} \qquad (10.10)$$

In which V is the reaction volume, N_D the moles of drug (tetracycline or lincomycin), t the irradiation time, C_D and C_{Ox} the molar concentration of drug and oxygen, respectively, k_{hom} the rate constant, I_a the absorbed photon flow, n is an exponent ranging between 0.5 and 1, α and β the reaction orders of tetracycline and oxygen, respectively.

The experimental data suggest that the optical properties of the reacting solution do not change much during the photochemical degradation so that it may be assumed that the substrate and its oxydation intermediates have similar extinction coefficients. For this reason the absorbed photon flow, Ia, may be assumed constant during the photoreaction. All the experimental data obtained from the photochemical runs show exponential decreases of substrate concentration versus irradiation time, thus indicating first order kinetics with respect to the drug concentration. By assuming that the oxygen concentration in the solution is constant during the experiment (continuous bubbling), the reaction rate, Equation 10.10 can be written as:

$$-r_{hom} = -\frac{dC_D}{dt} = k'_{hom} C_D \qquad (10.11)$$

where k'_{hom} is the pseudo-first order rate constant and is equal to $k_{hom} I_a^n \cdot C_{Ox}$. It should be noted that k'_{hom} inversely depends on the initial drug concentration. Equation 10.11 can be integrated with the limiting condition that at t = 0, the substrate concentration is the initial one, $C_D = C_{D,0}$. The following relationship between C_D and t is determined:

$$C_D = C_{D,0} e^{(-k'_{hom} \cdot t)} \qquad (10.12)$$

The values of the observed rate constants were determined by applying a least squares best fitting procedure to the reactivity data. Table 10.2 reports the k'_{hom} values obtained from runs

carried out at different initial concentrations. The values reported in Table 10.3 indicate that, as expected, the values of k'_{hom} decrease with increasing initial drug concentration.

Table 10.3 Values of observed rate constants for reactions carried out in homogeneous regimen

Drug	Observed rate constants [s^{-1}]	50 ppm	75 ppm	100 ppm
Tetracycline	$k'_{homTC} \cdot 10^4$ [s^{-1}]	0.827	0.623	0.582
Lincomycin	$k'_{homLin} \cdot 10^4$ [s^{-1}]	0.182	0.168	0.021

Also, for the heterogeneous photocatalytic degradation the reactivity data fit well exponential curves, indicating that the degradation rate follows first order kinetics, as reported in the literature [420-426].

It must be remembered that the heterogeneous reaction occurs together with the homogeneous one, but the presence of the photocatalyst strongly reduces the intensity of the radiant field inside the reacting medium.

It can therefore be reasonably hypothesized that during the heterogeneous reaction the contribution of the homogeneous one to the overall drug degradation can be neglected, hypothesis supported by the results of the homogeneous runs upper reported. The rate of the heterogeneous photocatalytic reaction, ($-r_{hete}$), can be expressed in terms of the Langmuir–Hinshelwood model as:

$$-r_{hete} = -\frac{1}{S}\frac{dN_D}{dt} = -\frac{V}{S}\frac{dC_D}{dt} = k''\theta \tag{10.13}$$

where S is the photocatalyst active surface area, k'' the second order surface rate constant, and θ, the drug fractional site coverage which is given by:

$$\theta = \frac{K_D C_D}{1 + K_D C_D + \sum K_I C_I} \tag{10.14}$$

where K_D and K_I are the equilibrium adsorption constants of the drug and of the intermediate products, and C_D and C_I the concentrations in the fluid phase, respectively.

The first intermediates products generally are similar to the initial substrate and then it can be hypothesised that the interactions of the drug and the intermediate products with the catalyst surface are similar. For this reason it can be assumed that the values of the equilibrium adsorption constants are approximately equal [424, 426] and the following relationship can be written:

$$-\frac{dC_D}{dt} = \frac{S}{V}\left(\frac{k''K_D}{1 + K_D C_{D,0}}\right)C_D = \frac{S}{V}k_{hete}C_D \tag{10.15}$$

where $C_{D,0}$ is the initial drug concentration and k_{hete} is the observed first order rate constant. Equation 10.15 can be integrated with the limiting condition that at the beginning of the reaction, t = 0, the substrate concentration is the initial one, $C_D = C_{D,0}$. The integral relationship between C_D and t is:

$$C_D = C_{D,0}e^{\left(\frac{S}{V}k_{hete}t\right)} \tag{10.16}$$

By applying a least squares best fitting procedure to the experimental data, the values of the observed rate constants were determined and are reported in Table 10.4.

Table 10.4 Values of observed rate constants for reactions carried out in heterogeneous regimen

Drug	Observed rate constants [$m \cdot s^{-1}$]	50 ppm	75 ppm	100 ppm
Tetracycline	$k_{hete} \cdot 10^9$ [$m \cdot s^{-1}$]	21.0	13.0	9.0
Lincomycin	$k_{hete} \cdot 10^9$ [$m \cdot s^{-1}$]	3.9	3.2	2.4

The dependence of k_{hete} on the initial drug concentration may be linearized by considering its definition as:

$$\frac{1}{k_{hete}} = \frac{1}{k''} C_{D,0} + \frac{1}{k'' K_D} \tag{10.17}$$

Equation 10.17 represents a straight line by plotting $1/k_{hete}$ versus the initial tetracycline concentrations, $C_{T,0}$ (see Figure 10.11A). The value of the second order rate constant, k'' and of the equilibrium adsorption constant, K_T have been obtained by means of a least squares best fitting procedure by using HP2 3%N as the photocatalyst.

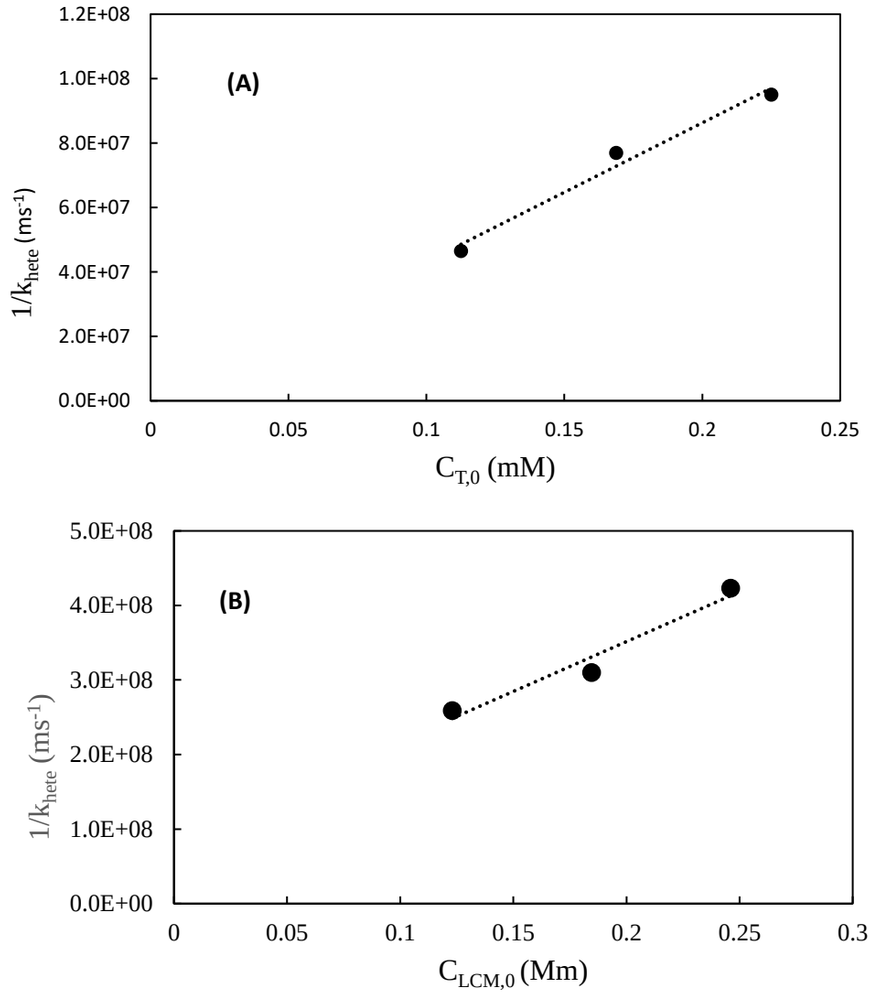

Figure 10.11 Values of $1/k_{hete}$ versus the initial concentrations for TC (A) and LCM (B) in the presence of HP2 3%N as the photocatalyst

The value of k'' obtained is $2.32 \cdot 10^{-9}$ $mM \cdot m \cdot s^{-1}$ whereas the value of K_T is 10952.5 mM^{-1}.

Figure 10.11B shows the plot of $1/k_{hete}$ versus the initial concentration of Lincomycin. Also in this case a straight line well fit the data. By applying a least square best fitting procedure the following values were determined: k'' is $7.48 \cdot 10^{-10}$ $mM \cdot m \cdot s^{-1}$ and K_L is 15.9 mM^{-1}.

It can be noticed that, under the operative conditions used, the second order reaction rate for Tetracycline is higher that tat of Lincomycin as well the adsorption constant, this last one indicates that under the same concentration the fractional sites coverage for Tetracycline is higher than that of Lincomycin.

10.7 Conclusions

Heterogeneous photocatalysis in the presence of differently modified TiO_2 based semiconductors was successfully applied to degrade drugs such as tetracycline, oxytetracycline and lincomycin present in wastewater. Homogeneous irradiation leads to partial degradation of both tetracycline and oxytetracycline and no degradation of lincomycin and causes almost negligible mineralization for all the drugs.

Photocatalysis increases both the reaction rate of the main compounds and the mineralization of the organic intermediates. TiO_2 based home prepared photocatalysts performed well and in some cases better than the commercial ones. The nitrogen doped TiO_2 samples were the best photocatalysts both for the degradation and the mineralization of the drugs, obtaining results comparable or superior to those obtained with the commercial TiO_2 powders also under simulated solar light irradiation. The experimental runs in the presence of selected scavengers highlighted that $O_2^{\bullet-}$ radicals are the active species in the drugs degradation. First order kinetics described adequately the experimental results and allowed the determination of the kinetic parameters of the homogeneous and the heterogeneous systems for the degradation reactions in the presence of the best photocatalyst. The search for photocatalysts, prepared under simple and economical synthetic conditions, effective upon direct solar irradiation opens the door to the use of pilot-scale reactors for large-scale wastewater treatment.

SUMMARY, CONCLUSION AND PERSPECTIVES

In this Ph.D. thesis, we explored the use of heterogeneous photocatalysis for H_2 and high valued added chemicals production and decontamination purposes under mild experimental conditions such as ambient pressure and temperature using water as the solvent. In particular, photoreforming of biomass derivatives such as glycerol, glucose and fructose, partial oxidation of 5-hydroxymethyl-2- furfural (HMF) to 2,5-diformylfuran (FDC), 5-formyl-2-furancarboxylic acid (FCA) and 5-hydroxymethyl-2-furan carboxylic acid (HMFCA) and aromatic alcohols to the corresponding aldehydes, was investigated. The degradation of common organic drugs such as tetracycline (TC), oxytetracycline (OTC) and lincomycin (LCM) was also studied in the presence of different photocatalysts.

Our effort was addressed to the synthesis of photocatalysts with enhanced performance with respect to the commercial ones by focusing on:

- activation of the photocatalysts by solar light irradiation;
- enhancement of the photogenerated charges transfer;
- addressing the photocatalysts' surface properties;
- replacement of noble metals with less dangerous and expensive species;
- search for alternative TiO_2 photocatalysts;
- extension of the photocatalytic method to real scale photoreactors.

Home made (HP) TiO_2 samples (modified with Pt and Nb_2O_5) performed better than the wide world used commercial TiO_2-P25(Pt-P25) during the photoreforming of glucose and fructose for both hydrogen and valuable chemicals production.

Pt as cocatalyst on TiO_2 was successfully replaced by Cu_2O and MBi_2O_4 (M = Cu, Ni, Co, Zn). Cu_2O-P25 and MBi_2O_4-P25 coupled systems synthesized by a simple and economic ball milling method were active for H_2 production by means of glucose and glycerol photoreforming.

As an alternative TiO_2 photocatalyst, a ternary chalcogenide $ZnIn_2S_4$ (ZIS) was obtained by a simple hydrothermal method in which the carcinogen thioacetamide, universally used as a precursor, for the first time has been successfully replaced by the harmless thiourea.

The photocatalytic performance under simulated sunlight irradiation of ZIS was higher than that of P25. During the photoreforming of furfuryl alcohol bare ZIS was found to be more active than Pt-P25 for both H_2 and furfural production, giving rise to about 22 $\mu mol \cdot g^{-1} \cdot h^{-1}$ of H_2 along with a furfuryl alcohol conversion and furfural selectivity of about 49% and 81%, respectively. These results are encouraging considering the simplicity of preparation of the photocatalyst and the environment friendly experimental conditions in light of a future large-scale implementation of the process under solar light irradiation.

ZIS was very active for the green partial oxidation of different aromatic alcohols to their corresponding aldehyde and of HMF to high value compounds. The photocatalytic performance of ZIS was better than of TiO_2 P25 reaching high value for both alcohols' conversion and selectivity to the corresponding aldehydes. This opens the possibility to apply the photocatalytic method in real applications by coupling the system with a separation unit, for example a membrane system, to separate and recover the formed aldehydes.

Furthermore, the use of heterogeneous photocatalysis has been extended from the laboratory scale to pilot plant scale. The coupled Cu_2O-TiO_2 photocatalysts prepared by ball milling procedure was effective for H_2 generation under sunlight irradiation in a pilot-scale reactor (25L) in the presence of different sacrificial agents, namely glycerol, glucose and ethanol. The results presented in this study give us hope for possible application development in other pilot plants of photocatalytic materials prepared by ball milling to realize H_2 production without the use of noble metals.

The last part of the thesis was focused on the application of photocatalysis for water remediation purposes by following the degradation and mineralization of three organic drugs such as tetracycline, oxytetracycline and lincomycin dissolved in water. Also in this case the home prepared TiO_2 based photocatalysts showed higher activity than the commercial ones both for the photo-oxidation and the mineralization of the drugs. These results are promising in view of the use of the photocatalytic method for the future research in a pilot plant photoreactor.

REFERENCES

[1] Osman, A.I.; Chen, L.; Yang, M.; Msigwa, G.; Farghali, M.; Fawzy, S.; Yap, P.S. Cost, environmental impact, and resilience of renewable energy under a changing climate: A review. *Environ. Chem. Lett.* **2023**, *21*, 741–764. https://doi.org/10.1007/s10311-022-01440-4

[2] Jaiswal, K.K.; Yadav, S.; Shukla, A.; Awasthi, A.; Dixit, S.; Patel, V. Renewable and sustainable clean energy development and impact on social, economic, and environmental health. *Energy Nexus* **2022**, *7*, 100118. https://doi.org/10.1016/j.nexus.2022.100118

[3] Ali, S.; Anwar, S.; Nasreen, S. Renewable and Non-Renewable Energy and Its Impact on Environmental Quality in South Asian Countries. *Forman J. Econ. Stud.* **2017**, *13*, 177–194.

[4] Hoel, M.; Kverndokk, S. Depletion of fossil fuels and the impacts of global warming. *Resource Energy Econ.* **1996**, *18*, 115–136. https://doi.org/10.1016/0928-7655(96)00005-X

[5] Stern, N. *The Economics of Climate Change: The Stern Review*; HM Treasury: London, UK, **2007**.

[6] IPCC. Climate change 2007: The physical science basis. Contribution of Working Group I to the Fourth Assessment Report of the Intergovernmental Panel on Climate Change; Solomon, S., Qin, D., Manning, M., Chen, Z., Marquis, M., Averyt, K.B., Tignor, M., Miller, H.L. (Eds.); Cambridge University Press: Cambridge, UK, and New York, NY, USA, **2007**; pp. 1–996.

[7] Jacobson, M.Z. Review of solutions to global warming, air pollution, and energy security. *Energy Environ. Sci.* **2009**, *2*, 148–173. https://doi.org/10.1039/B809990C

[8] Belaïd, F.; Zrelli, M.H. Renewable and non-renewable electricity consumption, environmental degradation and economic development: Evidence from Mediterranean countries. *Energy Policy* **2019**, *133*, 110929. https://doi.org/10.1016/j.enpol.2019.110929

[9] McKendry, P. Energy production from biomass (part 1): Overview of biomass. *Bioresour. Technol.* **2002**, *83*, 37–46. https://doi.org/10.1016/S0960-8524(01)00118-3

[10] Ali, F.; Dawood, A.; Hussain, A.; et al. Fueling the future: Biomass applications for green and sustainable energy. *Discov. Sustain.* **2024**, *5*, 156. https://doi.org/10.1007/s43621-024-00309-z

[11] Wang, K.; Tester, J.W. Sustainable management of unavoidable biomass wastes. *Green Energy Res.* **2023**, *1*, 100005. https://doi.org/10.1016/j.gerr.2023.100005

[12] Roy, S.; Dikshit, P.K.; Sherpa, K.C.; Singh, A.; Jacob, S.; Rajak, R.C. Recent nanobiotechnological advancements in lignocellulosic biomass valorization: A review. *J. Environ. Manag.* **2021**, *297*, 113422. https://doi.org/10.1016/j.jenvman.2021.113422

[13] Briens, C.; Piskorz, J.; Berruti, F. Biomass valorization for fuel and chemicals production-A review. *Int. J. Chem. React. Eng.* **2008**, *6*. https://doi.org/10.2202/1542-6580.1674

[14] Naveen, S.; Aravind, S.; Yamini, B.; Vasudhareni, R.; Gopinath, K.P.; Arun, J.; Pugazhendhi, A. A review on solar energy intensified biomass valorization and value-added products production: Practicability, challenges, techno-economic and lifecycle assessment. *J. Clean. Prod.* **2023**, *405*, 137028. https://doi.org/10.1016/j.jclepro.2023.137028

[15] Lewis, N.S.; Nocera, D.G. Powering the Planet: Chemical Challenges in Solar Energy Utilization. *PNAS* **2006**, *103*, 15729–15735. https://doi.org/10.1073/pnas.0603395103.

[16] Ola, O.; Maroto-Valer, M.M. Transition Metal Oxide Based TiO_2 Nanoparticles for Visible Light Induced CO_2 Photoreduction. *Appl. Catal. A Gen.* **2015**, *502*, 114–121. https://doi.org/10.1016/j.apcata.2015.06.007.

[17] Camarillo, R.; Tostón, S.; Martínez, F.; Jiménez, C.; Rincón, J. Enhancing the Photocatalytic Reduction of CO_2 through Engineering of Catalysts with High Pressure Technology: Pd/TiO_2 Photocatalysts. *J. Supercrit. Fluids* **2017**, *123*, 18–27. https://doi.org/10.1016/j.supflu.2016.12.010.

[18] Fiorenza, R.; Bellardita, M.; Balsamo, S.A.; Gulino, A.; Condorelli, M.; Compagnini, G.; Scirè, S.; Palmisano, L. A Solar Photothermo-Catalytic Combined Process for the VOCs Combustion and the Subsequent CO_2 Valorization Using Noble Metal-Free Catalysts. *Catal. Today* **2023**, *413–415*, 113949. https://doi.org/10.1016/j.supflu.2016.12.010.

[19] Bellardita, M.; Feilizadeh, M.; Fiorenza, R.; et al. Selective Aqueous Oxidation of Aromatic Alcohols Under Solar Light in the Presence of TiO_2 Modified with Different Metal Species. *Photochem. Photobiol. Sci.* **2022**, *21*, 2139–2151. https://doi.org/10.1007/s43630-022-00284-2.

[20] Shen, R.; Xie, J.; Guo, P.; Chen, L.; Chen, X.; Li, X. Bridging the g-C_3N_4 Nanosheets and Robust CuS Cocatalysts by Metallic Acetylene Black Interface Mediators for Active and Durable Photocatalytic H_2 Production. *ACS Appl. Energy Mater.* **2018**, *1*, 2232–2241. https://doi.org/10.1021/acsaem.8b00311.

[21] Cao, S.; Wang, C.J.; Fu, W.F.; Chen, Y. Metal Phosphides as Co-Catalysts for Photocatalytic and Photoelectrocatalytic Water Splitting. *ChemSusChem* **2017**, *10*, 4306–4323. https://doi.org/10.1002/cssc.201701450.

[22] Wierzbicka, E.; Kaczmarek, M.; Dziubek, K.; Rybicka, J.; Olszewski, M.; Grzyb, T.; Głowacki, M.; Zubko, M.; Wierzbicki, M. Reduced Grey Brookite for Noble Metal Free Photocatalytic H_2 Evolution. *J. Mater. Chem. A* **2021**, *9*, 1168–1179. https://doi.org/10.1039/d0ta09066b.

[23] United Nations. *Sustainable Development Goals*. United Nations Sustainable Development. Available online: https://www.un.org/sustainabledevelopment/sustainable-development-goals/ (accessed on 9 October 2024).

[24] European Commission. Communication from the Commission to the European Parliament, the European Council, the Council, the European Economic and Social Committee and the Committee of the Regions: *The European Green Deal*. COM/2019/640 final, 11 December 2019. Available online: https://eur-lex.europa.eu/legal-content/EN/TXT/?uri=CELEX%3A52019DC0640 (accessed on 9 October 2024).

[25] Lagioia, G.; Spinelli, M.P.; Amicarelli, V. Blue and Green Hydrogen Energy to Meet European Union Decarbonisation Objectives: An Overview of Perspectives and the Current State of Affairs. *Int. J. Hydrogen Energy* **2023**, *48*, 1304–1322. https://doi.org/10.1016/j.ijhydene.2022.10.044.

[26] Zhang, J.; Davis, D.; Brear, M.J. The Role of Hydrogen in Decarbonizing a Coupled Energy System. *J. Clean. Prod.* **2022**, *346*, 131082. https://doi.org/10.1016/j.jclepro.2022.131082.

[27] Oshiro, K.; Fujimori, S. Role of Hydrogen-Based Energy Carriers as an Alternative Option to Reduce Residual Emissions Associated with Mid-Century Decarbonization Goals. *Appl. Energy* **2022**, *313*, 118803. https://doi.org/10.1016/j.apenergy.2022.118803.

[28] Colangelo, G.; Spirto, G.; Milanese, M.; de Risi, A. Hydrogen Production from Renewable Energy Resources: A Case Study. *Energy Convers. Manag.* **2024**, *311*, 118532. https://doi.org/10.1016/j.enconman.2024.118532.

[29] Reda, B.; Elzamar, A.A.; AlFazzani, S.; et al. Green Hydrogen as a Source of Renewable Energy: A Step Towards Sustainability, An Overview. *Environ. Dev. Sustain.* **2024**. https://doi.org/10.1007/s10668-024-04892-z.

[30] Ni, M.; Leung, M.K.H.; Sumathy, K.; Leung, D.Y.C. Potential of Renewable Hydrogen Production for Energy Supply in Hong Kong. *Int. J. Hydrogen Energy* **2006**, *31*, 1401–1412. https://doi.org/10.1016/j.ijhydene.2005.11.005.

[31] Bellardita, M.; García-López, E.I.; Marcì, G.; Palmisano, L. Photocatalytic Formation of H_2 and Value-Added Chemicals in Aqueous Glucose (Pt)-TiO_2 Suspension. *Int. J. Hydrogen Energy* **2016**, *41*, 5934–5947. https://doi.org/10.1016/j.ijhydene.2016.02.103.

[32] Ishaq, T.; Yousaf, M.; Bhatti, I.A.; Batool, A.; Asghar, M.A.; Mohsin, M.; Ahmad, M. A Perspective on Possible Amendments in Semiconductors for Enhanced Photocatalytic Hydrogen Generation by Water Splitting. *Int. J. Hydrogen Energy* **2021**, *46*, 39036–39057. https://doi.org/10.1016/j.ijhydene.2021.09.165.

[33] Li, Y.; Somorjai, G.A. Nanoscale Advances in Catalysis and Energy Applications. *Nano Lett.* **2010**, *10*, 2289–2295. https://doi.org/10.1021/nl101807g.

[34] Steyn, J.W.; Render, C.L. Hydrogen as Energy Carrier. Available from: https://www.ownerteamconsult.com/hydrogen-as-energy-carrier/. Accessed on: 2 November 2024.

[35] Azizimehr, E.; Armaghani, T.; Ghasemiasl, R.; Kaabi Nejadian, A.; Javadi, M.A. A Comprehensive Review of Recent Developments in Hydrogen Production Methods Using a New Parameter. *Int. J. Hydrogen Energy* **2024**, *72*, 716–729. https://doi.org/10.1016/j.ijhydene.2024.05.219.

[36] Kothari, R.; Buddhi, D.; Sawhney, R.L. Comparison of Environmental and Economic Aspects of Various Hydrogen Production Methods. *Renewable Sustainable Energy Rev.* **2008**, *12*, 553–563. https://doi.org/10.1016/j.rser.2006.07.012.

[37] Nikolaidis, P.; Poullikkas, A. A Comparative Overview of Hydrogen Production Processes. *Renewable Sustainable Energy Rev.* **2017**, *67*, 597–611. https://doi.org/10.1016/j.rser.2016.09.044.

[38] Dincer, I. *Comprehensive Energy Systems*; Elsevier: Amsterdam, The Netherlands, 2018.

[39] Acar, C.; Dincer, I. Impact Assessment and Efficiency Evaluation of Hydrogen Production Methods. *Int. J. Energy Res.* **2015**, *39*, 1757–1768. https://doi.org/10.1002/er.3302.

[40] Rodriguez, C.A.; Modestino, M.A.; Psaltis, D.; Moser, C. Design and Cost Considerations for Practical Solar-Hydrogen Generators. *Energy Environ. Sci.* **2014**, *7*, 3828–3835. https://doi.org/10.1039/c4ee01453g.

[41] Wang, Y.; Li, H.; He, P.; Zhou, H. Controllable Hydrogen Generation from Water. *ChemSusChem* **2010**, *3*, 571–574. https://doi.org/10.1002/cssc.201000049.

[42] Nazir, H.; Jose, S.; Prasad, M.; Muthusubramanian, M.; Hussain, A.; Perez, A.; Zuniga, J. Is the H_2 Economy Realizable in the Foreseeable Future? Part I: H_2 Production Methods. *Int. J. Hydrogen Energy* **2020**, *45*, 13777–13788. https://doi.org/10.1016/j.ijhydene.2020.03.092.

[43] Fujishima, A.; Honda, K. Electrochemical Photolysis of Water at a Semiconductor Electrode. *Nature* **1972**, *238*, 37–38. https://doi.org/10.1038/238037a0.

[44] He, X.; Kai, T.; Ding, P. H. Heterojunction Photocatalysts for Degradation of the Tetracycline Antibiotic: A Review. *Environ. Chem. Lett.* **2021**, *19*, 4563–4601. https://doi.org/10.1007/s10311-021-01295-8.

[45] Meng, X.; Liu, Z.; Deng, C.; Zhu, M.; Wang, D.; Li, K.; Jiang, M. Microporous Nano-MgO/Diatomite Ceramic Membrane with High Positive Surface Charge for Tetracycline Removal. *J. Hazard. Mater.* **2016**, *320*, 495–503. https://doi.org/10.1016/j.jhazmat.2016.09.063.

[46] Li, Z.; Guo, C.; Lyu, J.; Hu, Z.; Ge, M. Tetracycline Degradation by Persulfate Activated with Magnetic Cu/$CuFe_2O_4$ Composite: Efficiency, Stability, Mechanism and Degradation Pathway. *J. Hazard. Mater.* **2019**, *373*, 85–96. https://doi.org/10.1016/j.jhazmat.2019.03.075.

[47] Han, Y.; Liu, H.; Wang, H.; Zhang, Y.; Xu, X.; Chen, W. Removal of Veterinary Antibiotics from Swine Wastewater Using Anaerobic and Aerobic Biodegradation. *Sci. Total Environ.* **2020**, *709*, 136094. https://doi.org/10.1016/j.scitotenv.2019.136094.

[48] Changanaqui, K.; Brillas, E.; Alarcón, H.; Sirés, I. ZnO/TiO_2/Ag_2Se Nanostructures as Photoelectrocatalysts for the Degradation of Oxytetracycline in Water. *Electrochim. Acta* **2020**, *331*, 135194. https://doi.org/10.1016/j.electacta.2019.135194.

[49] Bellardita, M.; Loddo, V.; Palmisano, L. Formation of High Added Value Chemicals by Photocatalytic Treatment of Biomass. *Mini Rev. Org. Chem.* **2020**, *17*, 884–901. https://doi.org/10.2174/1570193x17666200131112856.

[50] Bellardita, M.; García-López, E.I.; Marcì, G.; Nasillo, G.; Palmisano, L. Photocatalytic Solar Light H_2 Production by Aqueous Glucose Reforming. *Eur. J. Inorg. Chem.* **2018**, *2018*, 4522–4532. https://doi.org/10.1002/ejic.201800663.

[51] Parrino, F.; Bellardita, M.; García-López, E.I.; Marcì, G.; Loddo, V.; Palmisano, L. Heterogeneous Photocatalysis for Selective Formation of High-Value-Added Molecules: Some Chemical and Engineering Aspects. *ACS Catal.* **2018**, *8*, 11191–11225. https://doi.org/10.1021/acscatal.8b03712.

[52] Shen, R.; Xie, J.; Xiang, Q.; Chen, X.; Jiang, J.; Li, X. Ni-Based Photocatalytic H_2-Production Cocatalysts. *Chinese J. Catal.* **2019**, *40*, 240–288. https://doi.org/10.1016/S1872-2067(19)63294-8.

[53] Singh, R.; Dutta, S. A Review on H_2 Production through Photocatalytic Reactions Using TiO_2/TiO_2-Assisted Catalysts. *Fuel* **2018**, *220*, 607–620. https://doi.org/10.1016/j.fuel.2018.01.058.

[54] Christoforidis, K.C.; Fornasiero, P. Photocatalytic Hydrogen Production: A Rift into the Future Energy Supply. *ChemCatChem* **2017**, *9*, 1523–1544. https://doi.org/10.1002/cctc.201601659.

[55] Pecoraro, C.M.; Bellardita, M.; Loddo, V.; Di Franco, F.; Palmisano, L.; Santamaria, M. A Facile Way to Synthesize Noble Metal-Free TiO_2-Based Catalysts for Glycerol Photoreforming. *J. Ind. Eng. Chem.* **2023**, *118*, 247–258. https://doi.org/10.1016/j.jiec.2022.11.010.

[56] Pecoraro, C.M.; Bellardita, M.; Loddo, V.; Virtù, D.; Di Franco, F.; Santamaria, M. Photocatalytic and Photoelectrocatalytic H_2 Evolution Combined with Valuable Furfural Production. *Appl. Catal. A Gen.* **2023**, *650*, 118987. https://doi.org/10.1016/j.apcata.2023.118987.

[57] Pinaud, B.A.; Benck, J.D.; Seitz, L.C.; Forman, A.J.; Chen, Z.; Deutsch, T.G.; ...; Jaramillo, T.F. Technical and Economic Feasibility of Centralized Facilities for Solar Hydrogen Production via Photocatalysis and Photoelectrochemistry. *Energy Environ. Sci.* **2013**, *6*, 1983–2002. https://doi.org/10.1039/c3ee40831k.

[58] Goto, Y.; Hisatomi, T.; Wang, Q.; Higashi, T.; Ishikiriyama, K.; Maeda, T.; Domen, K. A Particulate Photocatalyst Water-Splitting Panel for Large-Scale Solar Hydrogen Generation. *Joule* **2018**, *2*, 509–520. https://doi.org/10.1016/j.joule.2018.01.013.

[59] Martha, S.; Sahoo, P.C.; Parida, K.M. An Overview on Visible Light Responsive Metal Oxide Based Photocatalysts for Hydrogen Energy Production. *RSC Adv.* **2015**, *5*(76), 61535–61553. https://doi.org/10.1039/c5ra11682a.

[60] Mills, A.; Le Hunte, S. An Overview of Semiconductor Photocatalysis. *J. Photochem. Photobiol. A Chem.* **1997**, *108*, 1–35. https://doi.org/10.1016/S1010-6030(97)00118-4.

[61] Bard, A.J. Design of Semiconductor Photoelectrochemical Systems for Solar Energy Conversion. *J. Phys. Chem.* **1982**, *86*, 172–177. https://doi.org/10.1021/j100391a008.

[62] Chen, X.; Shen, S.; Guo, L.; Mao, S.S. Semiconductor-Based Photocatalytic Hydrogen Generation. *Chem. Rev.* **2010**, *110*, 6503–6570. https://doi.org/10.1021/cr100164b.

[63] Kong, D.; Zheng, Y.; Kobielusz, M.; Wang, Y.; Bai, Z.; Macyk, W.; Wang, X.; Tang, J. Recent Advances in Visible Light-Driven Water Oxidation and Reduction in Suspension Systems. *Mater. Today* **2018**, *21*, 897–924. https://doi.org/10.1016/j.mattod.2018.04.009.

[64] Chen, X.; Shen, S.; Guo, L.; Mao, S.S. Semiconductor-Based Photocatalytic Hydrogen Generation. *Chem. Rev.* **2010**, *110*, 6503–6570. https://doi.org/10.1021/cr1001645.

[65] Shen, Z.K.; Yuan, Y.J.; Pei, L.; Yu, Z.T.; Zou, Z. Black Phosphorus Photocatalysts for Photocatalytic H_2 Generation: A Review. *Chem. Eng. J.* **2020**, *386*, 123997. https://doi.org/10.1016/j.cej.2020.123997.

[66] Chen, X.; Mao, S.S. Titanium Dioxide Nanomaterials: Synthesis, Properties, Modifications and Applications. *Chem. Rev.* **2007**, *107*, 2891–2959. https://doi.org/10.1021/cr0500535.

[67] Mu, R.; Zhao, Z.J.; Dohnálek, Z.; Gong, J. Structural Motifs of Water on Metal Oxide Surfaces. *Chem. Soc. Rev.* **2017**, *46*, 1785–1806. https://doi.org/10.1039/c6cs00864j.

[68] Ismael, M. Latest Progress on the Key Operating Parameters Affecting the Photocatalytic Activity of TiO_2-Based Photocatalysts for Hydrogen Fuel Production: A Comprehensive Review. *Fuel* **2021**, *303*, 121207. https://doi.org/10.1016/j.fuel.2021.121207.

[69] Xu, M.; Gao, Y.; Martinez Moreno, E.; Kunst, M.; Muhler, M.; Wang, Y.; Idriss, H.; Wöll, C. Photocatalytic Activity of Bulk TiO_2 Anatase and Rutile Single Crystals Using Infrared Absorption Spectroscopy. *Phys. Rev. Lett.* **2011**, *106*, 138302. https://doi.org/10.1103/PhysRevLett.106.138302.

[70] Nakata, K.; Fujishima, A. TiO_2 Photocatalysis: Design and Applications. *J. Photochem. Photobiol. C* **2012**, *13*, 169–189. https://doi.org/10.1016/j.jphotochemrev.2012.07.001.

[71] Hashimoto, K.; Irie, H.; Fujishima, A. TiO_2 Photocatalysis: A Historical Overview and Future Prospects. *Jpn. J. Appl. Phys.* **2005**, *44*, 8269–8285. https://doi.org/10.1143/JJAP.44.8269.

[72] Dong, H.; Zeng, G.; Tang, L.; Fan, C.; Zhang, C.; He, X.; He, Y. An Overview on Limitations of TiO_2-Based Particles for Photocatalytic Degradation of Organic Pollutants and the Corresponding Countermeasures. *Water Res.* **2015**, *79*, 128–146. https://doi.org/10.1016/j.watres.2015.04.038.

[73] Umair, M.; Loddo, V.; Palmisano, L.; Pintar, A.; Žerjav, G.; Palmisano, G.; Al Jitan, S.; Bellardita, M. Investigating the Activity of Modified TiO_2 Photocatalysts Used

for the Photoreforming of Biomass Derivatives. *J. Photochem. Photobiol. A* **2024**, *453*, 115654. https://doi.org/10.1016/j.jphotochem.2023.115654.

[74] (a) Yan, J.; Wu, G.; Guan, N.; Li, L. Nb_2O_5/TiO_2 Heterojunctions: Synthesis Strategy and Photocatalytic Activity. *Appl. Catal. B Environ.* **2014**, *152*, 280–288. https://doi.org/10.1016/j.apcatb.2014.01.049.

[74] (b) Catrinck, M. N.; Ribeiro, E. S.; Monteiro, R. S.; Ribas, R. M.; Barbosa, M. H. P.; Teófilo, R. F. Direct Conversion of Glucose to 5-Hydroxymethylfurfural Using a Mixture of Niobic Acid and Niobium Phosphate as a Solid Acid Catalyst. *Fuel* **2017**, *210*, 67–74. https://doi.org/10.1016/j.fuel.2017.08.035.

[74] (c) Huang, F.; Jiang, T.; Xu, X.; Chen, L.; Laurenczy, G.; Fei, Z.; Dyson, P. J. A $TiO_2/Nb_2O_5{\cdot}nH_2O$ Heterojunction Catalyst for Conversion of Glucose into 5-Hydroxymethylfurfural in Water. *Catal. Sci. Technol.* **2020**, *10* (23), 7857–7864. https://doi.org/10.1039/d0cy01601b.

[74] (d) Marzo, M.; Gervasini, A.; Carniti, P. Improving Stability of Nb_2O_5 Catalyst in Fructose Dehydration Reaction in Water Solvent by Ion-Doping. *Catal. Today* **2012**, *192* (1), 89–95. https://doi.org/10.1016/j.cattod.2011.12.014.

[74] (e) Weingarten, R.; Tompsett, G. A.; Conner, W. C.; Huber, G. W. Design of Solid Acid Catalysts for Aqueous-Phase Dehydration of Carbohydrates: The Role of Lewis and Brønsted Acid Sites. *J. Catal.* **2011**, *279* (1), 174–182. https://doi.org/10.1016/j.jcat.2011.01.013;

[74] (f) Qi, X.; Watanabe, M.; Aida, T. M.; Smith, R. L. Catalytical Conversion of Fructose and Glucose into 5-Hydroxymethylfurfural in Hot Compressed Water by Microwave Heating. *Catal. Commun.* **2008**, *9* (13), 2244–2249. https://doi.org/10.1016/j.catcom.2008.04.025.

[74] (g) Reche, M. T.; Osatiashtiani, A.; Durndell, L. J.; Isaacs, M. A.; Silva, Â.; Lee, A. F.; Wilson, K. Niobic Acid Nanoparticle Catalysts for the Aqueous Phase Transformation of Glucose and Fructose to 5-Hydroxymethylfurfural. *Catal. Sci. Technol.* **2016**, *6* (19), 7334–7341. https://doi.org/10.1039/C6CY01129B.

[75] Umair, M.; Palmisano, G.; Al Sakkaf, R.; Al Jitan, S.; Pintar, A.; Žerjav, G.; Palmisano, L.; Loddo, V.; Bellardita, M. Pt-Nb_2O_5-TiO_2 Based Semiconductors for Photo-Reforming of Glucose and Fructose Aqueous Solutions. *Appl. Surf. Sci.* **2024**, *648*, 159030. https://doi.org/10.1016/j.apsusc.2023.159030.

[76] (a) Qiao, P.; Wang, X.; Dai, M.; Piao, R.; Liu, H.; Wang, W.; Wang, Y.; Song, H. Ag and Cu_2O Bimetal Co-Modified TiO_2 Nanotubes with Enhanced Photocatalytic Performance. *Mater. Lett.* **2024**, *359*, 135923. https://doi.org/10.1016/j.matlet.2024.135923.

[76] (b) Mao, J.-X.; Wang, J.-C.; Gao, H.; Shi, W.; Jiang, H.-P.; Hou, Y.; Li, R.; Zhang, W.; Liu, L. S-Scheme Heterojunction of $CuBi_2O_4$ Supported Na-Doped P25 for Enhanced Photocatalytic H_2 Evolution. *Int. J. Hydrogen Energy* **2022**, *47* (13), 8214–8223. https://doi.org/10.1016/j.ijhydene.2021.12.133.

[76] (c) Ohno, T.; Akiyoshi, M.; Umebayashi, T.; Asai, K.; Mitsui, T.; Matsumura, M. Preparation of S-Doped TiO_2 Photocatalysts and Their Photocatalytic Activities under Visible Light. *Appl. Catal., A* **2004**, *265* (1), 115–121. https://doi.org/10.1016/j.apcata.2004.01.007.

[76] (d) Fontelles-Carceller, O.; Muñoz-Batista, M. J.; Conesa, J. C.; Fernández-García, M.; Kubacka, A. UV and Visible Hydrogen Photo-Production Using Pt-Promoted Nb-Doped TiO_2 Photocatalysts: Interpreting Quantum Efficiency. *Appl. Catal., B* **2017**, *216*, 133–145. https://doi.org/10.1016/j.apcatb.2017.05.022.

[76] (e) Ikeda, S.; Sugiyama, N.; Pal, B.; Marcí, G.; Palmisano, L.; Noguchi, H.; Uosaki, K.; Ohtani, B. Photocatalytic Activity of Transition-Metal-Loaded Titanium (IV) Oxide Powders Suspended in Aqueous Solutions: Correlation with Electron–Hole

Recombination Kinetics. *Phys. Chem. Chem. Phys.* **2001**, *3* (2), 267–273. https://doi.org/10.1039/b008028o.

[76] (f) Sun, X.; Liu, H.; Dong, J.; Wei, J.; Zhang, Y. Preparation and Characterization of Ce/N-Codoped TiO_2 Particles for Production of H_2 by Photocatalytic Splitting Water under Visible Light. *Catal. Lett.* **2010**, *135*, 219–225. https://doi.org/10.1007/s10562-010-0302-7.

[77] Iwasaki, M.; Hara, M.; Kawada, H.; Tada, H.; Ito, S. Cobalt Ion-Doped TiO_2 Photocatalyst Response to Visible Light. *J. Colloid Interface Sci.* **2000**, *224*, 202–204. https://doi.org/10.1006/jcis.1999.6694.

[78] Liu, Y.; Wang, Z.; Fan, W.; Geng, Z.; Feng, L. Enhancement of the Photocatalytic Performance of Ni-Loaded TiO_2 Photocatalyst under Sunlight. *Ceram. Int.* **2014**, *40*, 3887–3893. https://doi.org/10.1016/j.ceramint.2013.08.030.

[79] hen, W.-T.; Chan, A.; Sun-Waterhouse, D.; Moriga, T.; Idriss, H.; Waterhouse, G. I. N. Ni/TiO_2: A Promising Low-Cost Photocatalytic System for Solar H_2 Production from Ethanol–Water Mixtures. *J. Catal.* **2015**, *326*, 43–53. https://doi.org/10.1016/j.jcat.2015.03.008.

[80] Wang, K.; Yoshiiri, K.; Rosa, L.; Wei, Z.; Juodkazis, S.; Ohtani, B.; Kowalska, E. TiO_2/Au/TiO_2 Plasmonic Photocatalyst with Enhanced Photocatalytic Activity and Stability under Visible-Light Irradiation. *Catal. Today* **2022**, *397*, 257–264. https://doi.org/10.1016/j.cattod.2021.09.023.

[81] Gupta, B.; Melvin, A. A.; Matthews, T.; Dash, S.; Tyagi, A. K. TiO_2 Modification by Gold (Au) for Photocatalytic Hydrogen (H_2) Production. *Renew. Sustain. Energy Rev.* **2016**, *58*, 1366–1375. https://doi.org/10.1016/j.rser.2015.12.236.

[82] Jiang, Q.; Zhang, C.; Wang, Y.; Xu, J.; Zhao, J.; Wang, X.; Guo, S. Unraveling the Role of Ion Migration in the Water Splitting Performance of NiFeOx Hybrids. *J. Am. Chem. Soc.* **2014**, *136*, 2268–2271. https://doi.org/10.1021/ja412058x.

[83] Low, J.; Jiang, C.; Cheng, B.; Wageh, S.; Al-Ghamdi, A. A.; Yu, J. A Review of Direct Z-Scheme Photocatalysts. *Small Methods* **2017**, *1*, 1700080. https://doi.org/10.1002/smtd.201700080.

[84] Du, H.; Liu, Y.-N.; Shen, C.-C.; Xu, A.-W. Nanoheterostructured Photocatalysts for Improving Photocatalytic Hydrogen Production. *Chin. J. Catal.* **2017**, 38, 1295–1306. https://doi.org/10.1016/S1872-2067(17)62866-3.

[85] Qi, K.; Cheng, B.; Yu, J.; Ho, W. A Review on TiO_2-Based Z-Scheme Photocatalysts. *Chinese J. Catal.* **2017**, 38, 1936–1955. https://doi.org/10.1016/S1872-2067(17)62962-0.

[86] Wang, Y.; Ding, Z.; Arif, N.; Jiang, W.-C.; Zeng, Y.-J. 2D Material Based Heterostructures for Solar Light Driven Photocatalytic H_2 Production. *Mater. Adv.* **2022**, *3*, 3389–3417. https://doi.org/10.1039/D2MA00047A.

[87] Zhou, P.; Yu, J.; Jaroniec, M. All-Solid-State Z-Scheme Photocatalytic Systems. *Adv. Mater.* **2014**, *26*, 7784–7791. https://doi.org/10.1002/adma.201400288.

[88] Maeda, K. Z-Scheme Water Splitting Using Two Different Semiconductor Photocatalysts. *ACS Catal.* **2013**, *3*, 1486–1503. https://doi.org/10.1021/cs4002089.

[89] Bellardita, M.; Fiorenza, R.; D'Urso, L.; Spitaleri, L.; Gulino, A.; Compagnini, G.; Scirè, S.; Palmisano, L. Exploring the Photothermo-Catalytic Performance of Brookite TiO_2-CeO_2 Composites. *Catalysts* **2020**, *10*, 765. https://doi.org/10.3390/catal10070765

[90] Zhang, L.; Zhang, J.; Yu, H.; Yu, J. Emerging S-Scheme Photocatalyst. *Adv. Mater.* **2022**, *34*, 2107668. https://doi.org/10.1002/adma.202107668.

[91] Xu, Q.; Zhang, L.; Cheng, B.; Fan, J.; Yu, J. S-Scheme Heterojunction Photocatalyst. *Chem* **2020**, *6*, 1543–1559. https://doi.org/10.1016/j.chempr.2020.04.007.

[92] Wang, X.; Sayed, M.; Ruzimuradov, O.; Zhang, J.; Fan, Y.; Li, X.; Bai, X.; Low, J. A Review of Step-Scheme Photocatalysts. *Appl. Mater. Today* **2022**, *29*, 101609. https://doi.org/10.1016/j.apmt.2022.101609.

[93] Wang, Y.; Ding, Z.; Arif, N.; Jiang, W.-C.; Zeng, Y.-J. 2D Material Based Heterostructures for Solar Light Driven Photocatalytic H_2 Production. *Mater. Adv.* **2022**, *3*, 3389–3417. https://doi.org/10.1039/d2ma00191h.

[94] Bowker, M.; Gilbert, L.; Counsell, J.; Morgan, C. Dehydrogenation Versus Decarbonylation of Oxygenates on Pd (110): Pure, Clean Pd Is a Poor Catalyst. *J. Phys. Chem. C* **2010**, *114*, 17142–17147. https://doi.org/10.1021/jp104837t.

[95] Shen, R.; Xie, J.; Ding, Y.; Liu, S.-Y.; Adamski, A.; Chen, X.; Li, X. Carbon Nanotube-Supported Cu_3P as High-Efficiency and Low-Cost Cocatalysts for Exceptional Semiconductor-Free Photocatalytic H_2 Evolution. *ACS Sustain. Chem. Eng.* **2019**, *7*, 3243–3250. https://doi.org/10.1021/acssuschemeng.8b05185.

[96] Shen, R.; Xie, J.; Lu, X.; Chen, X.; Li, X. Bifunctional Cu_3P Decorated g-C_3N_4 Nanosheets as a Highly Active and Robust Visible-Light Photocatalyst for H_2 Production. *ACS Sustain. Chem. Eng.* **2018**, *6*, 4026–4036. https://doi.org/10.1021/acssuschemeng.7b04403.

[97] Lu, X.; Xie, J.; Liu, S.-Y.; Adamski, A.; Chen, X.; Li, X. Low-Cost Ni_3B/$Ni(OH)_2$ as an Ecofriendly Hybrid Cocatalyst for Remarkably Boosting Photocatalytic H_2 Production over g-C_3N_4 Nanosheets. *ACS Sustain. Chem. Eng.* **2018**, *6*, 13140–13150. https://doi.org/10.1021/acssuschemeng.8b02653.

[98] He, K.; Xie, J.; Yang, Z.; Shen, R.; Fang, Y.; Ma, S.; Chen, X.; Li, X. Earth-Abundant WC Nanoparticles as an Active Noble-Metal-Free Co-Catalyst for the Highly Boosted Photocatalytic H_2 Production over g-C_3N_4 Nanosheets under Visible Light. *Catal. Sci. Technol.* **2017**, *7*, 1193–1202. https://doi.org/10.1039/C7CY00029D.

[99] Wen, J.; Xie, J.; Zhang, H.; Zhang, A.; Liu, Y.; Chen, X.; Li, X. Constructing Multifunctional Metallic Ni Interface Layers in the g-C_3N_4 Nanosheets/Amorphous NiS Heterojunctions for Efficient Photocatalytic H_2 Generation. *ACS Appl. Mater. Interfaces* **2017**, *9*, 14031–14042. https://doi.org/10.1021/acsami.7b02701.

[100] Wen, J.; Xie, J.; Yang, Z.; Shen, R.; Li, H.; Luo, X.; Chen, X.; Li, X. Fabricating the Robust g-C_3N_4 Nanosheets/Carbons/NiS Multiple Heterojunctions for Enhanced Photocatalytic H_2 Generation: An Insight into the Trifunctional Roles of Nanocarbons. *ACS Sustain. Chem. Eng.* **2017**, *5*, 2224–2236. https://doi.org/10.1021/acssuschemeng.6b02490.

[101] Cao, S.; Piao, L.; Chen, X. Emerging Photocatalysts for Hydrogen Evolution. *Trends Chem.* **2020**, *2*, 57–70. https://doi.org/10.1016/j.trechm.2019.06.009.

[102] Wang, C.; Zhang, X.; Wei, Y.; Kong, L.; Chang, F.; Zheng, H.; Wu, L.; Zhi, J.; Liu, Y. Correlation between Band Alignment and Enhanced Photocatalysis: A Case Study with Anatase/TiO_2(B) Nanotube Heterojunction. *Dalton Trans.* **2015**, *44*, 13331–13339. https://doi.org/10.1039/C5DT01860A.

[103] Asahi, R.; Morikawa, T.; Irie, H.; Ohwaki, T. Nitrogen-Doped Titanium Dioxide as Visible-Light-Sensitive Photocatalyst: Designs, Developments, and Prospects. *Chem. Rev.* **2014**, *114*, 9824–9852. https://doi.org/10.1021/cr5000738.

[104] Peh, C.K.N.; Gao, M.; Ho, G.W. Harvesting Broadband Absorption of the Solar Spectrum for Enhanced Photocatalytic H_2 Generation. *J. Mater. Chem. A* **2015**, *3*, 19360–19367. https://doi.org/10.1039/c5ta05042a.

[105] Xu, S.; Sun, D.D. Significant Improvement of Photocatalytic Hydrogen Generation Rate over TiO_2 with Deposited CuO. *Int. J. Hydrogen Energy* **2009**, *34*, 6096–6104. https://doi.org/10.1016/j.ijhydene.2009.05.119.

[106] Yamakata, A.; Ishibashi, T.A.; Onishi, H. Microsecond Kinetics of Photocatalytic Oxidation on Pt/TiO_2 Traced by Vibrational Spectroscopy. *Chem. Phys. Lett.* **2003**, *376*, 576–580. https://doi.org/10.1016/S0009-2614(03)01034-0.

[107] Yamakata, A.; Ishibashi, T.A.; Kato, H.; Kudo, A.; Onishi, H. Photodynamics of $NaTaO_3$ Catalysts for Efficient Water Splitting. *J. Phys. Chem. B* **2003**, *107*, 14383–14387. https://doi.org/10.1021/jp036473k.

[108] Liu, X.; et al. Photothermal Effect of Infrared Light to Enhance Solar Catalytic Hydrogen Generation. *Catal. Commun.* **2017**, *102*, 13–16. https://doi.org/10.1016/j.catcom.2017.08.014.

[109] Khani, Y.; Tahay, P.; Bahadoran, F.; Safari, N.; Soltanali, S.; Alavi, A. Synergic Effect of Heat and Light on the Catalytic Reforming of Methanol over Cu/x-TiO_2 (x = La, Zn, Sm, Ce) Nanocatalysts. *Appl. Catal. A Gen.* **2020**, *594*, 117456. https://doi.org/10.1016/j.apcata.2020.117456.

[110] Malato, S.; Maldonado, M.I.; Fernández-Ibáñez, P.; Oller, I.; Polo, I.; Sánchez-Moreno, R. Decontamination and Disinfection of Water by Solar Photocatalysis: The Pilot Plants of the Plataforma Solar de Almería. *Mater. Sci. Semicond. Process* **2016**, *42*, 15–23. https://doi.org/10.1016/j.mssp.2015.07.017.

[111] Puga, A.V. Photocatalytic Production of Hydrogen from Biomass-Derived Feedstocks. *Coord. Chem. Rev.* **2016**, *315*, 1–66. https://doi.org/10.1016/j.ccr.2015.12.009.

[112] Shimura, K.; Yoshida, H. Heterogeneous Photocatalytic Hydrogen Production from Water and Biomass Derivatives. *Energy Environ. Sci.* **2011**, *4*, 2467–2481. https://doi.org/10.1039/c1ee01120k.

[113] Chiarello, G.L.; Ferri, D.; Selli, E. Effect of the CH_3OH/H_2O Ratio on the Mechanism of the Gas-Phase Photocatalytic Reforming of Methanol on Noble Metal-Modified TiO_2. *J. Catal.* **2011**, *280*, 168–177. https://doi.org/10.1016/j.jcat.2011.03.013.

[114] Chiarello, G.L.; Aguirre, M.H.; Selli, E. Hydrogen Production by Photocatalytic Steam Reforming of Methanol on Noble Metal-Modified TiO_2. *J. Catal.* **2010**, *273*, 182–190. https://doi.org/10.1016/j.jcat.2010.05.012.

[115] Sreethawong, T.; Puangpetch, T.; Chavadej, S.; Yoshikawa, S. Quantifying Influence of Operational Parameters on Photocatalytic H_2 Evolution over Pt-Loaded Nanocrystalline Mesoporous TiO_2 Prepared by Single-Step Sol-Gel Process with Surfactant Template. *J. Power Sources* **2007**, *165*, 861–869. https://doi.org/10.1016/j.jpowsour.2006.12.050.

[116] Speltini, A.; Sturini, M.; Dondi, D.; et al. Sunlight-Promoted Photocatalytic Hydrogen Gas Evolution from Water-Suspended Cellulose: A Systematic Study. *Photochem. Photobiol. Sci.* **2014**, *13*, 1410–1419. https://doi.org/10.1039/c4pp00128a.

[117] Speltini, A.; Sturini, M.; Maraschi, F.; Dondi, D.; Serra, A.; Profumo, A.; Buttafava, A.; Albini, A. Swine Sewage as Sacrificial Biomass for Photocatalytic Hydrogen Gas Production: Explorative Study. *Int. J. Hydrogen Energy* **2014**, *39*, 11433–11440. https://doi.org/10.1016/j.ijhydene.2014.05.168.

[118] ellardita, M.; Augugliaro, V.; Loddo, V.; Megna, B.; Palmisano, G.; Palmisano, L.; Puma, M.A. Selective Oxidation of Phenol and Benzoic Acid in Water via Home-Prepared TiO_2 Photocatalysts: Distribution of Hydroxylation Products. *Appl. Catal. A Gen.* **2012**, *441–442*, 79–89. https://doi.org/10.1016/j.apcata.2012.07.019.

[119] Ohno, T.; Sarukawa, K.; Matsumura, M. Photocatalytic Activities of Pure Rutile Particles Isolated from TiO_2 Powder by Dissolving the Anatase Component in HF Solution. *J. Phys. Chem. B* **2001**, *105*, 2417–2420. https://doi.org/10.1021/jp003211z.n

[120] Zhu, J.; Zheng, W.; He, B.; Zhang, J.; Anpo, M. Characterization of Fe–TiO_2 Photocatalysts Synthesized by Hydrothermal Method and Their Photocatalytic Reactivity for Photodegradation of XRG Dye Diluted in Water. *J. Mol. Catal. A Chem.* **2004**, *216*, 35–43. https://doi.org/10.1016/j.molcata.2004.01.008.

[121] Shi, J.; Chen, J.; Feng, Z.; Chen, T.; Lian, Y.; Wang, X.; Li, C. Photoluminescence Characteristics of TiO_2 and Their Relationship to the Photoassisted Reaction of Water/Methanol Mixture. *J. Phys. Chem. C* **2007**, *111*, 693–699. https://doi.org/10.1021/jp065744z.

[122] Bellardita, M.; García-López, E. I.; Marcì, G.; Palmisano, L. Photocatalytic Formation of H_2 and Value-Added Chemicals in Aqueous Glucose (Pt)-TiO_2 Suspension. *Int. J. Hydrogen Energy* **2016**, *41*, 5934–5947. https://doi.org/10.1016/j.ijhydene.2016.02.103.

[123] Rosseler, O.; Shankar, M. V.; Le Du, M. K.; Schmidlin, L.; Keller, N.; Keller, V. Solar Light Photocatalytic Hydrogen Production from Water over Pt and Au/TiO_2 (Anatase/Rutile) Photocatalysts: Influence of Noble Metal and Porogen Promotion. *J. Catal.* **2010**, *269*, 179–190. https://doi.org/10.1016/j.jcat.2009.11.006.

[124] Kandiel, T. A.; Feldhoff, A.; Robben, L.; Dillert, R.; Bahnemann, D. W. Tailored Titanium Dioxide Nanomaterials: Anatase Nanoparticles and Brookite Nanorods as Highly Active Photocatalysts. *Chemistry of Materials* **2010**, *22*, 2050–2060. https://doi.org/10.1021/cm903472p.

[125] Xu, H.; Zhang, L. Controllable One-Pot Synthesis and Enhanced Photocatalytic Activity of Mixed-Phase TiO_2 Nanocrystals with Tunable Brookite/Rutile Ratios. *J. Phys. Chem. C* **2009**, *113*, 1785–1790. https://doi.org/10.1021/jp8089903.

[126] Jitputti, J.; Pavasupree, S.; Suzuki, Y.; Yoshikawa, S. Synthesis and Photocatalytic Activity for Water-Splitting Reaction of Nanocrystalline Mesoporous Titania Prepared by Hydrothermal Method. *J. Solid State Chem.* **2007**, *180*, 1743–1749. https://doi.org/10.1016/j.jssc.2007.03.018.

[127] Testino, A.; Olivetti, A.; Guglielmi, M.; Nannetti, R.; Gori, G. Optimizing the Photocatalytic Properties of Hydrothermal TiO_2 by the Control of Phase Composition and Particle Morphology. A Systematic Approach. *J. Am. Chem. Soc.* **2007**, *129*, 3564–3575. https://doi.org/10.1021/ja067050+.

[128] Liu, G.; Zhang, X.; Wang, L.; Liu, Z.; Li, S.; Xie, Y. Nanosized anatase TiO_2 single crystals for enhanced photocatalytic activity. *Chem. Commun.* **2010**, *46*, 755–757. https://doi.org/10.1039/b919895d.

[129] Chae, S.Y.; Park, M.K.; Lee, S.K.; Kim, T.Y.; Kim, S.K.; Lee, W.I. Preparation of size-controlled TiO_2 nanoparticles and derivation of optically transparent photocatalytic films. *Chem. Mater.* **2003**, *15*, 3326–3331. https://doi.org/10.1021/cm030171d.

[130] Sun, W.; Zhang, S.; Liu, Z.; Wang, C.; Mao, Z. Studies on the enhanced photocatalytic hydrogen evolution over Pt/PEG-modified TiO_2 photocatalysts. *Int. J. Hydrogen Energy* **2008**, *33*, 1112–1117. https://doi.org/10.1016/j.ijhydene.2007.12.059.

[131] Sathish, M.; Viswanathan, B.; Viswanath, R.P. Alternate synthetic strategy for the preparation of CdS nanoparticles and its exploitation for water splitting. *Int. J. Hydrogen Energy* **2006**, *31*, 891–898. https://doi.org/10.1016/j.ijhydene.2005.08.002.

[132] Kudo, A. Photocatalyst materials for water splitting. *Catal. Surv. Asia* **2003**, *7*, 31–38. https://doi.org/10.1023/A:1023480507710.

[133] Guo, L.J.; Zhao, L.; Jing, D.W.; Lu, Y.J.; Yang, H.H.; Bai, B.F.; Zhang, X.M.; Ma, L.J.; Wu, X.M. Reprint of: Solar Hydrogen Production and Its Development in China. *Energy* **2010**, *35*, 4421–4438. https://doi.org/10.1016/j.energy.2010.08.010.

[134] Zinoviev, S.; Müller-Langer, F.; Das, P.; Bertero, N.; Fornasiero, P.; Kaltschmitt, M.; Centi, G.; Miertus, S. Next-Generation Biofuels: Survey of Emerging Technologies and Sustainability Issues. *ChemSusChem* **2010**, *3*, 1106–1133. https://doi.org/10.1002/cssc.201000052.

[135] Al-Madanat, O.; Alsalka, Y.; Dillert, R.; Bahnemann, D.W. Photocatalytic H_2 Production from Naphthalene by Various TiO_2 Photocatalysts: Impact of Pt Loading and Formation of Intermediates. *Catalysts* **2021**, *11*, 1–20. https://doi.org/10.3390/catal11010107.

[136] Al-Madanat, O.; AlSalka, Y.; Ramadan, W.; Bahnemann, D.W. TiO_2 Photocatalysis for the Transformation of Aromatic Water Pollutants into Fuels. *Catalysts* **2021**, *11*, 317. https://doi.org/10.3390/catal11030317

[137] Wu, G.; Chen, T.; Zhou, G.; Zong, X.; Li, C. H_2 Production with Low CO Selectivity from Photocatalytic Reforming of Glucose on Metal/TiO_2 Catalysts. *Sci. China Chem.* **2008**, *51*, 97–100. https://doi.org/10.1007/s11426-007-0132-7.

[138] Chaturvedi, S.; Dave, P.N. Photocatalytic Hydrogen Production. *Mater. Sci. Forum* **2013**, *764*, 151–168. https://doi.org/10.4028/www.scientific.net/msf.764.151.

[139] Pajares, A.; Wang, Y.; Kronenberg, M.J.; Ramírez de la Piscina, P.; Homs, N. Photocatalytic H_2 Production from Ethanol Aqueous Solution Using TiO_2 with Tungsten Carbide Nanoparticles as Co-Catalyst. *Int. J. Hydrogen Energy* **2020**, *45*(40), 20558–20567. https://doi.org/10.1016/j.ijhydene.2020.04.010.

[140] Sato, S.; White, J.M. Reactions of Water with Carbon and Ethylene Over Illuminated Pt/TiO_2. *Chem. Phys. Lett.* 1980, ***70***, 131–134. https://doi.org/10.1016/0009-2614(80)80077-7.

[141] Kawai, T.; Sakata, T. Photocatalytic Hydrogen Production from Water by the Decomposition of Poly-Vinylchloride, Protein, Algae, Dead Insects, and Excrement. *Chem. Lett.* **1981**, *10*(1), 81–84. https://doi.org/10.1246/cl.1981.81.

[142] Hashimoto, K.; Kawai, T.; Sakata, T. Photocatalytic Reactions of Hydrocarbons and Fossil Fuels with Water: Hydrogen Production and Oxidation. *J. Phys. Chem.* **1984**, *88*(18), 4083–4088. https://doi.org/10.1021/j150662a046

[143] Harada, H.; Sakata, T.; Ueda, T. Effect of Semiconductor on Photocatalytic Decomposition of Lactic Acid. *J. Am. Chem. Soc.* **1985**, *107*, 1773–1774. https://doi.org/10.1021/ja00299a043

[144] Jiang, Z.; Qi, R.; Huang, Z.; Shangguan, W.; Wong, R. J.; Lee, A. Impact of Methanol Photomediated Surface Defects on Photocatalytic H_2 Production Over Pt/TiO_2. *Energy Environ. Mater.* 2020, *3*, 202–208. https://doi.org/10.1002/eem2.12068.

[145] Yi, H.; Peng, T.; Ke, D.; Zan, L.; Yan, C. Photocatalytic H_2 Production from Methanol Aqueous Solution over Titania Nanoparticles with Mesostructures. *Int. J. Hydrogen Energy* 2008, *33*, 672–678. https://doi.org/10.1016/j.ijhydene.2007.10.034

[146] Serhan, M.; Jackemeyer, D.; Long, M.; Sprowls, M.; Diez Perez, I.; Maret, W.; Chen, F.; Tao, N.; Forzani, E. Total Iron Measurement in Human Serum with a Novel Smartphone-Based Assay. *IEEE J. Transl. Eng. Health Med.* **2020**, *8*, 1–9. https://doi.org/10.1109/JTEHM.2020.3005308

[147] Carraro, G.; Maccato, C.; Gasparotto, A.; Montini, T.; Turner, S.; Lebedev, O.I.; Gombac, V.; et al. Enhanced Hydrogen Production by Photoreforming of Renewable

Oxygenates through Nanostructured Fe_2O_3 Polymorphs. *Adv. Funct. Mater.* **2014**, *24*, 372–378. https://doi.org/10.1002/adfm.201302043.

[148] Esteban, J.; Yustos, P.; Ladero, M. Catalytic Processes from Biomass-Derived Hexoses and Pentoses: A Recent Literature Overview. *Catalysts* **2018**, *8*, 637. https://doi.org/10.3390/catal8120637

[149] Liu, X.; Duan, X.; Wei, W.; Wang, S.; Ni, B.J. Photocatalytic Conversion of Lignocellulosic Biomass to Valuable Products. *Green Chem.* **2019**, *21*, 4266–4289. https://doi.org/10.1039/c9gc01728c.

[150] Guo, F.; Fang, T.; Zhou, T.-J. Conversion of Fructose and Glucose into 5-Hydroxymethylfurfural with Lignin-Derived Carbonaceous Catalyst under Microwave Irradiation in Dimethyl Sulfoxide–Ionic Liquid Mixtures. *Bioresour. Technol.* **2012**, *112*, 313–318. https://doi.org/10.1016/j.biortech.2012.02.108.

[151] G. C. de Assis, I. M. A. Silva, T. G. dos Santos, T. V. dos Santos, M. R. Meneghetti, and S. M. P. Meneghetti, *Photocatalytic processes for biomass conversion*, *Catal. Sci. Technol*. **2021**, *11*, 2354-2360, https://doi.org/10.1039/d0cy02358b.

[152] Ma, B.; Wang, Y.; Guo, X.; Tong, X.; Liu, C.; Wang, Y.; Guo, X. Photocatalytic synthesis of 2,5-diformylfuran from 5-hydroxymethylfurfural or fructose over bimetallic Au-Ru nanoparticles supported on reduced graphene oxides. *Appl. Catal. A Gen.* **2018**, *552*, 70–76. https://doi.org/10.1016/j.apcata.2018.01.002.

[153] Zhang, Y.; Yang, S.; Wang, Z.; Qin, H.; Lyu, G.; Chen, J.; Yang, G. High Selective Conversion of Fructose to Lactic Acid by Photocatalytic Reforming of $BiOBr/Zn_x@SnO_{2-n}$ in Alkaline Condition. *J. Catal.* **2022**, *413*, 843–857. https://doi.org/10.1016/j.jcat.2022.07.042.

[154] Bellardita, M.; García-López, E.I.; Marcì, G.; Megna, B.; Pomilla, F.R.; Palmisano, L. Photocatalytic Conversion of Glucose in Aqueous Suspensions of Heteropolyacid-TiO_2 Composites. *RSC Adv.* **2015**, *5*, 59037–59047. https://doi.org/10.1039/c5ra09894g.

[155] Seadira, T.; Sadanandam, G.; Ntho, T.A.; Lu, X.; Masuku, C.M.; Scurrell, M. Hydrogen Production from Glycerol Reforming: Conventional and Green Production. *Rev. Chem. Eng.* **2018**, *34*, 695–726. https://doi.org/10.1515/revce-2016-0064.

[156] Lakshmana Reddy, N.; Cheralathan, K.K.; Durga Kumari, V.; Neppolian, B.; Muthukonda Venkatakrishnan, S. Photocatalytic Reforming of Biomass-Derived Crude Glycerol in Water: A Sustainable Approach for Improved Hydrogen Generation Using $Ni(OH)_2$-Decorated TiO_2 Nanotubes under Solar Light Irradiation. *ACS Sustainable Chem. Eng.* **2018**, *6*, 3754–3764. https://doi.org/10.1021/acssuschemeng.7b04118.

[157] Maslova, V.; Fasolini, A.; Offidani, M.; Albonetti, S.; Basile, F. Solar-Driven Valorization of Glycerol Towards Production of Chemicals and Hydrogen. *Catal. Today* **2021**, *380*, 147–155. https://doi.org/10.1016/j.cattod.2021.03.008.

[158] Vaiano, V.; Iervolino, G. Photocatalytic Hydrogen Production from Glycerol Aqueous Solution Using Cu-Doped ZnO under Visible Light Irradiation. *Appl. Sci.* **2019**, *9*, 2741. https://doi.org/10.3390/app9132741

[159] Montini, T.; Gombac, V.; Sordelli, L.; Delgado, J. J.; Chen, X.; Adami, G.; Fornasiero, P. Nanostructured Cu/TiO_2 Photocatalysts for H_2 Production from Ethanol and Glycerol Aqueous Solutions. *ChemCatChem* **2011**, *3*, 574–577. https://doi.org/10.1002/cctc.201000289.

[160] Sampaio, M. J.; Oliveira, J. W. L.; Sombrio, C. I. L.; Baptista, D. L.; Teixeira, S. R.; Carabineiro, S. A. C.; Silva, C. G.; Faria, J. L. Photocatalytic Performance of Au/ZnO Nanocatalysts for Hydrogen Production from Ethanol. *Appl. Catal. A Gen.* **2016**, *518*, 198–205. https://doi.org/10.1016/j.apcata.2015.10.013.

[161] Li, Y.-H.; Zhang, F.; Chen, Y.; Li, J.-Y.; Xu, Y.-J. Photoredox-Catalyzed Biomass Intermediate Conversion Integrated with H_2 Production over $Ti_3C_2T_x$/CdS Composites. *Green Chem.* **2020**, *22*, 163–169. https://doi.org/10.1039/c9gc03332g.

[162] Mamman, A. S.; Lee, J.-M.; Kim, Y.-C.; Hwang, I. T.; Park, N.-J.; Hwang, Y. K.; Chang, J.-S.; Hwang, J.-S. Furfural: Hemicellulose/Xylose-Derived Biochemical. *Biofuels, Bioproducts Biorefining: Innovation for a Sustainable Economy* **2008**, *2*, 438–454. https://doi.org/10.1002/bbb.95.

[163] Sitthisa, S.; An, W.; Resasco, D. E. Selective Conversion of Furfural to Methylfuran over Silica-Supported NiFe Bimetallic Catalysts. *J. Catal.* **2011**, *284*, 90–101. https://doi.org/10.1016/j.jcat.2011.09.005.

[164] Horikoshi, S.; Watanabe, N.; Mukae, M.; Hidaka, H.; Serpone, N. Mechanistic Examination of the Titania Photocatalyzed Oxidation of Ethanolamines. *New J. Chem.* **2001**, *25*, 999–1005. https://doi.org/10.1039/b102186i.

[165] Peng, S.; Dan, M.; Guo, F.; Wang, H.; Li, Y. Template Synthesis of $ZnIn_2S_4$ for Enhanced Photocatalytic H_2 Evolution Using Triethanolamine as Electron Donor. *Colloids Surf. A Physicochem. Eng. Asp.* **2016**, *504*, 18–25. https://doi.org/10.1016/j.colsurfa.2016.05.055.

[166] Li, Y.; Zhang, K.; Peng, S.; Lu, G.; Li, S. Photocatalytic Hydrogen Generation in the Presence of Ethanolamines over Pt/$ZnIn_2S_4$ under Visible Light Irradiation. *J. Mol. Catal. A Chem.* **2012**, *363–364*, 354–361. https://doi.org/10.1016/j.molcata.2012.07.011.

[167] Widsten, P.; Murton, K.; West, M. Production of 5-Hydroxymethylfurfural and Furfural from a Mixed Saccharide Feedstock in Biphasic Solvent Systems. *Ind. Crops Prod.* **2018**, *119*, 237–242. https://doi.org/10.1016/j.indcrop.2018.04.032.

[168] Chen, H.; Wan, K.; Zheng, F.; Zhang, Z.; Zhang, Y.; Long, D. Mechanism Insight into Photocatalytic Conversion of Lignin for Valuable Chemicals and Fuels Production: A State-of-the-Art Review. *Renew. Sustain. Energy Rev.* **2021**, *147*, 111217. https://doi.org/10.1016/j.rser.2021.111217.

[169] Shi, C.; Kang, F.; Zhu, Y.; Teng, M.; Shi, J.; Qi, H.; Huang, Z.; Si, C.; Jiang, F.; Hu, J. Photoreforming Lignocellulosic Biomass for Hydrogen Production: Optimized Design of Photocatalyst and Photocatalytic System. *Chem. Eng. J.* **2023**, *452*, 138980. https://doi.org/10.1016/j.cej.2022.138980.

[170] Xu, X.; Shi, L.; Zhang, S.; Ao, Z.; Zhang, J.; Wang, S.; Sun, H. Photocatalytic Reforming of Lignocellulose: A Review. *Chem. Eng. J.* **2023**, *469*, 143972. https://doi.org/10.1016/j.cej.2023.143972.

[171] Bulushev, D.A.; Ross, J.R.H. Towards Sustainable Production of Formic Acid. *ChemSusChem* **2018**, *11*, 821–836. https://doi.org/10.1002/cssc.201702075.

[172] Chou, C.F.; Chou, T.C. Paired Electrooxidation IV. Decarboxylation of Sodium Gluconate to D-Arabinose. *J. Appl. Electrochem.* **2003**, *33*, 741–745. https://doi.org/10.1023/a:1025005832155.

[173] Liu, L.-L.; Yi, T.; Zhao, X. Antitumor Effect of D-Erythrose in an Abdominal Metastatic Model of Colon Carcinoma. *Oncol. Lett.* **2015**, *9*, 769–773. https://doi.org/10.3892/ol.2014.2764.

[174] Xiao, X.; Jiang, J.; Zhang, L. Selective Oxidation of Benzyl Alcohol into Benzaldehyde over Semiconductors under Visible Light: The Case of $Bi_{12}O_{17}Cl_2$ Nanobelts. *Appl. Catal. B Environ.* **2013**, *142–143*, 487–493. https://doi.org/10.1016/j.apcatb.2013.05.047.

[175] Miyamura, H.; Matsubara, R.; Miyazaki, Y.; Kobayashi, S. Aerobic Oxidation of Alcohols at Room Temperature and Atmospheric Conditions Catalyzed by Reusable Gold Nanoclusters Stabilized by the Benzene Rings of Polystyrene Derivatives.

Angew. Chem. Int. Ed. **2007**, *46*, 4151–4154. https://doi.org/10.1002/anie.200700080.

[176] Higashimoto, S.; Suetsugu, N.; Azuma, M.; Ohue, H.; Sakata, Y. Efficient and Selective Oxidation of Benzylic Alcohol by O_2 into Corresponding Aldehydes on a TiO_2 Photocatalyst under Visible Light Irradiation: Effect of Phenyl-Ring Substitution on the Photocatalytic Activity. *J. Catal.* **2010**, *274*, 76–83. https://doi.org/10.1016/j.jcat.2010.06.006.

[177] Zhang, M.; Wang, Q.; Chen, C.; Zang, L.; Ma, W.; Zhao, J. Oxygen Atom Transfer in the Photocatalytic Oxidation of Alcohols by TiO_2: Oxygen Isotope Studies. *Angew. Chem. Int. Ed.* **2009**, *48*, 6081–6084. https://doi.org/10.1002/anie.200900322.

[178] Loddo, V.; Bellardita, M.; Roda, G.C.; Palmisano, L.; Parrino, F. Water Depollution by Advanced Oxidation Technologies. In *Sustainable Green Chemical Processes and their Allied Applications*; Inamuddin, Asiri, A., Eds.; Nanotechnology in the Life Sciences; Springer: Cham, 2020; pp. 1–15. https://doi.org/10.1007/978-3-030-42284-4_18.

[179] Changotra, R.; Rajput, H.; Dhir, A. Natural Soil Mediated Photo Fenton-Like Processes in Treatment of Pharmaceuticals: Batch and Continuous Approach. *Chemosphere* **2017**, *188*, 345–353. https://doi.org/10.1016/j.chemosphere.2017.09.016.

[180] Wols, B.A.; Hofman-Caris, C.H.M.; Harmsen, D.J.H.; Beerendonk, E.F. Degradation of 40 Selected Pharmaceuticals by UV/H_2O_2. *Water Res.* **2013**, *47*, 5876–5888. https://doi.org/10.1016/j.watres.2013.07.008.

[181] Wang, J.; Chu, L.; Wojnárovits, L.; Takács, E. Occurrence and Fate of Antibiotics, Antibiotic Resistant Genes (ARGs) and Antibiotic Resistant Bacteria (ARB) in Municipal Wastewater Treatment Plant: An Overview. *Sci. Total Environ.* **2020**, *744*, 140997. https://doi.org/10.1016/j.scitotenv.2020.140997.

[182] Wang, J.; Wang, S. Removal of Pharmaceuticals and Personal Care Products (PPCPs) from Wastewater: A Review. *J. Environ. Manag.* **2016**, *182*, 620–640. https://doi.org/10.1016/j.jenvman.2016.07.049.

[183] Jodeh, S.; Abdelwahab, F.; Jaradat, N.; Warad, I.; Jodeh, W. Adsorption of Diclofenac from Aqueous Solution Using Cyclamen Persicum Tubers Based Activated Carbon (CTAC). *J. Assoc. Arab Univ. Basic Appl. Sci.* **2016**, *20*, 32–38. https://doi.org/10.1016/j.jaubas.2014.11.002.

[184] Roberts, P.H.; Thomas, K.V. The Occurrence of Selected Pharmaceuticals in Wastewater Effluent and Surface Waters of the Lower Tyne Catchment. *Sci. Total Environ.* **2006**, *356*, 143–153. https://doi.org/10.1016/j.scitotenv.2005.04.031.

[185] Szabó, R.K.; Megyeri, C.; Illés, E.; Gajda-Schrantz, K.; Mazellier, P.; Dombi, A. Phototransformation of Ibuprofen and Ketoprofen in Aqueous Solutions. *Chemosphere* **2011**, *84*, 1658–1663. https://doi.org/10.1016/j.chemosphere.2011.05.012.

[186] Tran, H.T.T.; Kosslick, H.; Ibad, M.F.; Fischer, C.; Bentrup, U.; Vuong, T.H.; Nguyen, L.Q.; Schulz, A. Photocatalytic Performance of Highly Active Brookite in the Degradation of Hazardous Organic Compounds Compared to Anatase and Rutile. *Appl. Catal. B Environ.* **2017**, *200*, 647–658. https://doi.org/10.1016/j.apcatb.2016.07.017.

[187] Liu, W.; Sutton, N.B.; Rijnaarts, H.H.M.; Langenhoff, A.A.M. Anaerobic Biodegradation of Pharmaceutical Compounds Coupled to Dissimilatory Manganese (IV) or Iron (III) Reduction. *J. Hazard. Mater.* **2020**, *388*, 119361. https://doi.org/10.1016/j.jhazmat.2018.04.078.

[188] Taoufik, N.; Elmchaouri, A.; Anouar, F.; Korili, S.A.; Gil, A. Improvement of the Adsorption Properties of an Activated Carbon Coated by Titanium Dioxide for the

Removal of Emerging Contaminants. *J. Water Process Eng.* **2019**, *31*, 100876. https://doi.org/10.1016/j.jwpe.2019.100876.

[189] Souza, D. I. de; Dottein, E. M.; Giacobbo, A.; Rodrigues, M. A. S.; Pinho, M. N. de; Bernardes, A. M. Nanofiltration for the Removal of Norfloxacin from Pharmaceutical Effluent. *J. Environ. Chem. Eng.* **2018**, *6*, 6147–6153. https://doi.org/10.1016/j.jece.2018.09.034.

[190] Nguyen, L. N.; Hai, F. I.; McDonald, J. A.; Khan, S. J.; Price, W. E.; Nghiem, L. D. Continuous Transformation of Chiral Pharmaceuticals in Enzymatic Membrane Bioreactors for Advanced Wastewater Treatment. *Water Sci. Technol.* **2017**, *76*, 1816–1826. https://doi.org/10.2166/wst.2017.331.

[191] Mirzaei, R.; Yunesian, M.; Nasseri, S.; Gholami, M.; Jalilzadeh, E.; Shoeibi, S.; Mesdaghinia, A. Occurrence and Fate of Most Prescribed Antibiotics in Different Water Environments of Tehran, Iran. *Sci. Total Environ.* **2018**, *619–620*, 446–459. https://doi.org/10.1016/j.scitotenv.2017.07.272.

[192] Taoufik, N.; Boumya, W.; Achak, M.; Sillanpää, M.; Barka, N. Comparative Overview of Advanced Oxidation Processes and Biological Approaches for the Removal of Pharmaceuticals. *J. Environ. Manag.* **2021**, *288*, 112404. https://doi.org/10.1016/j.jenvman.2021.112404.

[193] Wu, S.; Li, X.; Tian, Y.; Lin, Y.; Hu, Y.H. Excellent Photocatalytic Degradation of Tetracycline over Black Anatase-TiO_2 under Visible Light. *Chem. Eng. J.* **2021**, *406*, 126747. https://doi.org/10.1016/j.cej.2020.126747.

[194] Khan, A.H.; Khan, N.A.; Ahmed, S.; Dhingra, A.; Singh, C.P.; Khan, S.U.; Mohammadi, A.A.; Changani, F.; Yousefi, M.; Alam, S.; Vambol, S.; Vambol, V.; Khursheed, A.; Ali, I. Application of Advanced Oxidation Processes Followed by Different Treatment Technologies for Hospital Wastewater Treatment. *J. Clean. Prod.* **2020**, *269*, 122411. https://doi.org/10.1016/j.jclepro.2020.122411.

[195] Abdel-Raouf, N.; Al-Homaidan, A.A.; Ibraheem, I.B.M. Microalgae and Wastewater Treatment. *Saudi J. Biol. Sci.* **2012**, *19*, 257–275. https://doi.org/10.1016/j.sjbs.2012.04.005.

[196] Zhang, T.; Liu, Y.; Rao, Y.; Li, X.; Yuan, D.; Tang, S.; Zhao, Q. Enhanced Photocatalytic Activity of TiO_2 with Acetylene Black and Persulfate for Degradation of Tetracycline Hydrochloride under Visible Light. *Chem. Eng. J.* **2020**, *384*, 123350. https://doi.org/10.1016/j.cej.2019.123350.

[197] Ayoub, K.; van Hullebusch, E. D.; Cassir, M.; Bermond, A. Application of Advanced Oxidation Processes for TNT Removal: A Review. *J. Hazard. Mater.* **2010**, *178*, 10–28. https://doi.org/10.1016/j.jhazmat.2010.02.042.

[198] Klavarioti, M.; Mantzavinos, D.; Kassinos, D. Removal of Residual Pharmaceuticals from Aqueous Systems by Advanced Oxidation Processes. *Environ. Int.* **2009**, *35*, 402–417. https://doi.org/10.1016/j.envint.2008.07.009.

[199] Rauf, M.A.; Ashraf, S.S. Fundamental Principles and Application of Heterogeneous Photocatalytic Degradation of Dyes in Solution. *Chem. Eng. J.* **2009**, *151*, 10–18. https://doi.org/10.1016/j.cej.2009.02.026.

[200] Mahdi, M.H.; Mohammed, T.J.; Al-Najar, J.A. Advanced Oxidation Processes (AOPs) for Treatment of Antibiotics in Wastewater: A Review. *IOP Conf. Ser. Earth Environ. Sci.* **2021**, *779*, 012109. https://doi.org/10.1088/1755-1315/779/1/012109.

[201] Cardoso, I.M.F.; Cardoso, R.M.F.; da Silva, J.C.G.E. Advanced Oxidation Processes Coupled with Nanomaterials for Water Treatment. *Nanomaterials* **2021**, *11*, 2045. https://doi.org/10.3390/nano11082045

[202] Wang, Y.; Han, D.; Wang, Z.; Gu, F. Efficient Photocatalytic Degradation of Tetracycline under Visible Light by an All-Solid-State Z-Scheme Ag_3PO_4/MIL-101

(Cr) Heterostructure with Metallic Ag as a Charge Transmission Bridge. *ACS Appl. Mater. Interfaces* **2023**, *15*, 22085–22100. https://doi.org/10.1021/acsami.3c01255.

[203] Chen, X.; Yao, L.; He, J.; Li, J.; Xu, S.; Li, N.; Zhu, Y.; Chen, X.; Zhu, R. Enhanced Degradation of Tetracycline under Natural Sunlight through the Synergistic Effect of Ag_3PO_4/MIL-101(Fe) Photocatalysis and Fenton Catalysis: Mechanism, Pathway, and Toxicity Assessment. *J. Hazard. Mater.* **2023**, *449*, 131024. https://doi.org/10.1016/j.jhazmat.2023.131024.

[204] Zeinali Heris, S.; Etemadi, M.; Mousavi, S.B.; Mohammadpourfard, M.; Ramavandi, B. Preparation and Characterizations of TiO_2/ZnO Nanohybrid and Its Application in Photocatalytic Degradation of Tetracycline in Wastewater. *J. Photochem. Photobiol. A Chem.* **2023**, *443*, 114893. https://doi.org/10.1016/j.jphotochem.2023.114893.

[205] Majumdar, A.; Ghosh, U.; Pal, A. Novel 2D/2D g-C_3N_4/Bi_4NbO_8Cl Nano-Composite for Enhanced Photocatalytic Degradation of Oxytetracycline under Visible LED Light Irradiation. *J. Colloid Interface Sci.* **2021**, *584*, 320-331. https://doi.org/10.1016/j.jcis.2020.09.101.

[206] Hassandoost, R.; Kotb, A.; Movafagh, Z.; Esmat, M.; Guegan, R.; Endo, S.; Jevasuwan, W.; Fukata, N.; Sugahara, Y.; Khataee, A.; Yamauchi, Y.; Ide, Y.; Doustkhah, E. Nanoarchitecturing Bimetallic Manganese Cobaltite Spinels for Sonocatalytic Degradation of Oxytetracycline. *Chem. Eng. J.* **2022**, *431*, 133851. https://doi.org/10.1016/j.cej.2021.133851.

[207] Wang, M.; Zhang, B.; Wang, J.; Cai, C.; Xin, Y.; Liu, H. Degradation of Lincomycin in Aqueous Solution with Hydrothermal Treatment: Kinetics, Pathway, and Toxicity Evaluation. *Chem. Eng. J.* **2018**, *343*, 138–145. https://doi.org/10.1016/j.cej.2018.03.008.

[208] Zhu, X.; Wang, X.; Wang, L.; Fan, X.; Li, X.; Jiang, Y. Biodegradation of Lincomycin in Wastewater by Two-Level Bio-Treatment Using Chloroperoxidase and Activated Sludge: Degradation Route and Eco-Toxicity Evaluation. *Environ. Technol. Innov.* **2020**, *20*, 101114. https://doi.org/10.1016/j.eti.2020.101114.

[209] Li, Y.; Fu, L.; Li, X.; Wang, Y.; Wei, Y.; Tang, J.; Liu, H. Novel Strains with Superior Degrading Efficiency for Lincomycin Manufacturing Biowaste. *Ecotoxicol. Environ. Saf.* **2021**, *209*, 111802. https://doi.org/10.1016/j.ecoenv.2020.111802.

[210] Li, L.; Sun, J.; Liu, B.; Zhao, D.; Ma, J.; Deng, H.; Li, X.; Hu, F.; Liao, X.; Liu, Y. Quantification of Lincomycin Resistance Genes Associated with Lincomycin Residues in Waters and Soils Adjacent to Representative Swine Farms in China. *Front. Microbiol.* **2013**, *4*, 364. https://doi.org/10.3389/fmicb.2013.00364.

[211] Huang, X.; Zheng, J.; Liu, C.; Liu, L.; Liu, Y.; Fan, H. Removal of Antibiotics and Resistance Genes from Swine Wastewater Using Vertical Flow Constructed Wetlands: Effect of Hydraulic Flow Direction and Substrate Type. *Chem. Eng. J.* **2017**, *308*, 692-699. https://doi.org/10.1016/j.cej.2016.09.110

[212] Rhodes, G.; Huys, G.; Swings, J.; McGann, P.; Hiney, M.; Smith, P.; Pickup, R.W. Distribution of Oxytetracycline Resistance Plasmids Between Aeromonads in Hospital and Aquaculture Environments: Implication of Tn1721 in Dissemination of the Tetracycline Resistance Determinant Tet A. *Appl. Environ. Microbiol.* **2000**, *66*, 3883-3890. https://doi.org/10.1128/AEM.66.9.3883-3890.2000

[213] Yang, L.-H.; Ying, G.-G.; Su, H.-C.; Stauber, J.L.; Adams, M.S.; Binet, M.T. Growth-Inhibiting Effects of 12 Antibacterial Agents and Their Mixtures on the Freshwater Microalga *Pseudokirchneriella subcapitata*. *Environ. Toxicol. Chem.* **2008**, *27*, 1201–1208. https://doi.org/10.1897/07-541.1.

[214] Yang, C.; Zhang, X.; Qin, J.; Shen, X.; Yu, R.; Ma, M.; Liu, R. Porous Carbon-Doped TiO_2 on TiC Nanostructures for Enhanced Photocatalytic Hydrogen Production under Visible Light. *J. Catal.* **2017**, *347*, 36–44. https://doi.org/10.1016/j.jcat.2016.11.041.

[215] Yuan, Y.-J.; Ye, Z.-J.; Lu, H.-W.; Hu, B.; Li, Y.-H.; Chen, D.-Q.; Zhong, J.-S.; Yu, Z.-T.; Zou, Z.-G. Constructing Anatase TiO_2 Nanosheets with Exposed (001) Facets/Layered MoS2 Two-Dimensional Nanojunctions for Enhanced Solar Hydrogen Generation. *ACS Catal.* **2016**, *6*, 532–541. https://doi.org/10.1021/acscatal.5b02036.

[216] Ramachandran, S.; Fontanille, P.; Pandey, A.; Larroche, C. Gluconic Acid: Properties, Applications and Microbial Production. *Food Technol. Biotechnol.* **2006**, *44*, 185–195. https://www.cabidigitallibrary.org/doi/full/10.5555/20063143534

[217] Bernstein, E.F.; Brown, D.B.; Schwartz, M.D.; Kaidbey, K.; Ksenzenko, S.M. The Polyhydroxy Acid Gluconolactone Protects against Ultraviolet Radiation in an In Vitro Model of Cutaneous Photoaging. *Dermatol. Surg.* **2004**, *30*, 189–195.

[218] Shi, C.; An, Y.; Gao, G.; Xue, J.; Algadi, H.; Huang, Z.; Guo, Z. Insights into Selective Glucose Photoreforming for Coproduction of Hydrogen and Organic Acid over Biochar-Based Heterojunction Photocatalyst Cadmium Sulfide/Titania/Biochar. *ACS Sustainable Chem. Eng.* **2024**, *12*, 2538–2549. https://doi.org/10.1021/acssuschemeng.3c04835

[219] Eisapour, M.; Zhao, H.; Zhao, J.; Roostaei, T.; Li, Z.; Omidkar, A.; Hu, J.; Chen, Z. p-n Heterojunction of Nickel Oxide on Titanium Dioxide Nanosheets for Hydrogen and Value-Added Chemicals Coproduction from Glycerol Photoreforming. *J. Colloid Interface Sci.* **2023**, *647*, 255–263. https://doi.org/10.1016/j.jcis.2023.05.138.

[220] Henderson, M.A. A Surface Science Perspective on TiO_2 Photocatalysis. *Surf. Sci. Rep.* **2011**, *66*, 185–297. https://doi.org/10.1016/j.surfrep.2011.01.001

[221] Xu, F.; Xiao, W.; Cheng, B.; Yu, J. Direct Z-Scheme Anatase/Rutile Bi-Phase Nanocomposite TiO_2 Nanofiber Photocatalyst with Enhanced Photocatalytic H_2-Production Activity. *Int. J. Hydrogen Energy* **2014**, *39*, 15394–15402. https://doi.org/10.1016/j.ijhydene.2014.07.166

[222] Liu, Y.; Wang, Z.; Huang, W. Influences of TiO_2 Phase Structures on the Structures and Photocatalytic Hydrogen Production of CuOx/TiO_2 Photocatalysts. *Appl. Surf. Sci.* **2016**, *389*, 760–767. https://doi.org/10.1016/j.apsusc.2016.07.173.

[223] Sreethawong, T.; Suzuki, Y.; Yoshikawa, S. Photocatalytic Evolution of Hydrogen over Mesoporous TiO_2 Supported NiO Photocatalyst Prepared by Single-Step Sol–Gel Process with Surfactant Template. *Int. J. Hydrogen Energy* **2005**, *30*, 1053–1062. https://doi.org/10.1016/j.ijhydene.2004.09.007.

[224] Li, G.; Huang, J.; Chen, J.; Deng, Z.; Huang, Q.; Liu, Z.; Guo, W.; Cao, R. Highly Active Photocatalyst of Cu_2O/TiO_2 Octahedron for Hydrogen Generation. *ACS Omega* **2019**, *4*, 3392–3397. https://doi.org/10.1021/acsomega.8b03404.

[225] Muscetta, M.; Clarizia, L.; Race, M.; Andreozzi, R.; Marotta, R.; Di Somma, I. Visible—Light Driven Systems: Effect of the Parameters Affecting Hydrogen Production through Photoreforming of Organics in Presence of Cu_2O/TiO_2 Nanocomposite Photocatalyst. *Appl. Sci.* **2023**, *13*, 2337. https://doi.org/10.3390/app13042337

[226] Liu, R.; Yoshida, H.; Fujita, S.-i.; Arai, M. Photocatalytic Hydrogen Production from Glycerol and Water with NiO_x/TiO_2 Catalysts. *Appl. Catal. B Environ.* **2014**, *144*, 41–45. https://doi.org/10.1016/j.apcatb.2013.06.024.

[227] Bellardita, M.; García-López, E.I.; Marcì, G.; Nasillo, G.; Palmisano, L. Photocatalytic Solar Light H_2 Production by Aqueous Glucose Reforming. *Eur. J. Inorg. Chem.* **2018**, *2018*, 4522–4532. https://doi.org/10.1002/ejic.201800663.

[228] Lin, H.-Y.; Shih, C.-Y. Efficient One-Pot Microwave-Assisted Hydrothermal Synthesis of M (M = Cr, Ni, Cu, Nb) and Nitrogen Co-Doped TiO_2 for Hydrogen Production by Photocatalytic Water Splitting. *J. Mol. Catal. A Chem.* **2016**, *411*, 128–137. https://doi.org/10.1016/j.molcata.2015.10.026.

[229] Zhu, S.; Yao, F.; Yin, C.; Li, Y.; Peng, W.; Ma, J.; Zhang, D. Fe_2O_3/TiO_2 Photocatalyst of Hierarchical Structure for H_2 Production from Water under Visible Light Irradiation. *Microporous Mesoporous Mater.* **2014**, *190*, 10–16. https://doi.org/10.1016/j.micromeso.2014.01.018.

[230] Wang, Y.; Yu, J.; Xiao, W.; Li, Q. Microwave-Assisted Hydrothermal Synthesis of Graphene-Based Au–TiO_2 Photocatalysts for Efficient Visible-Light Hydrogen Production. *J. Mater. Chem. A* **2014**, *2*, 3847–3855. https://doi.org/10.1039/c3ta14908k.

[231] Zhang, Q.; Li, Z.; Wang, S.; Li, R.; Zhang, X.; Liang, Z.; Han, H.; Liao, S.; Li, C. Effect of Redox Cocatalysts Location on Photocatalytic Overall Water Splitting over Cubic $NaTaO_3$ Semiconductor Crystals Exposed with Equivalent Facets. *ACS Catal.* **2016**, *6*, 2182–2191. https://doi.org/10.1021/acscatal.5b02503.

[232] Jang, J.S.; Hong, S.J.; Kim, J.Y.; Lee, J.S. Heterojunction Photocatalyst $TiO_2/AgGaS_2$ for Hydrogen Production from Water under Visible Light. *Chem. Phys. Lett.* **2009**, *475*, 78–81. https://doi.org/10.1016/j.cplett.2009.05.012.

[233] Chen, L.-Y.; Zhang, W.-D. In_2O_3/g-C_3N_4 Composite Photocatalysts with Enhanced Visible Light Driven Activity. *Appl. Surf. Sci.* **2014**, *301*, 428–435. https://doi.org/10.1016/j.apsusc.2014.02.093.

[234] Xu, L.; Ni, L.; Shi, W.; Guan, J. Photocatalytic Activity for Hydrogen Evolution over Well-Dispersed Heterostructured In_2O_3/Ta_2O_5 Composites. *Chin. J. Catal.* **2012**, *33*, 1101–1108. https://doi.org/10.1016/S1872-2067(11)60382-3.

[235] Liu, B.; Ren, Y.; Zhang, Z. Aerobic Oxidation of 5-Hydroxymethylfurfural into 2,5-Furandicarboxylic Acid in Water under Mild Conditions. *Green Chem.* **2015**, *17*, 1610–1617. https://doi.org/10.1039/c4gc02019g.

[236] Gui, Z.; Cao, W.; Saravanamurugan, S.; Riisager, A.; Chen, L.; Qi, Z. Efficient Aerobic Oxidation of 5-Hydroxymethylfurfural in Aqueous Media with Au–Pd Supported on Zinc Hydroxycarbonate. *ChemCatChem* **2016**, *8*, 3636–3643. https://doi.org/10.1002/cctc.201600852.

[237] Wang, T.; Nolte, M. W.; Shanks, B. H. Catalytic Dehydration of C_6 Carbohydrates for the Production of Hydroxymethylfurfural (HMF) as a Versatile Platform Chemical. *Green Chem.* **2014**, *16*, 548–572. https://doi.org/10.1039/C3GC41365A.

[238] Su, T.; Liu, Q.; Lü, H.; Alasmary, F. A.; Zhao, D.; Len, C. Selective Oxidation of 5-Hydroxymethylfurfural to 5-Hydroxymethyl-2-furancarboxylic Acid Using Silver Oxide Supported on Calcium Carbonate. *Molecular Catal.* **2021**, *502*, 111374. https://doi.org/10.1016/j.mcat.2020.111374.

[239] Ilkaeva, M.; Krivtsov, I.; García-López, E. I.; Marcì, G.; Khainakova, O.; García, J. R.; Palmisano, L.; Díaz, E.; Ordóñez, S. Selective Photocatalytic Oxidation of 5-Hydroxymethylfurfural to 2,5-Furandicarboxaldehyde by Polymeric Carbon Nitride-Hydrogen Peroxide Adduct. *J. Catal.* **2018**, *359*, 212–222. https://doi.org/10.1016/j.jcat.2018.01.012.

[240] Siyo, B.; Schneider, M.; Radnik, J.; Pohl, M.-M.; Langer, P.; Steinfeldt, N. Influence of Support on the Aerobic Oxidation of HMF into FDCA over Preformed Pd Nanoparticle-Based Materials. *Appl. Catal. A Gen.* **2014**, *478*, 107–116. https://doi.org/10.1016/j.apcata.2014.03.020.

[241] Sheldon, R.A.; Arends, I.W.C.E.; Ten Brink, G.-J.; Dijksman, A. Green, Catalytic Oxidations of Alcohols. *Acc. Chem. Res.* **2002**, *35*, 774–781. https://doi.org/10.1021/ar010075n.

[242] Yamaguchi, K.; Mizuno, N. Efficient Heterogeneous Aerobic Oxidation of Amines by a Supported Ruthenium Catalyst. *Angew. Chem. Int. Ed.* **2003**, *42*, 1480–1483. https://doi.org/10.1002/anie.200250779.

[243] Bellardita, M.; García-López, E.I.; Marcì, G.; Krivtsov, I.; García, J.R.; Palmisano, L. Selective Photocatalytic Oxidation of Aromatic Alcohols in Water by Using P-Doped g-C_3N_4. *Appl. Catal. B Environ.* **2018**, *220*, 222–233. https://doi.org/10.1016/j.apcatb.2017.08.033.

[244] Qamar, M.; Elsayed, R.B.; Alhooshani, K.R.; Ahmed, M.I.; Bahnemann, D.W. Highly Efficient and Selective Oxidation of Aromatic Alcohols Photocatalyzed by Nanoporous Hierarchical Pt/Bi_2WO_6 in Organic Solvent-Free Environment. *ACS Appl. Mater. Interfaces* **2015**, *7*, 1257–1269. https://doi.org/10.1021/am507428r.

[245] Yang, Q.; Wang, T.; Han, F.; Zheng, Z.; Xing, B.; Li, B. Bimetal-Modified g-C_3N_4 Photocatalyst for Promoting Hydrogen Production Coupled with Selective Oxidation of Biomass Derivative. *J. Alloys Compd.* **2022**, *897*, 163177. https://doi.org/10.1016/j.jallcom.2021.163177.

[246] Yurdakal, S.; Augugliaro, V. Partial Oxidation of Aromatic Alcohols via TiO_2 Photocatalysis: The Influence of Substituent Groups on the Activity and Selectivity. *RSC Adv.* **2012**, *2*, 8375–8380. https://doi.org/10.1039/c2ra20960h.

[247] Warkad, I.R.; Paul, R.; Parthiban, S.; Gawande, M.B. Highly Selective Oxidation of Biomass-Derived Alcohols and Aromatic Alcohols to Aldehydes over Ti_3C_2-TiO_2 Nanocomposites under Visible Light. *J. Environ. Chem. Eng.* **2024**, *12*, 113128. https://doi.org/10.1016/j.jece.2024.113128.

[248] Tomita, O.; Otsubo, T.; Higashi, M.; Ohtani, B.; Abe, R. Partial Oxidation of Alcohols on Visible-Light-Responsive WO_3 Photocatalysts Loaded with Palladium Oxide Cocatalyst. *ACS Catal.* **2016**, *6*, 1134–1144. https://doi.org/10.1021/acscatal.5b01850.

[249] Su, L.; Ye, X.; Meng, S.; Fu, X.; Chen, S. Effect of Different Solvent on the Photocatalytic Activity of $ZnIn_2S_4$ for Selective Oxidation of Aromatic Alcohols to Aromatic Aldehydes under Visible Light Irradiation. *Appl. Surf. Sci.* **2016**, *384*, 161–174. https://doi.org/10.1016/j.apsusc.2016.04.084.

[250] Wang, H.; Fan, W.; He, Y.; Wang, J.; Kondo, J. N.; Tatsumi, T. Selective Oxidation of Alcohols to Aldehydes/Ketones over Copper Oxide-Supported Gold Catalysts. *J. Catal.* **2013**, *299*, 10–19. https://doi.org/10.1016/j.jcat.2012.11.018.

[251] Guo, D.; Wang, Y.; Zhao, P.; Bai, M.; Xin, H.; Guo, Z.; Li, J. Selective Aerobic Oxidation of Benzyl Alcohol Driven by Visible Light on Gold Nanoparticles Supported on Hydrotalcite Modified by Nickel Ion. *Catalysts* **2016**, *6*, 64. https://doi.org/10.3390/catal6050064

[252] Lucarelli, C.; Lolli, A.; Giugni, A.; Grazia, L.; Albonetti, S.; Monticelli, D.; Vaccari, A. Efficient and Ecofriendly Route for the Solvent-Free Synthesis of Piperonal and Aromatic Aldehydes Using Au/CeO_2 Catalyst. *Appl. Catal. B Environ.* **2017**, *203*, 314–323. https://doi.org/10.1016/j.apcatb.2016.10.030.

[253] Davies, A.K.; McKellar, J.F.; Phillips, G.O.; Reid, A.G. Photochemical Oxidation of Tetracycline in Aqueous Solution. *J. Chem. Soc. Perkin Trans. 2* **1979**, *3*, 369–375. https://doi.org/10.1039/P29790000369.

[254] Addamo, M.; Augugliaro, V.; Paola, A.D.; et al. Removal of Drugs in Aqueous Systems by Photoassisted Degradation. *J. Appl. Electrochem.* **2005**, *35*, 765–774. https://doi.org/10.1007/s10800-005-1630-y.

[255] Sun, H.; Zhou, T.; Kang, J.; Zhao, Y.; Zhang, Y.; Wang, T.; Yin, X. High-Efficient Degradation of Oxytetracycline by Visible Photo-Fenton Process Using $MnFe_2O_4$/g-C_3N_4: Performance and Mechanisms. *Separation Purif. Technol.* **2022**, *299*, 121771. https://doi.org/10.1016/j.seppur.2022.121771.

[256] Pereira, J.H.O.S.; Vilar, V.J.P.; Borges, M.T.; González, O.; Esplugas, S.; Boaventura, R.A.R. Photocatalytic Degradation of Oxytetracycline Using TiO_2 under Natural and

Simulated Solar Radiation. *Solar Energy* **2011**, *85*, 2732–2740. https://doi.org/10.1016/j.solener.2011.08.012.

[257] Safari, G.H.; Hoseini, M.; Seyedsalehi, M.; et al. Photocatalytic Degradation of Tetracycline Using Nanosized Titanium Dioxide in Aqueous Solution. *Int. J. Environ. Sci. Technol.* **2015**, *12*, 603–616. https://doi.org/10.1007/s13762-014-0706-9.

[258] Wang, P.; Yap, P.-S.; Lim, T.-T. C–N–S Tridoped TiO_2 for Photocatalytic Degradation of Tetracycline under Visible-Light Irradiation. *Appl. Catal. A Gen.* **2011**, *399*, 252–261. https://doi.org/10.1016/j.apcata.2011.04.008.

[259] Mohammadi, M.; Sabbaghi, S.; Binazadeh, M.; Ghaedi, S.; Rajabi, H. Type-1 α-Fe_2O_3/TiO_2 Photocatalytic Degradation of Tetracycline from Wastewater Using CCD-Based RSM Optimization. *Chemosphere* **2023**, *336*, 139311. https://doi.org/10.1016/j.chemosphere.2023.139311.

[260] Sharma, M.; Mandal, M.K.; Pandey, S.; Kumar, R.; Dubey, K.K. Visible-Light-Driven Photocatalytic Degradation of Tetracycline Using Heterostructured Cu_2O–TiO_2 Nanotubes, Kinetics, and Toxicity Evaluation of Degraded Products on Cell Lines. *ACS Omega* **2022**, *7*, 33572–33586. https://doi.org/10.1021/acsomega.2c04576.

[261] Ahmadi, M.; Ramezani Motlagh, H.; Jaafarzadeh, N.; Mostoufi, A.; Saeedi, R.; Barzegar, G.; Jorfi, S. Enhanced Photocatalytic Degradation of Tetracycline and Real Pharmaceutical Wastewater Using MWCNT/TiO_2 Nano-Composite. *J. Environ. Manag.* **2017**, *186*, 55–63. https://doi.org/10.1016/j.jenvman.2016.09.088.

[262] Wang, W.; Fang, J.; Shao, S.; Lai, M.; Lu, C. Compact and Uniform TiO_2@g-C_3N_4 Core-Shell Quantum Heterojunction for Photocatalytic Degradation of Tetracycline Antibiotics. *Appl. Catal. B Environ.* **2017**, *217*, 57–64. https://doi.org/10.1016/j.apcatb.2017.05.037.

[263] Phakathi, N.A.; Tichapondwa, S.M.; Chirwa, E.M.N. Photocatalytic Degradation of Tetracycline Using Visible-Light-Driven Porous g-C_3N_4 Nanosheets Catalyst. *Chem. Eng. Trans.* **2022**, *96*, 391–396. https://doi.org/10.3303/CET2296066.

[264] Gaffar, S.; Kumar, A.; Alam, J.; Riaz, U. Efficient Visible Light–Induced Photocatalytic Degradation of Tetracycline Hydrochloride Using $CuFe_2O_4$ and PANI/$CuFe_2O_4$ Nanohybrids. *Environ. Sci. Pollut. Res.* **2023**, *30*, 108878–108888. https://doi.org/10.1007/s11356-023-29976-7.

[265] Liu, W.; Wei, C.; Peng, R.; Chu, R.; Sun, H.; Zhang, X.; Xie, F. Persulfate Assisted Photocatalytic Degradation of Tetracycline by Bismuth Titanate under Visible Light Irradiation. *New J. Chem.* **2022**, *46*, 10854–10862. https://doi.org/10.1039/d2nj01404a.

[266] Kaushal, S.; Kumar, A.; Bains, H.; Singh, P.P. Photocatalytic Degradation of Tetracycline Antibiotic and Organic Dyes Using Biogenic Synthesized CuO/Fe2O3 Nanocomposite: Pathways and Mechanism Insights. *Environ. Sci. Pollut. Res.* **2023**, *30*, 37092–37104. https://doi.org/10.1007/s11356-022-24848-y.

[267] Semeraro, P.; Bettini, S.; Sawalha, S.; Pal, S.; Licciulli, A.; Marzo, F.; Lovergine, N.; Valli, L.; Giancane, G. Photocatalytic Degradation of Tetracycline by ZnO/γ-Fe_2O_3 Paramagnetic Nanocomposite Material. *Nanomaterials* **2020**, *10*, 1458. https://doi.org/10.3390/nano10081458

[268] Nguetsa Kuate, L.J.; Chen, Z.; Lu, J.; Wen, H.; Guo, F.; Shi, W. Photothermal-Assisted Photocatalytic Degradation of Tetracycline in Seawater Based on the Black g-C_3N_4 Nanosheets with Cyano Group Defects. *Catalysts* **2023**, *13*, 1147. https://doi.org/10.3390/catal13071147

[269] Chen, F.; Yang, Q.; Sun, J.; Yao, F.; Wang, S.; Wang, Y.; Wang, X.; et al. Enhanced Photocatalytic Degradation of Tetracycline by AgI/BiVO4 Heterojunction under

Visible-Light Irradiation: Mineralization Efficiency and Mechanism. *ACS Appl. Mater. Interfaces* **2016**, *8*, 32887–32900. https://doi.org/10.1021/acsami.6b12278.

[270] Jia, X.; Wang, F.; Xu, X.; Liu, C.; Zhang, L.; Jiao, S.; Zhu, G.; Wang, X.; Yu, G. Highly Efficient Photocatalytic Degradation of Tetracycline by Modifying UiO-66 via Different Regulation Strategies. *ACS Omega* **2023**, *8*, 27375–27385. https://doi.org/10.1021/acsomega.3c02762.

[271] Oluwole, A.O.; Olatunji, O.S. Photocatalytic Degradation of Tetracycline in Aqueous Systems under Visible Light Irradiation Using Needle-Like SnO_2 Nanoparticles Anchored on Exfoliated g-C_3N_4. *Environ. Sci. Eur.* **2022**, *34*. https://doi.org/10.1186/s12302-021-00588-7.

[272] Zhang, X.-X.; Wang, X.-J.; Niu, Y.-Y. Photocatalytic Degradation of Tetracycline by Supramolecular Materials Constructed with Organic Cations and Silver Iodide. *Catalysts* **2022**, *12*, 1581. https://doi.org/10.3390/catal12121581

[273] Doosti, M.; Jahanshahi, R.; Laleh, S.; Sobhani, S.; Sansano, J.M. Solar Light Induced Photocatalytic Degradation of Tetracycline in the Presence of ZnO/$NiFe_2O_4$/Co_3O_4 as a New and Highly Efficient Magnetically Separable Photocatalyst. *Front. Chem.* **2022**, *10*, 1013349. https://doi.org/10.3389/fchem.2022.1013349.

[274] Li, S.; Wang, C.; Liu, Y.; Cai, M.; Wang, Y.; Zhang, H.; Guo, Y.; Zhao, W.; Wang, Z.; Chen, X. Photocatalytic Degradation of Tetracycline Antibiotic by a Novel $Bi_2Sn_2O_7$/Bi_2MoO_6 S-Scheme Heterojunction: Performance, Mechanism Insight, and Toxicity Assessment. *Chem. Eng. J.* **2022**, *429*, 132519. https://doi.org/10.1016/j.cej.2021.132519.

[275] Zhang, Y.; Zhou, J.; Chen, X.; Wang, L.; Cai, W. Coupling of Heterogeneous Advanced Oxidation Processes and Photocatalysis in Efficient Degradation of Tetracycline Hydrochloride by Fe-Based MOFs: Synergistic Effect and Degradation Pathway. *Chem. Eng. J.* **2019**, *369*, 745–757. https://doi.org/10.1016/j.cej.2019.03.108.

[276] Huang, J.; Xue, P.; Wang, S.; Han, S.; Lin, L.; Chen, X.; Wang, Z. Fabrication of Zirconium-Based Metal-Organic Frameworks@Tungsten Trioxide (UiO-66-NH_2@WO_3) Heterostructure on Carbon Cloth for Efficient Photocatalytic Removal of Tetracycline Antibiotic under Visible Light. *J. Colloid Interface Sci.* **2022**, *606*, 1509–1523. https://doi.org/10.1016/j.jcis.2021.08.108.

[277] Zhang, Z.; Du, C.; Zhang, Y.; Yu, G.; Xiong, Y.; Zhou, L.; Liu, Y. et al. Degradation of Oxytetracycline by Magnetic MOFs Heterojunction Photocatalyst with Persulfate: High Stability and Wide Range. *Environ. Sci. Pollut. Res.* **2022**, 1–11. https://doi.org/10.1007/s11356-021-17971-9.

[278] Ma, Y.; Wang, R.; Gao, C.; Han, R. Carbon Nanotube-Loaded Copper-Nickel Ferrite Activated Persulfate System for Adsorption and Degradation of Oxytetracycline Hydrochloride. *J. Colloid Interface Sci.* **2023**, *640*, 761–774. https://doi.org/10.1016/j.jcis.2023.03.001.

[279] Di Paola, A.; Addamo, M.; Augugliaro, V.; García-López, E.; Loddo, V.; Marcì, G.; Palmisano, L. Photodegradation of Lincomycin in Aqueous Solution. *Int. J. Photoenergy* **2006**, *2006*, 047418. https://doi.org/10.1155/IJP/2006/47418.

[280] Gao, B.; Dong, S.; Liu, J.; Liu, L.; Feng, Q.; Tan, N.; Liu, T.; Bo, L.; Wang, L. Identification of Intermediates and Transformation Pathways Derived from Photocatalytic Degradation of Five Antibiotics on $ZnIn_2S_4$. *Chem. Eng. J.* **2016**, *304*, 826–840. https://doi.org/10.1016/j.cej.2016.07.029.

[281] Do, T.C.M.V.; Nguyen, D.Q.; Nguyen, K.T.; Le, P.H. TiO_2 and Au-TiO_2 Nanomaterials for Rapid Photocatalytic Degradation of Antibiotic Residues in Aquaculture Wastewater. *Materials* **2019**, *12*, 2434. https://doi.org/10.3390/ma12152434

[282] Augugliaro, V.; García-López, E.; Loddo, V.; Malato-Rodríguez, S.; Maldonado, I.; Marcì, G.; Molinari, R.; Palmisano, L. Degradation of Lincomycin in Aqueous Medium: Coupling of Solar Photocatalysis and Membrane Separation. *Solar Energy* **2005**, *79*, 402–408. https://doi.org/10.1016/j.solener.2005.02.020.

[283] Deng, Y.; Liu, J.; Huang, Y.; Ma, M.; Liu, K.; Dou, X.; Wang, Z.; Qu, S.; Wang, Z. Engineering the Photocatalytic Behaviors of g/C_3N_4-Based Metal-Free Materials for Degradation of a Representative Antibiotic. *Adv. Funct. Mater.* **2020**, *30*, 2002353. https://doi.org/10.1002/adfm.202002353.

[284] Kontogiannis, A.; Evgenidou, E.; Nannou, C.; Bikiaris, D.; Lambropoulou, D. MOF-Based Photocatalytic Degradation of the Antibiotic Lincomycin Enhanced by Hydrogen Peroxide and Persulfate: Kinetics, Elucidation of Transformation Products and Toxicity Assessment. *J. Environ. Chem. Eng.* **2022**, *10*, 108112. https://doi.org/10.1016/j.jece.2022.108112.

[285] Choudhury, B.; Borah, B.; Choudhury, A. Ce–Nd Codoping Effect on the Structural and Optical Properties of TiO_2 Nanoparticles. *Mater. Sci. Eng. B* **2013**, *178*, 239–247. https://doi.org/10.1016/j.mseb.2012.11.017.

[286] Fiorenza, R.; Bellardita, M.; Scirè, S.; Palmisano, L. Effect of the Addition of Different Doping Agents on Visible Light Activity of Porous TiO_2 Photocatalysts. *Mol. Catal.* **2018**, *455*, 108–120. https://doi.org/10.1016/j.mcat.2018.06.002.

[287] Parker, J.C.; Siegel, R.W. Calibration of the Raman Spectrum to the Oxygen Stoichiometry of Nanophase TiO_2. *Appl. Phys. Lett.* **1990**, *57*, 943–945. https://doi.org/10.1063/1.104274.

[288] Maučec, D.; Šuligoj, A.; Ristić, A.; Dražić, G.; Pintar, A.; Novak Tušar, N. Titania versus Zinc Oxide Nanoparticles on Mesoporous Silica Supports as Photocatalysts for Removal of Dyes from Wastewater at Neutral pH. *Catal. Today* **2018**, *310*, 32–41. https://doi.org/10.1016/j.cattod.2017.05.061.

[289] Li, J.; Sun, X.; Xin, B.; Wang, B.; Cai, W.; Fu, H. The Preparation and Characterization of La Doped TiO_2 Nanoparticles and Their Photocatalytic Activity. *J. Solid State Chem.* **2004**, *177*, 3375–3382. https://doi.org/10.1016/j.jssc.2004.05.064.

[290] Di Paola, A.; Bellardita, M.; Marcì, G.; Palmisano, L.; Parrino, F.; Amadelli, R. Preparation of Sm-loaded Brookite TiO_2 Photocatalysts. *Catal. Today* **2011**, *161*, 35–40. https://doi.org/10.1016/j.cattod.2010.11.016.

[291] Abazović, N. D.; Čomor, M. I.; Dramićanin, M. D.; Jovanović, D. J.; Ahrenkiel, S. P.; Nedeljković, J. M. Photoluminescence of Anatase and Rutile TiO_2 Particles. *J. Phys. Chem. B* **2006**, *110*, 25366–25370. https://doi.org/10.1021/jp064454f.

[292] Jedsukontorn, T.; Ueno, T.; Saito, N.; Hunsom, M. Facile Preparation of Defective Black TiO_2 through the Solution Plasma Process: Effect of Parametric Changes for Plasma Discharge on Its Structural and Optical Properties. *J. Alloys Compd.* **2017**, *726*, 567–577. https://doi.org/10.1016/j.jallcom.2017.08.028.

[293] Bellardita, M.; Garlisi, C.; Venezia, A.M.; Palmisano, G.; Palmisano, L. Influence of Fluorine on the Synthesis of Anatase TiO_2 for Photocatalytic Partial Oxidation: Are Exposed Facets the Main Actors?. *Catal. Sci. Technol.* **2018**, *8*, 1606–1620. https://doi.org/10.1039/c7cy02382k.

[294] Murcia, J.J.; Hidalgo, M.C.; Navío, J.A.; Vaiano, V.; Ciambelli, P.; Sannino, D. Photocatalytic Ethanol Oxidative Dehydrogenation over Pt/TiO_2: Effect of the Addition of Blue Phosphors. *Int. J. Photoenergy* **2012**, *2012*, 687262. https://doi.org/10.1155/2012/687262.

[295] He, W.; Liu, Y.; Wamer, W.G.; Yin, J.-J. Electron Spin Resonance Spectroscopy for the Study of Nanomaterial-Mediated Generation of Reactive Oxygen Species. *J. Food Drug Anal.* **2014**, *22*, 49-63. https://doi.org/10.1016/j.jfda.2014.01.004.

[296] Chong, R.; Li, J.; Ma, Y.; Zhang, B.; Han, H.; Li, C. Selective Conversion of Aqueous Glucose to Value-Added Sugar Aldose on TiO_2-Based Photocatalysts. *J. Catal.* **2014**, *314*, 101–108. https://doi.org/10.1016/j.jcat.2014.03.009.

[297] Songtawee, S.; Rungtaweevoranit, B.; Klaysom, C.; Faungnawakij, K. Tuning Brønsted and Lewis Acidity on Phosphated Titanium Dioxides for Efficient Conversion of Glucose to 5-Hydroxymethylfurfural. *RSC Adv.* **2021**, *11*, 29196–29206. https://doi.org/10.1039/d1ra06002c.

[298] Bellardita, M.; Feilizadeh, M.; Fiorenza, R.; Scirè, S.; Palmisano, L.; Loddo, V. Selective Aqueous Oxidation of Aromatic Alcohols under Solar Light in the Presence of TiO_2 Modified with Different Metal Species. *Photochem. Photobiol. Sci.* **2022**, *21*, 2139–2151. https://doi.org/10.1007/s43630-022-00284-2.

[299] Nogueira, M.V.; Lustosa, G.M.M.M.; Kobayakawa, Y.; Kogler, W.; Ruiz, M.; Monteiro Filho, E.S.; Zaghete, M.A.; Perazolli, L.A. Nb-Doped TiO_2 Photocatalysts Used for Reduction of CO_2 to Methanol. *Adv. Mater. Sci. Eng.* **2018**, *2018*, 7326240. https://doi.org/10.1155/2018/7326240.

[300] Kreissl, H.T.; Nakagawa, K.; Peng, Y.-K.; Koito, Y.; Zheng, J.; Tsang, S.C.E. Niobium Oxides: Correlation of Acidity with Structure and Catalytic Performance in Sucrose Conversion to 5-Hydroxymethylfurfural. *J. Catal.* **2016**, *338*, 329–339. https://doi.org/10.1016/j.jcat.2016.03.007.

[301] Pecoraro, C.M.; Bellardita, M.; Loddo, V.; Di Franco, F.; Palmisano, L.; Santamaria, M. A Facile Way to Synthesize Noble Metal-Free TiO_2-Based Catalysts for Glycerol Photoreforming. *J. Ind. Eng. Chem.* **2023**, *118*, 247–258. https://doi.org/10.1016/j.jiec.2022.11.010.

[302] Etacheri, V.; Di Valentin, C.; Schneider, J.; Bahnemann, D.; Pillai, S.C. Visible-Light Activation of TiO_2 Photocatalysts: Advances in Theory and Experiments. *J. Photochem. Photobiol. C Photochem. Rev.* **2015**, *25*, 1–29. https://doi.org/10.1016/j.jphotochemrev.2015.08.003.

[303] Takai, A.; Kamat, P.V. Capture, Store, and Discharge: Shuttling Photogenerated Electrons Across TiO_2–Silver Interface. *ACS Nano* **2011**, *5*, 7369–7376. https://doi.org/10.1021/nn202294b.

[304] Al Jitan, S.; Li, Y.; Bahamon, D.; Žerjav, G.; Tatiparthi, V.S.; Aubry, C.; Sinnokrot, M.; Matouk, Z.; Rajput, N.; Gutierrez, M.; Al-Ali, K.; Hashaikeh, R.; Pintar, A.; Vega, L.F.; Palmisano, G. Unprecedented Photocatalytic Conversion of Gaseous and Liquid CO_2 on Graphene-Impregnated Pt/Cu-TiO_2: The Critical Role of Cu Dopant. *J. Environ. Chem. Eng.* **2023**, *11*, 109485. https://doi.org/10.1016/j.jece.2023.109485.

[305] Segovia-Guzmán, M.O.; Román-Aguirre, M.; Verde-Gomez, J.Y.; Collins-Martínez, V.H.; Zaragoza-Galán, G.; Ramos-Sánchez, V.H. Green Cu_2O/TiO_2 Heterojunction for Glycerol Photoreforming. *Catal. Today* **2020**, *349*, 88–97. https://doi.org/10.1016/j.cattod.2018.05.031.

[306] Bellardita, M.; Garlisi, C.; Venezia, A.M.; Palmisano, G.; Palmisano, L. Influence of Fluorine on the Synthesis of Anatase TiO_2 for Photocatalytic Partial Oxidation: Are Exposed Facets the Main Actors? *Catal. Sci. Technol.* **2018**, *8*, 1606–1620. https://doi.org/10.1039/c7cy02382k.

[307] Huo, J.; Hu, Y.; Jiang, H.; Li, C. In Situ Surface Hydrogenation Synthesis of Ti^{3+} Self-Doped TiO_2 with Enhanced Visible Light Photoactivity. *Nanoscale* **2014**, *6*, 9078–9084. https://doi.org/10.1039/c4nr00972j.

[308] Vijay Kumar, V.; Naresh, G.; Deepa, S.; Ganga Bhavani, P.; Nagaraju, M.; Sudhakar, M.; Chary, K.V.R.; Tardio, J.; Bhargava, S.K.; Venugopal, A. Influence of W on the Reduction Behaviour and Brønsted Acidity of Ni/TiO_2 Catalyst in the Hydrogenation

of Levulinic Acid to Valeric Acid: Pyridine Adsorbed DRIFTS Study. *Appl. Catal. A Gen.* **2017**, *531*, 169–176. https://doi.org/10.1016/j.apcata.2016.10.032.

[309] Addamo, M.; Del Arco, M.; Bellardita, M.; et al. Photoactivity of Nanostructured TiO_2 Catalysts in Aqueous System and Their Surface Acid-Base, Bulk, and Textural Properties. *Res. Chem. Intermed.* **2007**, *33*, 465–479. https://doi.org/10.1163/156856707779238685.

[310] Zaki, M.I.; Hasan, M.A.; Al-Sagheer, F.A.; Pasupulety, L. In Situ FTIR Spectra of Pyridine Adsorbed on SiO_2–Al_2O_3, TiO_2, ZrO_2, and CeO_2: General Considerations for the Identification of Acid Sites on Surfaces of Finely Divided Metal Oxides. *Colloids Surf. A Physicochem. Eng. Asp.* **2001**, *190*, 261–274. https://doi.org/10.1016/S0927-7757(01)00690-2.

[311] Ding, L.; Li, M.; Zhao, Y.; Zhang, H.; Shang, J.; Zhong, J.; Sheng, H.; Chen, C.; Zhao, J. The Vital Role of Surface Brönsted Acid/Base Sites for the Photocatalytic Formation of Free ·OH Radicals. *Appl. Catal. B Environ.* **2020**, *266*, 118634. https://doi.org/10.1016/j.apcatb.2020.118634.

[312] Zhao, J.; Wang, Y.; Li, Y.; Yue, X.; Wang, C. Phase-Dependent Enhancement for CO_2 Photocatalytic Reduction over CeO_2/TiO_2 Catalysts. *Catal. Sci. Technol.* **2016**, *6*, 7967–7975. https://doi.org/10.1039/C6CY01365A.

[313] Colmenares, J.C.; Magdziarz, A.; Bielejewska, A. High-Value Chemicals Obtained from Selective Photo-Oxidation of Glucose in the Presence of Nanostructured Titanium Photocatalysts. *Bioresour. Technol.* **2011**, *102*, 11254–11257. https://doi.org/10.1016/j.biortech.2011.09.101.

[314] Román-Leshkov, Y.; Moliner, M.; Labinger, J.A.; Davis, M.E. Mechanism of Glucose Isomerization Using a Solid Lewis Acid Catalyst in Water. *Angew. Chem. Int. Ed.* **2010**, *49*, 8954–8957. https://doi.org/10.1002/anie.201004689.

[315] Oropeza, F.E.; Dzade, N.Y.; Pons-Martí, A.; Yang, Z.; Zhang, K.H.L.; De Leeuw, N.H.; Hensen, E.J.M.; Hofmann, J.P. Electronic Structure and Interface Energetics of $CuBi_2O_4$ Photoelectrodes. *J. Phys. Chem. C* **2020**, *124*, 22416–22425. https://doi.org/10.1021/acs.jpcc.0c08455.

[316] Wang, F.; Yang, H.; Zhang, Y. Enhanced Photocatalytic Performance of $CuBi_2O_4$ Particles Decorated with Ag Nanowires. *Mater. Sci. Semicond. Process.* **2018**, *73*, 58–66. https://doi.org/10.1016/j.mssp.2017.09.029.

[317] Zhu, X.; Guan, Z.; Wang, P.; Zhang, Q.; Dai, Y.; Huang, B. Amorphous TiO_2-Modified $CuBi_2O_4$ Photocathode with Enhanced Photoelectrochemical Hydrogen Production Activity. *Chin. J. Catal.* **2018**, *39*, 1704–1710. https://doi.org/10.1016/S1872-2067(18)63127-4.

[318] Jagadeesh, C.; Suresh, P.; Sailaja, B.B.V. Photocatalytic Properties of $CuBi_2O_4$ Prepared by the Co-Precipitation Method: Degradation of Rose Bengal and Possible Reaction Mechanism under Visible Light Irradiation. *Int. J. Curr. Adv. Res.* **2017**, *6*, 8605–8610. https://doi.org/10.24327/ijcar.2017.8610.1392.

[319] Yurdakal, S.; Garlisi, C.; Özcan, L.; Bellardita, M.; Palmisano, G. Chapter 4 - (Photo)catalyst Characterization Techniques: Adsorption Isotherms and BET, SEM, FTIR, UV–Vis, Photoluminescence, and Electrochemical Characterizations. In *Heterogeneous Photocatalysis*; Marcì, G., Palmisano, L., Eds.; Elsevier: Amsterdam, The Netherlands, 2019; pp. 87–152. https://doi.org/10.1016/B978-0-444-64015-4.00004-3.

[320] Zhang, F.X.; Saxena, S.K. Raman Studies of Bi_2CuO_4 at High Pressures. *Appl. Phys. Lett.* **2006**, *88*, 141926. https://doi.org/10.1063/1.2189450.

[321] Popović, Z.V.; Kliche, G.; Cardona, M.; Liu, R. Vibrational Properties of Bi_2CuO_4. *Phys. Rev. B* **1990**, *41*, 3824. https://doi.org/10.1103/PhysRevB.41.3824.

[322] Fiorenza, R.; Bellardita, M.; Scirè, S.; Palmisano, L. Photocatalytic H_2 Production over Inverse Opal TiO_2 Catalysts. *Catal. Today* **2019**, *321–322*, 113–119. https://doi.org/10.1016/j.cattod.2017.12.011.

[323] Deiana, C.; Fois, E.; Coluccia, S.; Martra, G. Surface Structure of TiO_2 P25 Nanoparticles: Infrared Study of Hydroxy Groups on Coordinative Defect Sites. *J. Phys. Chem. C* **2010**, *114*, 21531–21538. https://doi.org/10.1021/jp107671k.

[324] Mino, L.; Spoto, G.; Bordiga, S.; Zecchina, A. Particles Morphology and Surface Properties as Investigated by HRTEM, FTIR, and Periodic DFT Calculations: From Pyrogenic TiO_2 (P25) to Nanoanatase. *J. Phys. Chem. C* **2012**, *116*, 17008–17018. https://doi.org/10.1021/jp303942h.

[325] Nakamura, R.; Imanishi, A.; Murakoshi, K.; Nakato, Y. In Situ FTIR Studies of Primary Intermediates of Photocatalytic Reactions on Nanocrystalline TiO_2 Films in Contact with Aqueous Solutions. *J. Am. Chem. Soc.* **2003**, *125*, 7443–7450. https://doi.org/10.1021/ja029503q.

[326] Praveen, P.; Viruthagiri, G.; Mugundan, S.; Shanmugam, N. Structural, Optical and Morphological Analyses of Pristine Titanium Dioxide Nanoparticles – Synthesized via Sol–Gel Route. *Spectrochim. Acta Part A Mol. Biomol. Spectrosc.* **2014**, *117*, 622–629. https://doi.org/10.1016/j.saa.2013.09.037.

[327] Djaballah, A. M.; Bellardita, M.; Palmisano, L.; Loddo, V.; Umair, M.; Pecoraro, C. M.; Bagtache, R.; Trari, M. Facile Preparation of $CuBi_2O_4/TiO_2$ Hetero-Systems Employed for Simulated Solar-Light Selective Oxidation of 4-Methoxybenzyl Alcohol Model Compound. *Molecular Catal.* **2023**, *546*, 113251. https://doi.org/10.1016/j.mcat.2023.113251.

[328] Fiorenza, R.; Bellardita, M.; Barakat, T.; Scirè, S.; Palmisano, L. Visible Light Photocatalytic Activity of Macro-Mesoporous TiO_2-CeO_2 Inverse Opals. *J. Photochem. Photobiol. A Chem.* **2018**, *352*, 25–34. https://doi.org/10.1016/j.jphotochem.2017.10.052.

[329] Jiao, J.; Wei, Y.; Zhao, Z.; Liu, J.; Li, J.; Duan, A.; Jiang, G. Photocatalysts of 3D Ordered Macroporous TiO_2-Supported CeO_2 Nanolayers: Design, Preparation, and Their Catalytic Performances for the Reduction of CO_2 with H_2O under Simulated Solar Irradiation. *Ind. Eng. Chem. Res.* **2014**, *53*, 17345–17354. https://doi.org/10.1021/ie503333b.

[330] Aguirre, M.E.; Zhou, R.; Eugene, A.J.; Guzman, M.I.; Grela, M.A. Cu_2O/TiO_2 Heterostructures for CO_2 Reduction through a Direct Z-Scheme: Protecting Cu_2O from Photocorrosion. *Appl. Catal. B Environ.* **2017**, *217*, 485–493. https://doi.org/10.1016/j.apcatb.2017.05.058.

[331] Wei, T.; Zhu, Y.-N.; An, X.; Liu, L.-M.; Cao, X.; Liu, H.; Qu, J. Defect Modulation of Z-Scheme TiO_2/Cu_2O Photocatalysts for Durable Water Splitting. *ACS Catal.* **2019**, *9*, 8346–8354. https://doi.org/10.1021/acscatal.9b01786.

[332] Wang, S.; Wang, D.; Tian, B.; et al. Synergistic Cu^+/Cu^0 on Cu_2O-Cu Interfaces for Efficient and Selective C_{2^+} Production in Electrocatalytic CO_2 Conversion. *Sci. China Mater.* **2023**, *66*, 1801–1809. https://doi.org/10.1007/s40843-022-2344-2.

[333] Pecoraro, C. M.; Mino, L.; Kozyr, E.; Palmisano, L.; di Franco, F.; Loddo, V.; Santamaria, M.; Bellardita, M. Pt–TiO_2 Catalysts for Glycerol Photoreforming: Comparison of Anatase, Brookite and Rutile Polymorphs. *Chem. Commun.* **2024**, *60*, 3782–3785. https://doi.org/10.1039/d4cc00353e.

[334] Bellardita, M.; Virtù, D.; Di Franco, F.; Loddo, V.; Palmisano, L.; Santamaria, M. Heterogeneous Photocatalytic Aqueous Succinic Acid Formation from Maleic Acid Reduction. *Chem. Eng. J.* **2022**, *431*, 134131. https://doi.org/10.1016/j.cej.2021.134131.

[335] Bellardita, M.; El Nazer, H.A.; Loddo, V.; Parrino, F.; Venezia, A.M.; Palmisano, L. Photoactivity under Visible Light of Metal Loaded TiO_2 Catalysts Prepared by Low Frequency Ultrasound Treatment. *Catal. Today* **2017**, *284*, 92–99. https://doi.org/10.1016/j.cattod.2016.11.026.

[336] Kumaravel, V.; Imam, M.D.; Badreldin, A.; Chava, R.K.; Do, J.Y.; Kang, M.; Abdel-Wahab, A. Photocatalytic Hydrogen Production: Role of Sacrificial Reagents on the Activity of Oxide, Carbon, and Sulfide Catalysts. *Catalysts* **2019**, *9*, 276. https://doi.org/10.3390/catal9030276

[337] Acar, C.; Dincer, I.; Zamfirescu, C. A Review on Selected Heterogeneous Photocatalysts for Hydrogen Production. *Int. J. Energy Res.* **2014**, *38*, 1903–1920. https://doi.org/10.1002/er.3211.

[338] Popugaeva, D.; Tian, T.; Ray, A.K. Hydrogen Production from Aqueous Triethanolamine Solution Using Eosin Y-Sensitized ZnO Photocatalyst Doped with Platinum. *Int. J. Hydrogen Energy* **2020**, *45*, 11097–11107. https://doi.org/10.1016/j.ijhydene.2020.02.055.

[339] Núñez, J.; Fresno, F.; Collado, L.; Jana, P.; Coronado, J.M.; Serrano, D.P.; de la Peña O'Shea, V.A. Photocatalytic H_2 Production from Aqueous Methanol Solutions Using Metal-Co-Catalysed Zn_2SnO_4 Nanostructures. *Appl. Catal. B Environ.* **2016**, *191*, 106–115. https://doi.org/10.1016/j.apcatb.2016.03.020.

[340] Huang, B.-S.; Chang, F.-Y.; Wey, M.-Y. Photocatalytic Properties of Redox-Treated Pt/TiO_2 Photocatalysts for H_2 Production from an Aqueous Methanol Solution. *Int. J. Hydrogen Energy* **2010**, *35*, 7699–7705. https://doi.org/10.1016/j.ijhydene.2010.05.103.

[341] Gunawan, D.; Lau, L.Y.; Yuwono, J.A.; Kumar, P.V.; Oppong-Antwi, L.; Kuschnerus, I.; Chang, S.L.Y.; et al. Revealing the Activity and Selectivity of Atomically Dispersed Ni in $Zn_3In_2S_6$ for Benzyl Alcohol Photoreforming. *Chem. Eng. J.* **2024**, 150215. https://doi.org/10.1016/j.cej.2024.150215.

[342] Nwosu, U.; Wang, A.; Palma, B.; Zhao, H.; Khan, M.A.; Kibria, M.; Hu, J. Selective Biomass Photoreforming for Valuable Chemicals and Fuels: A Critical Review. *Renew. Sustain. Energy Rev.* **2021**, *148*, 111266. https://doi.org/10.1016/j.rser.2021.111266.

[343] Parrino, F.; Bellardita, M.; García-López, E.I.; Marcì, G.; Loddo, V.; Palmisano, L. Heterogeneous Photocatalysis for Selective Formation of High-Value-Added Molecules: Some Chemical and Engineering Aspects. *ACS Catal.* **2018**, *8*, 11191–11225. https://doi.org/10.1021/acscatal.8b03093.

[344] Chen, X.; Zhang, L.; Zhang, B.; Guo, X.; Mu, X. Highly Selective Hydrogenation of Furfural to Furfuryl Alcohol over Pt Nanoparticles Supported on g-C_3N_4 Nanosheets Catalysts in Water. *Sci. Rep.* **2016**, *6*, 28558. https://doi.org/10.1038/srep28558.

[345] Li, X.; Hu, J.; Yang, T.; Yang, X.; Qu, J.; Li, C. M. Efficient Photocatalytic H_2-Evolution Coupled with Valuable Furfural-Production on Exquisite 2D/2D $LaVO_4$/g-C_3N_4 Heterostructure. *Nano Energy* **2022**, *92*, 106714. https://doi.org/10.1016/j.nanoen.2021.106714.

[346] Tan, C.-L.; Qi, M.-Y.; Tang, Z.-R.; Xu, Y.-J. Cocatalyst Decorated $ZnIn_2S_4$ Composites for Cooperative Alcohol Conversion and H_2 Evolution. *Appl. Catal. B Environ.* **2021**, *298*, 120541. https://doi.org/10.1016/j.apcatb.2021.120541.

[347] Palmisano, G.; Yurdakal, S.; Augugliaro, V.; Loddo, V.; Palmisano, L. Photocatalytic Selective Oxidation of 4-Methoxybenzyl Alcohol to Aldehyde in Aqueous Suspension of Home-Prepared Titanium Dioxide Catalyst. *Adv. Synth. Catal.* **2007**, *349*, 964–970. https://doi.org/10.1002/adsc.200600435.

[348] Hu, Y.; Huang, W.; Wang, H.; He, Q.; Zhou, Y.; Yang, P.; Li, Y.; Li, Y. Metal-Free Photocatalytic Hydrogenation Using Covalent Triazine Polymers. *Angew. Chem. Int. Ed.* **2020**, *59*, 14378–14382. https://doi.org/10.1002/anie.202006618.

[349] Wang, H.; Song, Y.; Xiong, J.; Bi, J.; Li, L.; Yu, Y.; Liang, S.; Wu, L. Highly Selective Oxidation of Furfuryl Alcohol over Monolayer Titanate Nanosheet under Visible Light Irradiation. *Appl. Catal. B Environ.* **2018**, *224*, 394–403. https://doi.org/10.1016/j.apcatb.2017.10.069.

[350] Augugliaro, V.; Loddo, V.; López-Muñoz, M.J.; Márquez-Alvarez, C.; Palmisano, G.; Palmisano, L.; Yurdakal, S. Home-Prepared Anatase, Rutile, and Brookite TiO_2 for Selective Photocatalytic Oxidation of 4-Methoxybenzyl Alcohol in Water: Reactivity and ATR-FTIR Study. *Photochem. Photobiol. Sci.* **2009**, *8*, 663–669. https://doi.org/10.1039/b818353h.

[351] Bellardita, M.; Escolano-Casado, G.; Palmisano, L.; Mino, L. Surface Processes in Selective Photocatalytic Oxidation of Hydroxybenzyl Alcohols by TiO_2 P25. *Catal. Today* **2023**, *413–415*, 113983. https://doi.org/10.1016/j.cattod.2022.12.014.

[352] Fónagy, O.; Szabó-Bárdos, E.; Horváth, O. 1,4-Benzoquinone and 1,4-Hydroquinone Based Determination of Electron and Superoxide Radical Formed in Heterogeneous Photocatalytic Systems. *J. Photochem. Photobiol. A: Chem.* **2021**, *407*, 113057. https://doi.org/10.1016/j.jphotochem.2020.113057.

[353] Muscetta, M.; Al Jitan, S.; Palmisano, G.; Andreozzi, R.; Marotta, R.; Cimino, S.; Di Somma, I. Visible Light-Driven Photocatalytic Hydrogen Production Using Cu_2O/TiO_2 Composites Prepared by Facile Mechanochemical Synthesis. *J. Environ. Chem. Eng.* **2022**, *10*, 107735. https://doi.org/10.1016/j.jece.2022.107735.

[354] Villachica-Llamosas, J.G.; Ruiz-Aguirre, A.; Colón, G.; Peral, J.; Malato, S. CuO–TiO_2 Pilot-Plant System Performance for Solar Photocatalytic Hydrogen Production. *Int. J. Hydrogen Energy* **2024**, *51*, 1069–1077. https://doi.org/10.1016/j.ijhydene.2023.07.149.

[355] Yu, J.; Hai, Y.; Jaroniec, M. Photocatalytic Hydrogen Production over CuO-Modified Titania. *J. Colloid Interface Sci.* **2011**, *357*, 223–228. https://doi.org/10.1016/j.jcis.2011.01.101.

[356] Gombac, V.; Sordelli, L.; Montini, T.; Delgado, J. J.; Adamski, A.; Adami, G.; Cargnello, M.; Bernal, S.; Fornasiero, P. CuO_x–TiO_2 Photocatalysts for H_2 Production from Ethanol and Glycerol Solutions. *J. Phys. Chem. A* **2010**, *114*, 3916–3925. https://doi.org/10.1021/jp907242q.

[357] Muscetta, M.; Andreozzi, R.; Clarizia, L.; Di Somma, I.; Marotta, R. Hydrogen Production through Photoreforming Processes over Cu_2O/TiO_2 Composite Materials: A Mini-Review. *Int. J. Hydrogen Energy* **2020**, *45*, 28531–28552. https://doi.org/10.1016/j.ijhydene.2020.07.225.

[358] Liu, Y.; Wang, Z.; Huang, W. Influences of TiO_2 Phase Structures on the Structures and Photocatalytic Hydrogen Production of CuO_x/TiO_2 Photocatalysts. *Appl. Surf. Sci.* **2016**, *389*, 760–767. https://doi.org/10.1016/j.apsusc.2016.07.173.

[359] Iervolino, G.; Vaiano, V.; Murcia, J.J.; Lara, A.E.; Hernández, J.S.; Rojas, H.; Navío, J.A.; Hidalgo, M.C. Photocatalytic Production of Hydrogen and Methane from Glycerol Reforming over Pt/TiO_2–Nb_2O_5. *Int. J. Hydrogen Energy* **2021**, *46*, 38678–38691. https://doi.org/10.1016/j.ijhydene.2021.09.111.

[360] Kouti, M.; Matouri, L. Fabrication of Nanosized Cuprous Oxide Using Fehling's Solution. *Scientia Iranica* **2010**, *17*, 73-78. Available online: https://api.semanticscholar.org/CorpusID:54534478.

[361] Fiorenza, R.; Bellardita, M.; D'Urso, L.; Compagnini, G.; Palmisano, L.; Scirè, S. Au/TiO_2-CeO_2 Catalysts for Photocatalytic Water Splitting and VOCs Oxidation Reactions. *Catalysts* **2016**, *6*, 121. https://doi.org/10.3390/catal6080121

[362] Gombac, V.; Sordelli, L.; Montini, T.; Delgado, J.J.; Adamski, A.; Adami, G.; Cargnello, M.; Bernal, S.; Fornasiero, P. CuO_x–TiO_2 Photocatalysts for H_2 Production from Ethanol and Glycerol Solutions. *J. Phys. Chem. A* **2010**, *114*, 3916-3925. https://doi.org/10.1021/jp907242q.

[363] López-Tenllado, F.J.; Hidalgo-Carrillo, J.; Montes, V.; Marinas, A.; Urbano, F.J.; Marinas, J.M.; Ilieva, L.; Tabakova, T.; Reid, F. A Comparative Study of Hydrogen Photocatalytic Production from Glycerol and Propan-2-ol on M/TiO_2 Systems (M = Au, Pt, Pd). *Catal. Today* **2017**, *280*, 58-64. https://doi.org/10.1016/j.cattod.2016.05.009.

[364] Quiroz-Cardoso, O.; Oros-Ruiz, S.; Solís-Gómez, A.; López, R.; Gómez, R. Enhanced Photocatalytic Hydrogen Production by CdS Nanofibers Modified with Graphene Oxide and Nickel Nanoparticles under Visible Light. *Fuel* **2019**, *237*, 227-235. https://doi.org/10.1016/j.fuel.2018.10.013.

[365] Herrmann, J.M. Heterogeneous Photocatalysis: State of the Art and Present Applications. *Top Catal* **2005**, *34*, 49–65. https://doi.org/10.1007/s11244-005-3788-2.

[366] Montini, T.; Gombac, V.; Sordelli, L.; Delgado, J.J.; Chen, X.; Adami, G.; Fornasiero, P. Nanostructured Cu/TiO_2 Photocatalysts for H_2 Production from Ethanol and Glycerol Aqueous Solutions. *ChemCatChem* **2011**, *3*, 574–577. https://doi.org/10.1002/cctc.201000289.

[367] Wang, G.; Chen, G.; Yu, Y.; Zhou, X.; Teng, Y. Mixed Solvothermal Synthesis of Hierarchical $ZnIn_2S_4$ Spheres: Specific Facet-Induced Photocatalytic Activity Enhancement and a DFT Elucidation. *RSC Adv.* **2013**, *3*, 18579–18586. https://doi.org/10.1039/c3ra42245c.

[368] Chen, Z.; Xu, J.; Ren, Z.; He, Y.; Xiao, G. Low Temperature Synthesis of $ZnIn_2S_4$ Microspheres as a Visible Light Photocatalyst for Selective Oxidation. *Catal. Commun.* **2013**, *41*, 83–86. https://doi.org/10.1016/j.catcom.2013.07.016.

[369] He, J.; Zhang, G.; Jiang, Y.; Jia, J.; Cao, J. Design and Synthesis of Two Dimensional-$ZnIn_2S_4$ Nanosheets with Sulfur Vacancies for Improving Photocatalytic Hydrogen Production Performance. *Prog. Nat. Sci. Mater. Int.* **2023**, *33*, 607–615. https://doi.org/10.1016/j.pnsc.2023.11.005.

[370] Pecoraro, C. M.; Di Franco, F.; Bellardita, M.; Loddo, V.; Santamaria, M. Enhancing H_2 Production Rate in PGM-Free Photoelectrochemical Cells by Glycerol Photo-Oxidation. *Int. J. Hydrogen Energy* **2024**, *49*, 322–336. https://doi.org/10.1016/j.ijhydene.2023.08.011.

[371] Santamaria, M.; Conigliaro, G.; Di Franco, F.; Megna, B.; Di Quarto, F. Electronic Properties of Thermal Oxides on Ti and Their Influence on Impedance and Photoelectrochemical Behavior of TiO_2 Nanotubes. *J. Electrochem. Soc.* **2017**, *164* (4), C113. https://doi.org/10.1149/2.0601704jes.

[372] Higashimoto, S.; Suetsugu, N.; Azuma, M.; Ohue, H.; Sakata, Y. Efficient and Selective Oxidation of Benzylic Alcohol by O_2 into Corresponding Aldehydes on a TiO_2 Photocatalyst under Visible Light Irradiation: Effect of Phenyl-Ring Substitution on the Photocatalytic Activity. *J. Catal.* **2010**, *274*, 76–83. https://doi.org/10.1016/j.jcat.2010.06.006.

[373] Palmisano, G.; Addamo, M.; Augugliaro, V.; Caronna, T.; García-López, E.; Loddo, V.; Palmisano, L. Influence of the Substituent on Selective Photocatalytic Oxidation of Aromatic Compounds in Aqueous TiO_2 Suspensions. *Chem. Commun.* **2006**, *9*, 1012–1014. https://doi.org/10.1039/b515853b.

[374] Yurdakal, S.; Palmisano, G.; Loddo, V.; Alagöz, O.; Augugliaro, V.; Palmisano, L. Selective Photocatalytic Oxidation of 4-Substituted Aromatic Alcohols in Water with

Rutile TiO_2 Prepared at Room Temperature. *Green Chem.* **2009**, *11*, 510–516. https://doi.org/10.1039/B819862D.

[375] Bellardita, M.; García-López, E. I.; Marcì, G.; Krivtsov, I.; García, J. R.; Palmisano, L. Selective Photocatalytic Oxidation of Aromatic Alcohols in Water by Using P-Doped g-C_3N_4. *Appl. Catal. B* **2018**, *220*, 222–233. https://doi.org/10.1016/j.apcatb.2017.08.033.

[376] Chen, Z.; Xu, J.; Ren, Z.; He, Y.; Xiao, G. High Efficient Photocatalytic Selective Oxidation of Benzyl Alcohol to Benzaldehyde by Solvothermal-Synthesized $ZnIn_2S_4$ Microspheres under Visible Light Irradiation. *J. Solid State Chem.* **2013**, *205*, 134–141. https://doi.org/10.1016/j.jssc.2013.07.015.

[377] Augugliaro, V.; Caronna, T.; Loddo, V.; Marcì, G.; Palmisano, G.; Palmisano, L.; Yurdakal, S. Oxidation of Aromatic Alcohols in Irradiated Aqueous Suspensions of Commercial and Home-Prepared Rutile TiO_2: A Selectivity Study. *Chem. Eur. J.* **2008**, *14*, 4640–4646. https://doi.org/10.1002/chem.200702044.

[378] Palazzolo, A.; Bellardita, M.; Di Paola, A.; Loddo, V.; Palmisano, L.; Augugliaro, V.; Yurdakal, S. Photocatalytic Oxidation of Aromatic Alcohols to Aldehydes over TiO_2: A New Method to Control Selectivity. *ChemSusChem* **2011**, *4*, 1431–1438. https://doi.org/10.1002/cssc.201100196.

[379] Bellardita, M.; Loddo, V.; Palmisano, G.; Pibiri, I.; Palmisano, L.; Augugliaro, V. Photocatalytic Green Synthesis of Piperonal in Aqueous TiO_2 Suspension. *Appl. Catal. B Environ.* **2014**, *144*, 607–613. https://doi.org/10.1016/j.apcatb.2013.07.070.

[380] Li, S.; Meng, L.; Tian, W.; Li, L. Engineering Interfacial Band Bending over $ZnIn_2S_4/SnS_2$ by Interface Chemical Bond for Efficient Solar-Driven Photoelectrochemical Water Splitting. *Adv. Energy Mater.* **2022**, *12*, 202200629. https://doi.org/10.1002/aenm.202200629.

[381] Balachandran, U.; Eror, N.G. Raman Spectra of Titanium Dioxide. *J. Solid State Chem.* **1982**, *42*, 276–282. https://doi.org/10.1016/0022-4596(82)90006-8.

[382] Balarabe, A.Y.; Paria, S.; Keita, D.S.; Baraze, A.R.I.B.; Kalugendo, E.; Tetteh, G.N.T.; Meringo, M.M.; Oumarou, M.N.I. Enhanced UV-Light Active α-Bi_2O_3 Nanoparticles for the Removal of Methyl Orange and Ciprofloxacin. *Inorg. Chem. Commun.* **2022**, *146*, 110204. https://doi.org/10.1016/j.inoche.2022.110204.

[383] Ho, C.-H.; Chan, C.-H.; Huang, Y.-S.; Tien, L.-C.; Chao, L.-C. The Study of Optical Band Edge Property of Bismuth Oxide Nanowires α-Bi_2O_3. *Opt. Express* **2013**, *21*, 11965–11972. https://doi.org/10.1364/OE.21.011965.

[384] In, J.; Yoon, I.; Seo, K.; Park, J.; Choo, J.; Lee, Y.; Kim, B. Polymorph-Tuned Synthesis of α- and β-Bi_2O_3 Nanowires and Determination of Their Growth Direction from Polarized Raman Single Nanowire Microscopy. *Chemistry - A European Journal* **2011**, *17*, 1304–1309. https://doi.org/10.1002/chem.201001684.

[385] Jiang, J.; Ou-yang, L.; Zhu, L.; Zheng, A.; Zou, J.; Yi, X.; Tang, H. Dependence of Electronic Structure of g-C_3N_4 on the Layer Number of Its Nanosheets: A Study by Raman Spectroscopy Coupled with First-Principles Calculations. *Carbon* **2014**, *80*, 213–221. https://doi.org/10.1016/j.carbon.2014.08.059.

[386] Zinin, P.V.; Ming, L.-C.; Sharma, S.K.; Khabashesku, V.N.; Liu, X.; Hong, S.; Endo, S.; Acosta, T. Ultraviolet and Near-Infrared Raman Spectroscopy of Graphitic C_3N_4 Phase. *Chem. Phys. Lett.* **2009**, *472*, 69–73. https://doi.org/10.1016/j.cplett.2009.02.068.

[387] Chen, Y.; Hu, S.; Liu, W.; Chen, X.; Wu, L.; Wang, X.; Liu, P.; Li, Z. Controlled Syntheses of Cubic and Hexagonal $ZnIn_2S_4$ Nanostructures with Different Visible-Light Photocatalytic Performance. *Dalton Trans.* **2011**, *40*, 2607–2613. https://doi.org/10.1039/c0dt01435d.

[388] Wang, J.; Sun, S.; Zhou, R.; Li, Y.; He, Z.; Ding, H.; Chen, D.; Ao, W. A Review: Synthesis, Modification and Photocatalytic Applications of $ZnIn_2S_4$. *J. Mater. Sci. Technol.* **2021**, *78*, 1–19. https://doi.org/10.1016/j.jmst.2020.09.045.

[389] Jiang, H.-Y.; Cheng, K.; Lin, J. Crystalline Metallic Au Nanoparticle-Loaded α-Bi_2O_3 Microrods for Improved Photocatalysis. *Phys. Chem. Chem. Phys.* **2012**, *14*, 12114–12121. https://doi.org/10.1039/C2CP42165H.

[390] Bellardita, M.; Yurdakal, S.; Tek, B.S.; Değirmenci, Ç.; Palmisano, G.; Loddo, V.; Palmisano, L.; Soria, J.; Sanz, J.; Augugliaro, V. Tuning the Selectivity to Aldehyde via pH Regulation in the Photocatalytic Oxidation of 4-Methoxybenzyl Alcohol and Vanillyl Alcohol by TiO_2 Catalysts. *J. Environ. Chem. Eng.* **2021**, *9*, 105308. https://doi.org/10.1016/j.jece.2021.105308.

[391] Gunjal, A.R.; Kulkarni, A.K.; Kawade, U.V.; Sethi, Y.A.; Sonawane, R.S.; Ook-Baeg, J.; Nagawade, A.V.; Kale, B.B. A Hierarchical SnS@$ZnIn_2S_4$ Marigold Flower-Like 2D Nano-Heterostructure as an Efficient Photocatalyst for Sunlight-Driven Hydrogen Generation. *Nanoscale Adv.* **2020**, *2*, 2577–2586. https://doi.org/10.1039/D0NA00175A.

[392] Wang, Y.; Kong, X.; Jiang, M.; Zhang, F.; Lei, X. A Z-Scheme $ZnIn_2S_4$/Nb_2O_5 Nanocomposite: Constructed and Used as an Efficient Bifunctional Photocatalyst for H_2 Evolution and Oxidation of 5-Hydroxymethylfurfural. *Inorg. Chem. Front.* **2020**, *7*, 437–446. https://doi.org/10.1039/c9qi01196j.

[393] Liu, C.; Zhang, Q.; Zou, Z. Recent Advances in Designing $ZnIn_2S_4$-Based Heterostructured Photocatalysts for Hydrogen Evolution. *J. Mater. Sci. Technol.* **2023**, *139*, 167–188. https://doi.org/10.1016/j.jmst.2022.08.030.

[394] Zhang, J.; Zhang, G.; Lan, H.; Sun, M.; Liu, H.; Qu, J. Synergetic Oxidation of the Hydroxyl Radical and Superoxide Anion Lowers the Benzoquinone Intermediate Conversion Barrier and Potentiates Effective Aromatic Pollutant Mineralization. *Environ. Sci. Technol.* **2023**, *57*, 12117–12126. https://doi.org/10.1021/acs.est.3c03406.

[395] Meng, Y.; Yang, S.; Li, H. Electro- and Photocatalytic Oxidative Upgrading of Bio-Based 5-Hydroxymethylfurfural. *ChemSusChem* **2022**, *15*, e202102581. https://doi.org/10.1002/cssc.202102581.

[396] Zhang, W.; Li, Q.; Xia, H. Photocatalytic Oxidation of 5-Hydroxymethylfurfural to Furandicarboxylic Acid over the Au-Ag/TiO_2 Catalysts under Visible Light Irradiation. *Appl. Surf. Sci.* **2023**, *613*, 156036. https://doi.org/10.1016/j.apsusc.2022.156036.

[397] Zhang, M.; Li, Z.; Xin, X.; Zhang, J.; Feng, Y.; Lv, H. Selective Valorization of 5-Hydroxymethylfurfural to 2,5-Diformylfuran Using Atmospheric O_2 and $MAPbBr_3$ Perovskite under Visible Light. *ACS Catal.* **2020**, *10*, 14793–14800. https://doi.org/10.1021/acscatal.0c04330.

[398] ElMetwally, A.E.; Sayed, M.S.; Zhou, Y.; Domena, J.B.; Shim, J.-J.; Leblanc, R.M.; Knecht, M.R.; Bachas, L.G. Photocatalytic Partial Oxidation of 5-Hydroxymethylfurfural to 2,5-Diformylfuran Using Exfoliated g-C_3N_4/Pd Nanoarchitectures. *J. Phys. Chem. C* **2022**, *126*, 15671–15684. https://doi.org/10.1021/acs.jpcc.2c04186.

[399] Athukoralalage Don K. Deshan, A.; Atanda, L.; Moghaddam, L.; Rackemann, D.W.; Beltramini, J.; Doherty, W.O.S. Heterogeneous Catalytic Conversion of Sugars into 2,5-Furandicarboxylic Acid. *Front. Chem.* **2020**, *8*, 659. https://doi.org/10.3389/fchem.2020.00659.

[400] Ulyankina, A.; Mitchenko, S.; Smirnova, N. Selective Photocatalytic Oxidation of 5-HMF in Water over Electrochemically Synthesized TiO_2 Nanoparticles. *Processes* **2020**, *8*, 647. https://doi.org/10.3390/pr806064

[401] Yurdakal, S.; Tek, B.S.; Alagöz, O.; Augugliaro, V.; Loddo, V.; Palmisano, G.; Palmisano, L. Photocatalytic Selective Oxidation of 5-(Hydroxymethyl)-2-Furaldehyde to 2,5-Furandicarbaldehyde in Water by Using Anatase, Rutile, and Brookite TiO_2 Nanoparticles. *ACS Sustainable Chem. Eng.* **2013**, *1*, 456–461. https://doi.org/10.1021/sc300142a.

[402] Shuwanto, H.; Lie, J.; Abdullah, H.; Pasaribu, S.P.; Masmur, I.; Tiffany; Nur, N.S.; Kastario. Medical Waste Utilization as a Carbon Source Assisting Nanothorn $ZnIn_2S_4$ for Photocatalytic Hydrogen Evolution and Hydrogenation Reaction. *J. Taiwan Inst. Chem. Eng.* **2024**, *159*, 105284. https://doi.org/10.1016/j.jtice.2023.105284.

[403] Yang, O.; Liang, J.; Luo, L.; Deng, R.; Li, G.; He, Q.; Chen, Y. Facile Defect Engineering in $ZnIn_2S_4$ Coupled with Carbon Dots for Rapid Diclofenac Degradation. *Chinese Chem. Lett.* **2021**, *32*, 2534–2538. https://doi.org/10.1016/j.cclet.2020.12.049.

[404] Song, Y.; Zhang, J.; Dong, X.; Li, H. A Review and Recent Developments in Full-Spectrum Photocatalysis Using $ZnIn_2S_4$-Based Photocatalysts. *Energy Technol.* **2021**, *9*, 2100033. https://doi.org/10.1002/ente.202100033.

[405] Yin, X.; Lv, B.; Kang, Y.; Liu, Y.; Wei, C.; Yu, J. Solvent-Induced $ZnIn_2S_4$ Nanosheets Self-Assembled Micro-Flowers to Boost the Photocatalytic Semi-Dehydrogenation of 1,2,3,4-Tetrahydroisoquinoline. *Catal. Lett.* **2023**, *153*, 570–583. https://doi.org/10.1007/s10562-022-04002-6.

[406] Umair, M.; Pecoraro, C.M.; Di Franco, F.; Santamaria, M.; Palmisano, L.; Loddo, V.; Bellardita, M. Efficient Photocatalytic Partial Oxidation of Aromatic Alcohols by Using $ZnIn_2S_4$ under Green Conditions. *ChemSusChem* **2024**, e202400404. https://doi.org/10.1002/cssc.202400404.

[407] Bao, X.; Liu, M.; Wang, Z.; Dai, D.; Wang, P.; Cheng, H.; Liu, Y.; Zheng, Z.; Dai, Y.; Huang, B. Photocatalytic Selective Oxidation of HMF Coupled with H_2 Evolution on Flexible Ultrathin g-C_3N_4 Nanosheets with Enhanced N–H Interaction. *ACS Catal.* **2022**, *12*, 1919–1929. https://doi.org/10.1021/acscatal.1c05357.

[408] Qiu, B.; Huang, P.; Lian, C.; Ma, Y.; Xing, M.; Liu, H.; Zhang, J. Realization of All-in-One Hydrogen-Evolving Photocatalysts via Selective Atomic Substitution. *Appl. Catal. B Environ.* **2021**, *298*, 120518. https://doi.org/10.1016/j.apcatb.2021.120518.

[409] Ma, H.L.; Yang, J.Y.; Dai, Y.; Zhang, Y.B.; Lu, B.; Ma, G.H. Raman Study of Phase Transformation of TiO_2 Rutile Single Crystal Irradiated by Infrared Femtosecond Laser. *Appl. Surf. Sci.* **2007**, *253*, 7497–7500. https://doi.org/10.1016/j.apsusc.2007.03.047.

[410] Di Paola, A.; Cufalo, G.; Addamo, M.; Bellardita, M.; Campostrini, R.; Ischia, M.; Ceccato, R.; Palmisano, L. Photocatalytic Activity of Nanocrystalline TiO_2 (Brookite, Rutile and Brookite-Based) Powders Prepared by Thermohydrolysis of $TiCl_4$ in Aqueous Chloride Solutions. *Colloids Surf. A Physicochem. Eng. Asp.* **2008**, *317*, 366–376. https://doi.org/10.1016/j.colsurfa.2007.11.005.

[411] Surmacki, J.; Wroński, P.; Szadkowska-Nicze, M.; Abramczyk, H. Raman Spectroscopy of Visible-Light Photocatalyst - Nitrogen-Doped Titanium Dioxide Generated by Irradiation with Electron Beam. *Chem. Phys. Lett.* **2013**, *566*, 54–59. https://doi.org/10.1016/j.cplett.2013.02.066.

[412] Umair, M.; Djaballah, A.M.; Bellardita, M.; Bagtache, R.; Palmisano, L.; Trari, M. Visible-Light Photoreforming of Biomass Derivatives through MBi_2O_4-P25 Heterostructures: Study of the Influence of Metals (M = Cu, Ni, Zn, Co). *Adv. Sustain. Syst.* **2024**, 2400298. https://doi.org/10.1002/adsu.202400298.

[413] Héquet, V.; Gonzalez, C.; Le Cloirec, P. Photochemical Processes for Atrazine Degradation: Methodological Approach. *Water Research* **2001**, *35*, 4253–4260. https://doi.org/10.1016/S0043-1354(01)00166-X.

[414] Raschke, U.; Werner, G.; Wilde, H.; Stottmeister, U. Photodecomposition of 4-Amino-1,2,4-Triazin-3,5-Diones and -Thiones in Oxygenated Aqueous Solutions. *J. Photochem. Photobiol. A: Chem.* **1998**, *115*, 191–197. https://doi.org/10.1016/S1010-6030(98)00265-2.

[415] Pal, S.; Moza, P.N.; Kettrup, A. Photochemistry of Pendimethalin. *J. Agric. Food Chem.* **1991**, *39*, 797–800. https://doi.org/10.1021/jf00004a037.

[416] Sanlaville, Y.; Guittonneau, S.; Mansour, M.; Feicht, E.A.; Meallier, P.; Kettrup, A. Photosensitized Degradation of Terbuthylazine in Water. *Chemosphere* **1996**, *33*, 353–362. https://doi.org/10.1016/0045-6535(96)00176-2.

[417] Di Paola, A.; Addamo, M.; Augugliaro, V.; García-López, E.; Loddo, V.; Marci, G.; Palmisano, L. Photolytic and TiO_2-Assisted Photodegradation of Aqueous Solutions of Tetracycline. *Fresenius Environ. Bull.* **2004**, *13*(11b), 1275–1280. Presented at the 12th International Symposium on Environmental Pollution and its Impact on Life in the Mediterranean Region, Antalya, Turkey, 4–8 October 2003.

[418] Addamo, M.; Augugliaro, V.; Di Paola, A.; et al. Removal of Drugs in Aqueous Systems by Photoassisted Degradation. *J. Appl. Electrochem.* **2005**, *35*, 765–774. https://doi.org/10.1007/s10800-005-1630-y.

[419] Turchi, C.S.; Ollis, D.F. Photocatalytic Degradation of Organic Water Contaminants: Mechanisms Involving Hydroxyl Radical Attack. *J. Catal.* **1990**, *122*, 178–192. https://doi.org/10.1016/0021-9517(90)90269-P.

[420] Okamoto, K.; Yamamoto, Y.; Tanaka, H.; Tanaka, M.; Itaya, A. Heterogeneous Photocatalytic Decomposition of Phenol over TiO_2 Powder. *Bull. Chem. Soc. Jpn.* **1985**, *58*, 2015–2022. https://doi.org/10.1246/bcsj.58.2015.

[421] Minero, C.; Aliberti, C.; Pelizzetti, E.; Terzian, R.; Serpone, N. Kinetic Studies in Heterogeneous Photocatalysis. 6. AM1 Simulated Sunlight Photodegradation over Titania in Aqueous Media: A First Case of Fluorinated Aromatics and Identification of Intermediates. *Langmuir* **1991**, *7*, 928–936. https://doi.org/0743-7463/91/2407-0928$02.50/0.

[422] D'Oliveira, J.C.; Al-Sayyed, G.; Pichat, P. Photodegradation of 2- and 3-Chlorophenol in Titanium Dioxide Aqueous Suspensions. Environ. Sci. Technol. **1990**, 24, 990–996. https://doi.org/10.1021/es00077a007

[423] Di Paola, A.; Augugliaro, V.; Palmisano, L.; Pantaleo, G.; Savinov, E. Heterogeneous Photocatalytic Degradation of Nitrophenols. *J. Photochem. Photobiol. A Chem.* **2003**, *155*, 207–214. https://doi.org/10.1016/S1010-6030(02)00390-8.

[424] Augugliaro, V.; Palmisano, L.; Sclafani, A.; Minero, C.; Pelizzetti, E. Photocatalytic Degradation of Phenol in Aqueous Titanium Dioxide Dispersions. *Toxicol. Environ. Chem.* **1988**, *16*, 89–109. https://doi.org/10.1080/02772248809357253.

[425] Wang, K.-H.; Hsieh, Y.-H.; Chou, M.-Y.; Chang, C.-Y. Photocatalytic Degradation of 2-Chloro and 2-Nitrophenol by Titanium Dioxide Suspensions in Aqueous Solution. *Appl. Catal. B Environ.* **1999**, *21*, 1–8. https://doi.org/10.1016/S0926-3373(98)00116-7.

[426] Augugliaro, V.; Palmisano, L.; Schiavello, M.; Sclafani, A.; Marchese, L.; Martra, G.; Miano, F. Photocatalytic Degradation of Nitrophenols in Aqueous Titanium Dioxide Dispersion. *Appl. Catal.* **1991**, *69*, 323–340. https://doi.org/10.1016/S0166-9834(00)83310-2.